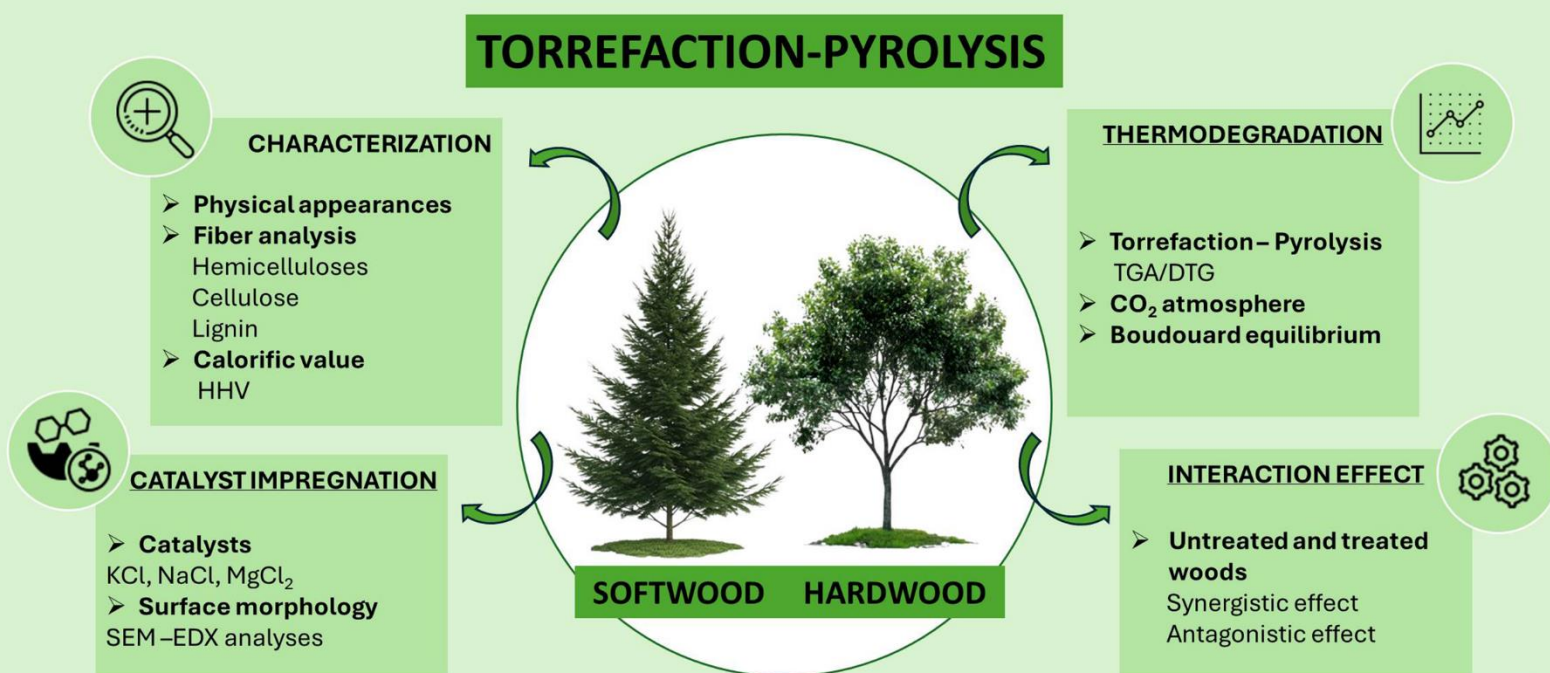# Green Energy and Fuel Research

Synergistic and Antagonistic Effects of Catalytic Torrefaction-Pyrolysis of Woody Biomass in a Carbon Dioxide Atmosphere for Biofuel Production

Scilight

Content

Vol.2 Iss.2 Jun 2025

Scilight

Harnessing Stress: Conventional and Unconventional Strategies for Enhancing Microalgal Productivity in Sustainable Biorefineries

Chia-En Chuang [1,†], Yu-Han Chien [1,†], Sheng-Yung Lin [1,†], Adi Kusmayadi [2], Jia-Hui Zhou [1], Chiao Ching Chang [1], Chen Rui Zhang [1] and Yoong Kit Leong [1,3,*]

[1] Department of Chemical and Materials Engineering, Tunghai University, Taichung 407, Taiwan
[2] Department of Mechanical Engineering, Politeknik Negeri Indramayu, Indramayu 45252, Indonesia
[3] Research Center for Smart Sustainable Circular Economy, Tunghai University, Taichung 407, Taiwan
* Correspondence: yoongkit1014@thu.edu.tw
† These authors contributed equally to this work.

Abstract: Microalgae are versatile platforms for producing biofuels and high-value metabolites, such as lipids, proteins, and carotenoids. Numerous stress strategies have been adopted to improve microalgal cultivation and biomolecule yield. This review examines how conventional stress factors (light and salinity) and unconventional treatments (electric field treatment) influence microalgal growth and metabolite accumulation. Light intensity, spectrum, and photoperiod significantly affect photosynthesis, biomass yield, and carotenoid biosynthesis, with moderate intensities found to enhance efficiency. However, excessive levels may induce photoinhibition. Salinity stress induces activation of antioxidant systems and lipid accumulation, optimizes biofuel properties. However, excessive high salinity can impair the growth of microalgae. In this review, we focused on the electric field treatment as a potential strategy for enhancing microalgal productivity, representing a major novelty of the study. Unlike traditional stress factors that primarily induce adaptive metabolic shifts, electric field treatment offers a unique and an understudied approach for modulating cellular physiology. Electric treatment technology offers an energy-efficient method for stimulating cell differentiation and enhancing lipid and pigment production while reducing environmental effects. Integrating these stress factors may be an attractive approach for controlling over microalgal metabolism, supporting sustainable and scalable biorefinery applications.

Keywords: light modulation; salinity stress; pulsed electric field; sustainable biofuel; stress-induced pathways; metabolic engineering

1. Introduction

Microalgae are crucial to the Earth's ecosystem, not only serving as oxygen producers, but also major carbon cycling regulators, contributing global climate regulation [1]. As primary producers, microalgae form the foundation of marine and freshwater food chains, providing organic matter essential for other aquatic organisms. Their ability to fix carbon dioxide makes them a potential tool for mitigating climate change. As the global demand for carbon reduction and carbon capture technologies grows, the unique characteristics of microalgae are increasingly studied in environmental science and sustainable development fields.

With the advancement of microalgae biotechnology and the development of large-scale production techniques, the applications of microalgae in energy, environmental protection, pharmaceuticals, and cosmetics continue to grow, making significant contributions to the sustainable development of green economy [2,3]. Compared to traditional crops, microalgae do not require large amounts of land and freshwater, and can be cultivated in closed or non-traditional environments. This makes them ideal sources of sustainable energy. Microalgae can produce valuable biomass such as lipids, proteins, and carbohydrates, which can be used to produce biofuels like biodiesel and bioethanol [4,5]. Furthermore, the bio-oil produced by microalgae is a major ingredient to the future development of renewable energy, capable of meeting energy demands without relying on traditional agricultural land. This efficient biofuel production method makes microalgae an important alterative approach for addressing the global energy shortage [6].

However, the growth of microalgae in extreme environments, particularly under conditions of high salinity, nutrient deficiencies, temperature fluctuations, and pH changes, is limited [7]. These factors can affect their growth and biomass production. Nevertheless, microalgae possess strong adaptive capabilities, enabling them to survive and continue growing under adverse conditions. Microalgae accumulate various energy reserves, such as lipids and starch, which help them maintain their growth under unfavorable environments. In nutrient-deficient or high-salinity environments, microalgae adapt to changes in external conditions by regulating their internal osmotic pressure, and they can convert some of their photosynthetic products into higher-energy substances, such as stored lipids. This is crucial for microalgae growth and biofuel production. Based on these adaptive abilities, microalgae have broad potential applications in environmental protection.

Although extensive research has been conducted on conventional stress factors such as light intensity and salinity, the impact of unconventional stressors like electric field treatment on microalgae metabolism has not been sufficiently investigated. This review provides a comprehensive analysis of conventional and unconventional stress conditions, emphasizing their influence on microalgae growth, biomass composition, and metabolite accumulation.

2. Effect of Light Stress on Microalgal Growth and Metabolites Accumulation

Light is a fundamental driver of microalgal growth and metabolism, influencing photosynthesis, pigment composition, biomass yield, and the accumulation of high-value compounds such as carotenoids and lipids. Numerous studies have demonstrated the significance of fine-tuning light intensity, quality (spectrum), and photoperiod in optimizing the growth and biochemical composition in diverse microalgal species, as shown in Figure 1 [8]. Therefore, understanding how different light regimes affect microalgal physiology is critical for improving commercial cultivation strategies, such as biofuels, nutraceuticals, cosmetics, or other valuable bioproducts.
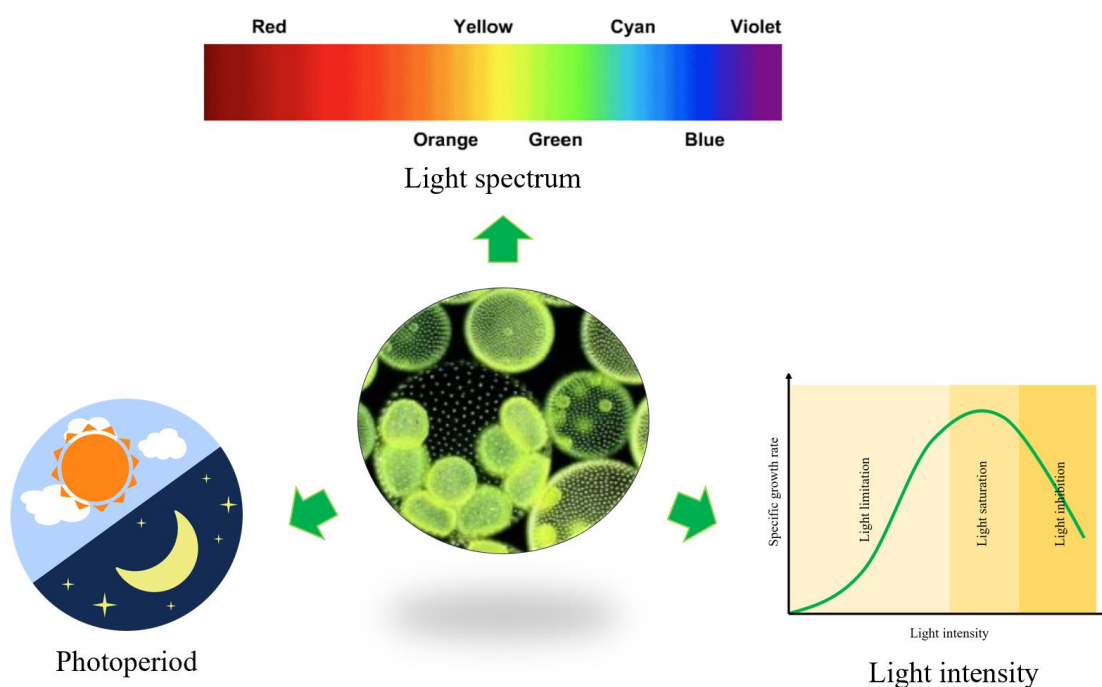
Figure 1. Light factors affecting microalgal growth and metabolite accumulation.

2.1. Influence of Light Stress on Microalgal Growth and Pigment Composition

Microalgae are phototrophic organisms that depend on photosynthetically active radiation (PAR, 400–700 nm) to drive photosynthesis. PAR can be expressed in terms of photosynthetic photon flux density (PPFD, μmol m^{-2} s^{-1}), which represents the number of photons available for photosynthesis, or as photosynthetic radiant flux density (PAR irradiance, W m^{-2}), which can be more useful when considering energy balances [9,10]. The amount of PAR that reaches the microalgal cells is influenced by multiple factors: the type of light source, the configuration and material of the cultivation vessel, the position of the cultures relative to the light source, and the optical properties of both the growth environment and the cells themselves. In dense cultures, mutual shading reduces the effective amount of light that reaches each cell, influencing pigment accumulation and overall productivity [11].

In photosynthetic organisms like green algae, light-harvesting complexes (LHCs) contain antenna pigments including chlorophyll a, chlorophyll b, and carotenoids. These pigments funnel absorbed light energy to the reaction centers of photosystems I and II, ensuring efficient utilization of available photons. Carotenoids, such as lutein and β-carotene, play critical roles in both light capture (particularly absorption in the blue light region) and photoprotection. They shield the photosynthetic apparatus from oxidative damage induced by high-intensity light, mitigating the formation of reactive oxygen species (ROS) [12,13].

2.2. Photoprotective Mechanisms against Light Stress in Microalgae

The xanthophyll cycle is a critical photoprotective mechanism that modulates carotenoid composition in response to changing light conditions. Under high light intensity condition, violaxanthin can be de-epoxidized to zeaxanthin, which helps dissipate excess energy as heat, reducing photodamage. Enzyme regulation within the cycle (e.g., violaxanthin de-epoxidase (VDE) and zeaxanthin epoxidase (ZEP)) is tightly controlled by light conditions [14,15].

In diatoms like *Phaeodactylum tricornutum*, multiple isoforms of ZEP and VDE are involved. High light intensity (700 µmol photons m^{-2} s^{-1}) early in the growth phase can upregulate VDE, VDL1, and ZEP3 while downregulating ZEP1, leading to the activation of both the diadinoxanthin and violaxanthin cycles and reducing fucoxanthin accumulation—a photoprotective adaptation to intense irradiance [15].

The regulatory effects of light intensity on carotenoid enzymes have been studied extensively in several model microalgal species. In *Haematococcus pluvialis*, high light intensity (150 µmol photons m^{-2} s^{-1}) induces the expression of ipiHp2, which encodes isopentenyl diphosphate isomerase (IDI)—an enzyme that shifts metabolism toward enhanced carotenoid accumulation [16]. Similarly, enzymes like phytoene synthase and phytoene desaturase are upregulated with a maximum increase of 4 to 5 times under high light intensity (200 µmol photons m^{-2} s^{-1}) in *Chlamydomonas reinhardtii*, leading to increased carotenoid content up to 1.3- to 1.5-fold [17]. In *Chromochloris zofingiensis*, elevated light intensity (400 µmol photons m^{-2} s^{-1}) upregulates lycopene beta cyclase (LCYB) while downregulating lycopene epsilon cyclase (LCYE), shifting carotenoid synthesis toward β-carotene at the expense of lutein.

This reprogramming under high light intensity is a photoprotective response aimed at mitigating oxidative stress. By enhancing carotenoid production, cells protect their photosystems against ROS. However, the trade-off is that very high light intensities may reduce overall growth [18]. Thus, commercial cultivation strategies must balance the desire for higher carotenoid yields while maintaining sufficient biomass production. Optimal conditions often involve moderately high but non-inhibitory light intensities.

In *Chromochloris zofingiensis*, increased β-carotene and astaxanthin production under high light intensity (400 µmol photons m^{-2} s^{-1}) is accompanied by alterations in xanthophyll cycle components. β-carotene hydroxylase (BCH) and β-carotene ketolase (BKT) enzymes are upregulated, promoting astaxanthin synthesis. However, the limited zeaxanthin availability caused by increased BKT activity modifies the violaxanthin cycle, upregulating VDE and downregulating ZEP and violaxanthin de-epoxidase–like (VDL), which promotes zeaxanthin conversion into astaxanthin and decreasing violaxanthin and neoxanthin levels [19].

Although not the primary focus here, light interacts with other environmental variables, such as nutrient availability (especially nitrogen), carbon sources, and mixing regimes. Some studies have reported that under mixotrophic conditions—where microalgae can utilize both inorganic (light-driven) and organic carbon sources— moderate increases in light intensity can improve CO_2 fixation. Simultaneously, the TCA cycle might be inhibited to optimize carbon metabolism, ensuring that photosynthesis and heterotrophy complement each other. Such synergy results in a high organic carbon utilization capacity and improved pollutant removal in wastewater treatments. Appropriate light intensities enhance the contribution of photosynthesis to growth and pollutant removal in these systems, underscoring the need for adoption of tailored lighting regimes in environmental biotechnology applications.

2.3. Effect of Light Intensity

Light intensity is a central parameter affecting microalgal growth, photosynthetic capacity, and the regulation of enzymes involved in carotenoid biosynthesis. Moderate increases in light intensity generally enhance photosynthetic efficiency and promote higher growth rates until a species-specific saturation point is reached [20]. Beyond this saturation point, further increases in light intensity can lead to photoinhibition, reducing photosynthetic efficiency, and ultimately lowering biomass yields [18]. Tables 1 and 2 displayed the effect of light quality and photoperiod on lipid and pigment accumulation by microalgae.

Table 1. Effect of light quality and photoperiod on lipid accumulation in microalgae.

Algal Species	Light Color	Light Intensity	Light Duration (Light:Dark)	Biomass Concentration (g/L)	Lipid Production	References
Amphiprora sp.	white	24 µmol/m^2/s	16:8	0.26	135.60 mg/L	[21]
Chlorella pyrenoidosa	white	4000 lux	19:5	0.61	170.00 mg/L	[22]
Chlorella sorokiniana C16	white	10,000 lux	24:0	5.20	27.0 wt%	[23]
Chlorella sorokiniana CY-1	white	8000 lux	24:0	2.12	11.21 wt%	[24]
Chlorella vulgaris	red	-	12:12	3.53	25.50 wt%	[25]
Chlorella vulgaris	-	-	-	3.46	55.2 wt%	[26]

Table 2. Effect of light quality and photoperiod on pigment accumulation in microalgae.

Pigment	Algal Species	Light Color	Light Intensity (µmol/m^2/s)	Light/Dark Period	Biomass Concentration (g/L)	Pigment Production	References
Astaxanthin	*Aurantiochytrium* sp. CJ6	White	250	Continuous (4 days)	9.01	78.3 µg/g	[27]
	Chromochloris zofingiensis	Blue	—	—	204.5	0.28 g/L	[28]
	Haematococcus pluvialis	White	480	Continuous	0.43	26.77 mg/L/d	[29]
	Haematococcus sp.	Red (5 days) followed by Blue (5 days)	40	Continuous	1.33	3.39 mg/L	[30]
	Oedocladium carolinianum	Red	—	Continuous	0.29	2.89 mg/L/d	[31]
Fucoxanthin	*Chaetoceros calcitrans*	Blue	110	12:12	—	3.2 mg/L/d	[32]
	Isochrysis sp.	—	200	12:12	—	6.11 mg/g	[33]
	Odontella aurita	Red/blue light (8:2 ratio)	300	Continuous	0.57	9.41 mg/L/d	[34]
	Pavlova sp.	White	75	Continuous	1.1	7.02 mg/L/d	[35]
	Phaeodactylum tricornutum	White	8.0	Continuous	6.0	26 mg/g	[36]
Lutein	*Chlorella sorokiniana* C16	White	10k lux	Continuous	5.2	17.4 mg/g	[23]
	C. sorokiniana F31	—	211	Continuous	—	15.55 mg/g	[37]
	C. sorokiniana FACHB-275	White	2200 Lux	Continuous	1.14	8.45 mg/g	[38]
	C. sorokiniana MB-1-M12	White	150	Continuous	3.54 (Auto), 2.77 (Mixo)	6.16 mg/g, 4.10 mg/L/d (Auto); 6.48 mg/g, 4.50 mg/L/d (Mixo)	[39]
	Chlorella sp. HS5	Dark	Dark conditions	Continuous	—	3.7 mg/g	[40]
	Chlorophyta MCH-35	Blue	80	Continuous	—	3 mg/g	[41]
	Coccomyxa subellipsoidea	White	240	Continuous	9.40	1.65 mg/g	[42]
	Scenedesmus sp. FSP3	White	1st stage—90, 2nd stage—160	Continuous	1.97	6.34 mg/g, 2.30 mg/L/d	[43]

Bialevich et al. showed that microalgae can increase their growth rates with rising light intensity until saturation. *Desmodesmus quadricauda* and *Parachlorella kessleri* reached saturation at around 250 µmol photons m^{-2} s^{-1}, while *Chlamydomonas reinhardtii* tolerated up to 500 µmol photons m^{-2} s^{-1} [44]. Similarly, Difusa et al. and others found that, although elevated light intensity can enhance lipid content in certain strains (e.g., *Scenedesmus* sp.), it may lower growth rates, suggesting the important of balancing between rapid biomass accumulation and formation of storage compounds like lipids [45].

Gim et al. explored the effects of light intensity (0–200 µmol photons m^{-2} s^{-1}) on three microalgae species—*Isochrysis galbana*, *Nannochloropsis oculata*, and *Dunaliella salina*. At 150 µmol photons m^{-2} s^{-1}, they observed peak fatty acid concentrations [46]. Specifically, *Isochrysis galbana* produced a biomass of 0.89 g/L with a lipid

content of 30.1% (dry weight), *Nannochloropsis oculata* achieved a biomass of 1.69 g/L with a lipid content of 38.5%, and *Dunaliella salina* reached a biomass of 1.17 g/L with a lipid content of 32.4%. They also found that excessive light induced oxidative damage, while low light limited photosynthetic efficiency. Moderate light intensities (80–150 µmol photons $m^{-2}\,s^{-1}$) offered the best condition for lipid accumulation, providing a balanced growth environment.

Cheirsilp & Torpee studied marine *Chlorella* sp. and *Nannochloropsis* sp. under mixotrophic conditions and varying light intensities (ranging from 2000 to 10,000 lux, approximately 30–150 µmol photons $m^{-2}\,s^{-1}$ depending on conversion) [47]. Notably, the biomass production increased as the light intensity was elevated up to a certain point but diminished lipid accumulation. For *Chlorella* sp., the maximum biomass was achieved at 8000 lux, with a dry weight of 3.97 g/L, while its lipid content reached 397.8 mg/L under the same conditions. In contrast, *Nannochloropsis* sp. continued to grow until 10,000 lux, reaching a peak biomass of 5.87 g/L and a lipid yield of 481.0 mg/L. However, at higher light intensities, lipid accumulation in both species decreased, suggesting a trade-off between growth and lipid production.

Under low light, photosynthetic efficiency and growth rates are generally reduced, limiting the large-scale cultivation. However, phytohormones like melatonin (MT) and indole-3-propionic acid (IPA) can redirect carbon flux toward carbohydrates and proteins, enhancing yields even under suboptimal light (as described in the CAMC systems discussion). Although the details are not well understood, this suggests that biochemical interventions or combined strategies may compensate for low-light conditions [48].

2.4. Effect of Light Quality

Besides intensity, light quality (spectral composition) also significantly affects microalgal photosynthesis and metabolism. Light-emitting diode (LED) technology has advanced rapidly, offering precise control over the wavelength distribution. Different spectral regions (e.g., blue: 450–475 nm; red: 630–660 nm) influence photosynthetic pigments and can shift metabolic pathways [49].

Kim et al. demonstrated that combining blue and red LED lights increased the production rate of *Scenedesmus* sp. by ~50% compared to a single-wavelength treatment [20]. The improved photosynthetic efficiency under mixed blue-red illumination was due to the complementarity of absorption peaks of chlorophylls and carotenoids. Blue light is absorbed efficiently by carotenoids and can enhance carotenoid synthesis, while red light tends to stimulate growth and enhance photosynthetic reaction center efficiency.

Similarly, You & Barnett observed that blending blue and red light enhanced the growth rate of *Porphyridium cruentum* by enhancing photosynthetic activity and reached its maximum cell density of 4×10^9 cells L^{-1} [50]. Studies on *C. vulgaris* have also indicated that red light alone or combined with other wavelengths can boost biomass accumulation with biomass increased from 2.07 to 2.64 g/mL [51].

2.5. Effect of Photoperiod and Temporal Light Modulation

The duration of the light period and the ratio of light-to-dark cycles (photoperiod) influence cellular metabolism, growth cycles, and resource allocation. Maltsev et al. found that a 16:8 h light/dark cycle efficiently balanced biomass production, increasing it by 22%, and ellicited a 19% increase in total fatty acid (TFA) content [8]. Light/dark cycles allow microalgae to repair photosynthetic machinery and balance their energy and carbon budgets. On the other hand, Vélez-Landa et al. demonstrated that a balanced light/dark cycle (12:12) achieved the highest biomass density of 6.3×10^6 cells/mL and lipid content of 50.42% in *Verrucodesmus verrucosus* [52]. The study found that continuous light (24:0) led to diminished lipid yields, while shorter dark periods (16:8) resulted in lower growth and lipid accumulation. Therefore, these indicated that some species grow better under continuous light. In contrast, others benefit from dark periods that support respiration, intracellular reorganization, and nighttime metabolic pathways such as carbohydrate catabolism or lipid remodeling.

Flashing light regimes or combined continuous-plus-flashing conditions have proven beneficial in some cases [51]. These light strategies can improve photon utilization efficiency by providing saturating light pulses interspersed with "recovery" intervals. The result can be more efficient use of photons and enhanced growth compared to continuous, non-modulated illumination.

Abu-Ghosh et al. investigated the combination of flashing light with continuous background light in *Dunaliella salina* [51]. The combined light regime significantly enhanced photosynthetic efficiency and growth beyond continuous or flashing light alone. At an intermediate light intensity of 250 µmol photons $m^{-2}\,s^{-1}$, the combined regime resulted in an optical density (OD) of 1.4, compared to 0.9 for continuous light and 1.1 for flashing light. Similarly, the dry biomass reached 2.52 g/L under the combined regime, surpassing the 1.87 g/L and 2.01 g/L observed under continuous and flashing light, respectively. Photosynthetic activity, measured as

oxygen production rates, was also significantly higher at 148.9 μmol O_2 (mmol Chl)$^{-1}$ s^{-1}, compared to 31.6 and 47.3 under continuous and flashing light alone.

Under optimal conditions, irradiating *C. vulgaris* with red light and combining this approach with indole-3-acetic acid (IAA) treatment can further enhance biomass production. Studies showed that red light stimulated photosynthetic capacity, respiration, and quantum yield, leading to higher biomass levels (3.19 g L^{-1}) compared to white light conditions (2.78 g L^{-1}) [25]. Combining IAA and red light increased biomass production to 3.53 g L^{-1}, translating to a 27% increase in productivity.

2.6. Commercial and Biotechnological Implications

Optimizing light conditions, intensity, spectrum, and photoperiod, may improve the large-scale cultivation of microalgae at industrial scales. Target compounds, such as lipids for biofuels or high-value pigments like astaxanthin and β-carotene, reach maximum accumulation under stress conditions associated with altered light regimes. For instance, high light stress can trigger carotenoid accumulation as a photoprotective mechanism, providing a valuable product. However, this often comes at the cost of slower growth rates or photoinhibition, which can reduce total volumetric yields [47].

To overcome the above limitations, dynamic lighting strategies and engineering approaches have been proposed. Photobioreactors can be designed to distribute light uniformly and minimize self-shading, or they can use artificial illumination (LEDs) to deliver customized light wavelengths and intensities at different growth stages. Pulsing or flashing lights and meticulously selected photoperiods can further enhance efficiency [46].

An accurate assessment of the available light for microalgae is often challenging. The quantity of PAR available to cells depends on the arrangement and properties of the cultivation system, whether it be photobioreactors, flasks, or open ponds. Mutual shading by cells in dense cultures, light scattering by flask walls, and reflection from surfaces are major factors limiting the measurement. In practice, PPFD is frequently measured outside the culture vessel as a proxy, but this can lead to discrepancies between measured and actual photon availability to the cells [9,10]. Such measurement challenges underscore the need for careful system design and calibration. In particularly, for large-scale applications, ensuring uniform light distribution and avoiding excessive shading are paramount for maximizing productivity.

Commercial microalgal production aims to maximize valuable compounds, such as carotenoids, lipids, and other bioproducts, while maintaining their growth rates. High light intensities and specific spectral qualities can increase carotenoid accumulation, but might simultaneously lower biomass yield due to photoinhibition. Achieving an optimal compromise is critical. Conditions that yield the highest pigment concentrations may not support rapid cell growth, reducing overall productivity on a volumetric basis [18].

One strategy is to modulate light intensities throughout cultivation. Early growth phases might benefit from moderate light to support robust biomass production, while later stages could involve a shift to higher light intensities or different wavelengths to boost carotenoid or lipid synthesis. Such dynamic lighting strategies leverage the physiological plasticity of microalgae [47].

Beyond physical and environmental controls, biochemical strategies can complement light optimization, such as adding phytohormones or manipulating nutrient levels. When tuned appropriately, red and blue light combinations can substantially boost biomass and target compound accumulation. Similarly, altering the nitrogen supply (reducing it at a certain growth phase) while providing optimal light intensities and qualities can force cells into a desired metabolic state, potentially increasing lipid or carotenoid yield without excessively compromising growth.

As the microalgae industry continues to develop, optimizing light conditions will enhance the degree of biomass production and accumulation of high-value compounds. Future research should aim to develop approaches for enhancing light regulation, adjusting light intensity, spectrum combinations, and photoperiods to achieve precise control of microalgal metabolic pathways. For example, moderate light intensities can be used in the early growth phase to promote biomass production, while higher light intensities or spectral shifts in later stages can induce carotenoid or lipid accumulation. Additionally, advancements in LED technology can generate new approaches of spectral control. The combination of blue and red light has been proven to enhance photosynthetic efficiency and product yield, and further refinement of spectral combinations could maximize productivity and energy efficiency.

Furthermore, the interaction between light and other environmental factors, such as nutrient availability and mixing conditions, need to be further investigated to optimize cultivation strategies for various applications. In wastewater treatment, for instance, tailored light conditions can improve microalgal carbon fixation and pollutant removal efficiency. Moreover, integrating biotechnological approaches, such as exogenous phytohormone

regulation or genetic modifications, may be effective in enhancing microalgal adaptability to light conditions and boost the production of target compounds. By combining these strategies, the commercialization of microalgae industry will be significantly improved and expanded to include diverse fields such as biofuels, nutritional supplements, and environmental remediation.

3. Effect of Salt Stress on Microalgal Growth and Metabolite Accumulation

3.1. Effect of Salinity on Biomass Production and Protein Accumulation

Literatures showed that moderate NaCl concentrations support photosynthesis, CO_2 fixation, and osmotic balance [53]. For examples, NaCl concentrations of 5–25 mM promoted growth of *Quadrigula closterioides*, with the highest lipid content of 50.94% dry weight recorded at 5 mM NaCl. However, as salinity exceeds 25 mM, growth and biomass production are inhibited, accompanied by morphological changes such as a shift from normal cell shape to spherical and even brown coloration, indicating an adaptive response to salt stress [54]. Similarly, moderate salinity levels (+100% to +400% NaCl) also enhance microalgal growth and biomass accumulation of *Scenedesmus obliquus*, with the highest biomass productivity of 0.206 g/L/d observed at +400% NaCl [55]. However, further increases in salinity to +600% and +800% NaCl resulted in significant biomass reductions of 32.2% and 50.3%, respectively, due to ROS accumulation and photosynthesis inhibition. Figure 2 depicts the effect of salt stress on microalgal growth and metabolite accumulation.
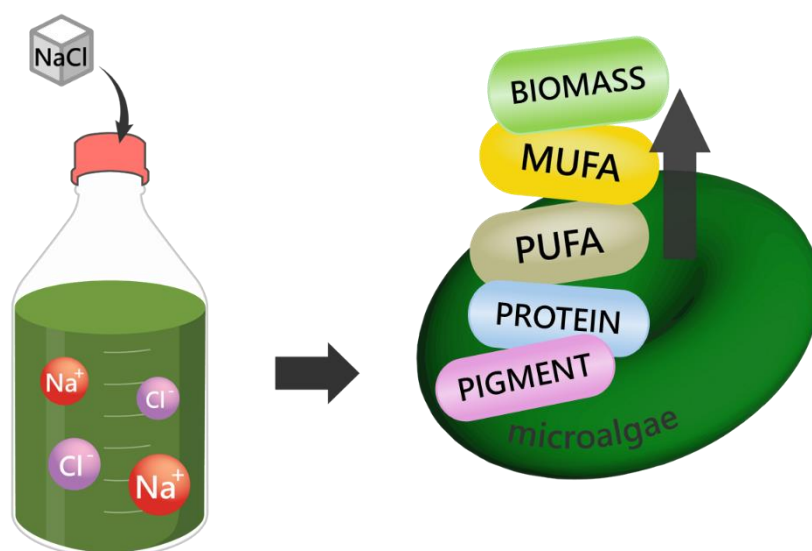

Figure 2. Effect of salt stress on microalgal growth and metabolite accumulation.

There are limited studies of salinity effect on protein accumulation. The *Vischeria punctata* strain IPPAS H-242 exhibited higher protein content of 259 mg/g DW under salt stress of 0.4 mM NaCl, which could be due to the need for cells to synthesize more proteins to cope with environmental stress [56]. The increased protein content may help maintain cellular functions and survival, particularly in response to oxidative stress and changes in osmotic pressure caused by salinity. Despite the overall increase in protein content, the level of D1 protein, which is associated with photosynthesis, significantly decreased under salt stress, suggesting that salt stress may impact the effectiveness of photosynthesis. The increase in total protein content under salt stress may be an adaptive mechanism for cells to withstand environmental pressures, but it also negatively affects certain key photosynthetic proteins. These changes are significant for understanding the physiological responses of microalgae under stress and their potential biotechnological applications.

3.2. Effect of Salinity on Lipid Accumulation

NaCl concentrations can significantly influence microalgal lipid content and quality, fatty acid composition, and eventually the fuel performance of biodiesel. Salinity stress can induce the generation of ROS, activates antioxidant enzyme systems (e.g., superoxide dismutase (SOD) and catalase (CAT)), and upregulates lipid synthesis-related gene expression, promoting triacylglycerol (TAG) accumulation and redirecting metabolic carbon flow from starch to lipid synthesis [57]. Additionally, optimal salinity stress was reported to increase the

production of fatty acid methyl ester (FAME) by up to 1.8 times and optimized its composition by increasing the proportions of saturated and monounsaturated fatty acids (e.g., C16:0 and C18:1), significantly improving biodiesel stability and combustion performance. However, excessive salinity can inhibit growth, although it may still induce lipid synthesis through oxidative stress. Therefore, salt stress serves as an effective induction strategy with broad applications in the production of microalgal biofuels and high-value products. Table 3 displayed the effect of salt stress on lipid accumulation by microalgae.

Table 3. Effect of salt stress on lipid accumulation in microalgae.

Algal Species	Conditions	Lipid Accumulation	References
Aurantiochytrium sp.	Natural seawater	62.4%	[58]
Botryococcus sp. NJD-1	10 g/L NaCl	54.5%	[59]
Chlamydomonas sp.	3% & 7% sea salt concentration	31.7–37.2%	[56]
Parachlorella kessleri IC-11	30 g/L NaCl	33.3% and 31.0% in Bold's Basal Medium and wastewater	[60]
Quadrigula closterioides	5 mM NaCl	50.94%	[54]
Scenedesmus quadricauda FACHB-1297	0.88 & 2.63 g/L salt and xylose concentration	39.33%	[57]
Scenedesmus sp.	100 mM NaCl & 10 mM H_2O_2	Increased by 226.4 µg/mg	[61]
Thraustochytrium sp. BM2	20 g/L NaCl	79%	[62,63]

Studies have shown that microalgae exhibit significant metabolic responses and lipid accumulation mechanisms under different salinity stress conditions, demonstrating the significance of salinity as a critical factor influencing lipid production. Most studies agreed that moderate salt concentrations significantly enhance lipid content, with some microalgae achieving lipid content exceeding 50%, such as *Botryococcus* sp. NJD-1 (10 g/L NaCl, lipid content and productivity of 54.5% and 110.5 mg/L/d) [59] and *Quadrigula closterioides* (5 mM NaCl, lipid content of 50.94%) [54]. Liu et al. also reported that under moderate salinity levels (0.88–2.63 g/L), *Scenedesmus quadricauda* FACHB-1297 effectively adapts to salt stress, achieving high biomass and lipid accumulation, with the highest lipid content of 39.33% observed at the optimal salinity of 2.63 g/L [57].

Under moderate salinity level, salt stress-induced ROS triggered antioxidant defenses and increased nicotinamide adenine nucleotide phosphate (NADPH) production through the pentose phosphate pathway and pyruvate-malate cycle, supporting fatty acid synthesis [59]. The generation of ROS activates antioxidant enzyme activity and upregulates lipid synthesis-related genes (e.g., glycerol-3-phosphate acyltransferase (GPAT) and diacylglycerol acyltransferase (DGAT)), promoting neutral lipids accumulation (particularly TAG) and redirecting metabolic flux from carbohydrates to storage lipids [57]. Neutral lipids are synthesized primarily via the acetyl-CoA-dependent Kennedy pathway as a byproduct of ROS detoxification [59]. Excessive salinity, however, results in ROS overaccumulation, inducing cellular damage and inhibiting the growth of microalgae and lipid accumulation [54].

However, Sorokina and colleagues revealed that high salt concentration (30 g/L) significantly enhanced neutral lipid accumulation of *Parachlorella kessleri* IC-11 cultivated in Bold's Basal Medium (BBM) and municipal wastewater (WW), with lipid content reaching 33.3% and 31.0% in BBM and WW, respectively [60]. Salt stress induced a reprogramming of carbon flux and energy storage, reducing adenosine metabolism in BBM and significantly affecting proline metabolism and the citric acid cycle in WW. It also increased the proportion of saturated fatty acids (SFA) and monounsaturated fatty acids (MUFA) in lipid composition, improving biodiesel quality. Nevertheless, high salt levels still causing some negative impact, where the chemical oxygen demand (COD) removal efficiency in WW was reduced, indicating that decreased biomass under salt stress limited wastewater treatment efficiency.

The combined application of gamma-aminobutyric acid (GABA) and salinity has been found to enhance lipid accumulation and biomass productivity in the green microalga *Ankistrodesmus* sp. EHY [64]. Under 2.5 g/L NaCl with 50 µM GABA, lipid content reached 59.42%, and lipid productivity increased to 235.13 mg/L·d, representing 1.36-fold and 1.27-fold increases compared to salinity alone and the control, respectively. Transcriptomic and metabolomic analyses revealed that the combination of GABA and moderate salinity also increased the levels of intermediates in the tricarboxylic acid (TCA) cycle and the GABA shunt, which served as carbon sources and energy for lipid accumulation. Furthermore, the combined treatment improved the fatty acid composition of biodiesel by increasing saturated and monounsaturated fatty acid content, enhancing fuel quality. In 5-L fermenter-scale experiments, the combined strategy significantly improved lipid content and productivity, demonstrating its potential for large-scale microalgal biofuel production.

Under single-stage cultivation conditions, the combined supplementation of glucose and salt significantly enhanced the biomass and lipid production efficiency of *Graesiella emersonii* NC-M1 [65]. Incorporation of 1.75 g/L glucose and 0.3 M NaCl, biomass concentration, lipid concentration, and lipid productivity increased by 3.3-fold, 4.63-fold, and 4.56-fold, respectively, compared to the control. Glucose promoted glycolysis and the pentose phosphate pathway, supporting rapid microalgal growth, while salt stress redirected carbon flux from starch synthesis to lipid synthesis, significantly increasing neutral lipid (particularly TAG) accumulation. Transcriptomic analysis revealed significant upregulation of genes related to cell proliferation, photosynthesis, and NADPH production, while starch synthesis genes were downregulated. Additionally, salt stress elevated intracellular ROS, further activating lipid synthesis-related genes and enhancing lipid accumulation. The combined strategy also optimized FAME profiles, increasing saturated and monounsaturated fatty acid content, while improving biodiesel properties such as cetane number, oxidative stability, and viscosity.

In a two-stage cultivation system, red light and salt stress significantly enhanced the production of high-value compounds in *Chlorella sorokiniana* and improved biodiesel quality [66]. During the second stage, 2-fold salt concentration (0.05 g/L NaCl) increased lipid content from 30.6% to 37.5%, representing a 22.54% improvement. Salt stress also induced the synthesis of polyunsaturated fatty acids (PUFAs) and promoted TAG accumulation by altering cell size and stability, though it caused a reduction in protein content, indicating a metabolic shift towards lipid synthesis. Furthermore, salt stress improved the FAME profile by increasing the proportion of saturated and monounsaturated fatty acids while reducing that of polyunsaturated fatty acids, thereby enhancing biodiesel stability and combustion performance. Integration of salt stress with red light further boosted photosynthetic pigment and lipid production, with carotenoid content increasing by 62.21% and lipid accumulation efficiency significantly enhanced.

Anand and colleagues explored the effects of multi-component stress conditions (salt concentration, nitrate, phosphate, and hydrogen peroxide) on the growth and lipid accumulation of *Scenedesmus* sp., evaluating their potential to enhance biodiesel quality [61]. The results showed that under conditions of 100 mM NaCl, 35.29 mM $NaNO_3$, 5.74 mM K_2HPO_4, and 10 mM H_2O_2, lipid content significantly increased to 226.4 μg/mg, which is 1.3 times higher than without H_2O_2.

Kato and coworkers demonstrated that salt-resistant *Chlamydomonas* sp. JSC4 mutant strains, developed through heavy ion beam mutagenesis and high-salinity adaptation, could grow in 7% seawater, achieving a biomass concentration of 4.08 g/L, which was higher than that of the parental strain [56]. It was further revealed that the expression of key genes related to salt-induced starch-to-lipid biosynthesis switching was suppressed in the salt-resistant strains, which may explain the reduced lipid synthesis. Furthermore, no cellular aggregation or hypertrophy occurred in the salt-resistant strains under salinity stress, indicating their enhanced salt tolerance.

3.3. Effect of Salinity on Pigment Accumulation

Under moderate salinity, photosynthesis in microalgae may be enhanced, thereby promoting the synthesis of pigments. Moderate salt level can induce the generation of appropriate levels of ROS, activating antioxidant enzyme systems such as SOD and CAT, thereby promoting the accumulation of antioxidant pigments like lutein and carotenoids. Conversely, high salt concentrations may suppress the expression of photosynthetic pigments like chlorophyll, causing metabolic shifts toward antioxidant pigment production, reflecting a trend of metabolic redistribution [67].

Patel et al. reported that *Chlorella sorokiniana* C16 demonstrated significant enhancement in lutein production under optimized conditions of light intensity, temperature, salinity, and nutrient levels. Under 10 k lux light intensity, 32 °C temperature, and 25% seawater dilution, lutein content reached a peak of 17.4 mg/g [23]. The two-stage cultivation strategy further increased lutein production to 71.13 mg/L, with the first stage promoting biomass growth and the second stage inducing lutein and lipid accumulation. Excessive light intensity (>15 k lux), salinity (100% seawater), or nutrient concentration (4X BS) inhibited lutein accumulation, highlighting the importance of moderate environmental conditions for optimal production.

Under salt stress conditions, *Golenkinia* sp. SDEC-16 exhibits enhanced pigment metabolism changes, particularly the accumulation of carotenoids [67]. As salt concentration increases to 3%, chlorophyll content decreases about 58.4%, while carotenoid content rises approximately 2.5 times compared to the control group, scavenging the salt-induced ROS. Under high-salinity conditions (3%), ROS production increases by 6.6 times, activating antioxidant enzymes such as SOD. Carotenoids, acting as auxiliary antioxidants, play a crucial role in alleviating oxidative stress. Moreover, salt stress inhibits the activity of Photosystem II (PSII), reducing photosynthetic efficiency and prompting cells to enhance carotenoid synthesis to protect the photosynthetic apparatus from damage.

4. Effect of Electric Field on Microalgal Growth and Metabolite Accumulation

Electric field technology is an innovative tool that relies on electrical energy, and is widely applied in biotechnology, energy conversion, and environmental protection [68]. By applying static or dynamic electric fields, this technology can influence cell membrane permeability, cell metabolism, and the release of intracellular components. In microalgae research, the application of electric fields has garnered significant attention for effectively optimizing growth conditions, enhancing biomass yield, and promoting the accumulation of high-value bioproducts. Table 4 and Figure 3 displayed the effect of electric field treatment on biomass production and metabolite accumulation of microalgae.

Table 4. Effect of electric treatment on biomass production and metabolite accumulation.

| Algal Species	Electric Treatment Condition	Results	References
Acutodesmus dimorphus	10 kV LE-PEF, 2 s on, 60 s off	28.8% increase in lipid productivity	[69]
Chlorella vulgaris	nsPEF, 10–50 kV/cm	Significant increase in growth	[70]
Chlorella vulgaris	nsPEF, 100 ns pulse width, 60–100 mA DC	17.5% increase in growth	[71]
Chlorella vulgaris	nsPEF	Increased cultivation efficiency and growth	[72]
Chlorella vulgaris	Medium electric field (2.7 kV/cm), 50 min	51% increase in growth	[73]
Chlorella vulgaris	Post-incubation after PEF	Maximized lipid bioaccessibility post-incubation	[74]
Haematococcus pluvialis	100 mA DC	20% increase in growth	[75]
Pavlova gyrans	Electric field treatment	Increased lipid production	[76]
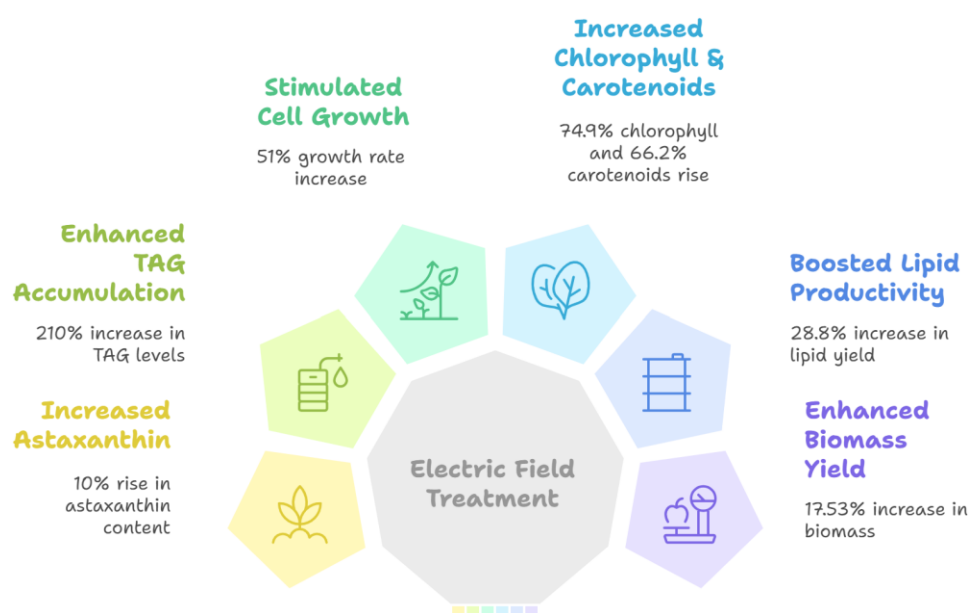
Figure 3. Effect of electric field treatment on microalgal growth and metabolite accumulation.

Periodic electrical treatment (100 mA applied every 4 days) enhanced growth and astaxanthin production of *Haematococcus pluvialis* [75]. Compared to the control, treated cultures exhibited a 20% increase in cell density and a 10% increase in astaxanthin content. This treatment also improved chlorophyll content (24.8 mg/L versus 19.8 mg/L) and accelerated nitrogen uptake, indicating enhanced nutrient utilization. Additionally, treated cells were smaller in size, suggesting active cell division and proliferation.

Mild electric stimulation at 4 V (31 mA cathodic current) for 4 h in a two-chamber electrochemical reactor equipped with carbon-cloth electrodes, using 100 mM sodium phosphate buffer (pH 7.0) and aeration at 100 mL/min, significantly enhanced the accumulation of neutral lipids and essential fatty acids in *Chlorella* sp. KR-1 [77]. Under these conditions, TAG content increased to 2.1 times that of untreated controls, while polyunsaturated fatty acids such as linoleic acid and linolenic acid increased by 36% and 57%, respectively.

The application of medium electric fields (1 to 10 kV/cm) to *Chlorella vulgaris* significantly stimulated cell growth, with a 51% increase in growth rate observed after 50 min of exposure to a moderate static electric field

(2.7 kV/cm) at a concentration of 0.4 g/L [73]. This growth enhancement was attributed to improved cell membrane permeability, facilitating nutrient uptake and promoting cell proliferation. However, prolonged exposure, such as 70 min, led to increased peroxide accumulation, resulting in oxidative stress and a decline in growth due to excessive ROS production, including hydroxyl radicals. At lower cell concentrations (e.g., 0.25 g/L), shorter treatment durations (e.g., 10 min) effectively promoted growth. Conversely, at higher concentrations, the optimal treatment duration increased, with a 70-min exposure found to be most effective for a concentration of 1.0 g/L.

Electric field treatment applied to the single-celled microalga *Pavlova gyrans* demonstrated a significant impact on its biochemical composition, despite not markedly promoting cell growth [76]. Under optimized conditions (0.54 V/cm), applied during the exponential growth phase on day 6 for durations of 6 h and 30 h, chlorophyll a and carotenoid content increased by 74.9% and 66.2%, respectively. Additionally, lipid, carbohydrate, and protein content rose by 4.72%, 18.7%, and 5.41%, respectively. These findings indicate that electric field treatment can effectively modulate the biochemical profile of microalgae, presenting a promising approach for regulating microalgal metabolism and enhancing biorefinery applications.

4.1. Pulsed Electric Field Treatment

Pulsed electric field (PEF) is a technology that applies high-intensity electric fields (10–50 kV/cm) to treat microalgae cells. In principal, PEF uses short-duration electrical pulses (ranging from nanoseconds to milliseconds) to induce electroporation in microalgae cell membranes, offering low energy consumption, lower thermal load, and efficient release of intracellular components [70].

For *Acutodesmus dimorphus*, optimized PEF treatment using a 10 kV low-energy pulse field (pulse cycle of 2 s on and 60 s off, lasting for 15 min, with six cycles per day) resulted in a 28.8% increase in lipid productivity [69]. PEF treatment at an electric field strength of 20 kV/cm, a pulse width of 5 μs, and an energy input of 31.8 kJ/kg, combined with post-PEF incubation at 25 °C or 37 °C for 12 h, or at 4 °C for 48 h, significantly enhanced lipid bioaccessibility in *Chlorella vulgaris*, increasing from 4–7.8% to 18.7–20.9% [74]. Microalgal lipid maintained good oxidative stability after 3 months of storage at 40 °C.

Nanosecond pulsed electric field (nsPEF) treatment significantly enhanced the biomass yield of *C. vulgaris*, achieving an increase of up to $17.53 \pm 10.46\%$ [71]. A pulse repetition frequency range of 1 Hz to 3.5 kHz ensured efficient treatment without excessive heat generation. Key parameters, including electric field strength, pulse repetition frequency, and pulse width, with the longest pulse width of 100 ns and electric field strength of 2.7 kV/cm is the most optimal for enhancing biomass yield while maintaining cell viability. The treatment primarily stimulated cell proliferation, suggesting that nsPEF enhances biomass production through mechanisms related to cellular and membrane processes. Furthermore, nsPEF treatment significantly reduced microbial contamination, achieving over a 1 $\log_{10}$ reduction in bacterial colony-forming units, while preserving the viability of *C. vulgaris* cells compared to untreated controls [72].

The PEF technology is a highly efficient, low-energy method for promoting microalgal growth as well as enhancing lipid and metabolite production, particularly in species like *Chlorella*. Optimizing parameters such as electric field strength, pulse frequency, and treatment duration minimizes energy consumption, reduces costs, and increases productivity. Based on these attributes, PEF appear to be economically and environmentally advantageous for sustainable industrial applications. As advancements progress, PEF and similar techniques are poised to further enhance microalgae biorefinery efficiency, supporting sustainable, cost-effective processes and contributing to the development of a circular bioeconomy.

5. Future Perspectives

In the field of microalgal cultivation, research has shown that environmental stress influences various aspects of metabolism, promoting lipid accumulation, protein stability, and pigment synthesis, making it a key strategy for enhancing the production efficiency of biofuels, nutritional supplements, and biopharmaceuticals. Moderate stress can alter carbon metabolism, shifting carbon flow from carbohydrate and protein synthesis toward lipid storage while optimizing fatty acid composition, to improve biodiesel stability and combustion performance [78,79]. In the future, application of genetic engineering and stress-adapted cultivation techniques are advocated to establish more resilient microalgal strains to sustain lipid production under high-stressed conditions, reduce biofuel production costs while integrating seawater cultivation and industrial wastewater utilization to drive sustainable energy development.

Environmental stress factors influence protein metabolism, and studies have identified stress-tolerant microalgae that exhibit high protein stability or even increase protein synthesis under high stress conditions. Therefore, transcriptomic and proteomic approaches should be adopted to analyze stress-induced protein

expression, to identify new bioactive or specialized microalgal proteins which can be applied to improve food nutrition, animal feed, and pharmaceuticals. Such genetic modifications can enhance protein synthesis in microalgae under stress, creating a sustainable protein source.

Given that environmental stress influences pigment metabolism, inhibiting chlorophyll synthesis while promoting the accumulation of carotenoids, lutein, and astaxanthin, future metabolic engineering and fermentation technologies aimed at enhancing pigment production efficiency and screening for stress-tolerant, high-yield microalgal strains, are needed to identify strains that provide sustainable source of natural pigments. Additionally, researchers should identify strategies that can modify environmental stress to improve microalgal pigment composition, antioxidant capacity and cellular protection mechanisms, thereby expand the applications of such microalgae in medicine and functional foods.

In summary, environmental stress not only enhances lipid accumulation but also regulates protein stability and pigment metabolism, demonstrating its potential contribution to the production of biofuels, nutrition, and high-value bioproduct development. In future, advancements in genetic modification, metabolic engineering, and intelligent cultivation technologies are advocated to improve microalgal salt tolerance and metabolic regulation, thereby drive large-scale their applications in renewable energy, environmental sustainability, and high-value industries, offering innovative solutions for global sustainable development.

6. Conclusions

Stress factors, both conventional (light and salinity) and unconventional (electric field treatment), are effective strategies for enhancing microalgal growth and metabolite production. Notably, light intensity, quality, and photoperiod significantly impact photosynthesis, enzymatic activity, and metabolic pathways, with moderate light boosting growth and efficiency. LED spectral control enables precise manipulation of pigment and metabolite synthesis. Salinity stress promotes lipid biosynthesis, antioxidant activity, and valuable metabolites, but it needs to be optimized to balance growth and productivity. Emerging methods like PEF treatment stimulate intracellular compound accumulation with low energy input, offering transformative potential for sustainable biomass processing. Integrating and optimizing these factors in scalable systems is key to producing high-value biomolecules and biofuels. Such advancements will support circular bioeconomy models, addressing global energy and resource sustainability challenges.

References

1. Caroppo, C.; Pagliara, P. Microalgae: A Promising Future. *Microorganisms* **2022**, *10*, 1488. https://doi.org/10.3390/microorganisms10081488.
2. Fernández, F.G.A.; Reis, A.; Wijffels, R.H.; et al. The role of microalgae in the bioeconomy. *New Biotechnol.* **2021**, *61*, 99–107. https://doi.org/10.1016/j.nbt.2020.11.011.
3. Viegas, C.; Gouveia, L.; Gonçalves, M. Aquaculture wastewater treatment through microalgal. Biomass potential applications on animal feed, agriculture, and energy. *J. Environ. Manag.* **2021**, *286*, 112187. https://doi.org/10.1016/j.jenvman.2021.112187.
4. Ramandani, A.A.; Lee, S.Y.; Jambrak, A.R.; et al. Synergizing food waste management and microalgae biorefinery for bioenergy production: Recent advance on direct and indirect conversion pathway. *Process Biochem.* **2025**, *151*, 14–26. https://doi.org/10.1016/j.procbio.2025.01.006.
5. Goh, B.H.H.; Ong, H.C.; Cheah, M.Y.; et al. Sustainability of direct biodiesel synthesis from microalgae biomass: A

critical review. *Renew. Sustain. Energy Rev.* **2019**, *107*, 59–74. https://doi.org/10.1016/j.rser.2019.02.012.

6. Ashokkumar, V.; Flora, G.; Kumar, G.; et al. Cutting-edge advances in alga *Botryococcus* for eco-friendly biofuels and high-value bioproducts—A critical review. *Algal Res.* **2024**, *83*, 103676. https://doi.org/10.1016/j.algal.2024.103676.

7. Barera, S.; Forlani, G. The role of proline in the adaptation of eukaryotic microalgae to environmental stress: An underestimated tool for the optimization of algal growth. *J. Appl. Phycol.* **2023**, *35*, 1635–1648. https://doi.org/10.1007/s10811-023-03017-9.

8. Maltsev, Y.; Maltseva, K.; Kulikovskiy, M.; et al. Influence of light conditions on microalgae growth and content of lipids, carotenoids, and fatty acid composition. *Biology* **2021**, *10*, 1060. https://doi.org/10.3390/biology10101060.

9. Begum, H.; Yusoff, F.M.D.; Banerjee, S.; et al. Availability and utilization of pigments from microalgae. *Crit. Rev. Food Sci. Nutr.* **2016**, *56*, 2209–2222. https://doi.org/10.1080/10408398.2013.764841.

10. Singh, S.P.; Singh, P. Effect of temperature and light on the growth of algae species: A review. *Renew. Sustain. Energy Rev.* **2015**, *50*, 431–444. https://doi.org/10.1016/j.rser.2015.05.024.

11. Fu, W.; Guomundsson, Ó.; Paglia, G.; et al. Enhancement of carotenoid biosynthesis in the green microalga *Dunaliella salina* with light-emitting diodes and adaptive laboratory evolution. *Appl. Microbiol. Biotechnol.* **2013**, *97*, 2395–2403. https://doi.org/10.1007/s00253-012-4502-5.

12. Leong, Y.K.; Chang, J.S. Lutein biosynthesis from microalgae — Recent advances and circular economy. *Environ. Technol. Innov.* **2023**, *30*, 103097. https://doi.org/10.1016/j.eti.2023.103097.

13. Saha, S.K.; Kazipet, N.; Murray, P. The carotenogenic *Dunaliella salina* CCAP 19/20 produces enhanced levels of carotenoid under specific nutrients limitation. *BioMed Res. Int.* **2018**, *2018*, 7532897. https://doi.org/10.1155/2018/7532897.

14. Jahns, P.; Holzwarth, A.R. The role of the xanthophyll cycle and of lutein in photoprotection of photosystem II. *Biochim. Et Biophys. Acta—Bioenerg.* **2012**, *1817*, 182–193. https://doi.org/10.1016/j.bbabio.2011.04.012.

15. Kuczynska, P.; Jemiola-Rzeminska, M.; Nowicka, B.; et al. The xanthophyll cycle in diatom *Phaeodactylum tricornutum* in response to light stress. *Plant Physiol. Biochem.* **2020**, *152*, 125–137. https://doi.org/10.1016/j.plaphy.2020.04.043.

16. Schulze, P.S.C.; Barreira, L.A.; Pereira, H.G.C.; et al. Light emitting diodes (LEDs) applied to microalgal production. *Trends Biotechnol.* **2014**, *32*, 422–430. https://doi.org/https://doi.org/10.1016/j.tibtech.2014.06.001.

17. Kou, Y.; Liu, M.; Sun, P.; et al. High light boosts salinity stress-induced biosynthesis of astaxanthin and lipids in the green alga *Chromochloris zofingiensis*. *Algal Res.* **2020**, *50*, 101976. https://doi.org/https://doi.org/10.1016/j.algal.2020.101976.

18. Gouveia, L.; Neves, C.; Sebastião, D.; et al. Effect of light on the production of bioelectricity and added-value microalgae biomass in a Photosynthetic Alga Microbial Fuel Cell. *Bioresour. Technol.* **2014**, *154*, 171–177. https://doi.org/10.1016/j.biortech.2013.12.049.

19. Zhang, Y.; Shi, M.; Mao, X.; et al. Time-resolved carotenoid profiling and transcriptomic analysis reveal mechanism of carotenogenesis for astaxanthin synthesis in the oleaginous green alga *Chromochloris zofingiensis*. *Biotechnol. Biofuels* **2019**, *12*, 287. https://doi.org/10.1186/s13068-019-1626-1.

20. Kim, T.H.; Lee, Y.; Han, S.H.; et al. The effects of wavelength and wavelength mixing ratios on microalgae growth and nitrogen, phosphorus removal using *Scenedesmus* sp. for wastewater treatment. *Bioresour. Technol.* **2013**, *130*, 75–80. https://doi.org/10.1016/j.biortech.2012.11.134.

21. Jayakumar, S.; Bhuyar, P.; Pugazhendhi, A.; et al. Effects of light intensity and nutrients on the lipid content of marine microalga (diatom) *Amphiprora* sp. for promising biodiesel production. *Sci. Total Environ.* **2021**, *768*, 145471. https://doi.org/10.1016/j.scitotenv.2021.145471.

22. Han, W.; Jin, W.; Ding, W.; et al. Effects of nutrient composition, lighting conditions, and metal ions on the growth and lipid yield of the high-lipid-yielding microalgae (*Chlorella pyrenoidosa*) cultivated in municipal wastewater. *J. Environ. Chem. Eng.* **2021**, *9*, 106491. https://doi.org/10.1016/j.jece.2021.106491.

23. Patel, A.K.; Vadrale, A.P.; Singhania, R.R.; et al. Enhanced mixotrophic production of lutein and lipid from potential microalgae isolate *Chlorella sorokiniana* C16. *Bioresour. Technol.* **2023**, *386*, 129477. https://doi.org/10.1016/j.biortech.2023.129477.

24. Cheah, W.Y.; Show, P.L.; Juan, J.C.; et al. Enhancing biomass and lipid productions of microalgae in palm oil mill effluent using carbon and nutrient supplementation. *Energy Convers. Manag.* **2018**, *164*, 188–197. https://doi.org/10.1016/j.enconman.2018.02.094.

25. Chang, W.; Li, Y.; Qu, Y.; et al. Mixotrophic cultivation of microalgae to enhance the biomass and lipid production with synergistic effect of red light and phytohormone IAA. *Renew. Energy* **2022**, *187*, 819–828. https://doi.org/10.1016/j.renene.2022.01.108.

26. Felix, C.; Ubando, A.; Madrazo, C.; et al. Non-catalytic in-situ (trans)esterification of lipids in wet microalgae *Chlorella vulgaris* under subcritical conditions for the synthesis of fatty acid methyl esters. *Appl. Energy* **2019**, *248*, 526–537. https://doi.org/10.1016/j.apenergy.2019.04.149.

27. Yen, S.W.; Nagarajan, D.; Chen, W.H.; et al. Fermentative production of astaxanthin from sorghum distillery residue by

an indigenous *Aurantiochytrium* sp. CJ6 strain using a continuous-feeding fed-batch process. *Bioresour. Technol.* **2023**, *376*, 128817. https://doi.org/10.1016/j.biortech.2023.128817.

28. Liu, M.; Chen, Y.; Zhu, C.; et al. Insight into the regulation mechanism of light spectra on astaxanthin biosynthesis in mixotrophic *Chromochloris zofingiensis*. *Algal Res.* **2024**, *82*, 103690. https://doi.org/10.1016/j.algal.2024.103690.

29. Ma, R.; Tao, X.; Wang, B.; et al. Hyper-production of astaxanthin from *Haematococcus pluvialis* by a highly efficient nitrogen feeding strategy accompanied with high light induction. *Algal Res.* **2025**, *85*, 103865. https://doi.org/10.1016/j.algal.2024.103865.

30. Cheirsilp, B.; Wantip, K.; Chai-issarapap, N.; et al. Enhanced production of astaxanthin and co-bioproducts from microalga *Haematococcus* sp. integrated with valorization of industrial wastewater under two-stage LED light illumination strategy. *Environ. Technol. Innov.* **2022**, *28*, 102620. https://doi.org/10.1016/j.eti.2022.102620.

31. Zhang, H.; Tan, Y.; Zhu, R.; et al. Red light trade-off regulating the negative effects of nitrogen concentration to improve lipid and astaxanthin production in the filamentous green microalga *Oedocladium carolinianum*. *Algal Res.* **2024**, *80*, 03510. https://doi.org/10.1016/j.algal.2024.103510.

32. Nur, M.M.A.; Liana, F.M.; Putri, A.N.L.D.; et al. Enhancing fucoxanthin production in Chaetoceros calcitrans under mixotrophic condition and LED wavelength shift strategy. *Biocatal. Agric. Biotechnol.* **2024**, *57*, 103120. https://doi.org/10.1016/j.bcab.2024.103120.

33. Bo, Y.; Wang, S.; Ma, F.; et al. The influence of spermidine on the build-up of fucoxanthin in *Isochrysis* sp. acclimated to varying light intensities. *Bioresour. Technol.* **2023**, *387*, 129688. https://doi.org/10.1016/j.biortech.2023.129688.

34. Zhang, H.; Gong, P.; Cai, Q.; et al. Maximizing fucoxanthin production in *Odontella aurita* by optimizing the ratio of red and blue light-emitting diodes in an auto-controlled internally illuminated photobioreactor. *Bioresour. Technol.* **2022**, *344*, 126260. https://doi.org/10.1016/j.biortech.2021.126260.

35. Chen, C.Y.; Liu, P.Y.; Chang, Y.H.; et al. Optimizing cultivation strategies and scaling up for fucoxanthin production using *Pavlova* sp. *Bioresour. Technol.* **2024**, *399*, 130609. https://doi.org/10.1016/j.biortech.2024.130609.

36. Weickert, S.; Schmid-Staiger, U.; Lewandowski, I. Influence of specific light availability and solvent on process economics—The production of fucoxanthin and eicosapentaenoic acid from *P. tricornutum* using flat-panel airlift photobioreactors with artificial light. *Algal Res.* **2023**, *75*, 103284. https://doi.org/10.1016/j.algal.2023.103284.

37. Zhao, X.; Yan, J.; Yang, T.; et al. Exploring engineering reduced graphene oxide-titanium dioxide (rGO-TiO2) nanoparticles treatment to effectively enhance lutein biosynthesis with *Chlorella sorokiniana* F31 under different light intensity. *Bioresour. Technol.* **2022**, *348*, 126816. https://doi.org/10.1016/j.biortech.2022.126816.

38. Zheng, H.; Wang, Y.; Li, S.; et al. Lutein production by microalgae using corn starch wastewater pretreated with rapid enzymatic hydrolysis. *Bioresour. Technol.* **2022**, *352*, 126940. https://doi.org/10.1016/j.biortech.2022.126940.

39. Chen, J.H.; Kato, Y.; Matsuda, M.; et al. Lutein production with *Chlorella sorokiniana* MB-1-M12 using novel two-stage cultivation strategies—Metabolic analysis and process improvement. *Bioresour. Technol.* **2021**, *334*, 125200. https://doi.org/10.1016/j.biortech.2021.125200.

40. Yu, H.Y.; Cho, D.H.; Seo, D.; et al. Microalga *Chlorella* sp. biomass containing high lutein prevents light-induced photooxidation and retinal degeneration in mice. *Algal Res.* **2024**, *82*, 103620. https://doi.org/10.1016/j.algal.2024.103620.

41. Diaz-MacAdoo, D.; Nagai, S.; Mata, M.T.; et al. Comparative analysis of carotenoid synthesis and transcriptome of a microalga *Chlorophyta* MCH-35, potential lutein producer, in response to different quality light. *Algal Res.* **2023**, *74*, 103206. https://doi.org/10.1016/j.algal.2023.103206.

42. Liu, Y.; Wei, D. Enhancing carbon dioxide fixation and co-production of protein and lutein in oleaginous *Coccomyxa subellipsoidea* by a stepwise light intensity and nutrients feeding strategy. *Bioresour. Technol.* **2023**, *376*, 128885. https://doi.org/10.1016/j.biortech.2023.128885.

43. Li, J.; Zhao, X.; Chang, J.S.; et al. A two-stage culture strategy for *Scenedesmus* sp. FSP3 for CO_2 fixation and the simultaneous production of lutein under light and salt stress. *Molecules* **2022**, *27*, 7497. https://doi.org/10.3390/molecules27217497.

44. Bialevich, V.; Zachleder, V.; Bišová, K. The effect of variable light source and light intensity on the growth of three algal species. *Cells* **2022**, *11*, 1293. https://doi.org/10.3390/cells11081293.

45. Difusa, A.; Talukdar, J.; Kalita, M.C.; et al. Effect of light intensity and pH condition on the growth, biomass and lipid content of microalgae *Scenedesmus* species. *Biofuels* **2015**, *6*, 37–44. https://doi.org/10.1080/17597269.2015.1045274.

46. Gim, G.H.; Ryu, J.; Kim, M.J.; et al. Effects of carbon source and light intensity on the growth and total lipid production of three microalgae under different culture conditions. *J. Ind. Microbiol. Biotechnol.* **2016**, *43*, 605–616. https://doi.org/10.1007/s10295-016-1741-y.

47. Cheirsilp, B.; Torpee, S. Enhanced growth and lipid production of microalgae under mixotrophic culture condition: Effect of light intensity, glucose concentration and fed-batch cultivation. *Bioresour. Technol.* **2012**, *110*, 510–516. https://doi.org/10.1016/j.biortech.2012.01.125.

48. Ho, S.H.; Chen, C.Y.; Chang, J.S. Effect of light intensity and nitrogen starvation on CO_2 fixation and lipid/carbohydrate

production of an indigenous microalga *Scenedesmus obliquus* CNW-N. *Bioresour. Technol.* **2012**, *113*, 244–252. https://doi.org/10.1016/j.biortech.2011.11.133.

49. Mahari, W.A.W.; Razali, W.A.W.; Khor, W.; et al. Light-emitting diodes (LEDs) for culturing microalgae and cyanobacteria. *Chem. Eng. J.* **2024**, *485*, 149619. https://doi.org/10.1016/j.cej.2024.149619.

50. You, T.; Barnett, S.M. Effect of light quality on production of extracellular polysaccharides and growth rate of *Porphyridium Cruentum. Biochem. Eng. J.* **2004**, *19*, 251–258. https://doi.org/https://doi.org/10.1016/j.bej.2004.02.004.

51. Abu-Ghosh, S.; Fixler, D.; Dubinsky, Z.; Iluz, D. Continuous background light significantly increases flashing-light enhancement of photosynthesis and growth of microalgae. *Bioresour. Technol.* **2015**, *187*, 144–148. https://doi.org/10.1016/j.biortech.2015.03.119.

52. Vélez-Landa, L.; Hernández-De León, H.R.; Pérez-Luna, Y.D.C.; et al. Influence of light intensity and photoperiod on the photoautotrophic growth and lipid content of the microalgae *Verrucodesmus verrucosus* in a photobioreactor. *Sustainability* **2021**, *13*, 6606. https://doi.org/10.3390/su13126606.

53. Chakravarty, S.; Mallick, N. Engineering a cultivation strategy for higher lipid accretion and biodiesel production by the marine microalga *Picochlorum soloecismus. Sustain. Chem. Pharm.* **2022**, *26*, 100635. https://doi.org/10.1016/j.scp.2022.100635.

54. Anahas AM, P.; Prasannabalaji, N.; Muralitharan, G. Unlocking the potential of coal mine microalgae strains: Enhanced biodiesel production and CO_2 sequestration through cultivation optimization. *Biomass Bioenergy* **2025**, *192*, 107489. https://doi.org/10.1016/j.biombioe.2024.107489.

55. Almutairi, A.W. Harnessing waste glycerol to mitigate salinity constraints in freshwater microalgae cultivation for enhanced biodiesel recovery. *J. King Saud Univ.-Sci.* **2024**, *36*, 103258. https://doi.org/10.1016/j.jksus.2024.103258.

56. Sinetova, M.A.; Sidorov, R.A.; Medvedeva, A.A.; et al. Effect of salt stress on physiological parameters of microalgae *Vischeria punctata* strain IPPAS H-242, a superproducer of eicosapentaenoic acid. *J. Biotechnol.* **2021**, *331*, 63–73. https://doi.org/10.1016/j.jbiotec.2021.03.001.

57. Liu, N.; Mou, Y.; Su, K.; et al. The effect of salinity stress on the growth and lipid accumulation of *Scenedesmus quadricauda* FACHB-1297 under xylose mixotrophic cultivation. *Process Saf. Environ. Prot.* **2022**, *165*, 887–894. https://doi.org/10.1016/j.psep.2022.07.051.

58. Chauhan, A.J.; Patel, A.K.; Chen, C.W.; et al. Enhanced production of high-value polyunsaturated fatty acids (PUFAs) from potential thraustochytrid *Aurantiochytrium* sp. *Bioresour. Technol.* **2023**, *370*, 128536. https://doi.org/10.1016/j.biortech.2022.128536.

59. Yang, Z.; Chen, J.; Tang, B.; et al. Metabolic interpretation of NaCl stress-induced lipid accumulation in microalgae for promising biodiesel production with saline wastewater. *Chem. Eng. Sci.* **2024**, *284*, 119447. https://doi.org/10.1016/j.ces.2023.119447.

60. Sorokina, K.N.; Samoylova, Y.V.; Parmon, V.N. Comparative analysis of microalgae metabolism on BBM and municipal wastewater during salt induced lipid accumulation. *Bioresour. Technol. Rep.* **2020**, *11*, 100548. https://doi.org/10.1016/j.biteb.2020.100548.

61. Anand, V.; Kashyap, M.; Sharma, M.P.; et al. Impact of hydrogen peroxide on microalgae cultivated in varying salt-nitrate-phosphate conditions. *J. Environ. Chem. Eng.* **2021**, *9*, 105814. https://doi.org/10.1016/j.jece.2021.105814.

62. Chen, C.Y.; Lee, M.H.; Dong, C.D.; et al. Enhanced production of microalgal lipids using a heterotrophic marine microalga *Thraustochytrium* sp. BM2. *Biochem. Eng. J.* **2020**, *154*, 107429. https://doi.org/10.1016/j.bej.2019.107429.

63. Chen, C.Y.; Lee, M.H.; Leong, Y.K.; et al. Biodiesel production from heterotrophic oleaginous microalga *Thraustochytrium* sp. BM2 with enhanced lipid accumulation using crude glycerol as alternative carbon source. *Bioresour. Technol.* **2020**, *306*, 123113. https://doi.org/10.1016/j.biortech.2020.123113.

64. Zhao, Y.; Li, Q.; Gu, D.; et al. The synergistic effects of gamma-aminobutyric acid and salinity during the enhancement of microalgal lipid production in photobioreactors. *Energy Convers. Manag.* **2022**, *267*, 115928. https://doi.org/10.1016/j.enconman.2022.115928.

65. Mandal, M.K.; Chaurasia, N. De novo transcriptomic analysis of *Graesiella emersonii* NC-M1 reveals differential genes expression in cell proliferation and lipid production under glucose and salt supplemented condition. *Renew. Energy* **2021**, *179*, 2004–2015. https://doi.org/10.1016/j.renene.2021.07.141.

66. Parveen, A.; Rawat, J.; Bhatnagar, P.; et al. Enhanced production of high-value compounds from *Chlorella sorokiniana* by two-stage cultivation under red light and salinity stress. *Biocatal. Agric. Biotechnol.* **2024**, *60*, 103315. https://doi.org/10.1016/j.bcab.2024.103315.

67. Ma, M.; Jiang, L.; He, Y.; et al. Multi-faceted effects of NaCl on salt-tolerant microalgae *Golenkinia* sp. SDEC-16. *Bioresour. Technol.* **2024**, *406*, 131016. https://doi.org/10.1016/j.biortech.2024.131016.

68. Pereira, R.N.; Jaeschke, D.P.; Mercali, G.D.; et al. Impact of ultrasound and electric fields on microalgae growth: A comprehensive review. *Braz. J. Chem. Eng.* **2023**, *40*, 607–622. https://doi.org/10.1007/s43153-022-00281-z.

69. La, H.J.; Choi, G.G.; Cho, C.; et al. Increased lipid productivity of *Acutodesmus dimorphus* using optimized pulsed

electric field. *J. Appl. Phycol.* **2016**, *28*, 931–938. https://doi.org/10.1007/s10811-015-0674-6.

70. Carullo, D.; Abera, B.D.; Casazza, A.A.; et al. Effect of pulsed electric fields and high pressure homogenization on the aqueous extraction of intracellular compounds from the microalgae *Chlorella vulgaris. Algal Res.* **2018**, *31*, 60–69. https://doi.org/10.1016/j.algal.2018.01.017.

71. Haberkorn, I.; Buchmann, L.; Hiestand, M.; et al. Continuous nanosecond pulsed electric field treatments foster the upstream performance of *Chlorella vulgaris*-based biorefinery concepts. *Bioresour. Technol.* **2019**, *293*, 122029. https://doi.org/10.1016/j.biortech.2019.122029.

72. Buchmann, L.; Böcker, L.; Frey, W.; et al. Energy input assessment for nanosecond pulsed electric field processing and its application in a case study with *Chlorella vulgaris. Innov. Food Sci. Emerg. Technol.* **2018**, *47*, 445–453. https://doi.org/10.1016/j.ifset.2018.04.013.

73. Nezammahalleh, H.; Ghanati, F.; Adams, T.A.; et al. Effect of moderate static electric field on the growth and metabolism of C*hlorella vulgaris. Bioresour. Technol.* **2016**, *218*, 700–711. https://doi.org/10.1016/j.biortech.2016.07.018.

74. Canelli, G.; Kuster, I.; Jaquenod, L.; et al. Pulsed electric field treatment enhances lipid bioaccessibility while preserving oxidative stability in *Chlorella vulgaris. Innov. Food Sci. Emerg. Technol.* **2022**, *75*, 102897. https://doi.org/10.1016/j.ifset.2021.102897.

75. Kim, J.Y.; Lee, C.; Jeon, M.S.; et al. Enhancement of microalga *Haematococcus pluvialis* growth and astaxanthin production by electrical treatment. *Bioresour. Technol.* **2018**, *268*, 815–819. https://doi.org/10.1016/j.biortech.2018.08.014.

76. Barreiros, M.; Maciel, F.; Pereira, R.S.; et al. Electric fields to support microalgae growth with a differentiated biochemical composition. *Innov. Food Sci. Emerg. Technol.* **2024**, *97*, 103829. https://doi.org/10.1016/j.ifset.2024.103829.

77. Choi, S.A.; Lee, S.Y.; Lee, J.; et al. Rapid induction of edible lipids in Chlorella by mild electric stimulation. *Bioresour. Technol.* 2019, 292. https://doi.org/10.1016/j.biortech.2019.121950.

78. Ramos, M.; Dias, A.P.S.; Puna, J.F.; et al. Biodiesel production processes and sustainable raw materials. *Energies* **2019**, *12*, 4408. https://doi.org/10.3390/en12234408.

79. Santos, S.; Puna, J.; Gomes, J. A review on bio-based catalysts (immobilized enzymes) used for biodiesel production. *Energies* **2020**, *13*, 3013. https://doi.org/10.3390/en13113013.

Scilight

Review

A Comprehensive Review of Thermoelectric Generators from Micropower Supply to Kilowatt System

Shuo Yang, Hao Chen and Ding Luo *

Shaanxi Key Laboratory of New Transportation Energy and Automotive Energy Saving, Chang'an University, Xi'an 710064, China
* Correspondence: Ding_L@outlook.com

Abstract: Energy crisis and carbon emissions are two increasingly prominent issues in our society. As one of the clean energy sources, thermoelectric power generation is a promising alternative energy technology to convert heat into electricity. As long as there is a heat source, thermoelectric generators can provide electricity for watches, sensors, electronics, spacecraft, etc., and can also be used to recover waste heat, such as automobile exhaust heat, industrial waste heat, ship waste heat, etc. This study proposes a novel classification paradigm based on power output (microwatt, 1 W–1 kW, >1 kW), systematically revealing the technological characteristics at each power level: the microwatt level relies on flexible materials and compatibility with human body heat, while the kilowatt level requires the integration of high-temperature materials and optimized thermal management. The study also demonstrates that performance can be significantly enhanced through asymmetric geometric designs and non-equilibrium synthesis processes. This work provides a comprehensive design framework, from material innovation to large-scale integration, for next-generation thermoelectric systems, addressing the theoretical gap in techno-economic analysis.

Keywords: thermoelectric generators; waste heat recovery; kilowatt; thermal management

1. Introduction

In recent years, fossil fuel consumption and carbon emissions caused by electricity production have been the focus of the whole society. Many countries have issued policies to reduce the use of primary energy and promote renewable energy development. The proportion of renewable energy in global electricity production is gradually increasing, as shown in Figure 1. The development of renewable energy has attracted great interest from researchers. As one of the renewable energy, thermoelectric power generation has incomparable advantages over other clean energy, such as, no moving component, no noise, weather independence, simple structure, no maintenance cost, long life, and so on [1–4], which has the potential to become a promising alternative energy technology.
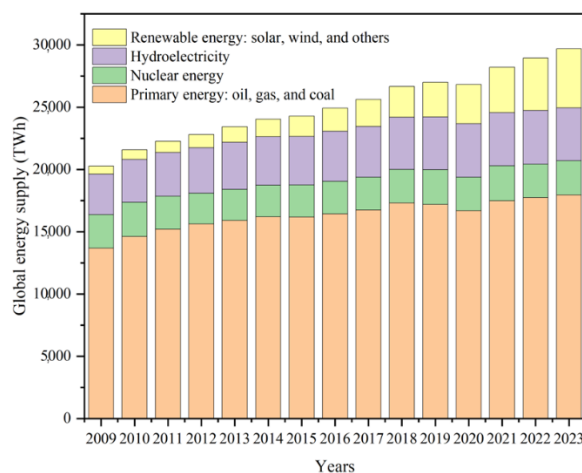

Figure 1. Global electricity production with different sources.

Thermoelectric generators (TEGs) can directly transfer heat into electricity when there is a temperature difference on both ends of TEGs. Various types of heat energy can be used to generate electricity by different TEG systems [5]. According to the different heat sources, the power generation level of TEG systems is quite different, from micro power supply to kilowatt system. Some preliminary TEG applications have been witnessed. The wearable TEG device can harvest body heat to provide power for watches or other electronics [6]. In space exploration, the spacecraft driven by the photovoltaic (PV) power supply does not work without light, which affects the normal progress of the exploration mission; The radiative TEG system can overcome the impact of the environment and continue to provide power, and NASA has started the relative research plan since 1951 [7]. To further enhance the efficiency of PV semiconductors, thermoelectric materials can be combined with PV materials to form a PV-TEG device, which can use both solar and thermal energy [8]. Zhao et al. [9] enhanced the efficiency of a photovoltaic-thermoelectric generator (PV-TEG) by integrating microchannel heat pipes and phase change materials; They further applied a hybrid optimization algorithm to perform multi-objective optimization on the system, achieving a remarkable electrical efficiency of 25.6% for the PV-TEG. Considering that about 1/3 of energy produced by burning fossil fuels is wasted in the form of exhaust heat, the automobile TEG system can be installed in the vehicle exhaust system to convert the exhaust heat into electricity and improve fuel efficiency [10–14]. Also, the thermoelectric power generation technology can be applied to recover other forms of waste heat, such as industrial waste heat [15], ship waste heat [16], etc. For instance, Zhuang et al. [17] conducted an in-depth numerical simulation study on industrial thermal environments and heat transfer characteristics of TEGs, thereby developing a novel industrial waste heat recovery TEG system that combines high power generation efficiency with operational stability. Innovatively, Li et al. [18] introduced a radiation shielding layer within the thermoelectric leg gaps, which effectively reduced heat loss and enhanced system conversion efficiency and output power by 15% and 9.5%, respectively. There is an increasing interest in thermoelectric power generation technology.

However, the TEG has not yet been widely commercialized due to its relatively low conversion efficiency and high cost of thermoelectric materials. The ability of the TEG to convert heat energy into electricity depends on the performance of thermoelectric materials, which is estimated by a dimensionless constant of figure-of-merit $ZT = \sigma\alpha^2 T\lambda^{-1}$, wherein σ is the electrical conductivity, α is the Seebeck coefficient, T is the absolute temperature, and λ is the thermal conductivity [19,20]. At present, Bi_2Te_3-based materials are the only commercialized thermoelectric materials because of the relatively high ZT value near room temperature, about 1. The ideal conversion efficiency of the TEG can be estimated by the ZT value, that is

$$\eta = \frac{T_h - T_c}{T_h} \frac{\sqrt{1 + ZT} - 1}{\sqrt{1 + ZT} + \frac{T_c}{T_h}} \tag{1}$$

where T_h and T_c are the hot-side and cold-side temperatures, respectively. Figure 2 shows the conversion efficiency of the TEG with different ZT values as well as the comparison with Carnot efficiency. In numerous application scenarios, such as automotive waste heat recovery, a temperature difference of 150 K can be easily achieved. When the ZT value exceeds the threshold value of 2 [20,21], the conversion efficiency can reach more than 10%, and the application of the TEG will become more competitive compared with other alternative energy conversion technologies such as the PV energy conversion. Researchers aim to identify thermoelectric materials with a ZT value of 2.0 using advanced material technologies.

With the progress of thermoelectric materials, an increasing number of thermoelectric power generation systems have been reported in different industries. TEG systems with different power generation levels feature different barriers that block their wide applications. For example, the micro power supplies, such as wearable TEG devices and self-powered sensors, need to satisfy the requirement of flexible structures to adapt to different heat source shapes. Kilowatt TEG systems require a heat exchanger with good heat transfer performance to improve the hot-side work temperature and a good electrical connection scheme to reduce the parasitic power losses. In the previous work, we provided a comprehensive review of thermoelectric technology, from materials to systems [22]. The thermoelectric applications were also reviewed and summarized [23]. As the development of TEG systems continues to flourish, new challenges emerge in different scenarios, thus a more recent and classified review is required.

In this review, TEG systems are classified according to different power generation levels. Section 2 introduces the basics of the TEG, including thermoelectric effects, thermoelectric materials, and the TEG design. Section 3 presents the development of thermoelectric micropower supplies. Section 4 comprehensively reviews TEG systems from 1 W to 1 kW. Section 5 introduces the application of TEGs in power generation systems that exceed 1 kW. The challenges and outlook for TEG systems are also discussed.
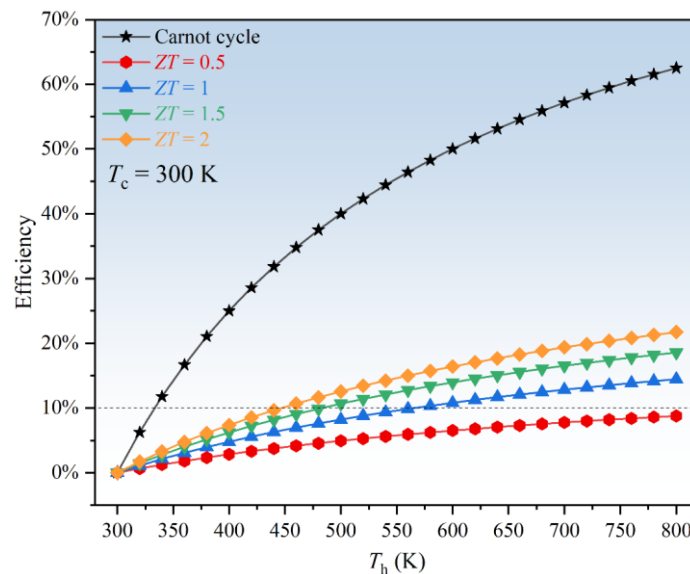
Figure 2. The conversion efficiency of the TEG with different *ZT* values.

2. Basics of the Thermoelectric Generator

As the basic power source of thermoelectric power generation systems, the TEG is composed of p- and n-type thermoelectric legs, metal connectors, and insulating plates, and presents a sandwich configuration, as shown in Figure 3. When the heat source applies a heat flux to one side of the TEG, the high temperature will induce the movement of the holes on p-type thermoelectric legs and the electrons of n-type thermoelectric legs towards the side with lower temperature, and the heat will be dissipated by a cooling source attached on the other side of the TEG. Multiple thermocouple pairs, connected in series, can amplify the voltage, and the current is produced once an external load is connected. This device has no mechanical moving parts and can generate power from heat sources such as industrial waste heat, automobile exhaust, or radioisotopes. The p- and n-type thermoelectric legs are connected electrically in series and thermally in parallel. To reduce parasitic power loss, metal connectors, usually made of copper, must have high thermal and electrical conductivity. To increase the temperature difference on both sides of the TEG, insulating plates possess high thermal conductivity [24] and are usually made of ceramics. The performance of AlN ceramic plate is better than Al_2O_3 based ceramic plate, but the cost is higher.
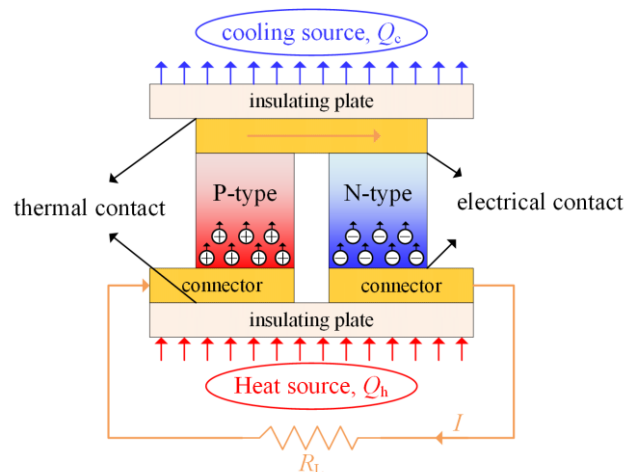
Figure 3. A diagram showing the working principle of the TEG.

2.1. Thermoelectric Effects

Thermoelectric effects include Seebeck, Peltier, and Thomson effects. The Seebeck effect was first discovered by Thomas Seebeck in 1821. When different conductors (or semiconductors) are connected and subjected to a temperature gradient, the Seebeck voltage will be generated. The Seebeck voltage is directly proportional to the Seebeck coefficient and temperature difference, which can be estimated by:

$$V = \alpha \Delta T \tag{2}$$

where α is the Seebeck coefficient, and ΔT is the temperature difference. Therefore, thermoelectric materials must have a high Seebeck coefficient to produce considerable voltage.

The Peltier effect, a fundamental aspect of the thermoelectric effect, can be considered the reverse of the Seebeck effect. First discovered by Jean Peltier in 1834, it involves the reversible conversion of electrical and thermal energy. When an external current I flows through a thermocouple made of two distinct conductor or semiconductor materials (A and B), Peltier heat is produced at the junction, alongside the Joule heating due to resistance. Peltier heat is generated at both ends of thermoelectric legs, wherein the end of carrier accumulation will release heat and the end of carrier dissipation will absorb heat. The amount of Peltier heat can be expressed as:

$$Q_{Peltier} = \pi I = \alpha I T \tag{3}$$

where π is the Peltier coefficient. Peltier coefficient and Seebeck coefficient are closely related through Kelvin relation, i.e., $\pi = \alpha T$. Due to the Peltier effect, thermoelectric materials were also used to fabricate thermoelectric coolers for cooling electronic devices [25].

The Thomson effect, discovered by William Thomson in 1854, describes a unique thermal phenomenon in a homogeneous material when both a temperature gradient and an electric current are present. When current flows through a thermoelectric material with a temperature gradient, the carriers generate additional heat due to changes in their kinetic energy (Thomson heat). If the current direction aligns with the temperature gradient, the material releases heat; otherwise, it absorbs heat. Thomson heat is directly proportional to the current and temperature gradient, which can be estimated by:

$$Q_{Thomson} = \tau I \Delta T \tag{4}$$

where τ is the Thomson coefficient. The Thomson coefficient τ is related to the temperature dependence of the Seebeck coefficient ($\tau = T \frac{d\alpha}{dT}$). Although the effect is weak, the directional sensitivity endows it with a unique value in dynamic temperature control scenarios.

In the global heat transfer process of thermoelectric legs, there are four kinds of heat: heat conduction, Peltier heat, Joule heat, and Thomson heat. The relationship among them is that the heat conduction is the largest, followed by Peltier heat, Joule heat, and Thomson heat [26].

2.2. Thermoelectric Materials

With the development of semiconductor physics, more and more ideal thermoelectric materials have been found, among which thermoelectric materials synthesized by tellurium (Te), bismuth (Bi), antimony (Sb), or selenium (Se) are the conventional Bi_2Te_3-based materials for the preparation of TEGs [27]. Owing to the modern synthesis and characterization techniques, conventional bulk thermoelectric materials with nanostructures have thrived, such as nanostructured Bi_2Te_3 [28], PbTe [29], and SiGe [30], and the *ZT* value has been improved to a certain extent. In addition to conventional thermoelectric materials, skutterudite, half-Heusler, and organic thermoelectric materials have also been widely used in different application scenarios. Based on the different working temperatures, thermoelectric materials are classified into three categories: low- (300–500 K), medium- (500–900 K), and high-temperature (>900 K) materials. Low-temperature thermoelectric materials mainly include Bi_2Te_3 and organic materials, medium-temperature thermoelectric materials mainly include PbTe and skutterudite, and high-temperature thermoelectric materials mainly include SiGe and half-Heusler. In recent years, with the continuous advancement in thermoelectric materials research, various novel thermoelectric materials have been developed to significantly enhance thermoelectric performance. This section systematically reviews and discusses recent research progress in the field of thermoelectric materials.

In the field of low-temperature thermoelectric materials, Kim et al. [31] developed a cost-effective synthesis strategy for Bi_2Te_3-based thermoelectric materials, as illustrated in Figure 4a. This technique employs rapid extrusion of excess liquid during the pressing process, significantly enhancing thermoelectric performance in bismuth telluride (Bi_2Te_3) specimens. The proposed methodology effectively circumvents electrical conductivity degradation through the strategic introduction of grain boundary dislocations, ultimately achieving a peak *ZT* value of 1.86 at 320 K. Wang et al. [32] effectively suppressed Te vacancies in n-type nanostructured Bi_2Te_3 through spark plasma sintering (SPS)-induced non-equilibrium reactions, as demonstrated in Figure 4b. This approach remarkably reduced thermal conductivity to $0.48 \ W \cdot m^{-1} \cdot K^{-1}$ while maintaining a *ZT* value of 1.1 at 420 K in the thermoelectric leg. Meroz et al. [33] demonstrated an optimized synthesis protocol for n-type $Bi_2Te_{2.4}Se_{0.6}$ by integrating the melt spinning technique with hot pressing; This hybrid processing strategy yielded a maximum *ZT*

value of 1.07 at 338.15 K, showcasing enhanced thermoelectric performance through combinatorial fabrication approaches. Zheng et al. [34] proposed a design scheme for a full-scale hierarchical structure (Figure 4d). This scheme achieved multiple scattering of phonons by introducing a high density of grain boundaries, dislocations, layer dislocations, twin boundaries and nanoholes, which significantly reduced the lattice thermal conductivity of the MgAgSb material over the entire temperature range. The thermoelectric material achieved a *ZT* value of 1.4.
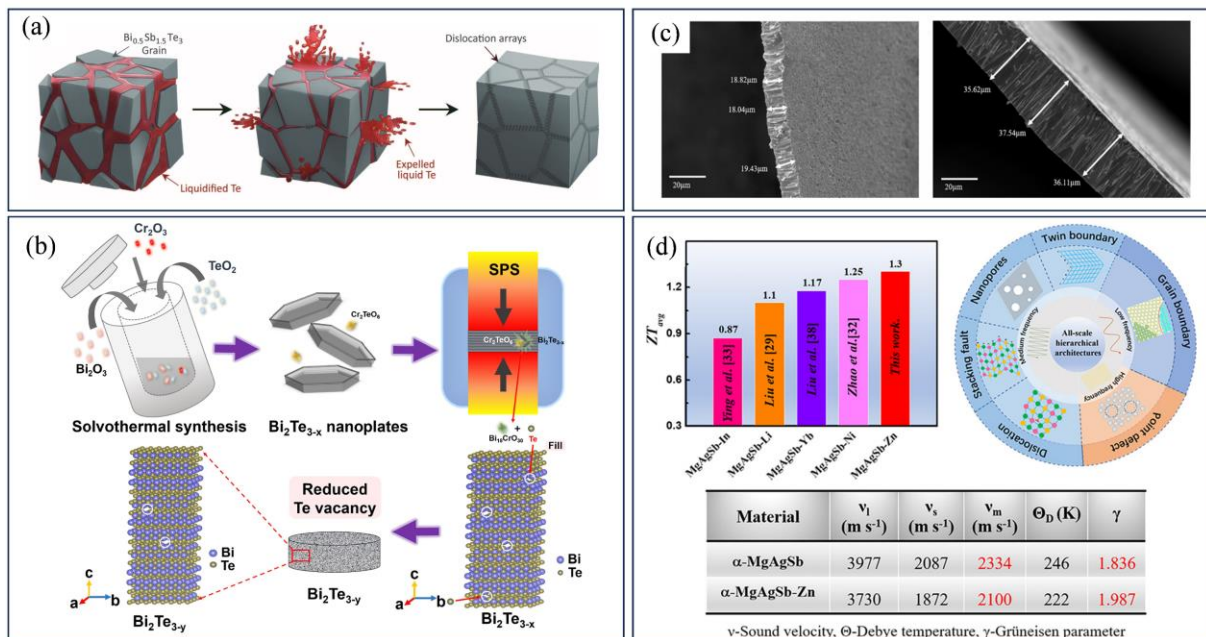

Figure 4. (**a**) Schematic illustration showing the generation of dislocation arrays during the liquid-phase compaction process. "Reprinted with permission from Ref. [31].2015, Kim, S.I."; (**b**) Non equilibrium reaction induced by spark plasma sintering. "Reprinted with permission from Ref. [32]. 2020, Wang, Y."; (**c**) SEM cross-sectional micrograph of Bi2Te2.4Se0.6 thin films after melt spinning at 600 and 300 rpm. "Reprinted with permission from Ref. [33]. 2020, Meroz, O."; (**d**) A design scheme of full-scale hierarchical structure. "Reprinted with permission from Ref. [34]. 2019, Zheng, Y.".

Research on medium- and high-temperature thermoelectric materials have achieved significant breakthroughs. Wu et al. [35] proposed an innovative strategy involving alternating regulation of interatomic interactions through lattice strain modulation while maintaining the original material composition. This methodology achieved a remarkable 58% reduction in lattice thermal conductivity without sacrificing carrier mobility, ultimately realizing an exceptional *ZT* value of 2.6 at 850 K in the engineered material system. Rogl et al. [36] successfully synthesized (R0) with a nominal composition of $(R_{0.33}Ba_{0.33}Yb_{0.33})_{0.35}Co_4Sb_{12.3}$ (R = Sr, La, DD, MM, SRMM, SRDD) massive n-type three filled and multi filled skutterudite materials. The experimental results show that the series of thermoelectric materials achieve the highest *ZT* value of 1.8 at 835 K. Tsai et al. [37] significantly reduced the thermal conductivity of the material by introducing Sb_2Te_3 alloying into GeTe-based thermoelectric materials, while maintaining a suitable carrier concentration over a wide compositional range. Owing to this optimization strategy, the material can achieve a *ZT* value > 2.6 at 720 K. Saiga et al. [38] systematically investigated the effect of Cu doping on $Ba_8Ga_{16}Sn_{30}$ crystal growth and its thermoelectric properties. The results show that the *ZT* values of p-type and n-type single crystals reach 0.88 and 1.45 at 520 K, respectively, with the n-type single crystals having the highest *ZT* values among all the substitution systems of $Ba_8Ga_{16}Sn_{30}$. Shi et al. [39] successfully optimized the synergistic optimization of high carrier concentration and mobility in n-type Mg_3Sb_2 alloys by introducing Y doping at the cationic position. It was found that the material's thermoelectric properties were significantly better than those of the previously reported n-type Mg_3Sb_2 system, achieving a *ZT* value as high as 1.8 at 700 K.

In different application scenarios, variations in operating temperature range cause significant differences in the thermoelectric material systems used. For example, micropower supplies typically operate in the low-temperature range, TEG systems in the 1 W to 1 kW order of magnitude are mostly deployed in the low or medium-temperature range, and TEG systems with power levels greater than 1 kW need to be matched to medium- or high-temperature operating environments. Table 1 systematically summarizes the peak *ZT* values of thermoelectric materials and their corresponding temperature regions in the above studies. Therefore, temperature matching and

material selection based on actual working conditions are of great significance for optimizing system performance, and key factors such as thermal stability of materials, temperature dependence of thermoelectric parameters, and interfacial compatibility need to be considered comprehensively.

Table 1. Optimum *ZT* values and operating temperatures of various thermoelectric materials.

Materials	Type	*ZT* Value	Temperature	Ref.
$Bi_{0.5}Sb_{1.5}Te_3$	p-type	1.86	320 K	[31]
$Bi_2Te_{2.86}$	n-type	1.1	420 K	[32]
$Bi_2Te_{2.4}Se_{0.6}$	n-type	1.07	338 K	[33]
$Mg_{0.97}Zn_{0.03}Ag_{0.9}Sb_{0.95}$	p-type	1.4	423 K	[34]
$Na_{0.03}Eu_{0.03}Sn_{0.02}Pb_{0.92}Te$	p-type	2.6	850 K	[35]
$(R_{0.33}Ba_{0.33}Yb_{0.33})_{0.35}Co_4Sb_{12.3}$	n-type	1.8	835 K	[36]
$(GeTe)_{0.95}(Sb_2Te_3)_{0.05}$	p-type	2.7	720 K	[37]
$Ba_8Ga_{16}Sn_{30}$	n-type	1.45	520 K	[38]
$Mg_{3.05-x}Y_xSbBi$	n-type	1.8	700 K	[39]

2.3. Design of the Thermoelectric Generator

Conventional TEGs typically employ symmetric cubic configurations for their thermoelectric semiconductors, as depicted in Figure 5a, where p-type and n-type thermoelectric legs maintain identical geometric dimensions. However, research has shown that geometric optimization of thermoelectric components, including asymmetric architectures and gradient cross-sections, can enhance performance. This structural optimization enables precise regulation of heat flux distribution, enhanced phonon scattering mechanisms, and minimized interfacial thermal losses, thereby establishing novel design paradigms for high-efficiency TEG systems. Luo et al. [40] proposed an L-shaped TEG configuration (Figure 5b) accounting for inherent material parameter disparities between p-type and n-type thermoelectric materials. This innovative configuration engineer's distinct height dimensions for p-type and n-type semiconductor legs. Experimental results demonstrate that under a temperature difference of 400 K, the L-shaped TEG yielded a maximum output power of 1.96 W with a conversion efficiency of 7.8%, representing 2.39% and 1.44% enhancements, respectively, compared to conventional π-type TEG counterparts. Wang et al. [41] proposed an X-type TEG configuration (Figure 5c) and systematically analyzed its thermoelectric and mechanical properties under steady-state conditions. The results show that under the temperature difference of 200 K, the maximum output power of the X-type thermoelectric module reaches 0.0847 W, and the conversion efficiency is 5.2%, which is about 4.57% higher than the traditional configuration. Luo et al. [42] proposed a ring-shaped TEG configuration with variable cross-sectional area (Figure 5d), in which the cross-sectional area of thermoelectric legs increases along the gradient of heat flow direction to alleviate the performance degradation caused by the decline of temperature gradient. The results show that the output power of the annular TEG is 76.66 W, and the conversion efficiency is 1.45%, which is 8.97% and 8.93% higher than the traditional configuration, respectively.

In addition, the two-stage TEG further improves the comprehensive performance of TEG by stacking two thermoelectric modules up and down. Enciso-Montes et al. [43] proposed a two-stage TEG configuration (Figure 5e) and systematically studied the influence of different thermoelectric leg shapes on TEG performance. The results show that although the efficiency of two-stage TEG and single-stage TEG is 3.9%, the peak voltage of two-stage TEG is 97.6 mV, which is significantly higher than that of single-stage TEG of 49.7 mV. Bian et al. [44] developed a two-stage TEG configuration (Figure 5f), in which different thermoelectric materials are used at the hot end and cold end to adapt to the corresponding temperature range. In this study, the non-dominated sorting genetic algorithm II (NSGA-II) was introduced for the first time to optimize TEG's electrical output performance and mechanical stability.

Considering the different optimal working temperatures of different thermoelectric materials and the temperature gradient of thermoelectric legs from the hot side to the cold side, the segmented design can effectively overcome the negative impact of the temperature drop, in which the high-temperature area adopts high- or medium-thermoelectric materials and the low-temperature area adopts medium- or low-temperature thermoelectric materials. Zhang et al. [45] prepared a Bi_2Te_3/Skutterudite segmented thermoelectric module (Figure 5g), and achieved a conversion efficiency of up to 12% at a temperature difference of 541 K, setting a record in the field, with an output power of 5.6 W. He et al. [46] developed a double-cone segmented thermoelectric generator (Figure 5h). The results show that, compared with the traditional segmented ring thermoelectric generator, the output power of the double cone segmented ring thermoelectric generator is increased by 20.23%, the energy efficiency is increased by 8.55%, and the economic cost is reduced by 21.36%. Sun et al. [47] combined the multi-objective genetic algorithm with the finite element method to optimize the multi-parameter and multi-objective of the segmented

annular TEG. The results show that the optimized segmented TEG has an output power of 0.04326 W and an efficiency of 9.63% at a temperature difference of 300 K, which is 32.839% and 61.915% higher than that before optimization, respectively.
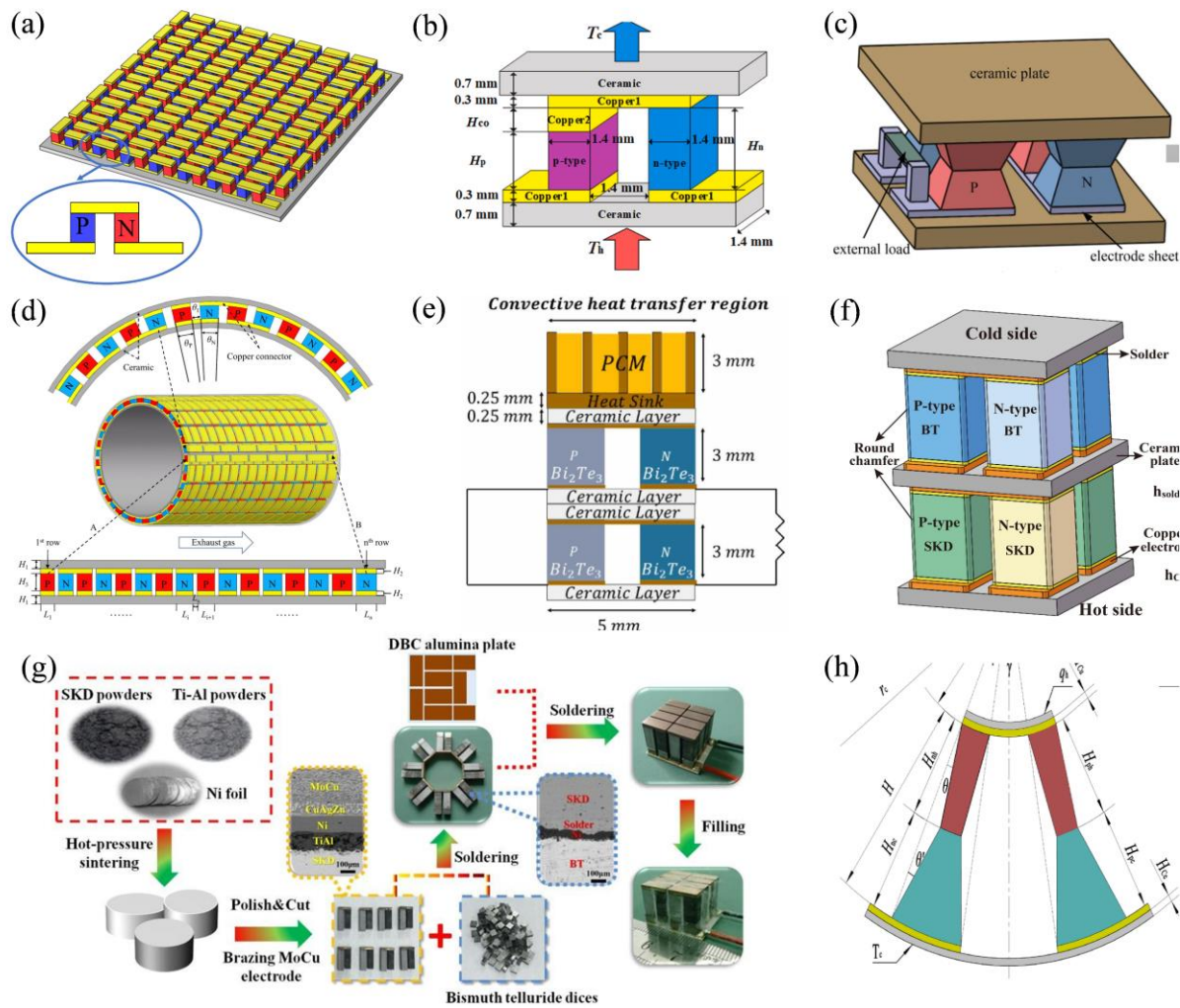

Figure 5. (**a**) Traditional π-type TEG; (**b**) L-type TEG. "Reprinted with permission from Ref. [40]. 2024, Luo, D."; (**c**) X-type TEG. "Reprinted with permission from Ref. [41]. 2020, Wang, R."; (**d**) Variable cross-sectional area annular TEG. "Reprinted with permission from Ref. [42]. 2024, Luo, D."; (**e**) Two-stage TEG. "Reprinted with permission from Ref. [43]. 2024, de Oca, O.Y.E.-M."; (**f**) Two-stage TEG with different thermoelectric materials between the upper and lower stages. "Reprinted with permission from Ref. [44]. 2025, Bian, M."; (**g**) Bi$_2$Te$_3$/Skutterudite segmented TEG. "Reprinted with permission from Ref. [45]. 2017, Zhang, Q."; (**h**) Biconical segmented annular TEG. "Reprinted with permission from Ref. [46]. 2024, He, H".

Table 2 summarizes the above studies. Based on the review and analysis of the TEG design strategy, it can be seen that the thermoelectric performance of TEG can be significantly improved through effective structural design (such as asymmetric configuration, segmented integration, multi-objective optimization, etc.). These design strategies provide important theoretical guidance and technical path for realizing high-performance TEG by optimizing heat flow distribution, interface contact resistance and electrical transport characteristics.

Table 2. Output performance and conversion efficiency of different types of TEGs.

Type of TEG	Improvement Measures	Temperature Difference	Output Power or Voltage	Conversion Efficiency	Ref.
L-Type	P-type and n-type thermal legs are designed with different heights	400 K	1.96 W	7.8%	[40]
X-Type	The cross-sectional area of the thermal leg gradually decreases from the upper and lower ends to the center	200 K	0.0847 W	5.2%	[41]

Table 2. *Cont.*

Type of TEG	Improvement Measures	Temperature Difference	Output Power or Voltage	Conversion Efficiency	Ref.
Asymmetric configuration	The cross-sectional area of the thermoelectric leg increases gradually along the direction of heat flow	-	76.66 W	1.45%	[42]
Two-stage TEG	Stack two layers of TEG	-	97.6 mV	3.9%	[43]
Two-stage TEG	Two layers of TEG are stacked, and different thermoelectric materials are used for hot end and cold-end TEG	300 K	-	6.89%	[44]
Segmented TEG	Bi_2Te_3/Skutteruditesegmented thermoelectric module	541 K	-	12%	[45]
Segmented TEG	Segmented annular TEG with double cone-shaped thermoelectric leg	-	-	-	[46]
Segmented TEG	Combining multiobjective genetic algorithm with finite element method	300 K	0.04326 W	9.63%	[47]

3. Micropower Supply

Due to the low power demand of microelectronic devices, thermoelectric power generation technology has broad application prospects in the field of micropower electronics. Thermoelectric micropower supplies include wearable thermoelectric devices that convert body heat into electricity, self-powered sensors, and microelectronics in the specific application environment.

3.1. Wearable Thermoelectric Devices

In recent years, with the rapid development of micro-nano processing technology and flexible electronic devices. The TEG can be integrated into wearable electronic devices owing to its miniaturization and flexible design, achieving self-powered energy collection of temperature differences between the human body and the environment. The current performance evaluation system for wearable TEG mainly focuses on two core indicators: output power density and wearing comfort. According to the differences in material systems and structural characteristics, wearable TEGs can be divided into two categories: traditional rigid TEGs represented by Bi_2Te_3, and flexible TEGs made of organic materials.

For the traditional rigid TEG, Nozariasbmarz et al. [48] studied the joint effect of material and device parameters on the efficiency of wearable TEG and developed a nanocomposite thermoelectric material based on Bi_2Te_3 (Figure 6a). The experimental results show that the power density of the nanocomposite TEG is 44 $\mu w \cdot cm^{-2}$ without airflow and can be increased to 156.5 $\mu w \cdot cm^{-2}$ under airflow, which is 4–7 times higher than that of similar commercial wearable TEG. Hyland et al. [49] proposed an efficient TEG design scheme for wearable applications and developed a functional T-shirt integrated with TEG (Figure 6b). By systematically measuring the power generation performance of TEG in different parts of the human body (such as the upper arm, forearm, chest, etc.), it is found that when TEG is installed in the upper arm, its output power reaches the maximum. Van et al. [50] realized TEG with high integration density through advanced assembly technology. The output power of the TEG reaches 91 μW at a 5 K temperature difference. Based on this technology, the research team successfully developed a wearable TEG prototype and verified the feasibility of its continuous power supply for electronic watches (Figure 6c). Van et al. [51] proposed a brain-computer system powered by wearable TEG (Figure 6d), with the output power of wearable TEG maintained at 2–2.5 mW (30 ± 2 $\mu w/cm^2$). However, due to the fixed geometry of the TEG based on Bi_2Te_3, they are difficult to fit the skin surface, resulting in low heat recovery efficiency. Organic thermoelectric materials have the advantage of flexible structure and can adapt to different shapes and sizes. Lv et al. [52] proposed a three-dimensional spring thermoelectric device with a basic double elastomer layer and air gap (Figure 6e). The device has excellent flexibility and compressibility, generating a power density of 416.22 nw/cm^2. Kim et al. [53] developed a self-powered wearable ECG system based on flexible PCB (Figure 6f). The system optimizes the performance of wearable TEG through a flexible radiator based on polymer so that its output power density reaches 38 $\mu w/cm^2$ in the initial 10 min and remains at 13 $\mu w/cm^2$ after 22 h of continuous operation so that it can continuously supply energy for ECG sensor and power management circuit. The aforemenioned research indicates that the flexible TEG of organic-inorganic composites enhances its bending (radius of curvature < 5 mm) and endows it with low thermal conductivity (<0.5 $w \cdot m^{-1} \cdot K^{-1}$), but its power density is usually lower than that of rigid wearable teg1-2 orders of magnitude.

Figure 6. (**i**) Nanocomposite thermoelectric materials based on Bi$_2$Te$_3$. "Reprinted with permission from Ref. [48]. 2020, Nozariasbmarz, A."; (**ii**) A T-shirt integrated with wearable TEG. "Reprinted with permission from Ref. [49]. 2016, Hyland, M."; (**iii**) Wearable TEG supplies power for electronic watches. "Reprinted with permission from Ref. [50]. 2021, Van Toan, N."; (**iv**) A brain-computer system powered by wearable TEG. "Reprinted with permission from Ref. [51]. 2008, Van Bavel, M."; (**v**) A three-dimensional spring thermoelectric device with basic double elastomer layer and air gap. "Reprinted with permission from Ref. [52]. 2021, Lv, H."; (**vi**) A self powered wearable ECG system based on flexible PCB. "Reprinted with permission from Ref. [53]. 2018, Kim, C.S."

3.2. Self-Powered Sensors

Automation and intelligence have become the development trend of modern industry. Thanks to this, intelligent sensors and microelectronics have made great development. More and more manufacturers incorporated sensors into products to improve their competitiveness. Current intelligent sensors and microelectronics require a few hundred microwatts or a few milliwatts of power to operate. Powering these devices typically requires extensive cabling from the battery, which often fails to satisfy the sensor's long-life demands. In some specific applications, sensors are required to work in extreme environments such as high temperature and vacuum. Wireless, long-life power supply, and extreme working environments are the main challenges that come to sensors. TEGs are an ideal candidate for these challenges. Beltrán et al. [54] proposed a TEG-powered vacuum pressure sensor and reported that the random error of the pressure signal was less than 10%. Kim et al. [55] designed a high-performance self-powered wireless sensor node powered by the flexible TEG, which can be used to remotely monitor the heat pipe temperature, ambient temperature, humidity, etc. Self-powered sensors and microelectronics are promising applications of TEGs. Guan et al. [56] developed a self-starting two-stage boost thermoelectric energy harvesting system, incorporating open-circuit voltage MPPT and low-power design; The system can self-start and efficiently supply power at an extremely low input of 20 mV/84 µW, driving microcontrollers and wireless sensors, with performance surpassing that of commercial solutions.

4. Thermoelectric Generator Systems from 1 W to 1 kW

At present, the output power of most TEG systems with preliminary application ranges from 1 W to 1 kW, including radiative TEG systems, solar thermoelectric generators, and automobile TEG systems. The recent developments, challenges, and prospects of these three TEG applications are discussed below.

4.1. Radiative Thermoelectric Generator System

In space exploration, satellites, and spacecraft require a long-term power supply to meet the needs of exploration missions. Current satellites and spacecraft are mainly powered by PV devices. However, due to the rotation of the planet, PV devices can receive sunlight for only half of the time at most, resulting in the deterioration of the lifespan of spacecraft. Radiative TEG systems utilize heat from natural radioactive decay as a power source. The exceptionally long half-lives of radioisotopes enable these systems to provide continuous electrical power for spacecraft over multi-decade timescales. In 1961, the PbTe-based radiative TEG system was first applied to the US Navy's Transit navigation satellite. The output power was about 2.7 W, but it operated for over fifteen years. Sponsored by NASA, radiative TEG systems with better performance have been developed continuously. In 1997, the Voyager I and II used 3 SiGe-based radiative TEG systems to provide 423 W of power for onboard electronics. This power is gradually reduced by about 7 W per year due to the decay of plutonium, and they are still in operation [57]. The success of radiative TEG systems developed by NASA has accelerated the application of thermoelectric power generation technology in space exploration, and an increasing number of countries have issued corresponding research plans.

4.2. Solar Application

Thermoelectric technology can also directly convert solar radiation into electricity based on the Seebeck effect. Unlike photovoltaic (PV) devices that directly convert light energy into electric energy, solar TEGs collect solar heat through a solar heat absorber and then transfer the heat to thermoelectric legs for power generation. Shittu et al. [58] analyzed the output performance of a segmented solar TEG through a numerical model and obtained that the output power was about 3 W under the radiation value of 11,000 W/m^2. Kraemer et al. [8] manufactured a skutterudite/Bi$_2$Te$_3$ segmented solar TEG and experimentally demonstrated its conversion efficiency under the direct normal irradiance of 211 kW/m^2. The experimental results showed that a peak efficiency of 7.4% was achieved. Cotfas et al. [59] prepared a metal oxide/additive composite absorption layer on the hot side of a solar TEG using spray deposition technology. The power generation increased by 25% under standard solar irradiance and by 82% under concentrated irradiance conditions. Cao et al. [60] proposed a solar TEG integrated with phase change materials and forced water cooling, achieving a power output of 6.42 mW and an output voltage of 307.3 mV at a solar irradiance of 1 kW/m², approximately 9 times higher than that of the traditional thermoelectric module (35.5 mV). Although the conversion efficiency of the solar TEG is still lower than that of PV devices, it is likely to become a promising alternative solar energy technology. However, the solar radiation in practical application is far lower than that in the laboratory. To be more competitive, the figure of merit of thermoelectric materials must be further improved. The high-performance heat absorber on the hot side of the solar TEG and the high-performance heat sink on the cold side of the solar TEG also help to improve its performance.

4.3. Automobile Thermoelectric Generator System

For automobile engines, about 1/3 of the thermal energy produced by burning fossil fuels is wasted in the form of waste heat with exhaust gas, resulting in serious energy waste and environmentally harmful emissions. The automobile thermoelectric generator (ATEG) system is considered a promising technology that can improve the fuel economy and reduce the use of fossil fuels. Automobile manufacturers and research institutes are trying to develop high-performance ATEG systems and integrate them into the vehicle exhaust system. However, the conversion efficiency of currently reported ATEG systems is about 2%, which seriously limits its wide commercial applications. Structure-based optimization is one of the most effective methods for improving the performance of ATEGs.

ATEGs primarily consist of heat exchangers (used to absorb heat from exhaust gases), thermoelectric modules (used to convert thermal energy into electrical energy), and radiators (used to maintain the cold-side temperature of the thermoelectric modules). The structural optimization of thermoelectric modules has been discussed in detail in Section 2.3. The optimization of the heat exchanger structure focuses primarily on enhancing its heat absorption efficiency. Luo et al. [61] proposed a convergent TEG (Figure 7a), which significantly enhanced the heat absorption efficiency of the heat exchanger, resulting in a 5.96% increase in the net output power of the TEG. To accommodate the circular exhaust pipe, Yang et al. [62] proposed a circular TEG with pin-fin type fins (Figure 7b) and determined the optimal structure of the TEG using Taguchi optimization; The net power reached

34.11 W, representing an 18.7% increase compared to the original design. Studies have shown that the installation of fins inside the heat exchanger can significantly enhance its heat absorption efficiency. Consequently, researchers aim to optimize the fin structure. Luo et al. [63] proposed a fin with dimples based on plate fins (Figure 7c) and determined the optimal design of the dimples through numerical simulations. The net output power increased by 10.09%. Ge et al. [64] introduced twisted-strip fins into the heat exchanger and optimized their pitch ratio, twist ratio, and tilt angle (Figure 7d), resulting in a 30% increase in the output power of the TEG.

Additionally, heat pipes exhibit exceptional heat transfer performance, fully meeting the high thermal conductivity requirements of ATEGs. Luo et al. [65] proposed a novel ATEG integrated with heat pipes, introducing the heat pipes into the heat exchanger (Figure 7e). The incorporation of heat pipes expanded the thermal side area of the heat exchanger, resulting in an output power of 213.19 W, representing a 42.95% increase. Pacheco et al. [66] longitudinally installed heat pipes inside the heat exchanger, significantly enhancing the temperature uniformity of the exchanger due to the high thermal conductivity of the heat pipes. Despite the promising results of the aforementioned studies, the generated electrical power remains insufficient to fully meet the power supply requirements of the vehicle. To achieve higher output power, a larger ATEG is necessary. To address this, Liu et al. [67] integrated four identical ATEGs in parallel into a vehicle (Figure 7f), achieving a maximum output power of 944 W in the tests. Zhang et al. [68] stacked multiple small heat exchangers together (Figure 7g), resulting in a maximum output power of 1002.6 W for the TEG, although this also resulted in a high-pressure drop. Although these large ATEGs generate exceptionally high output power, they occupy a significant portion of the vehicle's space. Therefore, maximizing the output power of ATEGs within limited space is an important research endeavor for future development.
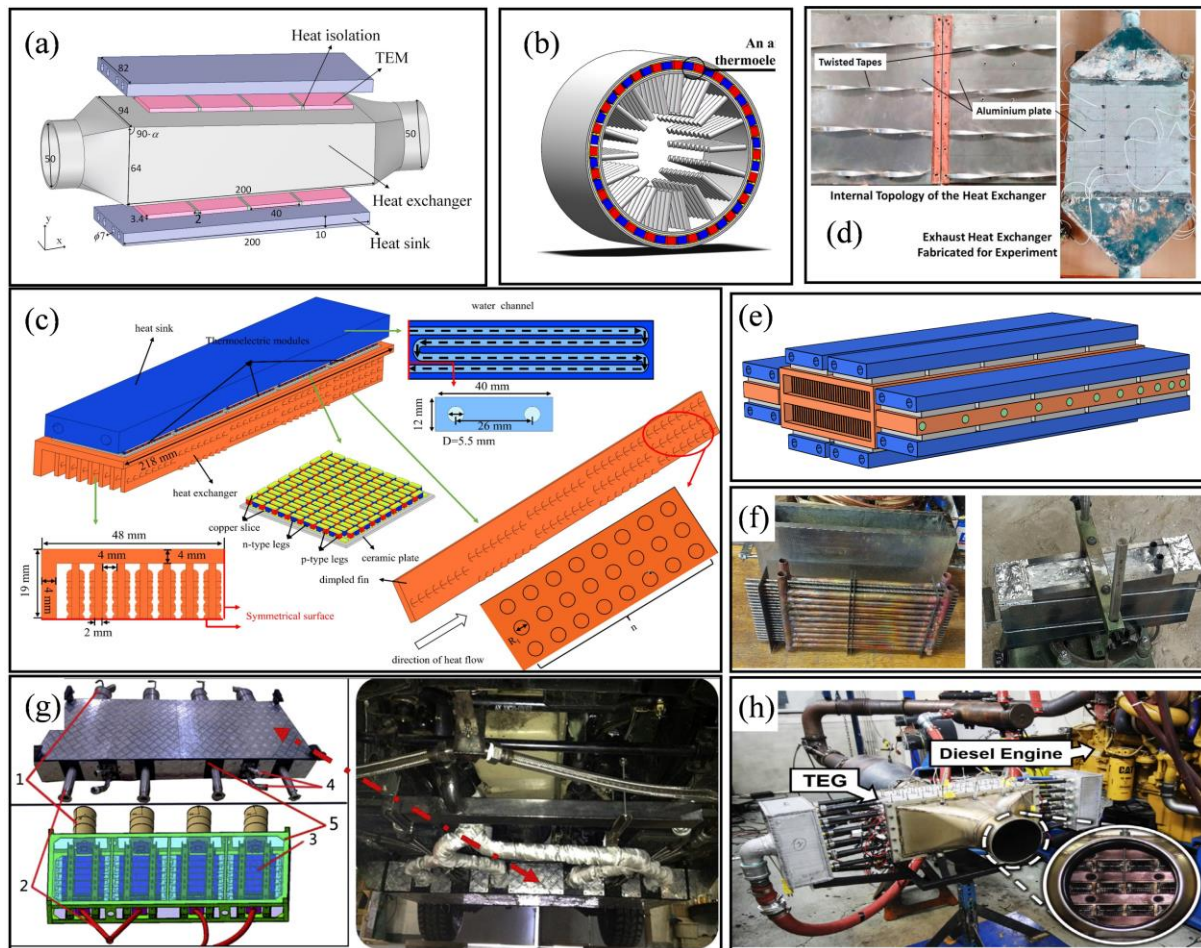

Figure 7. (**a**) Convergent TEG. "Reprinted with permission from Ref. [61]. 2019, Luo, D."; (**b**) Pin-fin type circular TEG. "Reprinted with permission from Ref. [62]. 2024, Yang, W."; (**c**) Fins with dimples. "Reprinted with permission from Ref. [63]. 2024, Luo, D."; (**d**) TEG with twisted band fins. "Reprinted with permission from Ref. [64]. 2025, Ge, M."; (**e**) Expand the hot side area of the heat exchanger using heat pipes. "Reprinted with permission from Ref. [65]. 2024, Luo, D."; (**f**) Using heat pipes to improve the temperature uniformity of heat exchangers. "Reprinted with permission from Ref. [66]. 2020, Pacheco, N."; (**g**) Four-TEG system. "Reprinted with permission from Ref. [67]. 2015, Liu, X."; (**h**) Compact TEG. "Reprinted with permission from Ref. [68]. 2015, Zhang, Y."

5. Thermoelectric Generator Systems Exceed 1 kW

In addition to recycling the waste heat in automobile exhaust, TEG can also be applied to the recovery of waste heat from ships and industrial waste gases. The exhaust gas temperature in these fields is usually high and the waste heat is huge. Therefore, the power generation capacity of TEG system in these application scenarios often exceeds 1 kW and even can achieve higher power output.

In ship application, TEG can recover heat energy from high-temperature exhaust gas emitted by the engine and further improve energy recovery efficiency by using other waste heat sources generated during ship operation, such as boiler exhaust gas and engine room waste heat. This waste heat recovery system can provide clean power for ships, reduce dependence on traditional generators, and effectively reduce fuel consumption and improve the overall energy efficiency of ships. Compared with TEGs applied to vehicles, the TEG system applied to ships can ignore the negative impact of increased weight. However, few studies have been perfomed to develop whole TEG system prototypes for ship waste heat recovery because it requires a large number of TEG modules and costs. Georgopoulou et al. [69] studied the waste heat recovery potential of TEGs for marine applications, and results showed that the installation of TEGs could generate about 26 kW of extra power, corresponding to 0.2% of the main engine power. Eddine et al. [16] analyzed and optimized the performance of a simplified ship TEG system through a theoretical model. Results showed that the Bi_2Te_3-based TEG module was more suitable for ship waste heat recovery, and its output power was 70% higher than that of the SiGe-based TEG. With the increasing demand for fuel economy, ship manufacturers are opting to utilize TEGs to optimize ship waste heat recovery, because it has a weight advantage, offers a free cooling source, and does not require maintenance.

In the industrial field, especially in high-temperature industrial processes (such as metallurgy, chemical industry, glass production, etc.), the TEG system can effectively extract heat energy generated from the high-temperature exhaust gases. TEG can achieve high power output by optimizing the heat exchange system and thermoelectric materials. In industrial waste heat recovery, technologies, such as the organic Rankine cycle, steam turbines, and Stirling engines, are increasingly being optimized. As a promising energy technology, various waste heat projects using TEGs have been studied. Luo et al. [15] proposed a novel TEG system to harvest waste heat from cement rotary kilns, in which 3480 Bi_2Te_3–PbTe TEG modules were applied on the walls of the kiln. The system performance was estimated using a mathematical model. Results showed that the system can produce about 211 kW of electrical power and recover more than 32.85% of the heat that used to be lost as waste heat through the kiln surface. Kuroki et al. [70] described a TEG system used for waste heat recovery in the steelmaking industry, which contains 896 Bi_2Te_3-based TEG modules. Experimental results showed that the system could generate 9 kW electricity when the slab temperature was about 1188 K and the slab width was 1.7 m. Although the conversion efficiency of the TEG system is low (~2%), it still enables considerable application prospects in the field of industrial waste heat recovery. The cost of installing TEG systems will be recovered within a few years because the furnace works 24 h a day.

Looking forward to the future, the application potential of TEG technology in the field of industrial waste heat recovery is still huge. With the continuous progress of thermoelectric materials, heat exchange technology, and system optimization design, the efficiency and output power of the TEG system need to be further optimized. In addition, with the increasing demand for energy conservation and environmental protection in the market, TEG, as a green and low-carbon energy recovery technology, is expected to be increasingly applied in industrial waste heat recovery, ship energy recovery, and other high-temperature waste gas utilization.

6. Conclusions

In this review, basic principles, recent advances, current challenges, and prospects of thermoelectric power generation from micropower supplies to kilowatt systems are discussed. As a basic power unit of the TEG system, the performance of the TEG module can be improved by applying high-performance thermoelectric materials and advanced structural design. For micropower supplies, the wearable TEG system should not only pay attention to performance improvement but also comfort, while the self-powered sensors and microelectronics mainly focus on the performance and application environment. For TEG systems from 1 W to 1 kW, preliminary applications have been achieved, such as radiative, stove, and automobile TEG systems, among which the automobile TEG system has the potential to generate over 1 kW of electricity. When TEGs are applied to waste heat recovery from the ship and industrial exhaust gas, the TEG system can easily generate an output power of more than 1 kW, and there is an increasing interest in using TEGs to reduce energy use. Ongoing developments in thermoelectric materials and devices will soon facilitate broader adoption of thermoelectric power generation technologies.

Despite these advancements, critical challenges persist in TEG applications, including inherent limitations in thermoelectric material efficiency (e.g., low *ZT* values at mid-to-low temperature ranges), interfacial thermal

resistance in system integration, and long-term stability under cyclic thermal stresses. Future studies should investigate nanostructured composites and topology-optimized modules to decouple electronic and thermal transport properties, as well as AI-driven design frameworks for hybrid energy systems. Emerging applications in IoT power supply and aerospace waste heat recovery, coupled with scalable manufacturing techniques like inkjet printing of thermoelectric films, are expected to accelerate the transition of TEGs from niche applications to industrial ubiquity.

Author Contributions: S.Y.: writing—original draft, visualization, conceptualization, investigation; H.C.: data curation, software; D.L.: writing—reviewing and editing, supervision, funding acquisition. All authors have read and agreed to the published version of the manuscript.

Data Availability Statement: Data will be made available on request.

References

1. Ge, M.; Li, Z.; Wang, Y.; et al. Experimental study on thermoelectric power generation based on cryogenic liquid cold energy. *Energy* **2021**, *220*, 119746. https://doi.org/10.1016/j.energy.2020.119746.

2. Luo, D.; Yu, Y.; Yan, Y.; et al. Increasing power densities in a thermoelectric generator by stacking and incorporating dual heat pipes. *Device* **2024**, *2*, 100435. https://doi.org/10.1016/j.device.2024.100435.

3. Luo, D.; Liu, Z.; Cao, J.; et al. Feasibility and parametric study of a groove-type thermoelectric generator under multiphysics field conditions. *Appl. Therm. Eng.* **2025**, *259*, 124972. https://doi.org/10.1016/j.applthermaleng.2024.124972.

4. Luo, D.; Wu, Z.; Zhang, Z.; et al. Transient thermal analysis of a thermoelectric-based battery thermal management system at high temperatures. *Energy* **2025**, *318*, 134833. https://doi.org/10.1016/j.energy.2025.134833.

5. He, T.; Nair, S.K.; Babu, P.; et al. A novel conceptual design of hydrate based desalination (HyDesal) process by utilizing LNG cold energy. *Appl. Energy* **2018**, *222*, 13–24. https://doi.org/10.1016/j.apenergy.2018.04.006.

6. Shih, W.-C.; Matsuda, M.; Konno, K.; et al. Tailored thermoelectric performance of poly(phenylene butadiynylene)s/carbon nanotubes nanocomposites towards wearable thermoelectric generator application. *Compos. Part B Eng.* **2024**, *286*, 111779. https://doi.org/10.1016/j.compositesb.2024.111779.

7. Bennett, G. Space Nuclear Power: Opening the Final Frontier. In Proceedings of the 4th International Energy Conversion Engineering Conference and Exhibit (IECEC), San Diego, CA, USA, 26–29 June 2006.

8. Kraemer, D.; Jie, Q.; McEnaney, K.; et al. Concentrating solar thermoelectric generators with a peak efficiency of 7.4%. *Nat. Energy* **2016**, *1*, 16153. https://doi.org/10.1038/nenergy.2016.153.

9. Zhao, R.; Zhu, N.; Zhao, X.; et al. Multi-objective optimization of a novel photovoltaic-thermoelectric generator system based on hybrid enhanced algorithm. *Energy* **2025**, *319*, 135046. https://doi.org/10.1016/j.energy.2025.135046.

10. Suresh Prasanna, C.; Harish, S.; Archana, J.; et al. Interfacial energy barrier tuning in MnO_2/MoS_2/Carbon fabric integrated with low resistance textrode for highly efficient wearable thermoelectric generator. *Carbon* **2024**, *218*, 118609. https://doi.org/10.1016/j.carbon.2023.118609.

11. Luo, D.; Li, Z.; Yang, S.; et al. Improved performance of the thermoelectric generator by combining vapor chambers and circular fins. *Energy* **2025**, *320*, 135354. https://doi.org/10.1016/j.energy.2025.135354.

12. Luo, D.; Yang, S.; Li, Z.; et al. Transient energy, exergy, and economic analysis of an automotive thermoelectric generator with different structures. *Appl. Energy* **2025**, *377*, 124494. https://doi.org/10.1016/j.apenergy.2024.124494.

13. Luo, D.; Yang, S.; Zhang, H.; et al. Performance improvement of an automotive thermoelectric generator by introducing a novel split fin structure. *Appl. Energy* **2025**, *382*, 125218. https://doi.org/10.1016/j.apenergy.2024.125218.

14. Yang, S.; Chen, H.; Yang, X.; et al. Design optimization of split fins in heat pipe-based thermoelectric generators. *Energy* **2025**, *322*, 135547. https://doi.org/10.1016/j.energy.2025.135547.

15. Luo, Q.; Li, P.; Cai, L.; et al. A Thermoelectric Waste-Heat-Recovery System for Portland Cement Rotary Kilns. *J. Electron. Mater.* **2015**, *44*, 1750–1762. https://doi.org/10.1007/s11664-014-3543-1.

16. Nour Eddine, A.; Chalet, D.; Faure, X.; et al. Optimization and characterization of a thermoelectric generator prototype for marine engine application. *Energy* **2018**, *143*, 682–695. https://doi.org/10.1016/j.energy.2017.11.018.

17. Miao, Z.; Meng, X.; Li, X. Design a high-performance thermoelectric generator by analyzing industrial heat transfer. *Appl. Energy* **2023**, *347*, 121403. https://doi.org/10.1016/j.apenergy.2023.121403.

18. Liu, X.; Wang, K.; Shen, Z. A novel strategy of inserting radiation shields to enhance the performance of thermoelectric generator systems for industrial high-temperature heat recovery. *Energy* **2024**, *301*, 131704. https://doi.org/10.1016/j.energy.2024.131704.

19. Luo, D.; Wang, R.C. Experimental Test and Estimation of the Equivalent Thermoelectric Properties for a Thermoelectric Module. *J. Energy Resour. Technol.-Trans. Asme* **2021**, *143*, 122102. https://doi.org/10.1115/1.4050132.

20. Luo, D.; Chen, H.; Chen, W.-H.; et al. Interdependent optimization strategies for material, module, and system designs in thermoelectric devices. *Device* **2025**, 100752. https://doi.org/10.1016/j.device.2025.100752.

21. Bell, L.E. Cooling, Heating, Generating Power, and Recovering Waste Heat with Thermoelectric Systems. *Science* **2008**, *321*, 1457. https://doi.org/10.1126/science.1158899.

22. Twaha, S.; Zhu, J.; Yan, Y.; et al. A comprehensive review of thermoelectric technology: Materials, applications, modelling and performance improvement. *Renew. Sustain. Energy Rev.* **2016**, *65*, 698–726. https://doi.org/10.1016/j.rser.2016.07.034.

23. Zheng, X.F.; Liu, C.X.; Yan, Y.Y.; et al. A review of thermoelectrics research—Recent developments and potentials for sustainable and renewable energy applications. *Renew. Sustain. Energy Rev.* **2014**, *32*, 486–503. https://doi.org/10.1016/j.rser.2013.12.053.

24. Luo, D.; Wang, R.; Yu, W.; et al. Parametric study of a thermoelectric module used for both power generation and cooling. *Renew. Energy* **2020**, *154*, 542–552. https://doi.org/10.1016/j.renene.2020.03.045.

25. Wu, Y.; Ma, W.; Guo, Z.-Y. Governing equations of thermoelectric generators. *Int. J. Heat Mass Transf.* **2025**, *241*, 126737. https://doi.org/10.1016/j.ijheatmasstransfer.2025.126737.

26. Luo, D.; Wang, R.; Yu, W. Comparison and parametric study of two theoretical modeling approaches based on an air-to-water thermoelectric generator system. *J. Power Sources* **2019**, *439*, 227069. https://doi.org/10.1016/j.jpowsour.2019.227069.

27. Siddique, A.R.M.; Mahmud, S.; Heyst, B.V. A review of the state of the science on wearable thermoelectric power generators (TEGs) and their existing challenges. *Renew. Sustain. Energy Rev.* **2017**, *73*, 730–744. https://doi.org/10.1016/j.rser.2017.01.177.

28. Ma, Y.; Hao, Q.; Poudel, B.; et al. Enhanced Thermoelectric Figure-of-Merit in p-Type Nanostructured Bismuth Antimony Tellurium Alloys Made from Elemental Chunks. *Nano Lett.* **2008**, *8*, 2580–2584. https://doi.org/10.1021/nl8009928.

29. Ohta, M.; Biswas, K.; Lo, S.-H.; et al. Enhancement of Thermoelectric Figure of Merit by the Insertion of MgTe Nanostructures in p-type PbTe Doped with Na_2Te. *Adv. Energy Mater.* **2012**, *2*, 1117–1123. https://doi.org/10.1002/aenm.201100756.

30. Joshi, G.; Lee, H.; Lan, Y.; et al. Enhanced Thermoelectric Figure-of-Merit in Nanostructured p-type Silicon Germanium Bulk Alloys. *Nano Lett.* **2008**, *8*, 4670–4674. https://doi.org/10.1021/nl8026795.

31. Kim, S.I.; Lee, K.H.; Mun, H.A.; et al. Dense dislocation arrays embedded in grain boundaries for high-performance bulk thermoelectrics. *Science* **2015**, *348*, 109–114. https://doi.org/10.1126/science.aaa4166.

32. Wang, Y.; Liu, W.-D.; Shi, X.-L.; et al. Enhanced thermoelectric properties of nanostructured n-type Bi_2Te_3 by suppressing Te vacancy through non-equilibrium fast reaction. *Chem. Eng. J.* **2020**, *391*, 123513. https://doi.org/10.1016/j.cej.2019.123513.

33. Meroz, O.; Elkabets, N.; Gelbstein, Y. Enhanced Thermoelectric Properties of n-Type Bi_2Te_3–xSex Alloys following Melt-Spinning. *ACS Appl. Energy Mater.* **2020**, *3*, 2090–2095. https://doi.org/10.1021/acsaem.9b02133.

34. Zheng, Y.; Liu, C.; Miao, L.; et al. Extraordinary thermoelectric performance in MgAgSb alloy with ultralow thermal conductivity. *Nano Energy* **2019**, *59*, 311–320. https://doi.org/10.1016/j.nanoen.2019.02.045.

35. Wu, Y.; Chen, Z.; Nan, P.; et al. Lattice Strain Advances Thermoelectrics. *Joule* **2019**, *3*, 1276–1288. https://doi.org/10.1016/j.joule.2019.02.008.

36. Rogl, G.; Grytsiv, A.; Rogl, P.; et al. n-Type skutterudites (R,Ba,Yb)yCo4Sb12 (R = Sr, La, Mm, DD, SrMm, SrDD) approaching ZT ≈ 2.0. *Acta Mater.* **2014**, *63*, 30–43. https://doi.org/10.1016/j.actamat.2013.09.039.

37. Tsai, Y.-F.; Wei, P.-C.; Chang, L.; et al. Compositional Fluctuations Locked by Athermal Transformation Yielding High Thermoelectric Performance in GeTe. *Adv. Mater.* **2021**, *33*, 2005612. https://doi.org/10.1002/adma.202005612.

38. Saiga, Y.; Du, B.; Deng, S.K.; et al. Thermoelectric properties of type-VIII clathrate Ba8Ga16Sn30 doped with Cu. *J. Alloys Compd.* **2012**, *537*, 303–307. https://doi.org/10.1016/j.jallcom.2012.05.049.

39. Shi, X.; Zhao, T.; Zhang, X.; et al. Extraordinary n-Type Mg3SbBi Thermoelectrics Enabled by Yttrium Doping. *Adv. Mater.* **2019**, *31*, 1903387. https://doi.org/10.1002/adma.201903387.

40. Luo, D.; Liu, Z.; Cao, J.; et al. Performance investigation and optimization of an L-type thermoelectric generator. *Energy* **2024**, *307*, 132768. https://doi.org/10.1016/j.energy.2024.132768.

41. Wang, R.; Meng, Z.; Luo, D.; et al. A Comprehensive Study on X-Type Thermoelectric Generator Modules. *J. Electron. Mater.* **2020**, *49*, 4343–4354. https://doi.org/10.1007/s11664-020-08152-4.

42. Luo, D.; Zhang, H.; Cao, J.; et al. Innovative design of an annular thermoelectric generator for enhanced automotive waste heat recovery. *Energy Convers. Manag.* **2024**, *313*, 118584. https://doi.org/10.1016/j.enconman.2024.118584.

43. de Oca, O.Y.E.-M.; Olivares-Robles, M.A. Dynamic performance optimization of two-stage thermoelectric generator: Impact of different geometric leg shapes in each stage. *Energy Rep.* **2024**, *11*, 597–610. https://doi.org/10.1016/j.egyr.2023.12.032.

44. Bian, M.; Xu, Z.; Tang, X.; et al. Tri-objective and multi-parameter geometric optimization of two-stage radioisotope thermoelectric generator based on NSGA-II. *Appl. Therm. Eng.* **2025**, *258*, 124685. https://doi.org/10.1016/j.applthermaleng.2024.124685.

45. Zhang, Q.; Liao, J.; Tang, Y.; et al. Realizing a thermoelectric conversion efficiency of 12% in bismuth telluride/skutterudite segmented modules through full-parameter optimization and energy-loss minimized integration. *Energy Environ. Sci.* **2017**, *10*, 956–963. https://doi.org/10.1039/C7EE00447H.

46. He, H.; Xie, Y.; Zuo, Q.; et al. Optimization analysis for thermoelectric performance improvement of biconical segmented annular thermoelectric generator. *Energy* **2024**, *306*, 132397. https://doi.org/10.1016/j.energy.2024.132397.

47. Sun, Y.; Zhai, P.; Wang, S.; et al. Performance enhancement of segmented annular thermoelectric generator based on multi-parameter and multi-objective optimization. *Therm. Sci. Eng. Prog.* **2024**, *47*, 102245. https://doi.org/10.1016/j.tsep.2023.102245.

48. Nozariasbmarz, A.; Suarez, F.; Dycus, J.H.; et al. Thermoelectric generators for wearable body heat harvesting: Material and device concurrent optimization. *Nano Energy* **2020**, *67*, 104265. https://doi.org/10.1016/j.nanoen.2019.104265.

49. Hyland, M.; Hunter, H.; Liu, J.; et al. Wearable thermoelectric generators for human body heat harvesting. *Appl. Energy* **2016**, *182*, 518–524. https://doi.org/10.1016/j.apenergy.2016.08.150.

50. Van Toan, N.; Thi Kim Tuoi, T.; Van Hieu, N.; et al. Thermoelectric generator with a high integration density for portable and wearable self-powered electronic devices. *Energy Convers. Manag.* **2021**, *245*, 114571. https://doi.org/10.1016/j.enconman.2021.114571.

51. Van Bavel, M.; Leonov, V.; Yazicioglu, R.F.; et al. Wearable battery-free wireless 2-channel EEG systems powerd by energy scavengers. *Sens. Transducers J.* **2008**, *94*.

52. Lv, H.; Liang, L.; Zhang, Y.; et al. A flexible spring-shaped architecture with optimized thermal design for wearable thermoelectric energy harvesting. *Nano Energy* **2021**, *88*, 106260. https://doi.org/10.1016/j.nanoen.2021.106260.

53. Kim, C.S.; Yang, H.M.; Lee, J.; et al. Self-Powered Wearable Electrocardiography Using a Wearable Thermoelectric Power Generator. *ACS Energy Lett.* **2018**, *3*, 501–507. https://doi.org/10.1021/acsenergylett.7b01237.

54. Beltrán-Pitarch, B.; García-Cañadas, J. A novel vacuum pressure sensor using a thermoelectric device. *Vacuum* **2020**, *172*, 109088. https://doi.org/10.1016/j.vacuum.2019.109088.

55. Kim, Y.J.; Gu, H.M.; Kim, C.S.; et al. High-performance self-powered wireless sensor node driven by a flexible thermoelectric generator. *Energy* **2018**, *162*, 526–533. https://doi.org/10.1016/j.energy.2018.08.064.

56. Guan, M.; Wang, K.; Xu, D.; et al. Design and experimental investigation of a low-voltage thermoelectric energy harvesting system for wireless sensor nodes. *Energy Convers. Manag.* **2017**, *138*, 30–37. https://doi.org/10.1016/j.enconman.2017.01.049.

57. Champier, D. Thermoelectric generators: A review of applications. *Energy Convers. Manag.* **2017**, *140*, 167–181. https://doi.org/10.1016/j.enconman.2017.02.070.

58. Shittu, S.; Li, G.; Xuan, Q.; et al. Electrical and mechanical analysis of a segmented solar thermoelectric generator under non-uniform heat flux. *Energy* **2020**, *199*, 117433. https://doi.org/10.1016/j.energy.2020.117433.

59. Cotfas, D.T.; Enesca, A.; Cotfas, P.A. Enhancing the performance of the solar thermoelectric generator in unconcentrated and concentrated light. *Renew. Energy* **2024**, *221*, 119831. https://doi.org/10.1016/j.renene.2023.119831.

60. Cao, Z.; Li, W. A day-night solar thermoelectric generator enabled by phase change material and forced water cooling. *Sol. Energy* **2024**, *268*, 112315. https://doi.org/10.1016/j.solener.2024.112315.

61. Luo, D.; Wang, R.; Yu, W.; et al. Modelling and simulation study of a converging thermoelectric generator for engine waste heat recovery. *Appl. Therm. Eng.* **2019**, *153*, 837–847. https://doi.org/10.1016/j.applthermaleng.2019.03.060.

62. Yang, W.; Jin, C.; Zhu, W.; et al. Taguchi optimization and thermoelectrical analysis of a pin fin annular thermoelectric generator for automotive waste heat recovery. *Renew. Energy* **2024**, *220*, 119628. https://doi.org/10.1016/j.renene.2023.119628.

63. Luo, D.; Li, Z.; Yan, Y.; et al. Design and optimization of a thermoelectric generator with dimple fins to achieve higher net power. *Appl. Therm. Eng.* **2024**, *252*, 123735. https://doi.org/10.1016/j.applthermaleng.2024.123735.

64. Ge, M.; Zhao, C.; Xiao, Y.; et al. Experimental study on enhancing thermoelectric performance of exhaust thermoelectric generator using multi-orifice plate. *J. Clean. Prod.* **2025**, *486*, 144446. https://doi.org/10.1016/j.jclepro.2024.144446.

65. Luo, D.; Yang, S.; Yan, Y.; et al. Performance improvement of the automotive thermoelectric generator by extending the hot side area of the heat exchanger through heat pipes. *Energy Convers. Manag.* **2024**, *310*, 118472. https://doi.org/10.1016/j.enconman.2024.118472.

66. Pacheco, N.; Brito, F.P.; Vieira, R.; et al. Compact automotive thermoelectric generator with embedded heat pipes for thermal control. *Energy* **2020**, *197*, 117154. https://doi.org/10.1016/j.energy.2020.117154.

67. Liu, X.; Deng, Y.D.; Li, Z.; et al. Performance analysis of a waste heat recovery thermoelectric generation system for automotive application. *Energy Convers. Manag.* **2015**, *90*, 121–127. https://doi.org/10.1016/j.enconman.2014.11.015.

68. Zhang, Y.; Cleary, M.; Wang, X.; et al. High-temperature and high-power-density nanostructured thermoelectric generator for automotive waste heat recovery. *Energy Convers. Manag.* **2015**, *105*, 946–950. https://doi.org/10.1016/j.enconman.2015.08.051.

69. Georgopoulou, C.A.; Dimopoulos, G.G.; Kakalis, N.M.P. A modular dynamic mathematical model of thermoelectric elements for marine applications. *Energy* **2016**, *94*, 13–28. https://doi.org/10.1016/j.energy.2015.10.130.

70. Kuroki, T.; Kabeya, K.; Makino, K.; et al. Thermoelectric Generation Using Waste Heat in Steel Works. *J. Electron. Mater.* **2014**, *43*, 2405–2410. https://doi.org/10.1007/s11664-014-3094-5.

Thermal Reactions and Byproducts from the Waste-to-Energy Process of Flame Retardant-Containing Wastes—A Review

Chun-Yun Hsiao and Sheng-Lun Lin *

Department of Environmental Engineering, National Cheng Kung University, No.1, University Rd, East Dist, Tainan 70101, Taiwan
* Correspondence: z11208011@ncku.edu.tw or cbmsgml@gmail.com; Tel.: +886-6-275-7575 (ext. 65845)

Abstract: The increasing global concern about global warming has spurred researchers and industries to actively explore low-carbon energy alternatives to reduce carbon emissions and lessen dependence on traditional energy sources. Waste-to-energy (WTE) conversion has emerged as a promising solution in this pursuit. However, the prevalence of flame retardants (FRs) in various household materials poses a challenge to WTE processes. FRs, commonly added to prevent fire hazards, include chlorine-, phosphorus-, and nitrogen-based variants, each with specific applications and fire suppression mechanisms. Thermal treatment technologies, such as incineration, pyrolysis, gasification, and hydrothermal treatment, are currently employed for energy conversion. While effective in reducing waste volume and degrading most FRs, these processes can generate secondary pollutants, including polychlorinated dioxins, with complex reaction pathways that are difficult to control. This necessitates stringent management measures to mitigate the associated environmental risks. In contrast, non-thermal degradation techniques, such as chemical degradation, photocatalysis, biodegradation, and electrochemical methods, offer more environmentally friendly alternatives. However, current technological limitations constrain their application scope and efficiency. This review aims to comprehensively examine the pollutant emission behaviors of FRs during thermal treatment processes for energy conversion, highlight the associated environmental risks, and assess the potential of non-thermal degradation techniques. By analyzing these aspects, the review seeks to provide scientific insights and technological support for achieving waste valorization and low-carbon sustainability.

Keywords: waste-to-energy; persistent organic pollutants; flame retardant; thermal treatment; non-thermal degradation

1. Introduction

In recent years, global warming has become an increasingly critical issue. To minimize carbon emissions and decrease reliance on traditional energy sources, efforts are being made worldwide to explore low-carbon energy alternatives. Renewable energy, which refers to naturally occurring energy sources that can be directly utilized or processed for reuse, is key in reducing carbon emissions while mitigating air and water pollution. This category encompasses various technologies, including solar energy, bioenergy, geothermal energy, wind energy, and ocean energy. Among these, waste-to-energy (WTE) conversion has gained significant attention as a viable form of renewable energy. On the other hand, to enhance fire resistance and prevent flame propagation, thereby ensuring safety and protecting lives and property, FRs are now widely incorporated into everyday products. These include textiles, electronic devices, building materials, automotive components, and plastics [1]. With the widespread use of these products, the demand for FRs has also increased.

With the widespread use of various products, the consumption of FRs has increased significantly. Due to their high stability and persistence in the environment, FRs have gradually become a serious environmental concern. Numerous studies have indicated that these compounds are present in the air, water, soil, and even living organisms, posing potential risks to biological systems. Exposure to FRs has been linked to disruptions in the endocrine, nervous, reproductive, immune, and cardiovascular systems [2–4]. Moreover, when flame-retardant-containing waste undergoes thermal treatment for energy conversion, the process inevitably generates by-products, many of which also exhibit high stability. Organic chemicals that exhibit stability, toxicity, bioaccumulation, and

long-range environmental transport are classified as persistent organic pollutants (POPs). In the past, POPs did not receive sufficient attention; however, their widespread use has increased, their environmental hazards have become more apparent. In 1995, the United Nations Environment Programme (UNEP) called for global action to address POPs and compiled a list of the 12 most environmentally hazardous chemicals. In 2001, countries signed the Stockholm Convention, initially regulating only 12 chemicals. As research advanced and awareness of hazardous chemicals grew, the convention has been progressively updated, with 39 chemicals currently under regulation. Among the regulated substances are several brominated FRs, such as polybrominated biphenyls (PBBs), polybrominated diphenyl ethers (PBDEs), tetrabromobisphenol A (TBBPA), and hexabromocyclododecane (HBCD), as well as chlorinated FRs like short- and medium-chain chlorinated paraffins. The convention classifies chemicals into three categories based on their properties: Annex A (Elimination), Annex B (Restriction), and Annex C (Unintentional Production). All regulated FRs are listed under Annex A, requiring signatory countries to take measures to eliminate their production and use.

FRs can be classified into two categories based on their application: reactive and additive types. Reactive FRs form stable bonds by chemically reacting with the polymer matrix to create covalent links (e.g., TBBPA). In contrast, additive FRs are physically blended into the polymer without chemical bonding, making them more prone to leaching (e.g., PBDE and HBCDD) [5]. FRs can be categorized by composition into inorganic and organic types, with organic FRs generally exhibiting higher persistence and toxicity than inorganic ones. Organic FRs are further divided into three main types based on their chemical makeup: halogenated FRs (containing bromine or chlorine), phosphorus-based FRs (PFRs), and nitrogen-based FRs (NFRs). Initially, halogenated FRs, especially brominated FRs (BFRs), were the most popular due to their thermal stability, minimal impact on polymers, and lower cost compared to other FRs, leading to their widespread use. Studies show that most halogenated chemicals persist, bioaccumulate, and are toxic to the environment, animals, and humans. As a result, specific flame retardant components have since been regulated [6].

Although some BFRs have been banned or voluntarily phased out, specific emerging and existing BFRs continue to be used in industrialized countries. With increasing concerns over the hazards posed by halogenated FRs, interest in halogen-free alternatives has grown. PFRs have become widely adopted as substitutes for BFRs [7,8]. A Stapleton et al. [9] study illustrates this trend of PFRs replacing BFRs. They collected and analyzed 102 polyurethane foam samples from residential sofas purchased in the U.S. between 1985 and 2010. In samples purchased before 2005 (n = 41), polybrominated diphenyl ethers (PBDEs) related to the penta-bromodiphenyl ether mixture were the most common FRs, followed by tris(1,3-dichloro-2-propyl) phosphate (TDCPP; 24%). In samples purchased after 2005 (n = 61), TDCPP was the most frequently detected flame retardant, and mixtures of non-halogenated organic phosphate FRs, such as triphenyl phosphate (TPhP) and tris(4-butylphenyl) phosphate (TBPP), were also found. In 2017, the global consumption of organic phosphate esters (OPEs) was approximately 2.5 million tons [9].

PFRs are more biodegradable than BFRs and cause less environmental harm, making them a comparatively more eco-friendly option [10]. Subsequent research has found that some PFRs and their transformation products exhibit moderate to high persistence [11]. Increasing evidence suggests that these compounds pose health risks and can also induce biological effects, potentially causing significant environmental harm over time [7,12].

FRs enter the environment primarily through three pathways: (i) Emissions during the manufacturing process. Some products are heated during production, releasing trace amounts of FRs. (ii) Release from flame retardant-containing products during use. Products containing FRs can emit small amounts over time. In a study by Kajiwara, Desborough, Harrad, Takigami [13], it was found that decabromodiphenyl ether (DecaBDE) in flame-retardant textiles undergoes photodegradation when exposed to natural sunlight, indicating that these textiles may be a potential source of BFRs in dust. (iii) Waste disposal. This is the primary source of FRs in the environment. Both municipal and electronic waste contain FRs, and improper disposal poses a significant environmental risk [14]. FRs are commonly found in municipal waste, and improper disposal of these materials poses an essential environmental risk. Thermal treatment is one of the most widely used waste management techniques. However, this approach conflicts with the properties of FRs, raising concerns about its suitability. Although several existing reviews have examined the environmental risks or degradation pathways of specific FRs, most have been limited to a single type of FR or a specific treatment technology. Moreover, the behavior of FRs during high-temperature conversion processes remains insufficiently explored. In particular, the formation of toxic by-products and the variability in thermal decomposition mechanisms among different types of FRs have yet to be comprehensively investigated. In contrast, this review adopts an integrative perspective from a WTE standpoint, offering a comparative analysis of various types of FRs and major thermal treatment technologies. In addition, it explores the potential applications of non-thermal treatment methods to address current gaps in the literature. The novelty of this review lies in three key contributions: (i) It presents the first systematic comparison of the decomposition pathways and by-product formation mechanisms of different FR types, including halogenated, phosphorus-based,

and nitrogen-based compounds, under thermal treatment conditions, a topic often overlooked in energy conversion research. (ii) Beyond focusing on halogenated FRs, it also highlights the environmental risks and potential toxic by-products associated with phosphorus- and nitrogen-based FRs, areas that have received comparatively limited attention. (iii) While discussing thermal treatment strategies, the review further examines the complementary role and advantages of non-thermal degradation techniques in pollution control. It proposes the feasibility of integrated treatment approaches tailored to the characteristics of different waste streams.

2. Organic Flame Retardants

From past to present, commonly used organic FRs include BFRs, CFRs, PFRs, and NFR [15]. Table 1 summarizes the most representative compounds among various classes of organic flame retardants, along with a brief overview of their typical applications and current usage status. Figure 1 further illustrates the molecular structures of these compounds and their corresponding application areas. The development trends and practical applications of each type of flame retardant will be discussed in greater detail in the following sections.

Table 1. Different Types of Organic FRs.

Category	Examples	Remarks
BFRs	TBBPA, HBCD, PBDE, PBB	Formerly widespread in plastics and electronics, its use has significantly declined due to persistence and bioaccumulation concerns, though it's not entirely banned.
CFRs	Dechlorane Plus (DP) and chlorinated paraffins (CPs)	
PFRs	TDCPP, TPhP, tert-Butylated Triarylphosphate (TBPP), 9,10-dihydro-9-oxa-10-phosphaphenanthrene-10-oxide (DOPO)	Widely adopted halogen-free alternatives in foams, coatings, and electronics face some toxicity concerns.
NFRs	Pure melamine, melamine derivatives	Typically combined with PFRs, they work through endothermic decomposition and inert gas release. Effectiveness varies by formulation.

BFRs and CFRs are often collectively referred to as halogenated FRs due to their similar flame-retardant mechanisms and structures. Among these, bromine dominates in application because of its higher efficiency. Efficiency and stability are the two main factors determining which halogenated compounds can be used as FRs. Fluorinated compounds are too stable (C–F bond: 467 kJ/mol), while iodinated compounds are insufficiently stable to withstand processing temperatures (C–I bond: 228 kJ/mol). Therefore, only chlorine (C–Cl bond: 346 kJ/mol) and bromine (C–Br bond: 290 kJ/mol) are suitable for use as FRs [16]. Structurally, halogenated FRs can be divided into three major categories: aliphatic, aromatic, and alicyclic compounds. Due to their superior thermal stability, aromatic compounds are more commonly used.

Halogenated FRs (HFRs) are highly effective in flame retardation, do not significantly alter the properties of polymers when added, and are more cost-effective compared to other types of FRs. These advantages have made HFRs highly favored in industries such as electronics, plastics, and rubber. In the past, the most widely used BFRs included tetrabromobisphenol A (TBBPA), hexabromocyclododecane (HBCD), and polybrominated diphenyl ethers (PBDEs). However, the environmental and health concerns associated with traditional BFRs have drawn increasing attention in recent years, leading to the implementation of restrictions and bans on some BFRs.

Abbasi et al. [17] highlighted that although PBDEs have been gradually phased out, their emissions are expected to persist until 2050 due to the temporal and spatial lag in chemical management practices. The restrictions on traditional BFRs have, in turn, driven the development and adoption of next-generation BFRs [6], including novel brominated FRs (NBFRs). Among these, decabromodiphenyl ethane (DBDPE) is the most widely used, directly replacing commercial decabromodiphenyl ether mixtures. DBDPE is marketed for use in various applications such as plastics, resins, rubbers, adhesives, and textiles [18]. Studies indicate that NBFRs share similar physicochemical properties and hazard characteristics with traditional BFRs [19]. However, no comprehensive regulations currently govern the use of NBFRs.

For CFRs, Dechlorane Plus (DP) and chlorinated paraffins (CPs) are the most widely used. In January 2018, DP was listed as the 18th "Substance of Very High Concern (SVHC)" by the European Chemicals Agency (ECHA) [20]. CPs are categorized based on carbon chain length into short-chain (C10-13, SCCPs), medium-chain (C14-17, MCCPs), and long-chain (C > 17, LCCPs) chlorinated paraffins. SCCPs exhibit the highest potential toxicity, particularly to aquatic organisms [21]. In 2017, SCCPs were included in Annex A of the *Stockholm Convention* and are now regulated globally. While halogenated FRs have been widely used in the past, concerns over their environmental impact have led to a gradual shift towards halogen-free FRs in recent years.
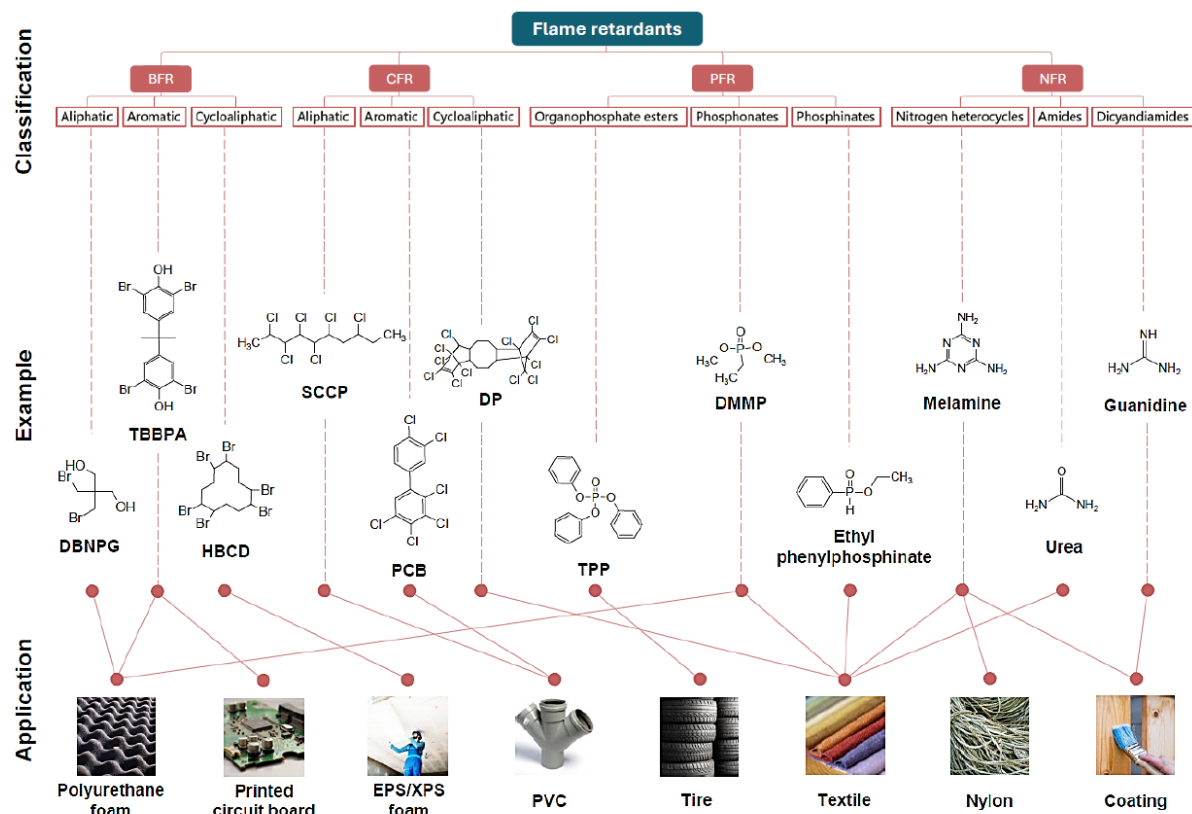
Figure 1. Flame retardant classification. (Dibromoneopentyl Glycol(DBNPG); Polychlorinated biphenyls(PCB); Triphenyl Phosphate (TPP); Dimethyl methyl phosphonate (DMMP)).

Halogen-free organic FRs can be broadly classified into PFRs and NFRs. These two types are often used synergistically to enhance the flame retardancy of materials. Based on the structure of phosphorus, PFRs can be categorized into three subgroups: organophosphate esters (OPEs), phosphonates, and phosphinates [8], with OPEs being the most commonly applied. In addition to structural classification, many studies prefer to categorize PFRs based on the presence or absence of halogens, dividing them into halogenated or non-halogenated PFRs. Generally, halogenated PFRs pose greater hazards, driving a trend toward replacing them with non-halogenated PFRs. PFRs are widely used in materials such as epoxy resins, unsaturated polyesters, polyurethane (PU) foams, and textiles.

The classification of NFRs is less defined and is rarely discussed in the literature. This review categorizes NFRs into three groups based on their structure: nitrogen heterocycles, amides, and dicyandiamides. Among these, melamine-based compounds are the most established NFRs and are commonly combined with PFRs. NFRs are characterized by their low toxicity, corrosiveness, and low smoke production, making them suitable for circuit breakers, public transportation applications, polyurethane flexible foams, nylon, and textiles [22–24]. While NFRs are generally safer than halogenated FRs, their applications are limited. They demonstrate excellent flame-retardant performance in certain materials, particularly nylon-based plastics, which are well-suited to the action mechanism of NFRs. However, in other materials, the flame-retardant efficacy of NFRs may be significantly reduced, failing to achieve comparable performance levels [25].

2.1. Flame Retardant Mechanisms

The flame-retardant mechanisms of organic FRs can be divided into two primary approaches: gas-phase action and condensed-phase action. Gas-phase active FRs decompose at high temperatures to release free radicals, inhibiting the free-radical chain reactions in the flame reaction zone. In contrast, condensed-phase active FRs suppress pyrolysis by promoting charring, intumescence, and the formation of protective barriers[26]. Figure 2 illustrates the flame-retardant mechanisms of different FRs. For BFRs, when exposed to heat or fire, the material releases gaseous bromine (Br_2, HBr, and Br), which reacts with free radicals such as $OH\cdot$ and $H\cdot$. This reaction interrupts the combustion chain reaction, effectively suppressing the flame propagation[27,28]. CFRs like BFRs belong to the category of halogenated FRs. Their flame-retardant mechanism is similar, relying on gas-phase action to inhibit the combustion reaction.
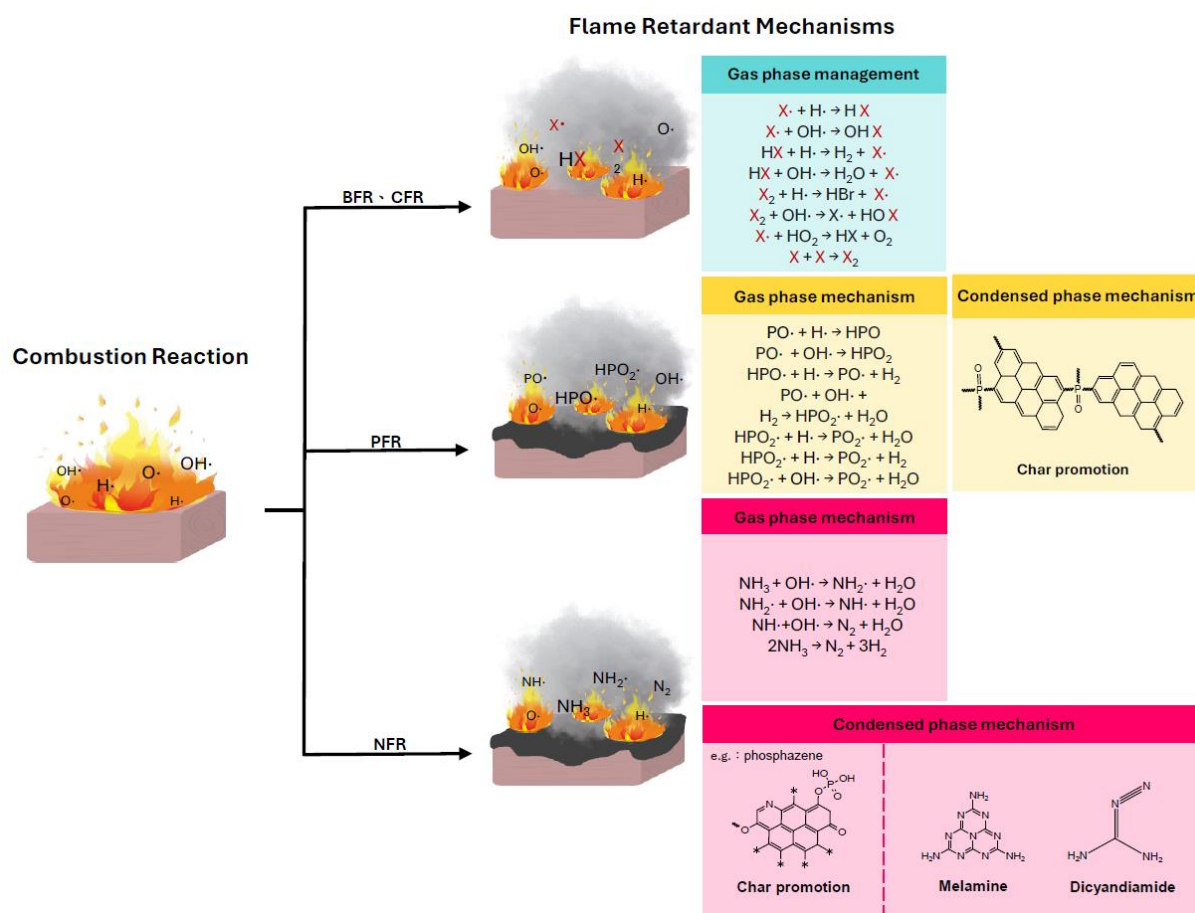
Flame Retardant Mechanisms

Combustion Reaction

Gas phase management

$$X\cdot + H\cdot \rightarrow HX$$
$$X\cdot + OH\cdot \rightarrow OHX$$
$$HX + H\cdot \rightarrow H_2 + X\cdot$$
$$HX + OH\cdot \rightarrow H_2O + X\cdot$$
$$X_2 + H\cdot \rightarrow HBr + X\cdot$$
$$X_2 + OH\cdot \rightarrow X\cdot + HOX$$
$$X\cdot + HO_2 \rightarrow HX + O_2$$
$$X + X \rightarrow X_2$$

Gas phase mechanism

$$PO\cdot + H\cdot \rightarrow HPO$$
$$PO\cdot + OH\cdot \rightarrow HPO_2$$
$$HPO\cdot + H\cdot \rightarrow PO\cdot + H_2$$
$$PO\cdot + OH\cdot +$$
$$H_2 \rightarrow HPO_2\cdot + H_2O$$
$$HPO_2\cdot + H\cdot \rightarrow PO_2\cdot + H_2O$$
$$HPO_2\cdot + H\cdot \rightarrow PO_2\cdot + H_2$$
$$HPO_2\cdot + OH\cdot \rightarrow PO_2\cdot + H_2O$$

Condensed phase mechanism

Char promotion

Gas phase mechanism

$$NH_3 + OH\cdot \rightarrow NH_2\cdot + H_2O$$
$$NH_2\cdot + OH\cdot \rightarrow NH\cdot + H_2O$$
$$NH\cdot + OH\cdot \rightarrow N_2 + H_2O$$
$$2NH_3 \rightarrow N_2 + 3H_2$$

Condensed phase mechanism

e.g.: phosphazene

Char promotion   Melamine   Dicyandiamide

Figure 2. Flame Retardant Mechanisms of Different FRs.

The flame-retardant mechanisms of PFRs operate through two primary modes: (i) gas-phase action and (ii) condensed-phase action. In the condensed phase, phosphates promote dehydration reactions in polymers, leading to char formation. The resulting char acts as a physical barrier to heat and mass transfer, significantly impeding the flow of heat and combustible fragments between the underlying polymer and the combustion zone [29–31]. In most cases, the flame-retardant mechanisms of PFRs involve gas-phase and condensed-phase actions simultaneously. This dual mechanism enhances flame retardancy and reduces toxic gas emissions. The volume of harmful gases released by PFRs is significantly lower than that of BFRs, leading to advocacy for PFRs as safer alternatives to BFRs.

NFRs can function in both the gas phase and the condensed phase. At high temperatures, NFRs release non-flammable gases, such as nitrogen and ammonia, which dilute combustible gases and inhibit the chain reactions of combustion [32,33]. In the condensed phase, two main mechanisms are observed: (i) Formation of a char layer. This typically occurs in phosphorus/nitrogen synergistic FRs. Phosphates create a dehydrating environment, while the presence of nitrogen enhances the charring reaction [34]. (ii) Formation of high-stability products. When melamine decomposes above 350 °C, it releases non-flammable ammonia gas and generates thermally stable compounds such as melamine and dicyandiamide, which improve the thermal stability of polymers [35].

2.2. Release of FRs during Normal Use

FRs are widely used in various consumer products and are released in trace amounts during use. Generally, the concentration of FRs indoors is higher than outdoors, and the types of FRs detected indoors are often associated with the products present. For example, in a study by Vojta, Melymuk, Klánová [36], significant increases in the concentrations of hexabromobenzene (HBB) and tris(2-chloropropyl) phosphate (TCIPP) were observed during computer installation and operation. Similarly, the addition of certain furniture and carpets significantly affected the levels of tris(1,3-dichloro-2-propyl) phosphate (TDCIPP) and tris(methylphenyl) phosphate (TMTP). However, this correlation is not absolute. The types of FRs used in similar products may vary, and a single product can often contain multiple FRs [37,38]. Furthermore, the formulation details of FRs in consumer products are typically not disclosed. As a result, pinpointing the exact sources of FRs in indoor environments is often challenging.

Regarding the mechanism of flame retardant migration from products to dust, Rauert, Lazarov, Harrad, Covaci, Stranger [39] proposed three hypotheses: (i) FRs volatilize from the product and settle into dust, (ii) wear and tear during product use cause the physical transfer of FRs, and (iii) FRs are removed from products through direct contact with dust on the product surface. Depending on the physicochemical properties of the FRs, these mechanisms apply to varying degrees for all FRs.

There are many factors that influence the extent of flame retardant release, and these may vary depending on usage methods, environmental conditions, and product age. Generally, additive FRs are more likely to be released into the environment because their bond with the polymer is less stable than reactive FRs. Additionally, the working temperature of the product has a significant impact. Higher emission rates are often observed in high-temperature indoor environments or when electronic products operate [40]. Kemmlein et al. [41] pointed out that an increase in temperature (to 60 °C) can lead to a 500-fold increase in the emission of various FRs. In a study by Carlsson et al. [42], a relationship between flame retardant emissions, operating temperature, and product age was also observed. After operating a video display unit at a normal temperature (50 °C) for one day, the concentration of triphenyl phosphate in the air rose to nearly 100 ng/m^3. However, after 183 days, it decreased to approximately 10 ng/m^3. Although the concentration decreased significantly, it was still ten times higher than the background value.

In indoor environments with high flame-retardant materials, such as public facilities, emissions may be even greater than in typical households. Takigami et al. [43] conducted a study in a hotel, collecting eight dust samples from different floors and analyzing substances such as BFRs and PFRs. The results showed that PBDEs and HBCD dominated the BFRs, with concentrations ranging from 9.8 to 1700 ng/g (median: 1200 ng/g) and 72 to 1300 ng/g (median: 740 ng/g). Additionally, the study highlighted that the concentration of flame retardant compounds varied across different areas, suggesting a link between the location of the source products and the concentration of FRs in the dust. Similarly, substantial differences in flame retardant concentrations and indoor environmental conditions were observed across different countries.

Among the four types of FRs discussed in this review, NFRs are less frequently mentioned in the literature regarding their emissions in indoor environments. Specifically, most studies focus on the food sector, melamine, and its derivatives. This is due to incidents in 2007–2008 when multiple countries experienced outbreaks of kidney stones and acute kidney injuries in pets and humans as a result of melamine ingestion [44]. Although there is relatively less research on environmental emissions of NFRs, it is not absent. Zhu and Kannan [45] investigated melamine and its derivatives in indoor dust across 12 countries, finding detectable levels in all dust samples. Among these, melamine was the dominant substance, followed by cyanuric acid. The global median concentrations were as follows: melamine 1800 ng/g, cyanuric acid 1100 ng/g, ammeline 48 ng/g, and ammelide 45 ng/g.

In conclusion, many factors influence the concentration of FRs in indoor environments, making it difficult to define the exact emission levels of various FRs. However, we can confirm that even under normal indoor temperature and usage conditions, FRs are released in trace amounts.

2.3. Reaction Temperature and Products

Different types of FRs have varied applications, which may be related to their properties and the temperatures at which they are used. Generally, BFRs are suitable for temperatures ranging from 105 °C to 300 °C [46,47]; CFRs are effective at temperatures below 285 °C [48], PFRs are appropriate for temperatures between 275 °C and 450 °C [49,50], and NFRs are used within a range of 250 °C to 450 °C, with the majority concentrated around 300 °C [23,51,52].

When FRs are heated, other by-products are formed in addition to the target products of the flame-retardant mechanism. Some of these byproducts can be particularly undesirable. Balabanovich et al. [53] mentioned that before HBr is released from BFRs, aliphatic compounds and ketones are first formed, followed by the release of phenols and bromophenols, and eventually, HBr is emitted. Furthermore, heating BFRs does not completely convert them into HBr; in addition to the possible conversion of highly BFRs into lower-brominated ones, brominated phenols, benzene compounds, and by-products such as PBDD/F can also be generated [54,55]. Some studies suggest that BFRs can act as precursors for PBDD/F. Due to their structural characteristics, certain BFRs (such as PBDEs) can directly convert into PBDD/F through simple condensation or other elimination steps. In contrast, most BFRs require more complex mechanisms to form these compounds [27]. The by-products generated during thermal degradation are equally toxic to living organisms, which is one of the reasons why some researchers have proposed replacing BFRs with PFRs. Different types of BFRs can result in varying proportions of by-products. Liang et al. [56] pointed out that highly brominated PBDEs favor the cleavage of ether bonds to form polybrominated benzenes, whereas less brominated PBDEs are more likely to transform into PBDD/Fs. Wang et al. [57] studied the formation mechanisms of PBDD/Fs across 65 PBDE congeners. The authors noted that the presence of polymers

lowers the optimal formation temperature of PBDFs from 600 °C to 350–400 °C. This phenomenon may be attributed to: (i) the decomposition of polymers providing unsaturated brominated hydrocarbons, eliminating the need for de novo synthesis of PBDD/Fs; and (ii) the free radicals generated during polymer chain scission, which facilitate the initial degradation of PBDEs. Both CFRs and BFRs belong to the halogenated FRs, sharing similar characteristics. The combustion of CFRs produces small toxic gas molecules (e.g., HCl and phosgene), chlorinated aromatic compounds (e.g., trichlorobenzene and chlorobenzene), and highly toxic substances such as PCDD/Fs [58].

The combustion of the other two types of FRs poses significantly less harm. PFRs generate phosphoric acid derivatives that may cause respiratory irritation but are generally not highly toxic upon heating. Purser [59] review mentioned that any phosphorus source combined with trimethylol-based polyols can produce bicyclic phosphates with strong neurotoxic effects in combustion by-products. However, the associated risks are relatively low since trimethylol-based polyols are not widely used. Among PFRs, halogen-containing variants are more hazardous, as they can generate chlorine-containing by-products like those derived from CFRs.

Upon heating, NFRs primarily produce nitrogen gas, ammonia, and certain stable condensed-phase products during combustion. However, they may also generate NOx and HCN, which are rarely discussed in the literature. HCN is highly toxic, inhibiting the cellular respiratory chain, ultimately leading to organismal death. That said, the amount of HCN produced can be significantly reduced. In their review, Singh and Jain [60] highlighted that adding ammonium polyphosphate (APP) to polyurethane foams can significantly reduce HCN emissions.

3. Thermal Treatment Technology

Under high-temperature conditions, the thermal degradation of BFRs generally progresses through several stages. Initially, the molecular structure of BFRs begins to break down, forming small molecules and free radicals. As degradation continues, a debromination reaction occurs, where bromine atoms are removed from the structure, resulting in debrominated intermediates such as aromatic hydrocarbons or other organic compounds. During this process, highly toxic dioxin-like compounds may form, and a small amount of partially degraded residues may remain. Figure 3 illustrates the thermal degradation pathways of pure TBBPA [60]. Seven primary dissociation pathways are identified: (1) cleavage of the C-CH3 bond, (2) monomolecular transfer of the phenolic hydrogen leading to bromine (Br) removal, (3) direct cleavage of the C-Br bond, (4) rupture of isopropylidene linkages accompanied by hydrogen migration, (5) cleavage of phenolic O-H bonds, (6) breaking of aromatic ring bonds, and (7) loss of hydrogen atoms from methyl groups. Among these, the cleavage of the C-CH3 bond requires the least energy and is thus the predominant pathway.

CFRs and BFRs belong to the halogenated flame retardant category, and their decomposition processes are broadly similar. During the thermal degradation of highly chlorinated paraffins (CP70) (Figure 4), a variety of substances are generated under different thermal conditions, including significant amounts of SCCPs, MCCPs, unsaturated analogs, and toxic chlorinated aromatic compounds [61]. SCCPs readily undergo further breakdown through dehydrochlorination, followed by cyclization or aromatization. Between 200 °C and 400 °C, this process predominantly breaks down PCBs. At higher temperatures (above 500 °C), asymmetric chain cleavage becomes the dominant reaction, generating more small molecules or free radicals, accelerating the addition reactions, and forming larger chlorinated aromatic compounds.

Currently, there is limited research summarizing the thermal degradation pathways of PFR and NFR, likely because their associated hazards are less significant compared to halogenated FRs. Nevertheless, at high temperatures, PFR and NFR undergo several critical thermal degradation steps. Initially, chemical bonds break, leading to the formation of small molecules and free radicals. Phosphorus compounds like phosphates may decompose into phosphoric acid, nitrogen oxides, and other organic by-products. During dephosphorylation or denitrogenation, phosphorus or nitrogen atoms may be removed from the molecular structure, producing degradation products that are more susceptible to further breakdown.

Thermal treatment technology is currently the most common method for waste disposal, offering a direct, rapid, and practical approach to significantly reduce the mass (by approximately 70–80%) and volume (by about 80–90%) of solid waste [62]. General thermal treatment processes include incineration, pyrolysis, gasification, and hydrothermal processes. However, a significant drawback of these thermal treatment techniques is that FRs may not be destroyed after heating. Some FRs can persist in the gas phase, particulate phase, or liquid phase, and under high-temperature conditions, they may transform into other harmful by-products, particularly derivatives of PCDD/F.

Table 2 provides a comparative overview of four major thermal treatment technologies, focusing on key parameters such as operational conditions, expected products, and post-treatment requirements. These factors are critical for evaluating flame retardants' behavior and ultimate fate under various waste-to-energy scenarios.
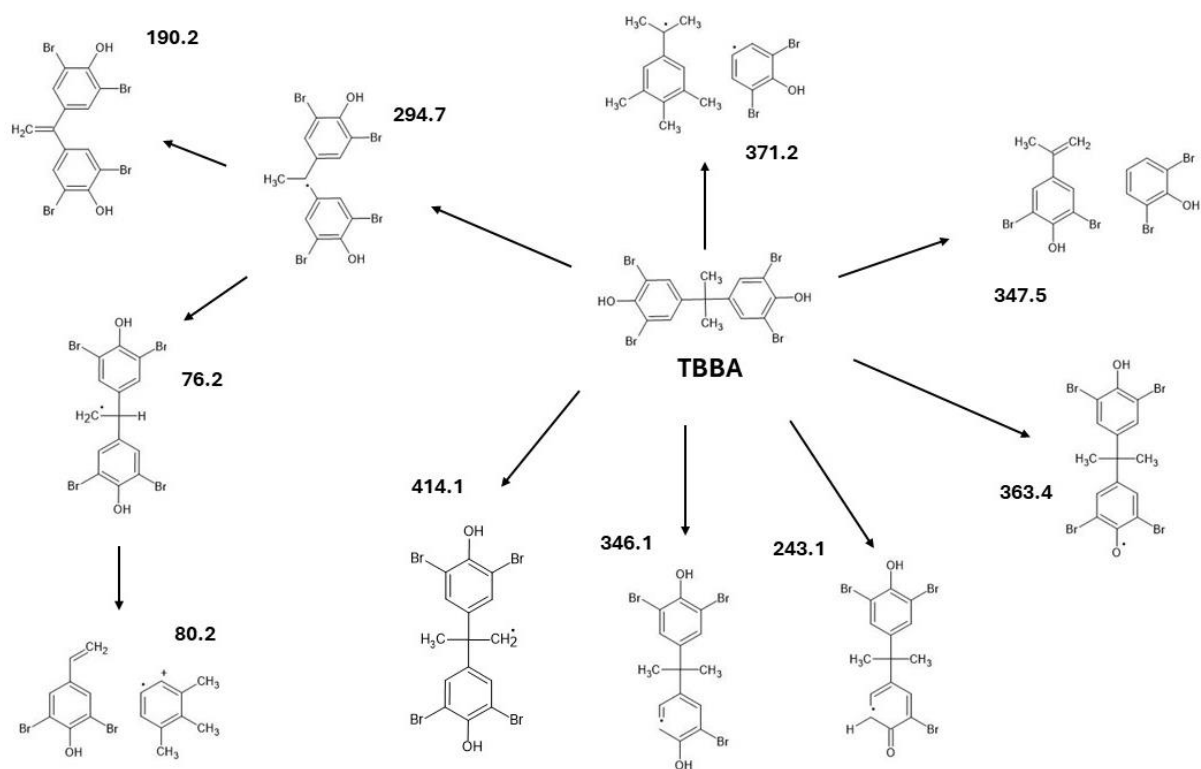
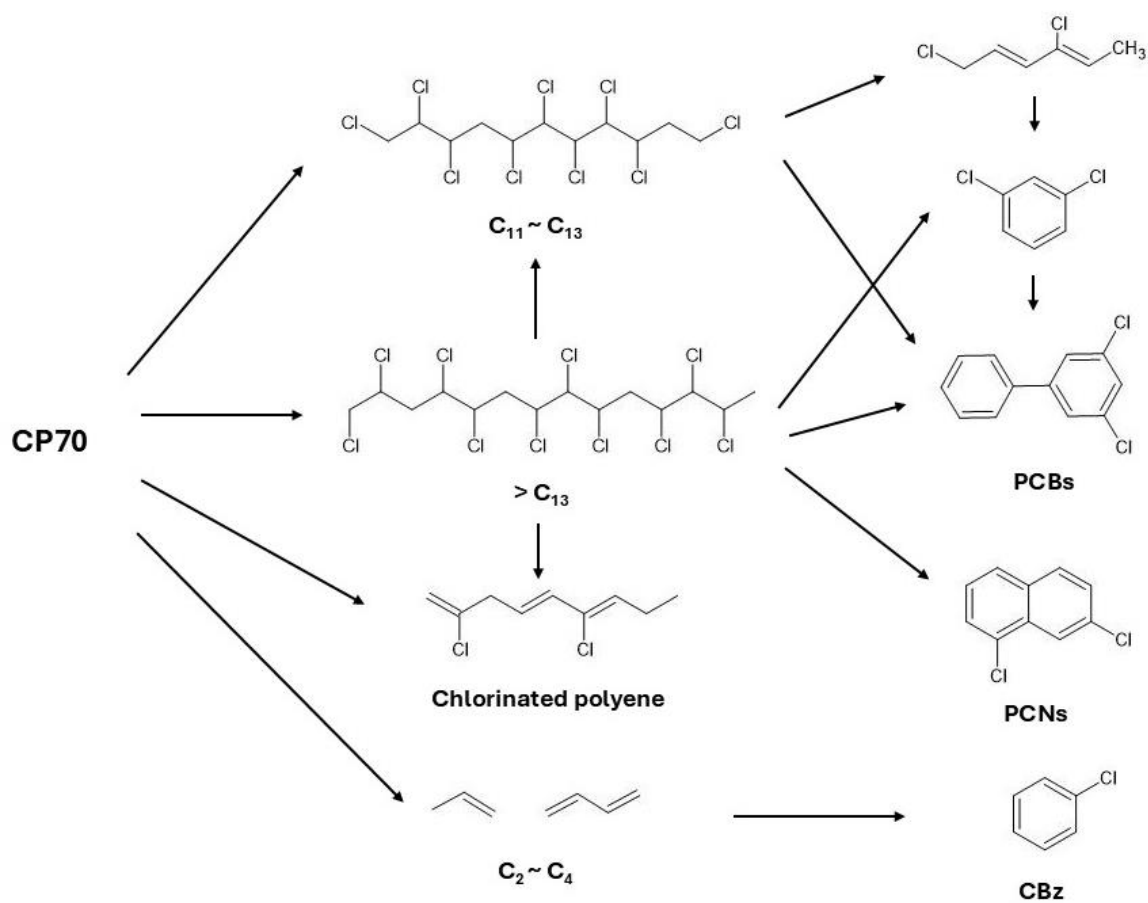**Figure 3.** TBBA thermal degradation pathway.

Figure 4. Thermal degradation of highly chlorinated paraffin (CP70).

Table 2. Heat treatment technology.

Treatments	Operating Conditions		Feed Conditions		Products	Post-Treatment Requirements
Incineration	• T^a = 800–1200 °C • O_2 present • P^a = 0.1 MPa • RT^b = seconds		• Solid particles • Moisture < 20% wt • Calorific value above 8–10 MJ/kg		• Flue gas • Ashes	• Flue gas control • Ash stabilization and disposal
Pyrolysis	• T^a = 300–900 °C • Nearly no O_2 • P^a = 0.1–5 MPa • RT = seconds		• High-carbon feedstock • Solid particles • Moisture < 20% wt		• Flue gas • Biochar • Bio-oil* • Ashes	• Oil purification • Biochar utilization
Gasification	• T^a = 700–1400 °C • O_2-deficient (limited O_2, CO_2, steam, or air) • P^a = 0.1–5 MPa • RT = seconds		• High-carbon feedstock • Solid particles • Moisture < 20% wt		• Syngas* • Ashes • Tar	• Product purification • Tar recycling
Hydrothermal	• T^a = 180–350 °C • Aqueous reaction • P^a = 5–22 MPa • RT = seconds		• Low-salinity wet feedstock • Solid particles		• Wastewater • Biochar • Bio-oil • Gas	• Product purification • Wastewater treatment • Biochar/bio-oil utilization

Note: [a] T: operation temperature; [b] P: operation pressure; [c] RT: resident time; * Major product.

3.1. Incineration

Incineration is the most common thermal treatment method and a well-established commercial process, making it one of the primary waste management techniques today. It operates at high temperatures of approximately 800 to 1200 °C to ensure the complete combustion and decomposition of the most harmful substances. However, the inevitable generation of substances such as polycyclic aromatic hydrocarbons (PAHs), polychlorinated biphenyls (PCBs), and polychlorinated dioxins (PCDDs) presents significant challenges, particularly in the control of pollutant gas emissions and the management of ash residues. Many studies indicate that the destruction rate of FRs during incineration can typically exceed 99%. Any undestroyed FRs are usually detected in the residual ash after combustion, while their presence in the flue gas is relatively minimal.

For instance, Sakai, Watanabe, Honda, Takatsuki, Aoki, Futamatsu, Shiozaki [63] conducted a study on the combustion of BFRs, using actual waste materials (such as the casings of discarded televisions and waste printed circuit boards) and custom samples (polyethylene resin containing PBDEs and ABS resin containing TBBP-A). After processing, they analyzed the concentration of PBDEs, finding residual concentrations in the ash ranging from 2.9 to 180 μg/g, which is 1 to 3 orders of magnitude lower than the concentrations in the original samples. PBDEs were detected in the flue gas only in one instance, with other measurements falling below detection limits. While PBDEs were almost nonexistent in the flue gas, by-products such as PBDD/DF, PCDD/DF, and PXDD/DF were detected.

The high destruction rates of FRs during incineration are also evident in the research conducted by Matsukami et al. [64]. They tested refuse-derived fuel (RDF) containing four different PFRs in a pilot-scale incinerator. They found detectable PFRs in the flue gas and ash, with overall destruction efficiencies exceeding 99.999%. The authors noted that PFRs were primarily destroyed during the initial combustion stage, indicating that the conditions in the primary combustion chamber are critical for the degradation and emission control of PFRs. Kwon et al. [65] conducted incineration of waste containing CFRs and found that CFRs were not detected in the flue gas at both 1100 °C and 850 °C. They also investigated dioxin formation under these two conditions, revealing that at a reaction temperature of 1100 °C, emissions were generally below the current limit value (5 ng I-TEQ/Sm^3). Consequently, the authors recommended adoption of strategies that minimize the risk of unintentionally generating dioxins and other persistent organic pollutants, operating temperatures should be maintained above 1100 °C. Research on the incineration of NFRs remains relatively limited, likely due to their lower environmental risk and certain application constraints. Current studies focus on developing novel NFRs to enhance their flame-retardant efficiency, applicability, and thermal stability, enabling broader use.

An essential aspect of thermal treatment technology is controlling by-product formation. Various methods are available to manage concentration, such as adding specific substances during the thermal process. For instance, adding chlorine, nitrogen, CaO, or coal can influence the formation of polychlorinated dibenzodioxins/furans (PCDD/Fs) [66]. However, the potential for these additives to trigger other adverse effects and their applicability

in practical operations requires further investigation. Additionally, research by Sakai et al. [63] has shown that mixtures of metals and higher cooling temperatures (300 °C) may promote the formation of PBDD/DF.

Waste composition is highly complex, and completely removing metal compounds necessitates screening and pretreatment, often posing practical challenges and significantly increasing treatment costs. Therefore, control measures must be implemented from other perspectives. For example, Yang et al. [67] successfully reduced the emissions of brominated persistent organic pollutants by over 97%, including PBDD/F and PBB emissions, and achieved a 61% reduction in PBDE emissions through controlling the startup of waste-to-energy incinerators.

While incineration technology can effectively destroy most FRs, some residues may still pose environmental threats due to the characteristics of the FRs. Additionally, the by-products generated during incineration require careful attention to prevent further environmental contamination. Kwon et al. [65] incinerated waste containing CFRs and did not detect CFRs in the exhaust gases at 1100 °C and 850 °C. They also investigated dioxin formation under these two conditions, and the results showed that at a reaction temperature of 1100 °C, the dioxin levels were generally below the current emission limit (5 ng I-TEQ/Sm^3). Therefore, the authors recommended that to reduce the potential for unintentional formation of persistent organic pollutants such as dioxins, the operating temperature should be above 1100 °C.

3.2. Pyrolysis

Unlike incineration, pyrolysis is conducted under anaerobic conditions, typically at 200 to 700 °C. It requires lower energy and converts biomass/biosolids into valuable products during heating. Compared to incineration, it does not emit large amounts of greenhouse gases, reducing gas generation by approximately 5% to 10% [68]. The generation of PCDD/F can also be reduced through pyrolysis. A study by Chen, Sun, Li, Lin, Xiang, Yan [69] indicated that the PCDD/F yield from the pyrolysis of waste tires was significantly lower than that in combustion flue gas, nearly reducing it by 100%. Due to these characteristics, pyrolysis has attracted considerable attention in recent years.

The products of pyrolysis can be categorized into three types: flue gas, biochar, and bio-oil. Among these products, oil constitutes the majority (50 wt%–70 wt%), followed by biochar (13 wt%–25 wt%), while gas production is the least (12 wt%–15 wt%) [69]. Therefore, pyrolysis easily leads to the accumulation of pollutants in the oil phase [70,71]. Ye et al. [72] pyrolyzed waste-printed circuit boards (WPCBs) containing BFRs at 500 °C and measured the organic bromine content in the oil phase at 151.13 mg/g. However, by adding certain substances to reduce the bromine content, varying proportions of composite additives (Fe_3O_4 and Si-Al zeolite) effectively lowered the bromine levels in the pyrolysis oil (10.45 to 20.24 mg/g). However, by adding different proportions of composite additives (Fe_3O_4 and Si-Al zeolite), the bromine content in pyrolysis oil was effectively reduced to between 10.45 and 20.24 mg/g [73]. Conducted pyrolysis studies on cotton fibers with and without phosphorus-nitrogen FRs. The results showed that at a pyrolysis temperature of 600 °C, the pyrolysis rate of cotton fibers without FRs reached 97.23%, while that of fibers containing FRs was only 76.53%. This indicates that the presence of FRs inhibited the pyrolysis reaction. Additionally, it was found that the yields of compounds such as ketones, aldehydes, esters, and ethers in the pyrolysis products significantly decreased, with mainly cyclic compounds like furan and glucan being produced. In a study on the pyrolysis of polyurethane (PU), Eschenbacher et al. [74] investigated the effects of TCPP (tris(1-chloro-2-propyl) phosphate) on the pyrolysis process. The results showed that when the pyrolysis temperature exceeded 700 °C, TCPP was no longer present in the products, indicating that it completely decomposed at high temperatures. Additionally, the study found that the formation of chlorine-containing products peaked at around 600 °C. Chen et al. [75] examined the distribution of nitrogen-containing products during PU pyrolysis and discovered that hydrogen cyanide (HCN) and ammonia (NH_3) were predominant in the gas phase, while the liquid phase contained amines, nitrogen heterocycles, and nitriles. Nitrogen oxides were nearly undetectable in the solid phase. Adding metal oxides or catalysts like CaO during pyrolysis promoted the formation of nitrogen gas (N_2) while suppressing the generation of NH_3 and HCN, contributing to a more environmentally friendly pyrolysis process. Recent advancements in flame retardant treatment through pyrolysis have also emerged. Cho et al. [76] demonstrated a method to increase the value of melamine using pyrolysis. Under CO_2 and Ni-catalysis conditions, melamine was completely converted into gaseous pyrolysis products, with an increased concentration of carbon monoxide (CO). This experiment provides an efficient approach to transforming melamine waste into valuable energy resources, such as syngas. Kumagai et al. [77] investigated the effects of calcium hydroxide ($Ca(OH)_2$) on the thermal decomposition of both phenol and epoxy resin paper-laminated printed circuit boards (PCBs) containing TBBPA. Their pyrolysis experiments revealed a maximum removal of 94% HBr, 98% brominated phenols, and 98% phosphorus from the gaseous and liquid products. Additionally, the inhibition of Br-induced metal volatilization improved the recovery rate in the solid fraction.

Charitopoulou et al. [78] evaluated the pyrolysis performance of waste electrical and electronic equipment containing TBBPA using five different catalysts: Al_2O_3, Fe/Al_2O_3, MgO, Fe/MgO, and zeolite. The study found that all the catalysts promoted the formation of phenolic compounds, valuable products for the chemical industry. Among the catalysts, Fe/Al_2O_3 was identified as the most effective, achieving a bromine reduction rate of over 75%. However, using catalysts introduces additional costs and poses the risk of secondary pollution, making catalytic methods less optimal for practical applications. Chen et al. [79] explored the co-pyrolysis of two types of waste, red mud and waste printed circuit boards, successfully fixing 89.55 wt% of the bromine in the solid residue and increasing the yield of light tar by 44.29%. Beyond the use of co-pyrolysis and catalysts, adjusting pyrolysis conditions may further enhance pollutant degradation, such as employing staged pyrolysis. Staged pyrolysis shows significant potential in regulating the formation of nitrogen-containing gaseous pollutants from agricultural biomass waste. Zhan et al. [80] demonstrated that, compared to single-stage pyrolysis at the appropriate temperature, two-stage pyrolysis reduced total nitrogen-containing pollutant yields by 57% to 60% for three different samples. Currently, research on the effects of staged pyrolysis on flame-retardant materials is still limited, but this approach may facilitate more efficient degradation of FRs, improving environmental performance.

3.3. Gasification

Gasification is similar to pyrolysis. It occurs at high temperatures (700–1000 °C) in a partial oxygen environment, converting materials into various gaseous components such as H_2, CO, CO_2, CH_4, and C_2H_6, which can be used as fuel. In addition, by-products like biochar and tar are also produced [81].

Research on the gasification of flame-retardant-containing materials is noticeably less prevalent compared to studies on pyrolysis and incineration. Sodium phytate, a potential material for PFRs, was investigated by Lidman Olsson et al. [82]. Their study examined the release behavior of sodium phytate during thermal treatment. It was found that at 1000 °C under an inert atmosphere, approximately 30% of phosphorus was released in the gaseous phase. This finding provides valuable insights into the characteristics of phosphorus release during the gasification process. In 2003, Yamawaki et al. [83] employed high-temperature (over 1200 °C) treatment combined with rapid cooling to suppress PBDDs/PBDFs emissions to very low levels. Although the authors did not explore the degradation of FRs, studies on incineration and pyrolysis indicate that thermal treatment technologies generally achieve high removal rates for FRs, though the generation of by-products is often unavoidable. Yamawaki et al.'s methodology significantly reduced the formation of PBDDs/PBDFs potentially generated by FRs, highlighting the potential of gasification in minimizing harmful by-products. In 2024, Lo et al. [84] suppressed hydrochloric acid and dioxin emissions through the co-gasification of calcium-containing waste and automobile shredder residue. Most studies on gasification focus on gas yield, tar formation [85–87], and the emission of certain pollutants, such as HCl and polychlorinated dibenzodioxins/furans (PCDD/F) [88]. Few investigations have delved deeply into the relationship between FRs and gasification. One reason for this gap may be that gasification requires higher temperatures than pyrolysis, which results in a lower risk of pollutant release and by-product formation from FRs. Additionally, gasification technology is considered an effective method for reducing pollutants, as it primarily aims to convert waste into syngas. This focus on waste-to-energy conversion has contributed to the relative scarcity of research on FRs in gasification processes.

3.4. Hydrothermal Treatment

Hydrothermal technology operates at medium to low temperatures (180–375 °C) and under high-pressure conditions, converting biomass into valuable products. The primary products can be solid fuels or bio-oil, depending on the operating conditions. Compared to traditional thermal treatment methods, Hydrothermal carbonization technology has the significant advantage of processing high-moisture feedstocks without requiring dewatering, which substantially reduces pretreatment costs [89].

Uddin et al. [90] used hydrothermal treatment to remove decabromodiphenyl ether (DBDE) from plastics. Their study found that at 280 °C, the process achieved high plastic recovery rates and optimal debromination, with most bromine extracted into the water phase as HBr.

Although PBDD/DFs formation can occur during hydrothermal treatment, the associated risks are relatively low. The process can be improved by adding certain catalysts, alkaline agents, or extending the treatment time [91]. Previous studies have shown that an alkaline environment facilitates debromination reactions, a phenomenon also observed by Yin et al. [92]. At temperatures above 300 °C, with a residence time over 30 min and the presence of alkaline additives, more than 80% of brominated epoxy resin can be broken, primarily into phenol. Zhan et al. [93] further enhanced hydrothermal debromination by introducing an alkaline sulfide system, achieving extraction

efficiencies of 85.60% for Sb and 90.13% for Br from flame-retardant plastics. Moreover, the plastic structure remained largely intact under optimal hydrothermal conditions, allowing for potential reuse.

However, the transformation of Cl during the hydrothermal process remains less understood. While co-hydrothermal technology has successfully removed Cl from the solid-phase products, challenges persist in managing Cl in the liquid phase to advance the practical application of this technique [94]. Xiu et al. [95] proposed an efficient dechlorination method for short-chain chlorinated paraffins using subcritical water with NaOH. This method achieved 100% dechlorination at low temperatures within a short reaction time (250 °C, 5 min), producing high-value hydrocarbons. However, the study did not use plastic waste as feedstock, indicating potential challenges in real-world applications. Thus, further exploration is required to optimize dechlorination processes for waste materials.

Currently, research on the hydrothermal treatment of PFR and NFR remains limited, likely because the degradation products of these substances pose lower environmental risks and are relatively easier to manage. Although studies specifically on PFR and NFR are scarce, considerable research has examined the transformation of phosphorus and nitrogen in waste materials. Phosphorus typically first converts to water-soluble phosphate ions (e.g., orthophosphate), which then precipitate by reacting with metal ions present in sludge or waste under high-temperature, high-pressure hydrothermal conditions [96–98]. Nitrogen compounds convert into inorganic nitrogen ions (e.g., NH_4^+, CN^-, NO_2^- and NO_3), with some nitrogen retained in the solid phase [99,100].

4. Non-thermal Treatment Technologies

Aside from thermal treatment, flame retardant degradation can also be achieved through chemical methods, photodegradation, microbial degradation, and electrochemical methods, each with its own advantages and drawbacks.

(1)   Chemical Degradation

This method efficiently breaks down FRs and allows for some flexibility in controlling the by-products. Common approaches include Fenton reactions, persulfate oxidation, hydrogen peroxide, and ferrate treatments [101–104]. The effectiveness of these chemical agents can vary depending on the specific FRs being treated. For example, Ma et al. [105] tested six organic solvents to degrade phosphonate-based epoxy resins and found that methanol in an alkaline environment provided the best results. However, challenges such as high reagent costs, risks of secondary pollution, and limited selectivity hinder large-scale application.

(2)   Photocatalysis

This promising technique uses visible or ultraviolet light to activate catalysts, generating free radicals that decompose pollutants. Despite its potential, photocatalysis faces challenges, such as high material costs and complex modification methods. Additionally, if photocatalysts are not promptly recovered, there may be issues with leaching new contaminants [106]. While this technique is commonly applied for pollutant removal in aqueous and gaseous phases, advancements in nanotechnology have enabled applications in soil, sediments, and waste treatment [107]. Preliminary photocatalytic studies on NBFRs and phosphorus FRs have laid a foundation [108–110]. However, factors such as identifying degradation by-products and changes in solution toxicity remain unresolved.

(3)   Biodegradation

This method uses microorganisms or enzymes to break down organic FRs, making it particularly suitable for phosphorus- and nitrogen-based retardants. Hou et al. [111] reported aerobic biodegradation of three halogen-free phosphorus FRs, achieving removal rates between 29.3% and 89.9% after 25 days, with Klebsiella identified as a key degrader. Although environmentally friendly and effective, biodegradation is time-consuming, sensitive to environmental conditions, and may produce more toxic intermediates [112], complicating large-scale implementation. Understanding the biochemical pathways, involved microorganisms, and potential by-products is crucial [113].

(4)   Electrochemical Methods

These can be divided into electrochemical reduction and oxidation pathways [114]. Due to the high electronegativity of halogenated compounds, reduction processes are generally more suitable [115]. Electrochemical techniques demonstrate high efficiency in removing organic pollutants Oturan et al. [116] and have also been applied to phosphorus FRs. For instance, Tang et al. [117] used electrochemical oxidation to degrade TDCPP, achieving effective degradation with low-toxicity intermediates. Despite their potential, electrochemical methods require further improvements, especially in electrode materials and efficiency, and they still face challenges related to high application costs and energy consumption.

Dong et al. [118] reviewed emerging catalytic methods for degrading BFRs, noting that most studies are conducted under controlled laboratory conditions with the addition of co-solvents such as methanol, acetone, or

acetonitrile, leading to high degradation efficiencies. Compared to traditional thermal treatment, non-thermal methods are often more environmentally friendly and energy efficient. However, limitations include narrow applicability, slow reaction rates, stringent conditions, and incomplete degradation. Further optimization and validation are needed for the practical implementation of non-thermal techniques.

5. Comprehensive Discussion

In practice, thermal treatment techniques are indeed effective for rapidly degrading FRs. Although the purpose of adding FRs seems at odds with thermal degradation, in reality, FRs have minimal impact on the decomposition temperature and mainly influence the composition of gases and the quality of residues during decomposition [119]. Boro and Tiwari [120] suggest that FRs could be removed before thermal degradation. However, given the wide variety of FRs and the complex composition of waste materials, removing them before thermal treatment is challenging.

Thermal treatment effectively reduces waste volume and many pollutants but can also result in pollutants redistributing into other media. Therefore, combining multiple techniques is recommended to minimize the drawbacks of single methods. Among several thermal treatment methods, incineration is generally not the most valuable approach [121]. In contrast, pyrolysis, gasification, and hydrothermal processes are more feasible alternatives, producing fewer pollutants and valuable by-products. Under specific conditions, hydrothermal processing can even desorb pollutants without compromising material properties, providing an additional recovery pathway.

For more complex waste compositions, several treatment approaches are recommended: (i) performing initial thermal degradation, followed by non-thermal techniques for pollutant removal, or concentrating pollutants for further treatment through adsorption; (ii) reducing pollutant emissions by reintroducing waste ash or sludge into the combustion system [122]; (iii) conducting hydrothermal pre-treatment to remove pollutants, then using other thermal processes to generate energy [123].

6. Conclusions

This review provides a comprehensive comparison of thermal and non-thermal technologies for the treatment of flame retardants (FRs), focusing on incineration, pyrolysis, gasification, and hydrothermal treatment. While thermal methods are effective in degrading FRs, they may produce toxic by-products. Non-thermal approaches such as photocatalysis, biodegradation, and electrochemical treatment offer environmentally friendly alternatives but face limitations in efficiency and scalability. This review identifies several key findings:

(i) Flame retardants exhibit markedly different thermal decomposition behaviors under various treatment conditions, with diverse by-product profiles;

(ii) Thermal technologies are generally effective in reducing FR residues but may result in incomplete mineralization and secondary pollution.

(iii) Non-thermal approaches offer lower environmental burdens and serve as valuable supplements to thermal methods, though their practical implementation remains limited by technological constraints.

Based on these insights, this review offers three main contributions:

(i) It presents the first integrative analysis comparing the behavior of multiple FR types—including both halogenated and non-halogenated compounds—across thermal and non-thermal treatment routes;

(ii) It evaluates the applicability and limitations of each method from a waste-to-energy perspective, and proposes the feasibility of multi-technology integration based on waste characteristics;

(iii) It emphasizes the importance of understanding by-product toxicity and transformation mechanisms as key factors in selecting and optimizing treatment strategies.

Future research should focus on bridging the gap between laboratory-scale studies and full-scale applications, optimizing pollution control systems for emerging flame retardants, and evaluating the long-term environmental impacts of transformation products to support safer and more sustainable waste management practices.

Author Contributions: C.-Y.H.: data curation, methodology, software, writing—original draft preparation; S.-L.L.: conceptualization, investigation, supervision, validation, writing—reviewing and editing. All authors have read and agreed to the published version of the manuscript.

Conflicts of Interest: The authors declare no conflict of interest.

References

1. Van der Schyff, V.; Kalina, J.; Abballe, A.; et al. Has Regulatory Action Reduced Human Exposure to Flame Retardants? *Environ. Sci. Technol.* **2023**, *57*, 19106–19124.

2. Feiteiro, J.; Rocha, S.M.; Mariana, M.; et al. Pathways involved in the human vascular Tetrabromobisphenol A response: Calcium and potassium channels and nitric oxide donors. *Toxicology* **2022**, *470*, 153158.

3. Xu, P.; Tao, B.; Zhou, Z.; et al. Occurrence, composition, source, and regional distribution of halogenated flame retardants and polybrominated dibenzo-p-dioxin/dibenzofuran in the soils of Guiyu, China. *Environ. Pollut.* **2017**, *228*, 61–71.

4. Hendriks, H.S.; Westerink, R.H. Neurotoxicity and risk assessment of brominated and alternative flame retardants. *Neurotoxicol. Teratol.* **2015**, *52*, 248–269.

5. Alaee, M.; Arias, P.; Sjödin, A.; et al. An overview of commercially used brominated flame retardants, their applications, their use patterns in different countries/regions and possible modes of release. *Environ. Int.* **2003**, *29*, 683–689.

6. Sharkey, M.; Harrad, S.; Abdallah, M.A.-E.; et al. Phasing-out of legacy brominated flame retardants: The UNEP Stockholm Convention and other legislative action worldwide. *Environ. Int.* **2020**, *144*, 106041.

7. Yao, C.; Yang, H.; Li, Y. A review on organophosphate flame retardants in the environment: Occurrence, accumulation, metabolism and toxicity. *Sci. Total Environ.* **2021**, *795*, 148837.

8. Van der Veen, I.; de Boer, J. Phosphorus flame retardants: Properties, production, environmental occurrence, toxicity and analysis. *Chemosphere* **2012**, *88*, 1119–1153.

9. Li, Q.; Guo, M.; Song, H.; et al. Size distribution and inhalation exposure of airborne particle-bound polybrominated diphenyl ethers, new brominated flame retardants, organophosphate esters, and chlorinated paraffins at urban open consumption place. *Sci. Total Environ.* **2021**, *794*, 148695.

10. Levchik, S.; Weil, E. Developments in phosphorus flame retardants. In *Advances in Fire Retardant Materials*; Elsevier: Amsterdam, The Netherlands, 2008; pp. 41–66.

11. Kung, H.-C.; Hsieh, Y.-K.; Huang, B.-W.; et al. An overview: Organophosphate flame retardants in the atmosphere. *Aerosol Air Qual. Res.* **2022**, *22*, 220148.

12. Miranda, R.G.; Sampaio, C.F.; Leite, F.G.; et al. Flame Retardants: New and Old Environmental Contaminants. In *The Toxicity of Environmental Pollutants*; IntechOpen: London, UK, 2022.

13. Kajiwara, N.; Desborough, J.; Harrad, S.; et al. Photolysis of brominated flame retardants in textiles exposed to natural sunlight. *Environ. Sci. Process. Impacts* **2013**, *15*, 653–660.

14. Chokwe, T.B.; Abafe, O.A.; Mbelu, S.P.; et al. A review of sources, fate, levels, toxicity, exposure and transformations of organophosphorus flame-retardants and plasticizers in the environment. *Emerg. Contam.* **2020**, *6*, 345–366.

15. Bergman, Å.; Rydén, A.; Law, R.J.; et al. A novel abbreviation standard for organobromine, organochlorine and organophosphorus flame retardants and some characteristics of the chemicals. *Environ. Int.* **2012**, *49*, 57–82.

16. Mack, A.G. Flame retardants, halogenated. In *Kirk-Othmer Encyclopedia of Chemical Technology*; Wiley: Hoboken, NJ, USA, 2000.

17. Abbasi, G.; Li, L.; Breivik, K. Global historical stocks and emissions of PBDEs. *Environ. Sci. Technol.* **2019**, *53*, 6330–6340.

18. McGrath, T.J.; Morrison, P.D.; Ball, A.S.; et al. Detection of novel brominated flame retardants (NBFRs) in the urban soils of Melbourne, Australia. *Emerg. Contam.* **2017**, *3*, 23–31.

19. Al-Omran, L.S. Physiochemical properties and environmental levels of legacy and novel brominated flame retardants. In *Flame Retardants*; IntechOpen: London, UK, 2018.

20. Gao, Y.; Cao, R.; Zhang, H.; et al. Analysis of emerging halogenated flame retardants in environment. In *Comprehensive Analytical Chemistry*; Elsevier: Amsterdam, The Netherlands, 2020; pp. 41–70.

21. van Mourik, L.M.; Gaus, C.; Leonards, P.E.; et al. Chlorinated paraffins in the environment: A review on their production, fate, levels and trends between 2010 and 2015. *Chemosphere* **2016**, *155*, 415–428.

22. Horacek, H.; Grabner, R. Advantages of flame retardants based on nitrogen compounds. *Polym. Degrad. Stab.* **1996**, *54*, 205–215.

23. Morgan, A.B. *Non-Halogenated Flame Retardant Handbook*; John Wiley & Sons: Hoboken, NJ, USA, 2021.

24. Lu, S.-Y.; Hamerton, I. Recent developments in the chemistry of halogen-free flame retardant polymers. *Prog. Polym. Sci.* **2002**, *27*, 1661–1712.

25. Levchik, S.V.; Weil, E.D. *Combustion and Fire Retardancy of Aliphatic Nylons*; Wiley: Hoboken, NJ, USA, 2000.

26. Geschwindner, C.; Goedderz, D.; Li, T.; et al. The effects of various flame retardants on the combustion of polypropylene: Combining optical diagnostics and pyrolysis fragment analysis. *Polym. Degrad. Stab.* **2023**, *211*, 110321.

27. Zhang, M.; Buekens, A.; Li, X. Brominated flame retardants and the formation of dioxins and furans in fires and combustion. *J. Hazard. Mater.* **2016**, *304*, 26–39.

28. Altarawneh, M.; Saeed, A.; Al-Harahsheh, M.; et al. Thermal decomposition of brominated flame retardants (BFRs): Products and mechanisms. *Prog. Energy Combust. Sci.* **2019**, *70*, 212–259.

29. Huo, S.; Song, P.; Yu, B.; et al. Phosphorus-containing flame retardant epoxy thermosets: Recent advances and future perspectives. *Prog. Polym. Sci.* **2021**, *114*, 101366.

30. Yang, S.; Zhang, Q.; Hu, Y. Synthesis of a novel flame retardant containing phosphorus, nitrogen and boron and its application in flame-retardant epoxy resin. *Polym. Degrad. Stab.* **2016**, *133*, 358–366.

31. Kundu, C.K.; Li, Z.; Song, L.; et al. An overview of fire retardant treatments for synthetic textiles: From traditional approaches to recent applications. *Eur. Polym. J.* **2020**, *137*, 109911.

32. Samani, P.; van der Meer, Y. Life cycle assessment (LCA) studies on flame retardants: A systematic review. *J. Clean. Prod.* **2020**, *274*, 123259.

33. Lu, S.; Chen, S.; Luo, L.; et al. Molecules Featuring the Azaheterocycle Moiety toward the Application of Flame-Retardant Polymers. *ACS Chem. Health Saf.* **2023**, *30*, 343–361.

34. Liu, J.; Zhang, X.; Liu, S.; et al. Char structure and charring mechanism of phosphazene-based epoxy resin during combustion. *Polym. Degrad. Stab.* **2022**, *200*, 109927.

35. Wang, Q.; Shi, W. Kinetics study of thermal decomposition of epoxy resins containing flame retardant components. *Polym. Degrad. Stab.* **2006**, *91*, 1747–1754.

36. Vojta, S.; Melymuk, L.; Klánová, J. Changes in flame retardant and legacy contaminant concentrations in indoor air during building construction, furnishing, and use. *Environ. Sci. Technol.* **2017**, *51*, 11891–11899.

37. Vojta, Š.; Bečanová, J.; Melymuk, L.; et al. Screening for halogenated flame retardants in European consumer products, building materials and wastes. *Chemosphere* **2017**, *168*, 457–466.

38. Kajiwara, N.; Noma, Y.; Takigami, H. Brominated and organophosphate flame retardants in selected consumer products on the Japanese market in 2008. *J. Hazard. Mater.* **2011**, *192*, 1250–1259.

39. Rauert, C.; Lazarov, B.; Harrad, S.; et al. A review of chamber experiments for determining specific emission rates and investigating migration pathways of flame retardants. *Atmos. Environ.* **2014**, *82*, 44–55.

40. Ni, Y.; Kumagai, K.; Yanagisawa, Y. Measuring emissions of organophosphate flame retardants using a passive flux sampler. *Atmos. Environ.* **2007**, *41*, 3235–3240.

41. Kemmlein, S.; Hahn, O.; Jann, O. Emissions of organophosphate and brominated flame retardants from selected consumer products and building materials. *Atmos. Environ.* **2003**, *37*, 5485–5493.

42. Carlsson, H.; Nilsson, U.; Östman, C. Video display units: An emission source of the contact allergenic flame retardant triphenyl phosphate in the indoor environment. *Environ. Sci. Technol.* **2000**, *34*, 3885–3889.

43. Takigami, H.; Suzuki, G.; Hirai, Y.; et al. Flame retardants in indoor dust and air of a hotel in Japan. *Environ. Int.* **2009**, *35*, 688–693.

44. Zhu, H.; Kannan, K. Melamine and cyanuric acid in foodstuffs from the United States and their implications for human exposure. *Environ. Int.* **2019**, *130*, 104950.

45. Zhu, H.; Kannan, K. Distribution profiles of melamine and its derivatives in indoor dust from 12 countries and the implications for human exposure. *Environ. Sci. Technol.* **2018**, *52*, 12801–12808.

46. Antoš, K.; Sedlář, J. Influence of brominated flame retardant thermal decomposition products on HALS. *Polym. Degrad. Stab.* **2005**, *90*, 188–194.

47. Luda, M.; Balabanovich, A.; Hornung, A.; et al. Thermal degradation of a brominated bisphenol a derivative. *Polym. Adv. Technol.* **2003**, *14*, 741–748.

48. Wang, P.; Zhang, Q.; Zhang, H.; et al. Sources and environmental behaviors of Dechlorane Plus and related compounds—A review. *Environ. Int.* **2016**, *88*, 206–220.

49. Nguyen, C.; Kim, J. Thermal stabilities and flame retardancies of nitrogen–phosphorus flame retardants based on bisphosphoramidates. *Polym. Degrad. Stab.* **2008**, *93*, 1037–1043.

50. Chen, X.; Hu, Y.; Jiao, C.; et al. Preparation and thermal properties of a novel flame-retardant coating. *Polym. Degrad. Stab.* **2007**, *92*, 1141–1150.

51. Camino, G.; Costa, L.; Di Cortemiglia, M.L. Overview of fire retardant mechanisms. *Polym. Degrad. Stab.* **1991**, *33*, 131–154.

52. Thirumal, M.; Khastgir, D.; Nando, G.; et al. Halogen-free flame retardant PUF: Effect of melamine compounds on mechanical, thermal and flame retardant properties. *Polym. Degrad. Stab.* **2010**, *95*, 1138–1145.

53. Balabanovich, A.; Hornung, A.; Merz, D.; et al. The effect of a curing agent on the thermal degradation of fire retardant brominated epoxy resins. *Polym. Degrad. Stab.* **2004**, *85*, 713–723.

54. Wang, X.; He, S.; Wang, G.; et al. Characterization of PBDD/F emissions from simulated polystyrene insulation foam via lab-scale programmed thermal treatment testing. *Chemosphere* **2018**, *211*, 926–933.

55. Wan, J.; Sun, J.; Zhao, X.-L.; et al. Emission of brominated pollutants from waste printed circuit boards during thermal treatment: A review. *Aerosol Air Qual. Res.* **2023**, *23*, 230135.

56. Liang, J.; Lu, G.; Wang, R.; et al. The formation pathways of polybrominated dibenzo-p-dioxins and dibenzofurans (PBDD/Fs) from pyrolysis of polybrominated diphenyl ethers (PBDEs): Effects of bromination arrangement and level. *J. Hazard. Mater.* **2020**, *399*, 123004.

57. Wang, Y.; Huang, J.; Long, Y.; et al. Influence of bromination arrangement and level on the formation of polybrominated dibenzo-p-dioxins and dibenzofurans from pyrolysis and combustion of polybrominated diphenyl ethers: Mechanisms and kinetics. *J. Clean. Prod.* **2024**, *435*, 140543.

58. Hart, J.R. Insights of potential by-product emissions from halogenated flame-retardant combustion by chemical equilibrium calculations. *Int. J. Chem. Model.* **2016**, *8*, 341–351.

59. Purser, D. Fire safety performance of flame retardants compared with toxic and environmental hazards. In *Polymer Green Flame Retardants*; Elsevier: Amsterdam, The Netherlands, 2014; pp. 45–86.

60. Saeed, A. Studies on the Decomposition of Selected Brominated Flame Retardants (BFRs) and Formation of Polybrominated Dibenzo-p-dioxins and Dibenzofurans (PBDD/Fs) and Mixed Halogenated Dibenzo-p-dioxins and Dibenzofurans (PXDD/Fs). Ph.D. Thesis, Murdoch University, Perth, WA, Australia, 2016.

61. Xin, S.; Gao, W.; Wang, Y.; et al. Identification of the released and transformed products during the thermal decomposition of a highly chlorinated paraffin. *Environ. Sci. Technol.* **2018**, *52*, 10153–10162.

62. Lombardi, L.; Carnevale, E.; Corti, A. A review of technologies and performances of thermal treatment systems for energy recovery from waste. *Waste Manag.* **2015**, *37*, 26–44.

63. Sakai, S.; Watanabe, J.; Honda, Y.; et al. Combustion of brominated flame retardants and behavior of its byproducts. *Chemosphere* **2001**, *42*, 519–531.

64. Matsukami, H.; Kose, T.; Watanabe, M.; et al. Pilot-scale incineration of wastes with high content of chlorinated and non-halogenated organophosphorus flame retardants used as alternatives for PBDEs. *Sci. Total Environ.* **2014**, *493*, 672–681.

65. Kwon, E.-H.; Yoon, Y.-S.; Jeon, T.-W.; et al. Study on Thermal Treatment of Chlorinated Flame Retardant in Waste Containing Halogen Flame Retardant. *J. Korean Soc. Hazard Mitig.* **2018**, *18*, 655–663.

66. Liang, Y.; Xu, D.; Feng, P.; et al. Municipal sewage sludge incineration and its air pollution control. *J. Clean. Prod.* **2021**, *295*, 126456.

67. Yang, H.-H.; Cheruiyot, N.K.; Lin, C.; et al. Control of extreme brominated persistent organic pollutant emissions from start-ups of waste-to-energy incinerators. *J. Clean. Prod.* **2022**, *345*, 131108.

68. Wang, R.; Xu, Z. Recycling of non-metallic fractions from waste electrical and electronic equipment (WEEE): A review. *Waste Manag.* **2014**, *34*, 1455–1469.

69. Hu, X.; Gholizadeh, M. Biomass pyrolysis: A review of the process development and challenges from initial researches up to the commercialisation stage. *J. Energy Chem.* **2019**, *39*, 109–143.

70. Tange, L.; Drohmann, D. Waste electrical and electronic equipment plastics with brominated flame retardants–from legislation to separate treatment–thermal processes. *Polym. Degrad. Stab.* **2005**, *88*, 35–40.

71. Grause, G.; Furusawa, M.; Okuwaki, A.; et al. Pyrolysis of tetrabromobisphenol-A containing paper laminated printed circuit boards. *Chemosphere* **2008**, *71*, 872–878.

72. Ye, Z.; Yang, F.; Lin, W.; et al. Improvement of pyrolysis oil obtained from co-pyrolysis of WPCBs and compound additive during two stage pyrolysis. *J. Anal. Appl. Pyrolysis* **2018**, *135*, 415–421.

73. Zhu, P.; Sui, S.; Wang, B.; et al. A study of pyrolysis and pyrolysis products of flame-retardant cotton fabrics by DSC, TGA, and PY–GC–MS. *J. Anal. Appl. Pyrolysis* **2004**, *71*, 645–655.

74. Eschenbacher, A.; Varghese, R.J.; Weng, J.; et al. Fast pyrolysis of polyurethanes and polyisocyanurate with and without flame retardant: Compounds of interest for chemical recycling. *J. Anal. Appl. Pyrolysis* **2021**, *160*, 105374.

75. Chen, G.; Liu, T.; Luan, P.; et al. Distribution, migration, and removal of N-containing products during polyurethane pyrolysis: A review. *J. Hazard. Mater.* **2023**, *453*, 131406.

76. Cho, S.-H.; Park, J.; Jung, S.; et al. Syngas Production via CO2-Mediated Melamine Pyrolysis. *ACS Sustain. Chem. Eng.* **2024**, *12*, 2476–2483.

77. Kumagai, S.; Grause, G.; Kameda, T.; et al. Thermal decomposition of tetrabromobisphenol-A containing printed circuit boards in the presence of calcium hydroxide. *J. Mater. Cycles Waste Manag.* **2017**, *19*, 282–293.

78. Charitopoulou, M.A.; Stefanidis, S.D.; Lappas, A.A.; et al. Catalytic pyrolysis of polymers with brominated flame-retardants originating in waste electric and electronic equipment (WEEE) using various catalysts. *Sustain. Chem. Pharm.* **2022**, *26*, 100612.

79. Chen, Y.; Ke, Y.; Liang, S.; et al. Enhanced bromine fixation and tar lightweighting in co-pyrolysis of non-metallic fractions of waste printed circuit boards with Bayer red mud. *Waste Manag.* **2023**, *162*, 72–82.

80. Zhan, H.; Zhuang, X.; Song, Y.; et al. Formation and regulatory mechanisms of N-containing gaseous pollutants during stage-pyrolysis of agricultural biowastes. *J. Clean. Prod.* **2019**, *236*, 117706.

81. Sajid, M.; Raheem, A.; Ullah, N.; et al. Gasification of municipal solid waste: Progress, challenges, and prospects. *Renew. Sustain. Energy Rev.* **2022**, *168*, 112815.

82. Lidman Olsson, E.O.; Glarborg, P.; et al. Release of P from pyrolysis, combustion, and gasification of biomass—A model compound study. *Energy Fuels* **2021**, *35*, 15817–15830.

83. Yamawaki, T. The gasification recycling technology of plastics WEEE containing brominated flame retardants. *Fire Mater.* **2003**, *27*, 315–319.

84. Lo, Y.-P.; Prabu, S.; Chang, M.-B.; et al. Hydrogen production and pollutants emission characteristics by co-gasified of paper-mill sludge and automobile shredder residues in a commercial scale fluidized bed gasifier. *Int. J. Hydrogen Energy* **2024**, *52*, 46–57.

85. Ciuffi, B.; Chiaramonti, D.; Rizzo, A.M.; et al. A critical review of SCWG in the context of available gasification technologies for plastic waste. *Appl. Sci.* **2020**, *10*, 6307.

86. Alvarez, J.; Kumagai, S.; Wu, C.; et al. Hydrogen production from biomass and plastic mixtures by pyrolysis-gasification. *Int. J. Hydrog. Energy* **2014**, *39*, 10883–10891.

87. Pinto, F.; Franco, C.; André, R.; et al. Co-gasification study of biomass mixed with plastic wastes. *Fuel* **2002**, *81*, 291–297.

88. Weiland, F.; Lundin, L.; Celebi, M.; et al. Aspects of chemical recycling of complex plastic waste via the gasification route. *Waste Manag.* **2021**, *126*, 65–77.

89. Lachos-Perez, D.; Torres-Mayanga, P.C.; Abaide, E.R.; et al. Hydrothermal carbonization and Liquefaction: Differences, progress, challenges, and opportunities. *Bioresour. Technol.* **2022**, *343*, 126084.

90. Uddin, M.A.; Bhaskar, T.; Kusaba, T.; et al. Debromination of flame retardant high impact polystyrene (HIPS-Br) by hydrothermal treatment and recovery of bromine free plastics. *Green Chem.* **2003**, *5*, 260–263.

91. Nose, K.; Hashimoto, S.; Takahashi, S.; et al. Degradation pathways of decabromodiphenyl ether during hydrothermal treatment. *Chemosphere* **2007**, *68*, 120–125.

92. Yin, J.; Li, G.; He, W.; et al. Hydrothermal decomposition of brominated epoxy resin in waste printed circuit boards. *J. Anal. Appl. Pyrolysis* **2011**, *92*, 131–136.

93. Zhan, L.; Zhao, X.; Ahmad, Z.; et al. Leaching behavior of Sb and Br from E-waste flame retardant plastics. *Chemosphere* **2020**, *245*, 125684.

94. Xue, Y.; Bai, L.; Chi, M.; et al. Co-hydrothermal carbonization of lignocellulose biomass and polyvinyl chloride: The migration and transformation of chlorine. *Chem. Eng. J.* **2022**, *446*, 137155.

95. Xiu, F.-R.; Bai, Q.; Qi, Y.; et al. An alkali-enhanced subcritical water treatment strategy of short-chain chlorinated paraffins: Dechlorination and hydrocarbons recovery. *Sci. Total Environ.* **2023**, *904*, 166574.

96. Tangredi, A.; Barca, C.; Ferrasse, J.-H.; et al. Effect of process parameters on phosphorus conversion pathways during hydrothermal treatment of sewage sludge: A review. *Chem. Eng. J.* **2023**, *463*, 142342.

97. Li, J.; Jin, J.; Zhao, Y.; et al. Enhancing phosphorus bioavailability in sewage sludge through co-hydrothermal treatment with biomass. *J. Water Process Eng.* **2023**, *51*, 103448.

98. Huang, R.; Tang, Y. Speciation dynamics of phosphorus during (hydro) thermal treatments of sewage sludge. *Environ. Sci. Technol.* **2015**, *49*, 14466–14474.

99. Aragón-Briceño, C.; Pozarlik, A.; Bramer, E.; et al. Hydrothermal carbonization of wet biomass from nitrogen and phosphorus approach: A review. *Renew. Energy* **2021**, *171*, 401–415.

100. Tang, L.; Hu, Z.; Gao, P.; et al. Transformation characteristics of nitrogen, sulfur and chlorine during microwave-assisted hydrothermal treatment of excavated waste. *J. Clean. Prod.* **2023**, *384*, 135638.

101. Song, Q.; Feng, Y.; Liu, G.; et al. Degradation of the flame retardant triphenyl phosphate by ferrous ion-activated hydrogen peroxide and persulfate: Kinetics, pathways, and mechanisms. *Chem. Eng. J.* **2019**, *361*, 929–936.

102. Yang, P.; Liu, J.; Korshin, G.V.; et al. New insights into the role of nitrite in the degradation of tetrabromobisphenol S by sulfate radical oxidation. *Environ. Sci. Technol.* **2022**, *56*, 17743–17752.

103. Chen, Z.; Wang, L.; Xu, H.; et al. Efficient heterogeneous activation of peroxymonosulfate by modified $CuFe_2O_4$ for degradation of tetrabromobisphenol A. *Chem. Eng. J.* **2020**, *389*, 124345.

104. Han, Q.; Dong, W.; Wang, H.; et al. Degradation of tetrabromobisphenol A by ferrate (VI) oxidation: Performance, inorganic and organic products, pathway and toxicity control. *Chemosphere* **2018**, *198*, 92–102.

105. Ma, C.; Guo, Z.; Fang, Z.; et al. Flame retardancy and chemical degradation of epoxy containing phenylphosphonate group under mild conditions. *Compos. Part B Eng.* **2022**, *239*, 109967.

106. Dang, Y.; Tang, K.; Wang, Z.; et al. Organophosphate esters (OPEs) flame retardants in water: A review of photocatalysis, adsorption, and biological degradation. *Molecules* **2023**, *28*, 2983.

107. Rani, M.; Sillanpää, M.; Shanker, U. An updated review on environmental occurrence, scientific assessment and removal of brominated flame retardants by engineered nanomaterials. *J. Environ. Manag.* **2022**, *321*, 115998.

108. Yuan, X.; Lacorte, S.; Cristale, J.; et al. Removal of organophosphate esters from municipal secondary effluent by ozone and UV/H_2O_2 treatments. *Sep. Purif. Technol.* **2015**, *156*, 1028–1034.

109. Antonopoulou, M.; Giannakas, A.; Bairamis, F.; et al. Degradation of organophosphorus flame retardant tris (1-chloro-2-propyl) phosphate (TCPP) by visible light N, S-codoped TiO_2 photocatalysts. *Chem. Eng. J.* **2017**, *318*, 231–239.

110. Ling, S.; Huang, K.; Tariq, M.; et al. Photodegradation of novel brominated flame retardants (NBFRs) in a liquid system: Kinetics and photoproducts. *Chem. Eng. J.* **2019**, *362*, 938–946.

111. Hou, R.; Wang, Y.; Zhou, S.; et al. Aerobic degradation of nonhalogenated organophosphate flame esters (OPEs) by enriched cultures from sludge: Kinetics, pathways, bacterial community evolution, and toxicity evaluation. *Sci. Total Environ.* **2021**, *760*, 143385.

112. Cámara, B.; Herrera, C.; González, M.; et al. From PCBs to highly toxic metabolites by the biphenyl pathway. *Environ. Microbiol.* **2004**, *6*, 842–850.

113. Segev, O.; Kushmaro, A.; Brenner, A. Environmental impact of flame retardants (persistence and biodegradability). *Int. J. Environ. Res. Public Health* **2009**, *6*, 478–491.

114. Zhang, M.; Shi, Q.; Song, X.; et al. Recent electrochemical methods in electrochemical degradation of halogenated organics: A review. *Environ. Sci. Pollut. Res.* **2019**, *26*, 10457–10486.

115. Huang, Z.; Deng, D.; Qiao, J.; et al. New insight into the cosolvent effect on the degradation of tetrabromobisphenol A (TBBPA) over millimeter-scale palladised sponge iron (Pd-s-Fe^0) particles. *Chem. Eng. J.* **2019**, *361*, 1423–1436.

116. Oturan, N.; Van Hullebusch, E.D.; Zhang, H.; et al. Occurrence and removal of organic micropollutants in landfill leachates treated by electrochemical advanced oxidation processes. *Environ. Sci. Technol.* **2015**, *49*, 12187–12196.

117. Tang, S.; Luo, Z.; Liao, J.; et al. Degradation and detoxification mechanisms of organophosphorus flame retardant tris (1, 3-dichloro-2-propyl) phosphate (TDCPP) during electrochemical oxidation process. *Chin. Chem. Lett.* **2023**, *34*, 108090.

118. Dong, J.; Li, G.; Gao, J.; et al. Catalytic degradation of brominated flame retardants in the environment: New techniques and research highlights. *Sci. Total Environ.* **2022**, *848*, 157695.

119. Ishii, A.; Amagai, K.; Furuhata, T.; et al. Thermal gasification behavior of plastics with flame retardant. *Fuel* **2007**, *86*, 2475–2484.

120. Boro, B.; Tiwari, P. Effect of metals and brominated flame retardants on thermal degradation kinetics of waste printed circuit board. *Thermochim. Acta* **2024**, *736*, 179747.

121. Bifulco, A.; Chen, J.; Sekar, A.; et al. Recycling of flame retardant polymers: Current technologies and future perspectives. *J. Mater. Sci. Technol.* **2024**, *199*, 156–183.

122. Tang, W.; Hsiao, C.-Y.; Lin, S.-L.; et al. Mitigation of PBDE net discharge in hazardous waste thermal treatment system through reintroducion of sludge and fly ash into GASMILD operations. *Chemosphere* **2024**, *364*, 143026.

123. Wang, Y.; Wu, K.; Liu, Q.; et al. Low chlorine oil production through fast pyrolysis of mixed plastics combined with hydrothermal dechlorination pretreatment. *Process Saf. Environ. Prot.* **2021**, *149*, 105–114.

Scilight

Review

A Mini-Review of Ion Exchange Membranes for Capacitive Deionization: Research Progress, Commercialization, and Patent Trends

Po-An Chen [1], Kuan-Ting Lee [2,*], and Jie-Lun Chang [1]

[1]   Department of Environmental Science and Engineering, Tunghai University, Taichung 407, Taiwan
[2]   Department of Chemical and Materials Engineering, Tunghai University, Taichung 407, Taiwan
*   Correspondence: s9832806@gmail.com or ktlee@thu.edu.tw

Abstract: With global water scarcity worsening, improving water treatment efficiency and sustainability has become a priority for governments worldwide. Ion exchange membranes (IEMs) in capacitive deionization (CDI) are regarded as a promising water treatment technology, capable of meeting the urgent demand for sustainable water resource utilization. In this mini-review, we have provided an overview of the research progress made in IEM-assisted CDI (MCDI), focusing on membrane materials, system configurations, patent analysis, and commercialization. Bibliometric and citation analyses reveal a surge in research and patent activity related to MCDI over the past five years, highlighting their growing global interest. The commercialization of MCDI is accelerating, driven by government funding in Europe, the U.S., Japan, and South Korea, alongside industry innovations improving efficiency and scalability. Patent analysis identifies dominant technical topics, patent strength, and the evolving patent numbers and expiration patterns of MCDI. Although challenges remain regarding cost, membrane durability, and scalability, MCDI is set to be a transformative technology in next-generation water purification and electrochemical separation systems. This review examines the current state of MCDI across various countries, offering insights into its role in advancing sustainable water resource management and enhancing water treatment technologies.

Keywords: ion exchange membranes; capacitive deionization; water treatment; commercialization; patent analysis

1. Ion Exchange Membranes

1.1. Overview and Bibliometric Analysis of IEMs

To comprehensively examine the research landscape of ion exchange membranes (IEMs), a bibliometric analysis is conducted using VOSviewer. This tool facilitates the construction and visualization of bibliometric networks, enabling researchers to systematically examine relationships among publication information and keywords in a structured graphical format [1–3]. Figure 1a illustrates a keyword co-occurrence network, where distinct research domains are represented as color-coded clusters. The red cluster primarily pertains to studies on anion exchange membranes, particularly in the context of alkaline environments and fuel cell applications. The green cluster focuses on ion transport mechanisms and membrane performance optimization. The blue cluster highlights topics such as proton conductivity, polymer chemistry, and nanocomposite development. Meanwhile, the yellow cluster encompasses research on electrodialysis, adsorption processes, and membrane-based water purification technologies. These thematic clusters underscore the interdisciplinary nature of IEM research, bridging fields such as energy storage, fuel conversion, water treatment, and environmental remediation. The dense interconnections within and between clusters reflect the growing complexity and integration of IEMs-related studies. Figure 1b illustrates the citation network analyzed using Litmaps, showcasing the interconnected relationships within academic literature. Litmaps is a platform that simplifies literature management and visualization, enabling researchers to track advancements in their fields while constructing citation networks that illuminate the relationships among scholarly works. In 2021, Jiang et al. [4] published an article titled "A comprehensive review on the synthesis and applications of ion exchange membranes," which provides a comprehensive overview of the synthesis of IEMs, their structural characteristics, and their diverse applications, with a particular focus on advancing the adaptability of membrane materials. In this study, conventional methods

such as solution casting and phase inversion, achieved membranes with high permselectivity, low electrical resistance, and improved ion exchange capacity, indicating the effectiveness of structural tuning and functional group modification in enhancing membrane performance, emphasized the importance of green synthesis approaches to address environmental concerns, and echoed the growing demand for next-generation IEMs in applications such as fuel cells, and redox flow batteries. This study serves as a pivotal reference point for research on IEMs. The interconnected citation pathways extending outward from the network reveal derivative studies that expand upon the original classifications, offering fresh insights into sustainable polymer development, hybrid membrane structures, ion-specific separations, as well as emerging applications such as redox-coupled electrodialysis and electrochemical energy recovery. Figure 1c presents the research conducted by Alkhadra et al. [5] in 2022 on the topic of Electrochemical methods for water purification, ion separations, and energy conversion, which has emerged as one of the most highly cited papers in recent years. This comprehensive review summarizes electrochemical strategies for water purification, ion separation, and energy conversion, emphasizing the primary advantages of electrochemical systems, including compact device design, high chemical selectivity, and minimal generation of secondary waste. Notably, this study advocates for the direct removal of contaminants from water rather than extracting water from contaminants. Additionally, it highlights advanced techniques such as shock electrodialysis and Faradaic deionization, establishing electrochemical membrane systems as essential tools for sustainable water and energy technologies in the future. The node located in the bottom-right corner of Figure 1c represents the latest research on IEMs published by Zhang et al. [6] in 2025. This study developed porous ion-exchange membranes by optimizing the ratio of sulfonated polyethersulfone, membrane porosity, and the density of active sites, thereby enhancing the selective transport of dye molecules. The results demonstrated outstanding water-dye separation performance, achieving a removal efficiency of up to 97.1%. Figure 1d depicts a time-resolved citation network, with the central green node representing a pivotal review [4]. The outward-extending green links indicate direct citation relationships with several influential works published between 2017 and 2021, focusing on topics such as enhancing membrane selectivity, diversifying applications, and integrating electrochemical processes. The dense clustering of blue nodes illustrates the concentrated activity in derivative studies, while the vertical arrangement of nodes reflects the chronological progression of scholarly contributions.
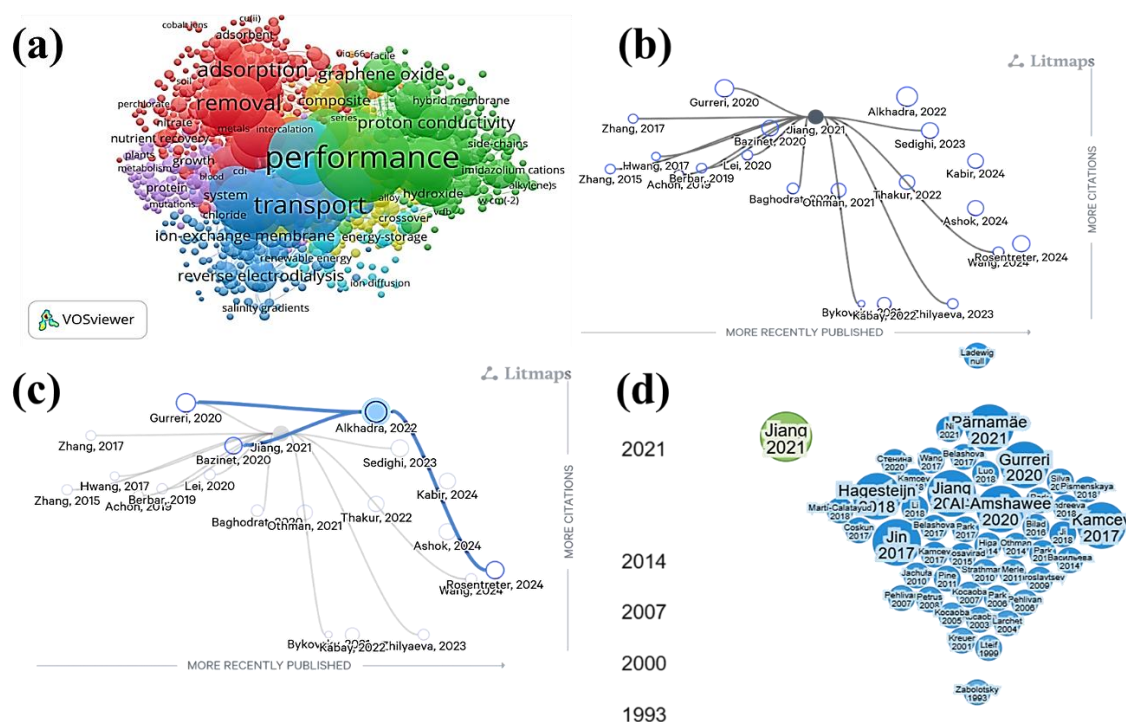

Figure 1. A bibliometric and citation-based analysis of research on ion-exchange membranes (IEMs). (**a**) A keyword co-occurrence map highlighting the primary thematic clusters. (**b**,**c**) Citation networks outlining the trajectory of core concepts related to IEMs. (**d**) Time-resolved citation clusters arranged chronologically.

1.2. IEMs Materials and Fabrication

As the research focus and interdisciplinary applications of IEMs expand, the materials have undergone significant evolution in chemistry and fabrication processes. Early-generation membranes are largely based on perfluorosulfonic acid (PFSA) structures, such as Nafion, valued for their high proton conductivity and electrochemical stability [7]. However, these materials are limited by their high cost and limited performance under elevated temperatures or alkaline environments. Consequently, the development of alternative materials to overcome these limitations has emerged as a critical challenge in advancing IEM technology. Recently, materials such as sulfonated polyetheretherketone (SPEEK), sulfonated aromatic polymers, sulfonated polyphenylene oxide biphenyl (sPPB), and proton-conductive multi-block copolymers have attracted significant attention due to their outstanding mechanical properties, chemical resistance, and tunable ion transport characteristics [8–10]. Notably, SPEEK membranes demonstrate remarkable proton conductivity and dimensional stability in PEMFCs, particularly under high-temperature and low-humidity conditions [11]. By fine-tuning their degree of sulfonation (DS), SPEEK serves as an effective, cost-efficient replacement for traditional, expensive PFSA membranes, while retaining sufficient electrochemical performance and chemical stability [12]. According to comparative membrane performance data (Table 1), PFSA membranes such as Nafion offer high proton conductivity (0.1–0.2 S/cm) and excellent chemical stability in both acidic and alkaline media, but suffer from moderate mechanical strength and thermal limits (≤ 363 K), with extremely high production costs [4,11]. In contrast, SPEEK provides adjustable conductivity (0.01–0.1 S/cm) and high thermal tolerance (up to 393 K), supported by a rigid backbone that enhances mechanical strength [10]. Other sulfonated polymers can be tailored for specific ion selectivity (e.g., Li^+/Mg^{2+}), and exhibit high thermal stability (up to 423 K), although their long-term stability remains environment-dependent [8,13].

In addition, recent advances in bioinspired membrane design have demonstrated how mimicking biological ion channels, such as those found in cell membranes, can significantly enhance ion selectivity, water permeability, and energy efficiency [14]. These membranes are typically engineered with nanopores or nanochannels that replicate the structural and electrostatic characteristics of natural transport proteins, enabling precise control over ion transport at the molecular level. For instance, a recent study developed a nanofluidic membrane that emulates charge-selective transport, achieving both high monovalent/divalent ion separation performance and reduced energy consumption [15]. This approach not only overcomes key limitations of conventional polymer membranes but also aligns with the broader movement toward sustainable and high-efficiency separation technologies. Bioinspired design thus offers a promising pathway for the development of next-generation IEMs that are more selective, durable, and compatible with low-energy desalination and resource recovery systems [15].

Table 1. Comparison of properties for ion exchange applications [4,8,10,11,13].

Property	Nafion (PFSA)	SPEEK	Other Sulfonated Polymers
Proton Conductivity	High (0.1–0.2 S/cm, high humidity)	Moderate (0.01–0.1 S/cm, tunable by DS)	Moderate-high (0.05–0.15 S/cm, structure-dependent)
Ion Selectivity	Low-moderate (monovalent ions)	Moderate-high (adjustable via DS)	High (tailorable for specific ions, e.g., Li^+/Mg^{2+})
Chemical Stability	Excellent (stable in strong acid/alkali)	Good (acid-stable, degrades in alkali)	Moderate-good (depends on chemistry)
Mechanical Strength	Moderate (often requires reinforcement)	High (rigid backbone)	High (aromatic backbone enhances strength)
Thermal Stability	Moderate (≤ 363 K)	High (up to 393 K)	High (up to 423 K, crosslinking-dependent)
Cost	Very high (perfluorinated synthesis)	Low-moderate (non-fluorinated)	Moderate (scalable but process-sensitive)
Lifetime	Long (5–10 years, fuel cell-validated)	Moderate (3–5 years, DS optimization needed)	Moderate (3–7 years, environment-dependent)
Primary Applications	PEM fuel cells, electrolyzes	MCDI, electrodialysis, high-T PEMFCs	Ion separation, Li recovery, acid/alkali treatment

1.3. Ion Transport Mechanisms and Developing Strategies for IEMs

IEMs have been widely and maturely employed in seawater desalination, wastewater treatment, and food-grade separations. However, limited research outcomes are available in lithium recovery, acid-base separation, and selective electrodialysis. The primary challenge lies in the need to further enhance the ion selectivity, mechanical stability, and chemical compatibility of IEMs in these applications [16–20]. Recent research findings

indicate that the integration of nanoscale architectures, topological layer-by-layer assembly, and surface functionalization plays a crucial role in enhancing IEMs' selectivity and fouling resistance [21–23]. Multi-topological and hierarchical membrane structures enhance the interface interactions between membranes and the electrolyte environment by precisely regulating ion-specific transport pathways [24,25]. Moreover, as manufacturing complexity and cost remain critical barriers to the commercial application of IEMs, achieving a balance between functionality and economic feasibility continues to be a significant challenge for materials scientists and engineers [26]. In addition to structural improvements, understanding the fundamental mechanisms of ion transport is crucial for rational membrane design. Ion movement within IEMs is primarily governed by the Donnan exclusion principle, where fixed charged groups embedded in the polymer matrix repel co-ions and facilitate counter-ion conduction [27]. The efficiency of this process is influenced by charge density, hydration enthalpy, and polymer segment mobility. Interestingly, optimizing the spatial distribution and chemical nature of fixed charge groups can significantly enhance counter-ion selectivity while suppressing undesired co-ion leakage [28]. In addition, polymer microstructure such as free volume, crosslinking density, and backbone rigidity plays a critical role in determining ion diffusion behavior and electrostatic interactions within the membrane phase [29].

Developing strategies to streamline synthesis processes, enhance reproducibility, and integrate membrane technologies into broader energy-water frameworks may provide effective solutions. Notably, integrating IEMs into CDI systems offers promising opportunities to improve ion removal efficiency, reduce energy consumption, and expand the functional versatility of membrane-based water treatment systems [27]. Furthermore, the application of artificial intelligence (AI) in membrane material discovery and structural optimization is emerging as a transformative approach to accelerate the development of high-performance IEMs. AI-driven strategies leverage machine learning algorithms to predict material properties, identify optimal polymer compositions, and simulate membrane behaviors under various operating conditions. These tools enable researchers to drastically reduce experimental workload by narrowing down candidate materials through data-informed models and high-throughput screening techniques. The use of AI frameworks in membrane design workflows has enabled the integration of molecular descriptors, physicochemical databases, and performance benchmarks to identify promising membrane formulations with enhanced ion conductivity and mechanical stability [28]. The incorporation of AI not only expedites the material discovery process but also facilitates the development of tailor-made membranes for specific applications such as lithium recovery, nutrient separation, and electrochemical desalination. As such, AI serves as a critical enabler for next-generation IEM design, supporting the convergence of data science and materials engineering to meet emerging water treatment demands [28].

2. Membrane Capacitive Deionization

Capacitive deionization (CDI) is a technology that applies a low voltage of less than 1.2 V across porous electrodes [29]. Owing to its low energy consumption, minimal chemical usage, and strong regeneration capabilities, it has emerged as a promising electrochemical method for water treatment [30]. Co-ion repulsion, limited ion selectivity, and low charge efficiency are notable drawbacks of conventional CDI systems. Particularly in high-salinity or complex water matrices, these issues become more pronounced [31]. To address the limitations of conventional CDI systems, the integration of IEMs has emerged as a promising strategy [32]. The membrane capacitive deionization (MCDI) is a system in which cation exchange membranes (CEMs) and anion exchange membranes (AEMs) are strategically placed near the electrodes. This configuration allows counter-ions to pass through while effectively blocking co-ions [31,33]. This configuration significantly enhances charge efficiency, reduces ion back-diffusion, and improves ion selectivity [34]. Recent research has focused on tailoring the microstructure and surface properties of IEMs, including porosity, functional group density, and hydrophilicity, to enhance ion transport kinetics and overall electrochemical performance [35]. This advancement has enabled MCDI to more efficiently treat high-salinity water, recover lithium, and selectively remove contaminants [36–39].

Figure 2 provides an overview of research advancements in MCDI over the past decade. Notably, since 2017, the number of published articles has increased substantially and has remained stable at approximately 50 to 55 publications per year. These records were retrieved from the Web of Science Core Collection using the keywords "capacitive deionization" and "ion exchange membrane," covering the period from 2010 to 2024. This growth is largely attributed to the substantial potential for ion-selective transport in MCDI systems. By positioning CEM and AEM layers between the feed solution and electrodes, MCDI achieves ion-selective mobility. This structural arrangement facilitates the formation of a more stable electric double layer while minimizing parasitic energy losses, thereby enhancing overall system performance. The lower section of Figure 2 illustrates the evolution of the MCDI module architecture. Early designs were based on a traditional layered configuration, consisting of current collectors, porous carbon electrodes, IEMs, and spacers, forming a foundational platform for ion removal

through electrosorption. This architecture established a solid basis for subsequent technological advancements and broader applications.

Recent advances in materials engineering have led to more sophisticated configurations that incorporate quaternized polymer-blend AEMs and high-surface-area activated carbon electrodes, contributing to enhanced ion selectivity, mechanical durability, and operational efficiency [40,41]. Concurrently, increasing attention has been given to the optimization of IEM microstructural properties such as porosity, water uptake, ion exchange capacity, and surface charge density, which govern deionization kinetics and system capacitance [27,31]. Building on these material and structural innovations, recent studies have further explored hybrid ion storage mechanisms, such as ion capacitive potential and pseudocapacitive behavior, to improve ion-specific removal rates and reduce energy consumption [30]. Novel membrane materials, including nanoporous ceramics, ionomer-based composites, and surface-functionalized polymers, have demonstrated promising results in improving electrosorption performance and operational stability [42,43]. Beyond technical improvements, the integration of IEMs has broadened the application scope of CDI systems. MCDI has proven effective not only for brackish water and ultrapure water production but also for lithium recovery, nutrient removal, and selective contaminant separation [31,38,39]. Its modular architecture, low energy requirements, and compatibility with renewable energy sources make MCDI a viable technology for decentralized and sustainable water treatment applications. In addition to material and structural innovations, recent research has increasingly focused on the integration of AI to further optimize the performance of MCDI systems. By leveraging machine learning algorithms, such as random forest and artificial neural networks, researchers have developed predictive models capable of estimating effluent ion concentrations with high accuracy [44]. These models enable real-time system adjustments, improving process control and overall operational stability. Through these applications, AI enhances not only ion selectivity and energy efficiency but also system adaptability in treating complex and dynamic water matrices. This data-driven approach represents a promising direction for the intelligent design and automation of next-generation MCDI technologies.
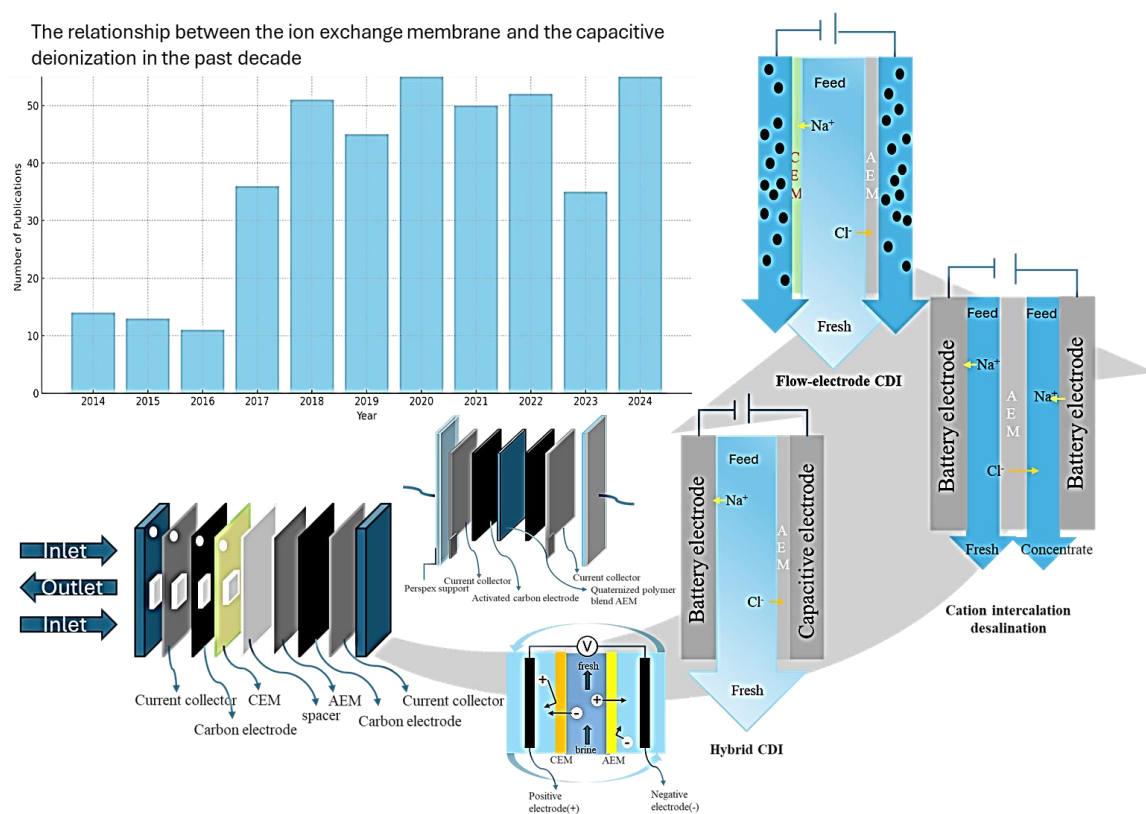

Figure 2. Research trends and system configurations of MCDI over the past decade.

3. Commercialization

Wastewater treatment methods include physical adsorption [45], electrochemistry [46] advanced oxidation [47,48], and biological treatment [49]. The intensifying global demand for clean and reliable water resources has driven growing attention toward MCDI as a next-generation desalination technology. According to the United Nations, nearly half of the world's population faces severe water scarcity during at least part of the year, highlighting the urgency for scalable, energy-efficient water treatment solutions [50]. In response, national

governments and international organizations have increased their support for advanced desalination research and infrastructure, with MCDI emerging as a promising candidate. The convergence of public-sector funding, regulatory initiatives, and private-sector innovation is accelerating the advancement and commercialization of MCDI systems [51]. As a result, MCDI is increasingly viewed as a critical enabler in the global effort to secure water sustainability, particularly in regions burdened by resource limitations and environmental stressors.

3.1. Europe

Europe has spearheaded approximately 60% of global MCDI pilot projects. Notably, the Netherlands-based Wettsus research center and Voltea collaboratively developed a flow-electrode CDI (FCDI) system, achieving a water recovery rate of up to 80%, which has been successfully applied in purifying agricultural irrigation water [52]. Additionally, Germany's Fraunhofer Institute, in partnership with FuMA-Tech (Bietigheim-Bissingen, Germany), utilized polyelectrolyte multilayer membranes (PEMs) to modify IEMs, significantly enhancing the selectivity of MCDI systems for monovalent and divalent ions, such as Na^+ and Ca^{2+} [52,53]. This technology has been employed in industrial cooling water recycling, effectively reducing chemical reagent usage by up to 80% [54].

3.2. United States

Since 2010, the U.S. Department of Energy (DOE) and the National Science Foundation (NSF) have been major supporters of research on CDI, with a particular focus on advancing low-cost carbon-based electrodes and functionalized IEMs [13,52]. These efforts aim to improve the system performance, energy efficiency, and cost-effectiveness of CDI in practical desalination applications. Evoqua Water Technologies has reportedly developed an MCDI system successfully applied to groundwater desalination in California. This achieves a salt adsorption capacity of approximately 18.5 mg/g, significantly higher than the typical value of 12 mg/g for conventional CDI systems [52]. Meanwhile, U.S.-based research teams are investigating SPEEK membranes, which exhibit a high ion exchange capacity (approximately 3.5 meq/g) and superior antifouling properties. These materials are being evaluated for their potential applications in greenhouse irrigation [13]. Furthermore, SPEEK's hydrophilicity and structural stability make it a promising candidate for prolonged electrochemical cycling, especially when combined with advanced porous electrodes [13]. MCDI has garnered significant attention in the United States for its high energy efficiency and modular design, making it a viable option for low-salinity water treatment [13,55]. However, the technology still faces several critical challenges, particularly in enhancing membrane durability and reducing system integration costs. However, the technology still faces several critical challenges, particularly in enhancing membrane durability and reducing system integration costs. In 2022, the Office of Naval Research and the U.S. Marine Corps highlighted that MCDI systems exhibit significant performance decline when applied to high-salinity waters. Such conditions are common in real-world applications and are not easily addressed through pilot-scale optimization. This situation raises practical concerns regarding energy efficiency and system scalability [56].

3.3. Japan

Japan has maintained a leading position in the production of IEMs, with companies such as Asahi Glass and ASTOM renowned for their Neosepta IEMs, celebrated for their exceptional chemical stability. These membranes are widely used in MCDI systems due to their superior durability and performance [13,57]. Furthermore, the Japanese government has set ambitious goals to integrate MCDI technology into 60% of industrial wastewater recovery projects by 2030 and reduce IEM production costs by 40% from current levels. Despite Japan's excellence in membrane manufacturing technologies, challenges persist in scaling up electrode production to meet industrial demands [55].

3.4. South Korea

In 2016, South Korea incorporated MCDI into its water technology innovation program, initially focusing on wastewater treatment in the electronics industry. Researchers have explored the potential of graphene oxide (GO)-based IEMs for MCDI applications. These membranes exhibit high water absorption capacity and ion exchange properties, significantly enhancing desalination performance. However, challenges remain in optimizing membrane thickness to balance mechanical stability and ion transport efficiency [58]. Leading South Korean companies, including Samsung (Suwon-si, Republic of Korea) and LG Chem (Seoul, Republic of Korea), are actively driving the commercialization of MCDI technology, aiming to process up to 8 million cubic meters of

water annually by 2030 [59]. Despite these efforts, South Korea faces challenges in scaling up practical applications and strengthening its competitiveness in international markets [60].

Driven by global policy support, industrial investment, and successful pilot-scale implementations, MCDI technology is steadily transitioning from laboratory research to commercial applications. As illustrated in Figure 3, the evolution of MCDI has followed a multi-phase trajectory, beginning with advancements in ion exchange membrane manufacturing and electrode material development. Subsequent efforts have focused on integrating hybrid ion storage mechanisms, optimizing system performance, and reducing energy consumption. These technological milestones have significantly improved system stability and efficiency, paving the way for commercial deployment. However, to fully realize MCDI's market potential, further research must address challenges such as membrane fouling, ion selectivity, cost reduction, and system scalability. Recent techno-economic analyses estimate that the levelized cost of water for full-scale MCDI systems ranges from 0.6 to 1.2 USD/m^3, depending on feedwater salinity and energy input. Which consisted of 10 pairs of activated carbon electrodes with a total effective surface area of 8000 cm^2. This remains significantly higher than the 0.3–0.6 USD/m^3 typically reported for mature reverse osmosis systems operating under similar conditions. Additionally, limited membrane lifetimes and modular integration constraints further elevate capital and maintenance costs, highlighting scalability as a persistent barrier to commercial competitiveness [26]. With the intensifying global water crisis, MCDI is increasingly recognized as a viable and sustainable solution for low-salinity desalination, resource recovery, and decentralized water treatment applications.
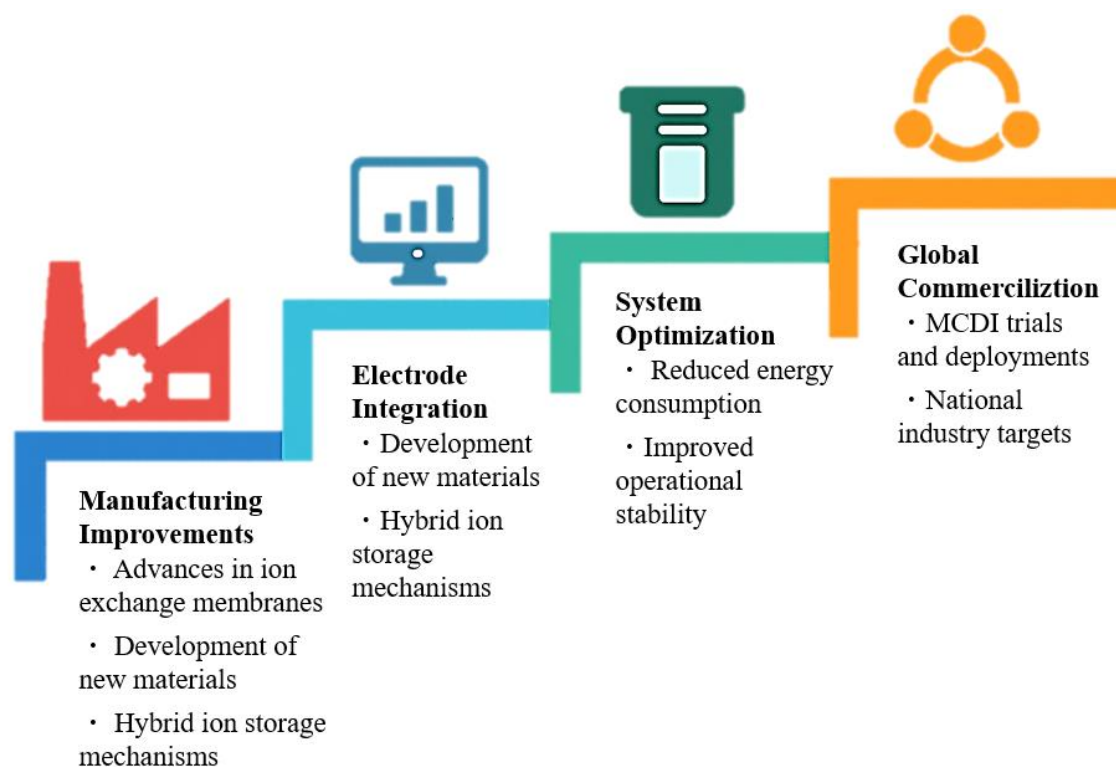
Figure 3. Technological evolution and commercialization pathway of MCDI.

4. Patent Analysis

This study primarily analyzes patents on the application of ion exchange membranes in capacitive deionization systems. The patent analysis was conducted using Innography, a patent analytics tool provided by Clarivate. Using the keywords 'Ion Exchange Membranes' and 'Capacitive Deionization,' approximately 500 active patents under protection have been identified, covering the period from 2002 to 2024. Notably, 78% of these patents were filed between 2015 and 2024, reflecting a significant increase in interest in applying ion exchange MCDI. Figure 4b,c present the distribution of these patents among various countries and institutions. The United States holds the largest share, comprising 32.70% of the total patents, followed by China (29.83%), South Korea (26.49%), EPO (5.97%), and India (5.01%). In terms of institutional distributions, the top five institutions ranked by the number of patents are Kraton Corporation (Houston, TX, USA) and Xylem Inc. (Washington, DC, USA) in the United States, Fujifilm Holding Corp. (Tokyo, Japan), Clariant AG (Muttenz, Switzerland), and Korea Institute of Energy Research (Daejeon, Republic of Korea). The number of patents held by these top five

institutions accounts for about 43% of the total patents. This study conducted a detailed analysis of its active patents utilizing patent hotspots. The results reveal that these patents can be categorized into five primary technical areas including deionization, desalination, exchange membrane, ion exchange, and water treatment. These five topics are deemed critical technological factors for the potential commercialization of MCDI systems in the future.

The United States utility patent US11261109B2, owned by Deutsches Wollforschungsinstitut (Aachen, Germany), was filed on 15 January 2016, granted on 1 March 2022, and is set to expire on 10 January 2037. This patent addresses critical limitations of conventional CDI, including low electrode regeneration efficiency and challenges in achieving continuous operation. It introduces a groundbreaking flow electrode capacitive deionization (FCDI) technique with a single-module continuous desalination system, thereby revolutionizing the fields of seawater desalination and ion separation. The FCDI system employs flow electrodes composed of activated carbon, graphene, and carbon nanotubes (CNTs), enabling dynamic ion adsorption and desorption. The ion-exchange membranes (IEMs) utilized in this technology range from 0.01 to 1 mm in thickness, with options for both anion-exchange membranes (AEMs) and cation-exchange membranes (CEMs). These components work in concert to optimize ion transport and separation efficiency. Notably, the patent demonstrates remarkable performance metrics: when treating a 1 g/L sodium chloride (NaCl) solution, the system achieves a desalination rate of 70% and a maximum water recovery rate of 80%. These results underscore the FCDI system's superior efficiency compared to traditional CDI methods. US11261109B2 facilitates applications in multiple sectors, including seawater desalination, industrial wastewater treatment for ion separation, recovery of valuable ions from process streams, and removal of contaminants such as nitrate and ammonium from potable water sources. By overcoming the limitations of conventional CDI, this patent paves the way for more sustainable and efficient water treatment solutions.
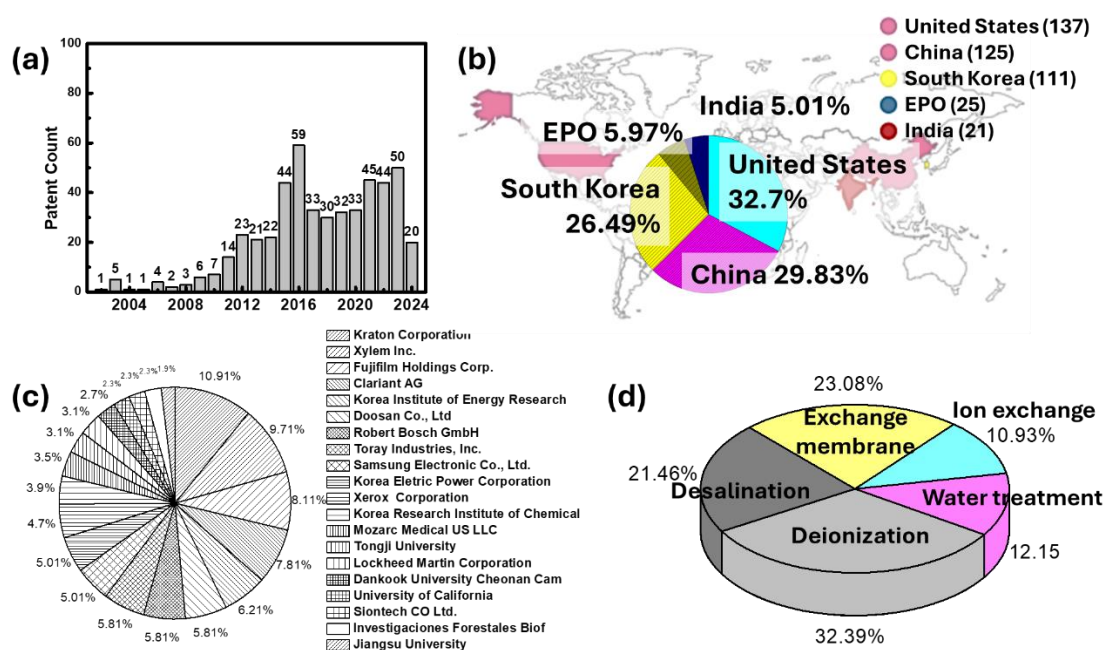

Figure 4. (**a**) Annual patent count from 2002 to 2024, (**b**) Global patent distribution and proportion, (**c**) Institutional distribution of patent ownership, (**d**) Distribution of patent topics.

Figure 5a presents the patent statistics in the United States, China, South Korea, and India from 2021 to 2024. Statistical results indicate that before 2023, the number of patents in various countries showed steady growth. Notably, in 2024, patent numbers across all countries experienced a significant decline, averaging a drop of more than 70%. This sharp decrease in patent filings may be related to the global focus on carbon reduction. Figure 5b presents the distribution of patent strength for MCDI between 2020 and 2024. Patent strength serves as a key metric for assessing the value and influence of patents, offering a thorough evaluation of their role in technological advancement, legal coverage, and market positioning. The assessment of patent strength typically incorporates factors like citation frequency, the breadth of the patent family, the number of claims, remaining patent lifespan, and the competitiveness of the relevant technical domain. Except for exchange membranes and water treatment, the patent strength of other topics has declined since 2023, likely due to the increasing focus on water resource

issues. Around 2022, desalination-related patents demonstrated particularly strong patent strength. Meanwhile, the patent strength of ion exchange technologies has remained below 5 since 2021, possibly due to the maturation of CDI technology.
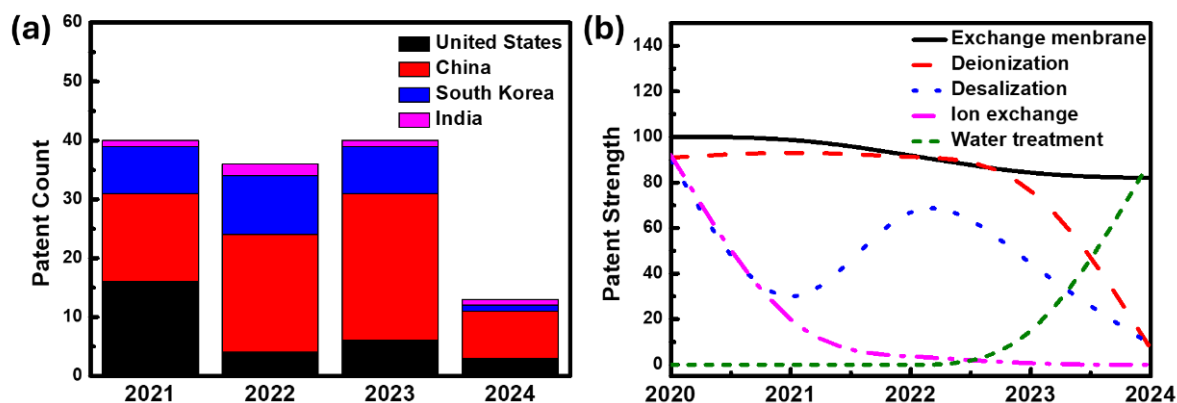

Figure 5. (**a**) Patent Statistics in the United States, China, South Korea, and India from 2021 to 2024, (**b**) Patent strength distribution of patent topics in the past five years.

Figure 6 illustrates the distribution of patents published, prioritized, and expired from 2001 to 2044. Statistical analysis indicates that the publication and priority year distributions of MCDI are quite similar. With respect to patent expiration, statistical data reveals that expired patents begin to emerge starting in 2025. Furthermore, projections indicate that approximately 51% of currently valid patents are expected to reach the end of their legal protection period between 2036 and 2042. The expiration of a patent marks the conclusion of its legally sanctioned exclusivity, whereby the patent holder's rights to restrict usage and commercialization cease to be enforceable. Typically, invention patents are granted a protection period of 20 years from the date of issuance, during which the patent holder retains the sole authority to regulate access, licensing, and implementation of the patented technology. Throughout this duration, third parties must obtain formal authorization to employ the innovation in any capacity. Upon expiration, the patented technology transitions into the public domain, permitting unrestricted utilization, modification, and further development by any entity, thereby fostering open innovation and technological dissemination. In order to conduct a more comprehensive analysis of the distribution of expired patents across various countries over the next four years, Figure 6b illustrates the distribution of expired patents in the United States, China, South Korea, and India from 2025 to 2029. Given the substantial patent holdings of the United States, it is expected that expiration will exhibit the highest volume of expired patents. In contrast, the number of expiration-related patents in China and South Korea is projected to peak around 2028, reflecting trends in technological development and intellectual property cycles within these jurisdictions.
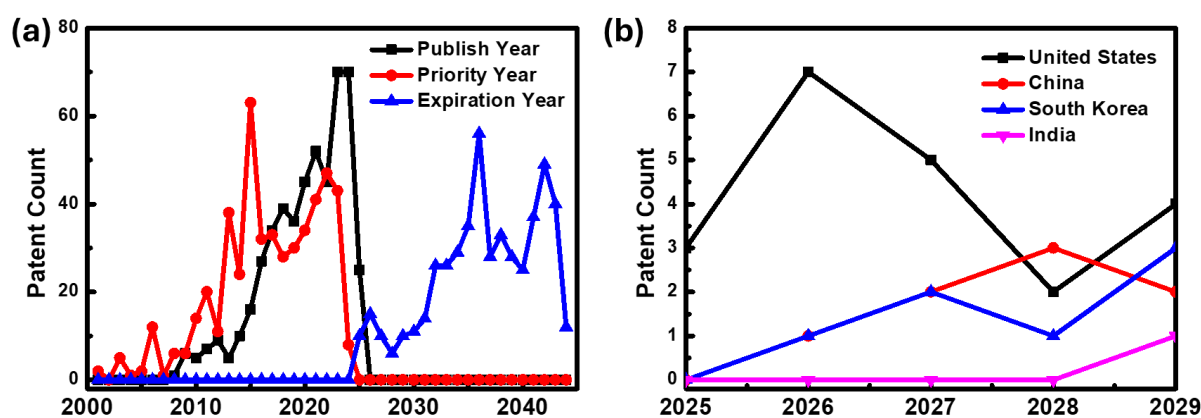

Figure 6. (**a**) Distribution of Patents Published, Prioritized, and Expired from 2001 to 2044, (**b**) Distribution of Expired Patents in the United States, China, South Korea, and India from 2025 to 2029.

5. Conclusions

The integration of IEMs has significantly improved the performance of CDI systems, particularly in applications such as brackish water treatment, ultrapure water production, and resource recovery. By advancing membrane materials, system architectures, and functional mechanisms, MCDI has emerged as a scalable and energy-efficient water treatment technology. Bibliometric and patent analyses over the past five years demonstrate a substantial global increase in research and patent activity related to MCDI. Notably, governmental funding from regions such as Europe, the United States, Japan, and South Korea, alongside industry-driven innovations, has accelerated the commercialization of this technology. Although challenges remain, including membrane fouling, limited-service life, and high production costs, recent advances in polymer chemistry, nanostructured membrane design, and hybrid charge storage have shown strong potential to address these issues. To further bridge the gap between laboratory advances and practical deployment, future research should prioritize integrative strategies. The application of AI can improve real-time system optimization, predictive maintenance, and adaptive control. At the same time, incorporating circular economy principles such as component reuse, energy recovery, and life-cycle-based system design can enhance both environmental and economic sustainability. Building upon these integrative strategies, continued collaboration between public institutions and private industry will be essential to drive real-world adoption of MCDI technologies. By fostering interdisciplinary research and strengthening international partnerships, the development and deployment of MCDI can be accelerated, enabling its broader application in decentralized water treatment and its long-term contribution to global water sustainability and environmental innovation.

References

1. Nandiyanto, A.B.D.; Al Husaeni, D.F. A bibliometric analysis of materials research in Indonesian journal using VOSviewer. *J. Eng. Res.* **2021**. https://doi.org/10.36909/jer.ASSEEE.16037.
2. Martins, J.; Gonçalves, R.; Branco, F. A bibliometric analysis and visualization of e-learning adoption using VOSviewer. *Univers. Access Inf. Soc.* **2024**, *23*, 1177–1191.
3. Lee, K.-T.; Cai, Y.-S.; Hou, Q.-Y.; et al. A Brief Overview of Green Hydrogen on Production, Regulations, and Commercialization. *Green Energy Fuel Res.* **2024**, *1*, 3–12.
4. Jiang, S.; Sun, H.; Wang, H.; et al. A comprehensive review on the synthesis and applications of ion exchange membranes. *Chemosphere* **2021**, *282*, 130817.
5. Alkhadra, M.A.; Su, X.; Suss, M.E.; et al. Electrochemical methods for water purification, ion separations, and energy conversion. *Chem. Rev.* **2022**, *122*, 13547–13635.
6. Zhang, Y.; Yu, X.; Liu, G.; et al. Tailored Porous Ion Exchange Membrane for Separation of Charged Organic Compound. Available online: https://ssrn.com/abstract=5147562 (accessed on 16 April 2025).
7. Zhang, S.; Tanioka, A.; Matsumoto, H. De novo ion-exchange membranes based on nanofibers. *Membranes* **2021**, *11*, 652.
8. Qian, H.; Xu, G.; Yang, S.; et al. Advancing lithium–magnesium separation: Pioneering swelling-embedded cation exchange membranes based on sulfonated poly (ether ether ketone). *ACS Appl. Mater. Interfaces* **2024**, *16*, 18019–18029.
9. Li, X.; Chen, G.; Zhao, Y.; et al. Sulfonated polyphenylene oxide-based artificial lung membrane with prominent selectivity of CO_2. *Sep. Purif. Technol.* **2025**, *358*, 130419.

10. Han, S.-Y.; Yu, D.M.; Mo, Y.-H.; et al. Ion exchange capacity controlled biphenol-based sulfonated poly (arylene ether sulfone) for polymer electrolyte membrane water electrolyzers: Comparison of random and multi-block copolymers. *J. Membr. Sci.* **2021**, *634*, 119370.

11. Tellez-Cruz, M.M.; Escorihuela, J.; Solorza-Feria, O.; et al. Proton exchange membrane fuel cells (PEMFCs): Advances and challenges. *Polymers* **2021**, *13*, 3064.

12. Lv, S.; Li, X.; Lu, M.; et al. Recent advances in non-perfluorinated sulfonic acid proton exchange membranes in the energy field. *J. Mater. Chem. A* **2024**, *12*, 9345–9370.

13. Porada, S.; Zhao, R.; van der Wal, A.; et al. Review on the science and technology of water desalination by capacitive deionization. *Prog. Mater. Sci.* **2013**, *58*, 1388–1442.

14. Luo, J.; Li, M.; Heng, Y. Bio-inspired design of next-generation ultrapermeable membrane systems. *NPJ Clean Water* **2024**, *7*, 4.

15. Bernardes, A.F.; Meng, Z.; Campos, L.C.; et al. Bio-inspired anti-fouling strategies for membrane-based separations. *Chem. Commun.* **2025**, *61*, 5064–5071.

16. Giacalone, F.; Catrini, P.; Gurreri, L.; et al. Exergy analysis of electrodialysis for water desalination: Influence of irreversibility sources. *Energy Convers. Manag.* **2022**, *258*, 115314.

17. Butylskii, D.Y.; Dammak, L.; Larchet, C.; et al. Selective recovery and re-utilization of lithium: Prospects for the use of membrane methods. *Russ. Chem. Rev* **2023**, *92*, 5074.

18. Mei, Y.; Liu, L.; Lu, Y.-C.; et al. Reverse electrodialysis chemical cell for energy harvesting from controlled acid–base neutralization. *Environ. Sci. Technol.* **2019**, *53*, 4640–4647.

19. Mubita, T.; Porada, S.; Biesheuvel, P.; et al. Strategies to increase ion selectivity in electrodialysis. *Sep. Purif. Technol.* **2022**, *292*, 120944.

20. Honarparvar, S.; Reible, D. Modeling multicomponent ion transport to investigate selective ion removal in electrodialysis. *Environ. Sci. Ecotechnol.* **2020**, *1*, 100007.

21. Wang, C.; Park, M.J.; Yu, H.; et al. Recent advances of nanocomposite membranes using layer-by-layer assembly. *J. Membr. Sci.* **2022**, *661*, 120926.

22. Lipton, J.; Weng, G.-M.; Röhr, J.A.; et al. Layer-by-layer assembly of two-dimensional materials: Meticulous control on the nanoscale. *Matter* **2020**, *2*, 1148–1165.

23. Schneider, R.; Facure, M.H.; Chagas, P.A.; et al. Tailoring the surface properties of micro/nanofibers using 0d, 1d, 2d, and 3d nanostructures: A review on post-modification methods. *Adv. Mater. Interfaces* **2021**, *8*, 2100430.

24. Yan, L.; Yang, X.; Zeng, H.; et al. Nanocomposite hydrogel engineered hierarchical membranes for efficient oil/water separation and heavy metal removal. *J. Membr. Sci.* **2023**, *668*, 121243.

25. Yang, L.; Xiao, H.; Qian, Y.; et al. Bioinspired hierarchical porous membrane for efficient uranium extraction from seawater. *Nat. Sustain.* **2022**, *5*, 71–80.

26. Reimonn, G.; Kamcev, J. Techno-economic perspective on the limitations and prospects of ion-exchange membrane technologies. *Curr. Opin. Chem. Eng.* **2025**, *47*, 101077.

27. Xu, F.; Yuan, L.; Zhao, R.; et al. Selective Ion Separation by Capacitive Deionization: A Comprehensive Review. *Materials* **2025**, *18*, 1107.

28. Schertzer, W.; Shukla, S.; Sose, A.; et al. AI-driven design of fluorine-free polymers for sustainable and high-performance anion exchange membranes. *J. Mater. Inform.* **2025**, *5*, 5.

29. Chang, W.-T.; Chen, P.-A.; Peng, C.-Y.; et al. Capacitive deionization and disinfection of saltwater using nanostructured (Cu–Ag)@ C/rGO composite electrodes. *Environ. Sci. Water Res. Technol.* **2023**, *9*, 883–889.

30. Chen, P.-A.; Liu, S.-H.; Wang, H.P. Pseudocapacitive Deionization of Saltwater by Mn_3O_4@ C/Activated Carbon. *ACS Omega* **2023**, *8*, 13315–13322.

31. Xiao, Q.; Ma, J.; Xu, L.; et al. Membrane capacitive deionization (MCDI) for selective ion separation and recovery: Fundamentals, challenges, and opportunities. *J. Membr. Sci.* **2024**, *699*, 122650.

32. Wang, H.; Liu, Y.; Li, Y.; et al. Tactics for boosting the desalination stability of capacitive deionization. *Chem. Eng. J.* **2024**, 153808.

33. Elewa, M.M.; El Batouti, M.; Al-Harby, N.F. A comparison of capacitive deionization and membrane capacitive deionization using novel fabricated ion exchange membranes. *Materials* **2023**, *16*, 4872.

34. Gamaethiralalage, J.; Singh, K.; Sahin, S.; et al. Recent advances in ion selectivity with capacitive deionization. *Energy Environ. Sci.* **2021**, *14*, 1095–1120.

35. Shu, G.; Song, Z.; Wang, W.; et al. Review of emerging multiple ion-exchange membrane electrochemical systems for effective energy conversion and storage. *Sustain. Energy Technol. Assess.* **2024**, *70*, 103926.

36. Volfkovich, Y.M. The Effect of Structure of Porous Components of Electrochemical Devices on Their Characteristics (A Review). *Russ. J. Electrochem.* **2023**, *59*, 347–418.

37. Salmeron-Sanchez, I.; Asenjo-Pascual, J.; Avilés-Moreno, J.R.; et al. Microstructural description of ion exchange

membranes: The effect of PPy-based modification. *J. Membr. Sci.* **2022**, *659*, 120771.

38. Yu, H.; Hossain, S.M.; Wang, C.; et al. Selective lithium extraction from diluted binary solutions using metal-organic frameworks (MOF)-based membrane capacitive deionization (MCDI). *Desalination* **2023**, *556*, 116569.

39. Tsai, S.-W.; Hackl, L.; Kumar, A.; et al. Exploring the electrosorption selectivity of nitrate over chloride in capacitive deionization (CDI) and membrane capacitive deionization (MCDI). *Desalination* **2021**, *497*, 114764.

40. Asadipour, E.; Ramani, V. Morphology Control of Immiscible Polymer-Blended Anion-Exchange Membranes. *ACS Appl. Energy Mater.* **2025**, *8*, 4681–4687.

41. Hager, L.; Hegelheimer, M.; Stonawski, J.; et al. Novel side chain functionalized polystyrene/O-PBI blends with high alkaline stability for anion exchange membrane water electrolysis (AEMWE). *J. Mater. Chem. A* **2023**, *11*, 22347–22359.

42. Nagar, A.; Islam, M.R.; Pradeep, T. New technologies for drinking water. *Technol. Solut. Water Sustain. Chall. Prospect.* **2023**, 123. https://doi.org/10.2166/9781789063714_0123.

43. Mohammed, N.; Lian, H.; Islam, M.S.; et al. Selective adsorption and separation of organic dyes using functionalized cellulose nanocrystals. *Chem. Eng. J.* **2021**, *417*, 129237.

44. Chae, S.H.; Hong, S.W.; Son, M. Metadata and feature importance analyses of membrane capacitive deionization models: Is a water treatment artificial intelligence panacea possible? *Desalination* **2024**, *585*, 117784.

45. Rashid, R.; Shafiq, I.; Akhter, P.; et al. A state-of-the-art review on wastewater treatment techniques: The effectiveness of adsorption method. *Environ. Sci. Pollut. Res.* **2021**, *28*, 9050–9066.

46. Muddemann, T.; Haupt, D.; Sievers, M.; et al. Electrochemical reactors for wastewater treatment. *ChemBioEng Rev.* **2019**, *6*, 142–156.

47. Lee, K.-T.; Ho, K.-Y.; Chen, W.-H.; et al. Construction and demolition waste as a high-efficiency advanced process for organic pollutant degradation in Fenton-like reaction to approach circular economy. *Environ. Pollut.* **2023**, *335*, 122246.

48. Lee, K.-T.; Chuah, X.-F.; Cheng, Y.-C.; et al. Pt coupled $ZnFe_2O_4$ nanocrystals as a breakthrough photocatalyst for Fenton-like processes–photodegradation treatments from hours to seconds. *J. Mater. Chem. A* **2015**, *3*, 18578–18585.

49. Narayanan, C.; Narayan, V. Biological wastewater treatment and bioreactor design: A review. *Sustain. Environ. Res.* **2019**, *29*, 1–17.

50. UN-Water. *Water Scarcity*; United Nations: New York City, NY, USA, 2021.

51. Khatoon, U.T.; Velidandi, A. An Overview on the Role of Government Initiatives in Nanotechnology Innovation for Sustainable Economic Development and Research Progress. *Sustainability* **2025**, *17*, 1250.

52. Suss, M.E.; Porada, S.; Sun, X.; et al. Water desalination via capacitive deionization: What is it and what can we expect from it? *Energy Environ. Sci.* **2015**, *8*, 2296–2319.

53. Hassanvand, A.; Wei, K.; Talebi, S.; et al. The role of ion exchange membranes in membrane capacitive deionisation. *Membranes* **2017**, *7*, 54.

54. Pawlowski, S.; Huertas, R.M.; Galinha, C.F.; et al. On operation of reverse electrodialysis (RED) and membrane capacitive deionisation (MCDI) with natural saline streams: A critical review. *Desalination* **2020**, *476*, 114183.

55. Zhao, R.; Biesheuvel, P.; Van der Wal, A. Energy consumption and constant current operation in membrane capacitive deionization. *Energy Environ. Sci.* **2012**, *5*, 9520–9527.

56. State, P. Electricity-Driven Water Purification Method May Extend to Saltier Waters. 2022. Available online: https://www.eurekalert.org/news-releases/964214?utm_source=chatgpt.com (accessed on 24 April 2025).

57. McNair, R.; Szekely, G.; Dryfe, R.A. Ion-exchange materials for membrane capacitive deionization. *ACS EST Water* **2020**, *1*, 217–239.

58. Jeon, S.-i.; Kim, N.; Jo, K.; et al. Improvement in the desalination performance of membrane capacitive deionization with a bipolar electrode via an energy recovery process. *Chem. Eng. J.* **2022**, *439*, 135603.

59. Kim, J.; Hong, S. Pilot study of emerging low-energy seawater reverse osmosis desalination technologies for high-salinity, high-temperature, and high-turbidity seawater. *Desalination* **2023**, *565*, 116871.

60. Kim, H.; Kim, S.; Lee, B.; et al. Emerging frontiers in multichannel membrane capacitive deionization: Recent advances and future prospects. *Langmuir* **2024**, *40*, 4567–4578.

Scilight

Article

Analysis of Thermal Properties in Co-Gasification of Municipal Solid Waste and Woody Biomass

Crossline Ajona [1,2] and Ayyadurai Saravanakumar [1,*]

[1] Centre for Research in Environment, Sustainability Advocacy and Climate Change, Directorate of Research and Virtual Education, SRM Institute of Science and Technology, Chengalpattu District, Kattankulathur 603203, Tamil Nadu, India

[2] Department of Chemistry, SRM Institute of Science and Technology, Chengalpattu District, Kattankulathur 603203, Tamil Nadu, India

* Correspondence: sara_mnes@yahoo.co.in or saravana7@rmist.edu.in

Abstract: Modern downdraft gasifiers used commercially are predominantly tailored for efficiently converting woody biomass, such as wood chips. However, substantial value also lies in the utilization of wood residues and Municipal Solid Waste (MSW), which are often underexploited. For gasifiers to serve a wider range of applications effectively, they must be capable of handling diverse waste inputs and adjusting their operation in real-time to suit varying material characteristics. This study centers on the advancement of a tar-free gasification system capable of processing MSW with high flexibility. The investigation outlines the systematic approach taken in designing, developing, and assessing the performance of this innovative gasifier. The core focus of the technology is to convert MSW into usable thermal energy through gasification. The prototype developed in this work features a square-shaped stratified fixed-bed downdraft gasifier, engineered to process up to 10 kg of feedstock per hour. It accommodates both pelletized and non-pelletized forms of MSW, offering versatility in input types. During experimental trials, the highest volume of producer gas 38 m^3/h. was recorded in the third trial phase, which utilized a balanced mixture of wood and MSW in equal proportions. This setup also yielded the highest calorific value of gas, calculated at 1250 kcal/Nm^3. By integrating advanced thermal flare systems that efficiently combust the produced gas, the developed gasifier significantly reduces thermal energy production costs. Furthermore, analyses of the mass and energy distribution confirmed an efficient and consistent relationship between the fuel input and the energy output, validating the system's operational effectiveness.

Keywords: municipal solid waste; woody biomass; down draft gasification

1. Introduction

The rapid growth in the consumption of goods and materials has led to a significant rise in municipal solid waste (MSW), posing a serious challenge to environmental protection and quality of life. MSW consists of a wide variety of discarded items, including metals, paper products, textiles, plastics, wood, and organic kitchen waste [1,2]. Municipal solid waste (MSW) management in India focuses not only on minimizing waste generation but also on ensuring effective treatment and maximizing recycling efforts. Oversight and regulation of waste management are primarily handled by various government bodies, including the Ministry of Environment, Forest and Climate Change (MoEFCC), the Ministry of Housing and Urban Affairs (formerly MoUD), the Central Pollution Control Board (CPCB), the National Environmental Engineering Research Institute (NEERI), and the respective State Pollution Control Boards (SPCBs). At the local level, the responsibility for on-ground implementation lies with Urban Local Bodies (ULBs). However, numerous studies have highlighted that ULBs often struggle to effectively enforce and manage MSW policies. Creating a robust and efficient MSW management framework requires aligning objectives with stakeholders' needs and expectations. The Government of India continues to support and encourage ULBs in enforcing regulations and applying relevant policies at the grassroots level. As of now, the revised Municipal Solid Waste (Management and Handling) Rules, 2015, are in the process of being finalized by the MoEFCC. According to the 2014 report by the Planning Commission of India, urban areas are home to approximately 377 million people, collectively generating around 62 million tonnes of MSW annually [3,4]. Urban centers are expected to produce about 165 million tonnes (MT) of municipal solid waste (MSW) yearly by 2031, rising by another 436 MT by 2050. By 2031 alone, this increasing garbage will need almost 23.5×10^7 m^3 of

landfill space, equivalent to 1175 hectares of land every year. Assuming a landfill height of 20 m, the total land required for disposal between 2031 and 2050 is projected to be 43,000 hectares if this trend continues. These estimates are predicted on a 0.45 kg/day per capita garbage production. Gasification technology stands out among the most effective and clean ways to solve the growing waste problem in an environmentally responsible way. A thermochemical process called gasification turns solid waste into syngas at high temperatures, usually about 600 °C, producing up to 1000 kWh of power from one tonne of MSW. The precise choice of operating temperature in a thermochemical conversion process depends on several critical factors, including the type of reactor used, the characteristics of the waste material, and the thermal behavior of the resulting ash. Different reactor configurations such as fixed-bed, fluidized-bed, and entrained-flow systems have distinct heat transfer patterns, residence time profiles, and flow dynamics, all of which affect the required temperature for efficient operation [5]. The nature of the waste, including moisture content, ash content, and proportions of cellulose, hemicellulose, and lignin, influences how the material responds to heat and the extent of volatile release during decomposition [6]. Feedstocks with high moisture require more energy input, which may reduce effective reaction temperatures, while high lignin or ash content may alter decomposition behavior [7]. The ash softening and melting points hold particular importance, as operation above these temperatures can cause slag formation, bed agglomeration, or equipment fouling [8]. Maintaining the operating temperature below the ash deformation point remains essential to ensure process stability and equipment longevity [9]. These factors together define a safe and optimal temperature range that balances reaction efficiency, syngas quality, and operational reliability. Solid waste gasification comprises several sequential phases combining endothermic and exothermic reactions [10,11].

Beginning at temperatures up to 160 °C, heating and drying combine physical and chemical processes. Drying is a complex process characterized by moisture evaporation. Releasing a major amount of volatile chemicals from carbonaceous fuel, pyrolysis is a vital and limiting stage. As schematically illustrated in Figure 1, the volatile compounds released during pyrolysis significantly contribute to the composition of the product gas in the subsequent gasification process. These volatiles create an environment rich in fuel gases that are readily ignitable around solid waste. The chemical makeup and structural properties of the waste primarily influence the nature, quantity, and characteristics of the chemical species generated during pyrolysis [12]. Additionally, factors such as temperature, pressure, the surrounding atmosphere, the composition of the waste, and the heating rate imposed by the specific reactor design play crucial roles in determining the outcomes of the pyrolysis process [13]. Because devolatilization releases a large variety of chemical components, it is essential to keep in mind that many of these components require hydrogen to form molecular bonds. Consequently, the process of devolatilization results in the depletion of hydrogen from the carbonaceous matrix that was present in the waste in the initial stages.
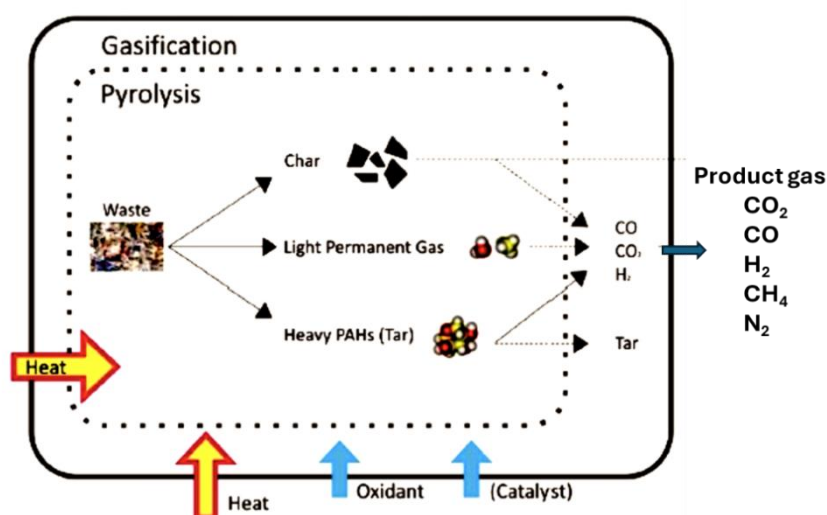

Figure 1. Schematic representation of Municipal Solid Waste to pyrolysis and gasification stages.

Numerous studies and performance evaluations have demonstrated that thermochemical conversion technologies play a vital role in integrated municipal solid waste (MSW) management systems [14–17]. These technologies form the backbone of many successful waste management operations implemented globally. Waste-to-energy (WtE) systems based on gasification can function as standalone solutions or be incorporated into integrated or modular frameworks that combine pyrolysis, gasification, and combustion processes [18]. These

systems are often categorized into three principal components: producer gas generation, producer gas usage, and gas purification. The producer gas generation section ascertains the kind and composition of syngas produced, contingent upon the properties of the solid waste and the gasification process employed. The producer gas usage section examines the appropriateness of syngas for various energy conversion devices—such as steam turbines, gas engines, or gas turbines—affected by characteristics including syngas temperature, heating value, and purity. This transitions to the third section, gas cleaning, which guarantees the elimination of contaminants such tar, dust, alkali metals, and other inorganic impurities to satisfy the operating standards of energy conversion apparatus. Over the past two decades, a wide range of gasification technologies have been developed [19–21]. Operating at lower equivalence ratios often results in incomplete char conversion and higher tar formation.

Although higher equivalence ratio (ER) values promote the oxidation of a portion of the syngas, which reduces its calorific value, they may also result in partial combustion within the downstream combustion chamber [22–25]. The most important differences among gasification technologies are determined by several fundamental factors, including the method of heat supply, whether it is direct or indirect; the operating pressure, where above-atmospheric pressure allows for increased throughput, higher hydrogen production, and smaller gas clean-up systems; and the operating temperature range, which influences the characteristics of bottom ash, often producing molten or vitreous slag that is easier to handle and dispose of. Even though high-pressure systems have performance advantages, they need much greater investment and operational expenses, which can make them unfeasible for waste-to-energy (WtE) applications. The feed mechanism, which is normally positioned at the top and moved by gravity, air flow, or mechanical methods, and the selection of the oxidant (air, oxygen, or oxygen-enriched air) are two more distinctions. Steam is primarily utilized for the gasification of coal or biomass. Through the utilization of the thermal gasifier designs, most of the technologies that are currently available for commercial use are designed to generate both heat and electricity from syngas. A small number of them, mainly in Japan, are equipped with a 'power gasifier' configuration or are specifically designed for the manufacturing of chemicals, most notably ammonia [26,27]. This study evaluates the feasibility of gasification as an environmentally sustainable method for managing municipal solid waste (MSW) by co-gasifying MSW with woody biomass in varying proportions, with a fixed air flow rate used as the primary performance measure. The energy efficiency of gasification shows clear differences between municipal solid waste (MSW) and woody biomass due to the composition and properties of the feedstocks. MSW contains a mixture of organic and inorganic materials, which causes variability in gas composition, higher moisture levels, and contaminants that reduce gasification efficiency. In contrast, woody biomass offers more uniform composition, with consistent cellulose, hemicellulose, and lignin content, resulting in cleaner syngas with higher hydrogen and carbon monoxide levels and energy efficiencies between 65 and 75%. MSW gasifiers, although effective at reducing waste volume and managing environmental concerns, often provide lower energy efficiencies, around 50 to 65%, due to feedstock variability and issues such as increased tar formation. Co-gasification of MSW with woody biomass provides a promising method to improve gas quality and energy recovery by balancing the feedstock properties. The biomass component stabilizes gasification reactions, reduces tar content, and increases the calorific value of syngas. This study uniquely evaluates co-gasification performance with varying proportions of MSW and woody biomass under a fixed air flow rate, focusing on how different ratios affect tar reduction, hydrogen and carbon monoxide yields, and thermal stability in a single reactor design. The co-gasification process achieves an energy efficiency near 85%, which surpasses that of individual feedstock gasification and demonstrates enhanced conversion performance.

The novelty of this work lies in the systematic analysis of co-gasification under controlled operational parameters that balance feedstock heterogeneity, revealing optimal conditions for maximum energy recovery and gas quality. By addressing parameters such as temperature control and ash behavior, this study provides essential insights to optimize gasification for heterogeneous feedstocks. The results show that co-gasification improves energy efficiency and syngas quality, offering a sustainable and scalable solution for urban waste management. This research significantly contributes to the advancement of integrated waste-to-energy technologies, supporting environmental protection and circular economic goals.

Notably, this study proposes a technically and economically feasible MSW gasifier model optimized for urban implementation, particularly suited for large metropolitan areas such as Delhi and Chennai, each spanning over 750 km². These cities generate substantial MSW volumes, and deploying gasification units could significantly improve waste management and generate clean energy on a large scale. The design leverages the co-gasification of MSW with readily available woody biomass, such as construction timber and horticultural debris, which are abundant in regions of Tamil Nadu, especially in the northern and southern districts. These materials are collected through local waste collection networks serving construction and landscaping activities.

In industrial zones such as the northern and western districts of Hyderabad, factories and institutional kitchens generate substantial quantities of food waste, which can serve as an additional feedstock for localized gasification

plants. The produced syngas can be utilized for thermal or electrical energy generation to power on-site operations, while the char/ash residue can be repurposed in nearby cement plants, thereby closing the loop in a circular economy model. This integrated approach demonstrates the viability of gasification as a practical, scalable, and environmentally sustainable solution for urban MSW management in India.

2. Materials and Methods

2.1. Pre-Treatment and Sorting Processes for Municipal Solid Waste (MSW)

The collection of municipal solid waste (MSW) took place across several districts in the Indian state of Tamil Nadu. A variety of inorganic materials, including paper, cardboard, plastics, textiles, rubber, leather, and wood, are commonly found in landfill waste. To determine the typical composition of the initial waste samples, these materials were sorted into four distinct categories. Type A includes paper and cardboard, which are often recyclable. Type B consists of plastics, a challenging material to manage due to its variety and resistance to biodegradation. Type C is made up of textile and rubber waste, both of which require specialized recycling processes. Finally, Type D contains wood waste and other inorganic elements, such as metals, which can be recycled or repurposed for different uses. This classification helps provide a clearer understanding of the waste composition and informs better waste management strategies. Since plastics typically surpassed the maximum permissible size of 4 cm for gasification and frequently created clogs in both the feeding system and the gasifier, they were completely removed from the feedstock. The remaining categories were each sampled at a weight of 75–80 kg and then sun-dried for a period of twenty-four hours before being gasified. The moisture level and dry mass of the material were determined by calculating the weight difference between the initial and final weights resulting from a fourteen-day drying interval.

2.2. Proximate and Ultimate Analysis

The feedstock used in this study was a combination of tamarind wood chips and municipal solid waste (MSW), both sourced and processed to meet the requirements for gasification experiments. The tamarind wood chips were specifically obtained from Tamil Nadu, India, a region known for its diverse agricultural practices, and they were selected for their suitability as a biomass source. The chips were measured to have an average size of approximately 10 cm in length and 6 cm in diameter, indicating a typical woody biomass structure that would be compatible with the gasification process. In addition to the wood chips, the feedstock included MSW, which was characterized by a more variable composition and particle size. The MSW was pre-processed to achieve a particle size range between 0.6 cm and 4 cm, ensuring that the material would be appropriately sized for the gasifier's operation. The particle size of MSW is important because it affects the material's residence time in the reactor, its exposure to heat and air, and consequently its overall conversion efficiency during the thermochemical processes of drying, pyrolysis, and gasification. By using both tamarind wood chips and MSW, the study aimed to explore the potential for co-gasification, where biomass and waste materials are converted into valuable energy products such as syngas. The combination of wood and MSW in different proportions offers a unique opportunity to evaluate the effects of different feedstock compositions on the performance of the gasification process, particularly in terms of gas composition, tar production, and overall system efficiency. Given the high initial moisture content of the MSW, which ranged from 60% to 70%, the material underwent pre-drying to reduce its moisture content to the maximum allowable limit of 35%. This moisture reduction was necessary to ensure stable operation in the transient-state gasifier, as described in Section 2.3. To determine the proximate composition of the feedstock, including moisture, volatile matter, fixed carbon, and ash content, a thermogravimetric analysis (TGA) was conducted using a thermal analyzer. The results of the proximate and ultimate analysis for the MSW feedstock are provided in Table 1.

Table 1. Proximate and ultimate analysis of MSW.

Proximate Analysis		Ultimate Analysis	
Moisture	5.33%	Moisture	5.33%
Volatile Matter	86.75%	Carbon	57.45%
Ash	3.10%	Hydrogen	7.70%
Fixed Carbon	4.82%	Oxygen	24.96%

2.3. Downdraft Gasifier Design

The downdraft gasifier used in this study has a rectangular configuration and operates with a mixture of municipal solid waste (MSW) and woody biomass. This arrangement is recognized for generating less tar while effectively enabling ash removal. As the feedstock moves downward through the gasifier, moisture is eliminated in the drying zone prior to entering the pyrolysis zone, where it undergoes thermochemical decomposition into char, tars, and gases. Certain unconverted substances experience combustion. In the next oxidation zone, tars undergo thermal cracking at high temperatures and oxidation, yielding comparatively clean product gas. This gasifier necessitates feedstock preconditioning to lower moisture content to acceptable levels. The system is designed to handle materials with high bulk density, meaning it can efficiently process dense, compact materials. It operates in a stratified downdraft mode, where the materials are subjected to a downward flow of gases. This mode allows heavier particles to settle at the bottom, while lighter particles are carried upwards, facilitating more efficient processing. Operating just above atmospheric pressure improves the system's efficiency by enhancing the conversion process. This configuration makes it particularly suitable for applications like thermal flare burners, which are used to burn off excess gases in various industrial operations. The system's design ensures stable and effective operation, even with materials that have a high density. Figure 2 depicts the design and operation of the system. The gasification zone is sustained at temperatures of 1200 °C or above to guarantee effective tar reduction. This gasifier design is appropriate for fuels with elevated bulk densities, such as wood and municipal solid waste (MSW), which in this investigation exhibited bulk densities of around 1000 kg/m^3 and 800 kg/m^3, respectively.
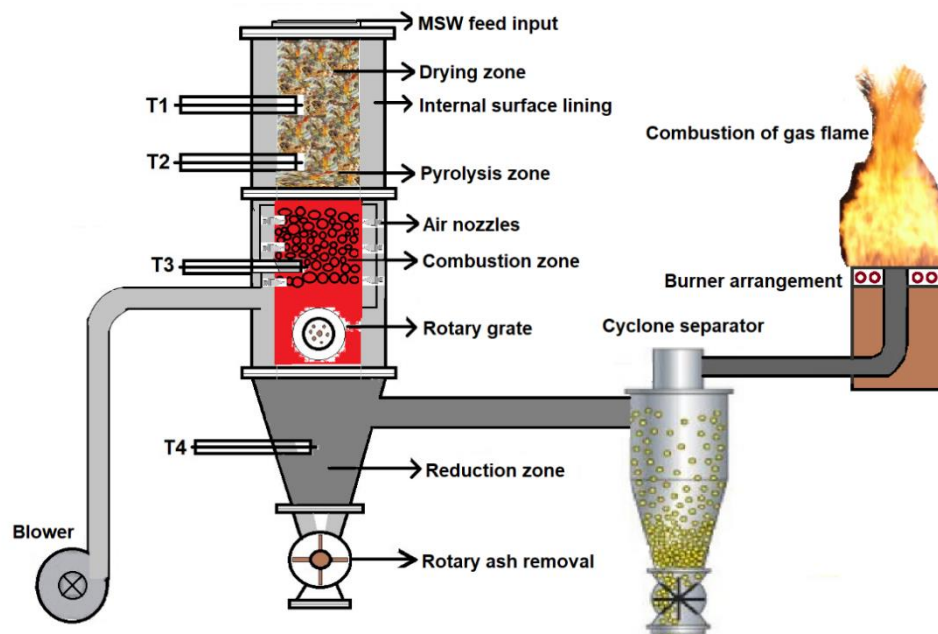

Figure 2. Schematic diagram of MSW stratified down draft gasifier.

The gasifier runs at sub-atmospheric pressure, specifically below 30 cm of the water column. The spinning grate mechanism and the centrally located air nozzle duct are two key design elements that help it run efficiently. The strategic design of these components maximizes the efficiency of the gasification process. The rotary grate is designed to reduce char ash formation, thus immediately enhancing overall gasification efficiency. The entire system is also well insulated, minimizing heat loss and enhancing performance, thus maximizing thermal efficiency. Particularly for the purpose of converting solid waste, the architecture is tuned to be able to tolerate reactions that take place within the gasification zone at extremely high temperatures. A comprehensive set of technical calculations serves as the foundation for this design technique. Figure 3 depicts a pilot-scale model of Yes the gasifier, which demonstrates the features of the producer gas flame at two different periods of operation: the first hour of operation and the eighth hour of operation.

Preliminary phase at the first hour   Final phase at the eighth hour

Figure 3. Producer gas flame from MSW gasification utilized at various operational stages.

2.4. Synergistic Gasification of Woody Biomass and Municipal Solid Waste

The feedstock was categorized into five distinct groups based on the weight proportions of wood waste and municipal solid waste (MSW) to examine their impact on the gasification process. These categories included 100% wood waste, a 75% wood waste and 25% MSW mixture, a 50:50 mix of wood waste and MSW, a 25% wood waste and 75% MSW mixture, and 100% MSW. The feedstock for each group was introduced into the gasifier at a consistent input rate of 9 kg/h, ensuring uniformity across all experimental runs. This method allowed for the systematic evaluation of how different ratios of wood waste and MSW affected key parameters such as gas quality, tar formation, and gas flow rate, providing insights into the potential for optimizing feedstock composition in the gasification process. To initiate the process, the reactor initially operated in suction mode to preheat the charcoal bed, facilitating ignition. Once stable combustion was achieved, the system switched to pressure mode for sustained operation. Within the reactor, the feedstock underwent sequential thermochemical transformations, drying, pyrolysis, gasification, and reduction each occurring in dedicated zones. The average residence time for each type of feedstock in the reactor was approximately one hour. Eight Type K thermocouples spread around the reactor bed captured temperature data. An orifice meter combined with a differential manometer was used to track air and gas flow rates. Averaged over five experimental runs, the data were shown in Table 2. This operational approach is especially appropriate for poorer nations, where labor costs are low and batch processes are financially feasible. Trial 3 demonstrated superior performance among the examined combinations, exhibiting elevated internal gasifier temperatures relative to the other trials, as elaborated in the subsequent sections.

Table 2. Operation parameters of the MSW down draft gasifier system.

Sl. No.	Particulars	Total Average Values						
		Total Operating Hours	Gasifier Zone Temperature °C				Air Flow Rate m³/h	Gas Flow Rate m³/h
			Combustion T 4	Reduction T 3	Pyrolysis T 2	Drying T 1		
1	Run 1 100% Wood	8:18	871.95	744.53	641.8	514.26	15	35
2	Run 2 75% Wood + 25% MSW	8:32	847.05	723.64	563.4	463.28	15	33
3	Run 3 50% Wood + 50%MSW	8:16	883.57	757.1	659.14	558.88	15	38
4	Run 4 25% Wood + 75%MSW	8:29	724.79	657.10	486.26	439.28	15	30
5	Run5 100% MSW	8:19	717.11	601.79	397.6	331.94	15	25

3. Mass and Energy Balance of MSW and Wood Waste

The mass balance of the entire system was determined by utilizing a constant air flow rate of 15 cubic meters per hour throughout the evaluation process. During the course of the experiment that lasted for 8.16 h, a total of

30 kg of municipal solid trash and wood waste were processed. Taking into consideration the amount of ash that is present in the municipal solid trash, this is equivalent to an average conversion rate of around 3.5 kg per hour. The flow rate of producer gas was measured to be 38 kg per hour on average. Several different causes are responsible for the disparity that exists between the anticipated and measured flow rates of producer gas. When it comes to the precision of the measurements made by the gas flow devices, there is a possibility of variations. Table 3 provides the input characterization of Municipal Solid Waste (MSW) and the corresponding producer gas composition.

Table 3. Input Characterization of Municipal Solid Waste (MSW) and Output Composition of Producer Gas.

Input	Output
MSW Analysis % Wet Basis	**Producer Gas Analysis in %**
C = 38.65	CO = 14
H = 6.24	H_2 = 15
O = 40.53	CH_4 = 2.5
N = 1.25	H_2O = 7.5
S = 0.23	CO_2 = 12
Cl = 0.60	N_2 = 48.7
Ash = 12.50	O_2 = 0.3
H_2O = 24.91	

Feed input:

$$\dot{m}_{C,fuel} = \dot{m}_{fuel} \cdot w_C \tag{1}$$

$$\dot{m}_{Hydrogen} = \dot{m}_{fuel} \cdot \left(w_H + \frac{2}{18} \cdot w_{moisture} \right) \tag{2}$$

$$\dot{m}_{Oxygen} = \dot{m}_{fuel} \cdot \left(w_O + \frac{16}{18} \cdot w_{moisture} \right) \tag{3}$$

Input air:

$$\dot{n}_{H,air} = \frac{2y_{H_2} \cdot Q_{air}}{22.4} \tag{4}$$

$$\dot{n}_{N,air} = \frac{2y_{N_2} \cdot Q_{air}}{22.4} \tag{5}$$

$$\dot{n}_{O,air} = \frac{\left(2y_{O_2} + y_{H_2} \right) \cdot Q_{air}}{22.4} \tag{6}$$

Output producer gas:

$$\dot{n}_{C,gas} = \frac{\left(y_{CO} + y_{CO_2} + y_{CH_4} \right) \cdot Q_{gas}}{22.4} \tag{7}$$

$$\dot{n}_{H,gas} = \frac{\left(2y_{H_2} + 2y_{H_2O} + 4y_{CH_4} \right) \cdot Q_{gas}}{22.4} \tag{8}$$

$$\dot{n}_{O,gas} = \frac{\left(y_{CO} + 2y_{CO_2} + y_{H_2O} \right) \cdot Q_{gas}}{22.4} \tag{9}$$

$$\dot{n}_{N,gas} = \frac{2y_{N_2} \cdot Q_{gas}}{22.4} \tag{10}$$

$$P_{in} = \dot{m}_{fuel} \cdot HHV_{fuel} \quad \left(MJ \ hr^{-1} \right)$$ (11)

4. Results and Discussion

4.1. Gasifier Performance

The instantaneous performance data, which includes the gas yield and heating value, are presented in Table 4 for each of the respective runs of the gasifier while it is in operation. The highest gas production was observed during Trial 3, which utilized a feedstock blend of 50 percent wood and 50 percent municipal solid waste. This trial achieved a peak gas flow rate of 38 m³/h, with the corresponding maximum energy content of the producer gas reaching 1250 kcal/Nm³. Throughout all five trials, the air flow rate was consistently maintained at 15 m³/h. However, in Trials 1 and 3, the process moves toward flame pyrolysis and peak gasification as more charcoal is gasified. This indicates that the process is progressing. Because higher pyrolysis temperatures result in larger pyrolysis reaction rates, they make it possible to increase the consumption of both wood and municipal solid waste. The capacity of this gasifier design to produce less tar is one of its most notable characteristics. This is accomplished by delivering a more consistent mixture of fuel and air through three rows of nozzles that are arranged in contrast to one another. It has been found that to achieve optimal performance, it is necessary to distribute wood, municipal solid waste, and air in a manner that is uniform both spatially and temporally.

Table 4. Performance results of the downdraft gasifier under various feedstock blends.

Key Values	MSW Downdraft Gasifier				
	Run 1	Run 2	Run 3	Run 4	Run 5
Composition of MSW	100% Wood	75% Wood + 25% MSW	50% Wood + 50% MSW	25% Wood + 75% MSW	100% MSW
Moisture content of (%)	5.33	20	5.33	25	25
Flow rate of air (m³/h)	15	15	15	15	15
Equivalence ratio	0.3	0.5	0.4	0.3	0.35
Flow rate of gas (m³/h)	35	33	38	30	25
Particulate (g)	0.5	0.3	0.2	0.5	0.4
Tar (%)	0.3	1.2	1.3	1	2
CO (%)	12	14	15	14	11
H_2 (%)	14	11	16	14.8	12
CH_4 (%)	3.5	3.2	3	3.4	6
CO_2 (%)	12	15	11.2	11.5	13
H_2O	9.5	7.4	6.1	6.8	7
N_2 (%)	48.8	49	48.5	48.7	50
O_2	0.2	0.4	0.2	0.8	1

4.2. Tar Concentration

Figure 4 shows the variation in tar concentrations and bed temperatures during different runs in the gasifier. Tar concentrations ranged from 0.3% to 2%, indicating fluctuations in the efficiency of the gasification process. Lower tar concentrations suggest more complete gasification, while higher concentrations indicate incomplete breakdown of volatile compounds. The temperature in the combustion zone reached 883 °C, which is ideal for the partial combustion of feedstock and providing heat for gasification, while the drying zone had a lower temperature of 331 °C, necessary for removing moisture from the feedstock before it enters the higher-temperature zones. These temperature variations are critical for optimizing the drying, pyrolysis, and gasification processes, influencing both tar formation and overall system efficiency. Temperature oscillations were noted in all areas of the bed during the studies, apart from the reactor's bottom. The principal factor contributing to this fluctuation is the intermittent activation of the feeding system. As the gasification process progressed and the municipal solid waste (MSW) level in the gasifier decreased, the addition of wood debris and MSW at the upper part of the bed led to a downward displacement of the bed. This displacement caused a significant shift throughout the bed, altering the temperature distribution. Figure 4 demonstrates that during Run 3, which involved 30 kg of wood waste combined with 30 kg of MSW, the system maintained optimal tar levels throughout the eight-hour continuous operation of a single fixed-bed batch. This performance in Run 3 was more favorable compared to the other experimental runs, highlighting the efficient balance between wood and MSW that contributed to better tar reduction and overall gasification efficiency.
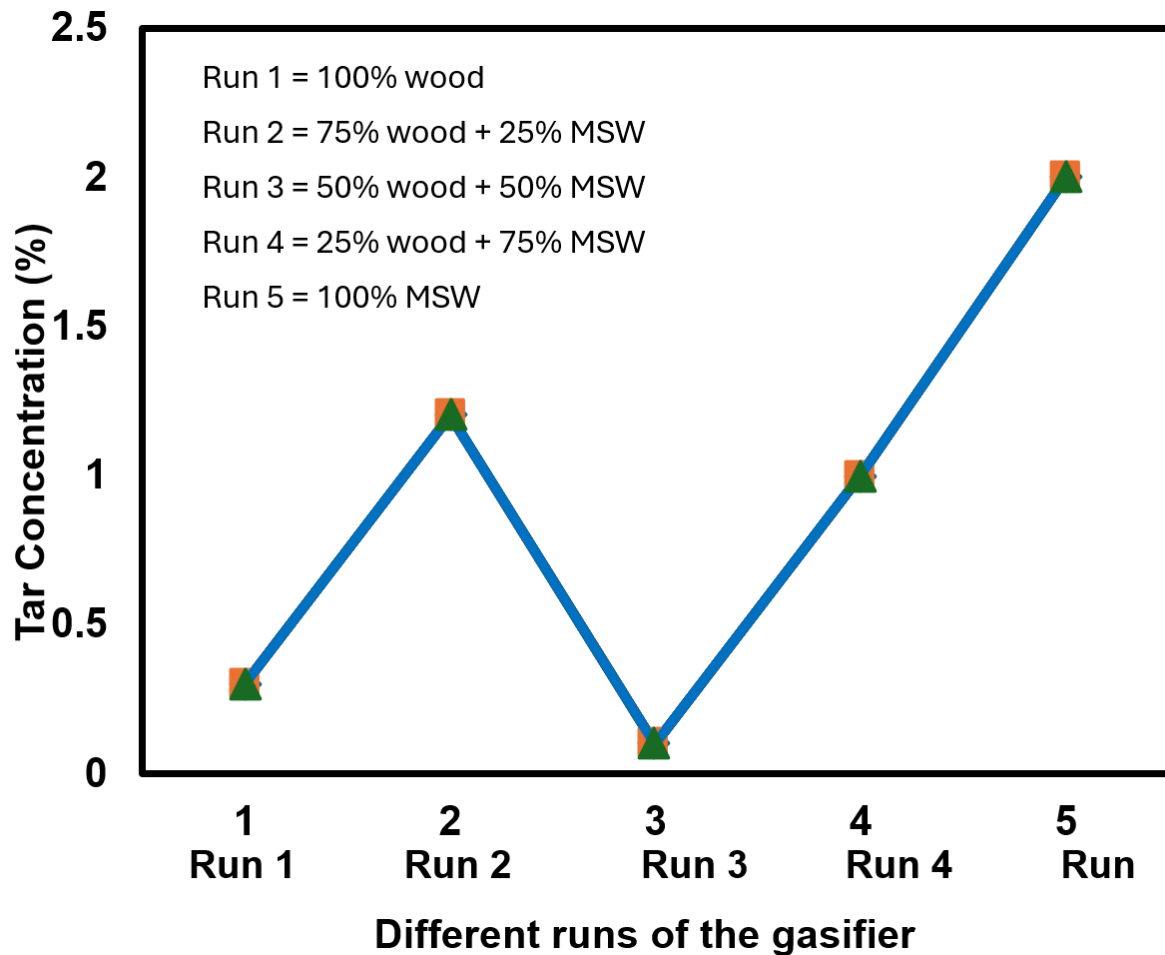
Figure 4. Tar yield profile under different operational runs.

4.3. Mass and Energy Balance

The energy input for the gasification process is calculated by multiplying the fuel consumption rate by the heat of combustion on an as-received basis. Given that the heat of combustion on a dry basis is 14.8 MJ/kg, and considering the moisture content of 24.91%, the heat of combustion on an as-received basis is 14.25 MJ/kg. With a fuel consumption rate of 30 kg/h, the energy input is calculated as 30 kg/h × 14.25 MJ/kg, resulting in an energy input of 427.5 MJ/h.

$$P_{in} = 30 \cdot 14.5 = 435 \ MJ \ hr^{-1} \tag{12}$$

The chemical energy in the producer gas is calculated by considering the molar flow rates of the combustible components in the gas and multiplying them by their respective higher heating values (HHV, in MJ/Nm³). HHV represents the energy content of a unit volume of gas, and by determining the flow rates of key combustibles such as hydrogen, carbon monoxide, methane, and other volatile compounds, the total chemical energy can be derived. This calculation helps in evaluating the energy output of the producer gas and assessing the efficiency of the gasification process.

$$P_{out,chemical} = \sum_i \dot{n}_i \cdot HHV_i = \frac{Q_{gas}}{22.4} \cdot \sum_i y_i \cdot HHV_i \quad \left(MJ \ hr^{-1} \right) \tag{13}$$

$$P_{out,chemical} = \frac{75}{22.4} \cdot \left(0.14 \cdot 283.0 + 0.15 \cdot 285.8 + 0.025 \cdot 890.4 \right) = 350 \ MJ \ hr^{-1} \tag{14}$$

Then the equation for the sensible heat becomes:

$$P_{gas.sensible} = \frac{v_{gas}}{22.4} . C_p \left(T_{gasout} - T_{ambient} \right) (MJ\ hr^{-1}) \tag{15}$$

Additionally, it is necessary to consider the heat that is lost to the environment in addition to the sensible heat that is transported by the producing gas. However, the exterior surface of the gasifier is not insulated, which results in an estimated loss of heat of roughly 10 MJ/h due to convection and radiation. The gasifier is coated with high-alumina refractory cement on the inside. With the information that has been provided, it is now possible to compute the total amount of energy that is being expelled from the system.

$$P_{out} = P_{out,\ chem} + P_{out,\ s} + P_l = 350 + 77 + 10 = 435\ MJ\ hr^{-1} \tag{16}$$

Comparing Equations (12) and (16)

$$P_{in} = 437 MJ\ hr^{-1} \qquad\qquad P_{out} = 435\ MJ\ hr^{-1}$$

The validity of the energy input-output assessment for the gasifier system is confirmed by the observed results, which show a significant agreement between the projected and actual heat and mass balance. This assessment indicated that the amount of fuel input closely aligned with the amount of oil produced, demonstrating that the system operates efficiently in terms of both energy and mass conversion. The examination of the mass and energy balance highlighted this close match, validating the accuracy of the energy input calculations and the system's overall performance in converting feedstock into useful products.

It is important to consider that gas samples were collected several hours into the run, which means that the composition of the residual fuel in the reactor may have changed over time. As the gasification process progresses, the fuel undergoes thermochemical transformations, and the distribution of volatile compounds, char, and gas may shift. This change in fuel composition could influence the gas composition and the overall performance of the system, potentially affecting the accuracy of the gas samples taken later in the process. Therefore, the timing of sample collection is crucial in ensuring the reliability of the data and the interpretation of the system's behavior. Although it is anticipated that drying took place at an early stage, it is also possible that the composition of the dry feedstock was altered because of extended heating. The mass and energy balance were carried out at a rate of 45 cubic meters per hour, which was optimal for air movement. It is noteworthy that the gasification process was able to attain an estimated efficiency of 98% under these conditions, which demonstrates the efficacy of the system in turning municipal solid waste into syngas.

4.4. Comparison with Experimental Results

The performance outcomes of the fabricated gasifier were compared with empirical data from prior investigations concerning woody biomass and municipal solid waste [28,29]. The findings predominantly align with the existing literature, as illustrated in Table 5. This unequivocally illustrates that the downdraft MSW gasifier created in this study is both technically robust and appropriate for practical use.

Table 5. Experimental data compared with other results.

Operating Parameters	Experimental Data		
	Saravanakumar et al. [29]	Shweta T and Somnath N [28]	Present Work
Feedstock	Wood	MSW	MSW + Wood
Running hours	5	4	8
Feed rate kg h^{-1}	10	6	9.38
Air flow rate m^{3}h^{-1}	29	35	15
Gas flow rate m^{3}h^{-1}	25	12.45	38
Total fuel consumed kg	65	24	90.50

4.5. Technology Implementation

The proposed MSW gasifier model could be well-suited for implementation in metropolitan areas such as Delhi and Chennai, which cover large urban regions of approximately 750 km^2 each. These cities, with their significant population and substantial amounts of municipal solid waste (MSW), could greatly benefit from the efficient waste-to-energy solutions offered by the gasifier model. By converting MSW into energy, the system could help address waste management challenges while simultaneously generating clean energy, making it a viable option for large-scale urban waste management and energy production in these densely populated cities.

Construction timber and horticultural debris are readily accessible via wood waste collectors, especially prevalent in the northern and southern districts of Tamil Nadu. These collectors generally provide garbage disposal services for building and landscaping sites. The industrial areas in the northern and western regions of Hyderabad contain numerous factories and canteens, generating a steady supply of food waste. Establishing gasification facilities in these places would enhance localized waste management and energy recovery. The produced gas can function as a thermal or electrical energy source for the facility, while the char ash byproduct may be employed in adjacent cement facilities, so supporting a circular economy model.

5. Conclusions

This study examines the co-gasification of municipal solid waste (MSW) and woody biomass in varying ratios to evaluate tar content, syngas composition, and the volumetric flow rate of the generated gas. Because of the lightweight and heterogeneous character of the waste, the fixed-bed stratified downdraft gasifier was able to work effectively up to a maximum of forty percent municipal solid waste content. After that point, bridging in the hopper occurred. An increase in the proportion of municipal solid waste (MSW) in the feedstock improved the quality of the producer gas, particularly by raising the concentrations of CO and H_2O. The highest gas flow rate of 38 Nm^3/h. was achieved with a 50:50 (*w/w*) mixture of wood waste and municipal solid waste, indicating optimal performance under these conditions. These results suggest that gasification serves as a promising, environmentally friendly technology for the value of municipal solid waste, offering a sustainable approach to energy recovery through the production of cleaner producer gas. This study presented a modified stratified downdraft gasifier design as a means of overcoming the various problems that are typically connected with traditional downdraft fixed-bed gasifiers, particularly those that involve high tar content. The unique configuration, which consisted of three rows of air nozzles that were opposite one another, made it possible to mix the feedstock and air in a regular manner, which led to a significant reduction in the development of tar. A demonstration of the reactor's thermal stability and operational reliability was carried out over the course of eight hours of continuous operation. The usefulness of this design for decentralized waste-to-energy applications is highlighted by the enhanced gas quality as well as the overall efficiency. As an additional point of interest, the mass and energy balance calculations demonstrated a high gasification efficiency when municipal solid waste was utilized, hence verifying the system's potential for practical implementation in urban and industrial settings.

Author Contributions: C.A: Conceptualization, Methodology, Visualization; A.S: Data curation, Writing—original draft preparation, Visualization, Investigation, Supervision, Software, Validation, Writing—reviewing and editing. All authors have read and agreed to the published version of the manuscript.

Institutional Review Board Statement: Not applicable.

Informed Consent Statement: Not applicable.

Data Availability Statement: Data will be available upon request.

Conflicts of Interest: The authors declare no conflict of interest.

Nomenclatures

P_{in}	Power intake (MJ/h)
Q_{gas}	Gas throughput rate (m^3/h)
$\dot{m}_{fuel}$	Rate of fuel consumption (kg/h)
HHV_{fuel}	Heat content of fuel (MJ/kg)
$P_{out,chem}$	Energy output from chemical reactions (MJ/h)
$\dot{n}_i$	Molar transfer rate i (kmol/h)
y_i	Relative amount of component i (m^3 m^{-3})
$c_{p,i}$	Specific heat of the substance i (kJ/kmol·K)
σ	Stefan Boltzmann constant (W/m^2·K^4)
ε	Radiative heat emission factor
A	External surface area of the gasifier (m^2)
$T_{gas\,out}$	Temperature of the gas leaving the system (K)
$T_{ambient}$	Temperature of the surroundings (K)
$P_{out,sensible}$	Sensible thermal energy (MJ h^{-1})

K	Reaction equilibrium factor
T_{eq}	Thermal balance temperature (K)
$A_i \dots E_i$	Heat capacity function coefficients for the species i
p_{CO2}	CO_2 component pressure (Pa)
p_{H2}	H_2 component pressure H_2 (Pa)
p_{CO}	CO component pressure CO (Pa)

References

1. Nimita Jebaranjitham, J.; Selvan Christyraj, J.D.; Prasannan, A.; et al. Current Scenario of Solid Waste Management Techniques and Challenges in COVID-19—A Review. *Heliyon* **2022**, *8*, e09855. https://doi.org/10.1016/J.HELIYON.2022.E09855.

2. Abubakar, I.R.; Maniruzzaman, K.M.; Dano, U.L.; et al. Environmental Sustainability Impacts of Solid Waste Management Practices in the Global South. *Int. J. Environ. Res. Public Health* **2022**, *19*, 12717. https://doi.org/10.3390/IJERPH191912717.

3. Report of the Task Force on Waste to Energy (Volume I) (In the Context of Integrated MSW Management). 2014. Available online: https://sbmurban.org/storage/app/media/pdf/Task_force_report_on_WTE.pdf (accessed on 7 May 2025).

4. Annual Report, Ministry of Environment, Forest and Climate Change. New Delhi, 2015. Available online: https://moef.gov.in/wp-content/uploads/2018/04/MinistryofEnvirormentAnnualReport2015-16English.pdf (accessed on 17 May 2023).

5. Guo, M.; Lin, J.; Yu, J.; et al. Configuration Optimization of a Biomass Chemical Looping Gasification (CLG) System Combined with CO_2 Absorption. *Renew. Energy* **2024**, *237*, 121459. https://doi.org/10.1016/J.RENENE.2024.121459.

6. Li, J.; Fu, W.; Bai, X.; et al. Oxidative Pyrolysis Characteristics and Exothermic Heat Release Effects of Cellulose, Hemicellulose, and Lignin. *Fuel* **2025**, *386*, 134212. https://doi.org/10.1016/J.FUEL.2024.134212.

7. Racero-Galaraga, D.; Rhenals-Julio, J.D.; Sofan-German, S.; et al. Proximate Analysis in Biomass: Standards, Applications and Key Characteristics. *Results Chem.* **2024**, *12*, 101886. https://doi.org/10.1016/J.RECHEM.2024.101886.

8. Puri, L.; Hu, Y.; Naterer, G. Critical Review of the Role of Ash Content and Composition in Biomass Pyrolysis. *Front. Fuels* **2024**, *2*, 1378361. https://doi.org/10.3389/FFUEL.2024.1378361.

9. Liu, Y.; Yin, K.; Wu, J.; et al. Ash Chemistry in Chemical Looping Process for Biomass Valorization: A Review. *Chem. Eng. J.* **2023**, *478*, 147429. https://doi.org/10.1016/J.CEJ.2023.147429.

10. Ranzi, E.; Faravelli, T.; Manenti, F. Pyrolysis, Gasification, and Combustion of Solid Fuels. In *Advances in Chemical Engineering*; Academic Press: Cambridge, MA, USA, 2016; Volume 49, pp 1–94. https://doi.org/10.1016/BS.ACHE.2016.09.001.

11. Gao, Y.; Wang, M.; Raheem, A.; et al. Syngas Production from Biomass Gasification: Influences of Feedstock Properties, Reactor Type, and Reaction Parameters. *ACS Omega* **2023**, *8*, 31620–31631. https://doi.org/10.1021/ACSOMEGA.3C03050.

12. Jayanarasimhan, A.; Pathak, R.M.; Shivapuji, A.M.; et al. Tar Formation in Gasification Systems: A Holistic Review of Remediation Approaches and Removal Methods. *ACS Omega* **2024**, *9*, 2060–2079. https://doi.org/10.1021/ACSOMEGA.3C04425.

13. Chen, D.; Yin, L.; Wang, H.; et al. Pyrolysis Technologies for Municipal Solid Waste: A Review. *Waste Manag.* **2014**, *34*, 2466–2486. https://doi.org/10.1016/J.WASMAN.2014.08.004.

14. Al-Rumaihi, A.; Shahbaz, M.; Mckay, G.; et al. A Review of Pyrolysis Technologies and Feedstock: A Blending Approach for Plastic and Biomass towards Optimum Biochar Yield. *Renew. Sustain. Energy Rev.* **2022**, *167*, 112715. https://doi.org/10.1016/J.RSER.2022.112715.

15. Kumar, A.; Thakur, A.K.; Gaurav, G.K.; et al. A Critical Review on Sustainable Hazardous Waste Management Strategies: A Step towards a Circular Economy. *Environ. Sci. Pollut. Res. 2023 3048* **2023**, *30*, 105030–105055. https://doi.org/10.1007/S11356-023-29511-8.

16. Brunner, P.H.; Morf, L.S. Waste to Energy, Indispensable Cornerstone for Circular Economy: A Mini-Review. *Waste Manag. Res.* **2025**, *43*, 26–38. https://doi.org/10.1177/0734242X241227376.

17. Farooq, A.; Haputta, P.; Silalertruksa, T.; et al. A Framework for the Selection of Suitable Waste to Energy Technologies for a Sustainable Municipal Solid Waste Management System. *Front. Sustain.* **2021**, *2*, 681690. https://doi.org/10.3389/FRSUS.2021.681690.

18. Materazzi, M.; Lettieri, P.; Taylor, R.; et al. Performance Analysis of RDF Gasification in a Two Stage Fluidized Bed–Plasma Process. *Waste Manag.* **2016**, *47*, 256–266. https://doi.org/10.1016/J.WASMAN.2015.06.016.

19. Dong, J.; Tang, Y.; Nzihou, A.; et al. Comparison of Waste-to-Energy Technologies of Gasification and Incineration Using Life Cycle Assessment: Case Studies in Finland, France and China. *J. Clean. Prod.* **2018**, *203*, 287–300.

https://doi.org/10.1016/J.JCLEPRO.2018.08.139.

20. Achinas, S.; Gramsbergen, M.; Achinas, V.; et al. *Waste-to-Energy Technologies: Industrial Progress for Boosting the Circular Economy*; Springer: Singapore, 2021. https://doi.org/10.1007/978-981-15-7525-9_106-1.

21. Seo, Y.-C.; Alam, M.T.; Yang, W.-S.; et al. Gasification of Municipal Solid Waste. In *Gasification for Low-grade Feedstock*; IntechOpen: London, UK, 2018. https://doi.org/10.5772/INTECHOPEN.73685.

22. Tauqir, W.; Zubair, M.; Nazir, H. Parametric Analysis of a Steady State Equilibrium-Based Biomass Gasification Model for Syngas and Biochar Production and Heat Generation. *Energy Convers. Manag.* **2019**, *199*, 111954. https://doi.org/10.1016/J.ENCONMAN.2019.111954.

23. Su, Y.; Luo, Y.; Chen, Y.; et al. Experimental and Numerical Investigation of Tar Destruction under Partial Oxidation Environment. *Fuel Process. Technol.* **2011**, *92*, 1513–1524. https://doi.org/10.1016/J.FUPROC.2011.03.013.

24. Valderrama Rios, M.L.; González, A. M.; Lora, E.E.S.; et al. Reduction of Tar Generated during Biomass Gasification: A Review. *Biomass Bioenergy* **2018**, *108*, 345–370. https://doi.org/10.1016/J.BIOMBIOE.2017.12.002.

25. Lan, W.; Chen, G.; Zhu, X.; et al. Progress in Techniques of Biomass Conversion into Syngas. *J. Energy Inst.* **2015**, *88*, 151–156. https://doi.org/10.1016/J.JOEI.2014.05.003.

26. Sher, F.; Hameed, S.; Smječanin Omerbegović, N.; et al. Cutting-Edge Biomass Gasification Technologies for Renewable Energy Generation and Achieving Net Zero Emissions. *Energy Convers. Manag.* **2025**, *323*, 119213. https://doi.org/10.1016/J.ENCONMAN.2024.119213.

27. Sikarwar, V.S.; Zhao, M.; Clough, P.; et al. An Overview of Advances in Biomass Gasification. *Energy Environ. Sci.* **2016**, *9*, 2939–2977. https://doi.org/10.1039/C6EE00935B.

28. Thakare, S.; Nandi, S. Study on Potential of Gasification Technology for Municipal Solid Waste (MSW) in Pune City. *Energy Procedia* **2016**, *90*, 509–517. https://doi.org/10.1016/J.EGYPRO.2016.11.218.

29. Saravanakumar, A.; Vijayakumar, P.; Hoang, A. T.; et al. Thermochemical Conversion of Large-Size Woody Biomass for Carbon Neutrality: Principles, Applications, and Issues. *Bioresour. Technol.* **2023**, *370*, 128562. https://doi.org/10.1016/J.BIORTECH.2022.128562.

Synergistic and Antagonistic Effects of Catalytic Torrefaction-Pyrolysis of Woody Biomass in a Carbon Dioxide Atmosphere for Biofuel Production

Elizabeth Wanchisn Smith [1], Ria Aniza [2,3,4], Anelie Petrissans [2,*], Rafael Lopes Quirino [1,*], Baptiste Colin [2], Mathieu Petrissans [2], and Wei-Hsin Chen [5,6,7]

[1] Biochemistry, Chemistry and Physics Department, Georgia Southern University, Statesboro, GA 30460, USA
[2] Université de Lorraine, INRAE, LERMAB, F-88000 Epinal, France
[3] International Doctoral Degree Program in Energy Engineering, National Cheng Kung University, Tainan 701, Taiwan
[4] Department of Environmental Engineering, Institut Teknologi Sepuluh Nopember, Surabaya 60111, Indonesia
[5] Department of Aeronautics and Astronautics, National Cheng Kung University, Tainan 701, Taiwan
[6] Research Center for Smart Sustainable Circular Economy, Tunghai University, Taichung 407, Taiwan
[7] Department of Mechanical Engineering, National Chin-Yi University of Technology, Taichung 411, Taiwan
* Correspondence: anelie.petrissans@univ-lorraine.fr (A.P.); rquirino@georgiasouthern.edu (R.L.Q.)

Abstract: Torrefaction-pyrolysis is the thermal treatment of biomass in an inert atmosphere between 105 °C and 800 °C to break carbon bonds and produce biofuels. The purpose of this study is to examine how woody biomass with different particle sizes (250 μm and 500 μm), wood types (Poplar and Fir), and catalyst types (K, Na, and Mg) responds to catalytic thermochemical conversion in a CO_2 environment. Torrefaction-pyrolysis of woody biomass shows the Boudouard equilibrium responds after 780 °C for K and Na-catalysts, except in samples impregnated with Mg-catalyst. When K-catalyst material is present, the C-O-C signal regarding the glycosidic linkages from cellulose and hemicelluloses in Fir is observed to decrease the most. This is related to the fact that Fir (22.43 wt.%) has nearly twice as many hemicelluloses as Poplar (12.18 wt.%), making it less thermally stable and more vulnerable to the prolonged drying required following catalyst impregnation.

Keywords: torrefaction; pyrolysis; catalytic reaction; CO_2 carrier gas; Boudouard equilibrium

1. Introduction

Carbon dioxide emissions reached 149% of pre-industrial levels while methane and nitrous oxide emissions reached 262% and 124%, respectively, in 2021 [1]. Thus, distinctive solutions are necessary to reduce GHG excessive production by changing the focus away from reliance on non-renewable fossil fuels and toward renewable, clean, and sustainable energy. Converting biomass to biofuel is a low-cost, competitive alternative to fossil fuels due to its carbon neutrality and availability [2–4]. Biomass, such as wood waste from the timber industry, is a prospective candidate for biomass-based renewable energy, with 95.1 million tons of dead biomass generated in the state of California alone between the years 2012 to 2017 [5]. Currently, the primary means of disposal is through mass burning, releasing carbon dioxide, particulate matter, and other pollutants into the atmosphere [6,7]. Utilizing woody biomass as a sustainable fuel source provides a practical way to get rid of these dead standing trees and use them as feedstock for making biofuel [8,9] in addition to woody furniture, building structures, and bio-composite [10–12].

Biomass is also a carbon-neutral fuel source since the amount of carbon emitted is equivalent to the amount captured during growth [13,14]. The energy from the conversion of sunlight and carbon dioxide during photosynthesis is stored in the carbon-carbon bonds found within the three main biopolymers of biomass [15]. Figure 1 is the illustration of the chemical structure of three biopolymers in wood. Cellulose is composed of a linear polymer chain of glucose monomers held tightly together by hydrogen bonding [9]. Lignin is composed of three main phenolic units organized randomly, resulting in variable structures serving to hold the material together [13]. Hemicelluloses are composed of short polysaccharide chains. Xylan is an example of a hemicellulose [16,17]. A thorough understanding of the chemical processes involved in breaking these bonds can lead to the efficient extraction of the energy in biomass. However, woody biomasses have high moisture content and heterogeneity in

addition to low bulk energy density, and low uniformity across different species, limiting their efficiency of conversion to biofuels when undergoing torrefaction-pyrolysis [17,18].
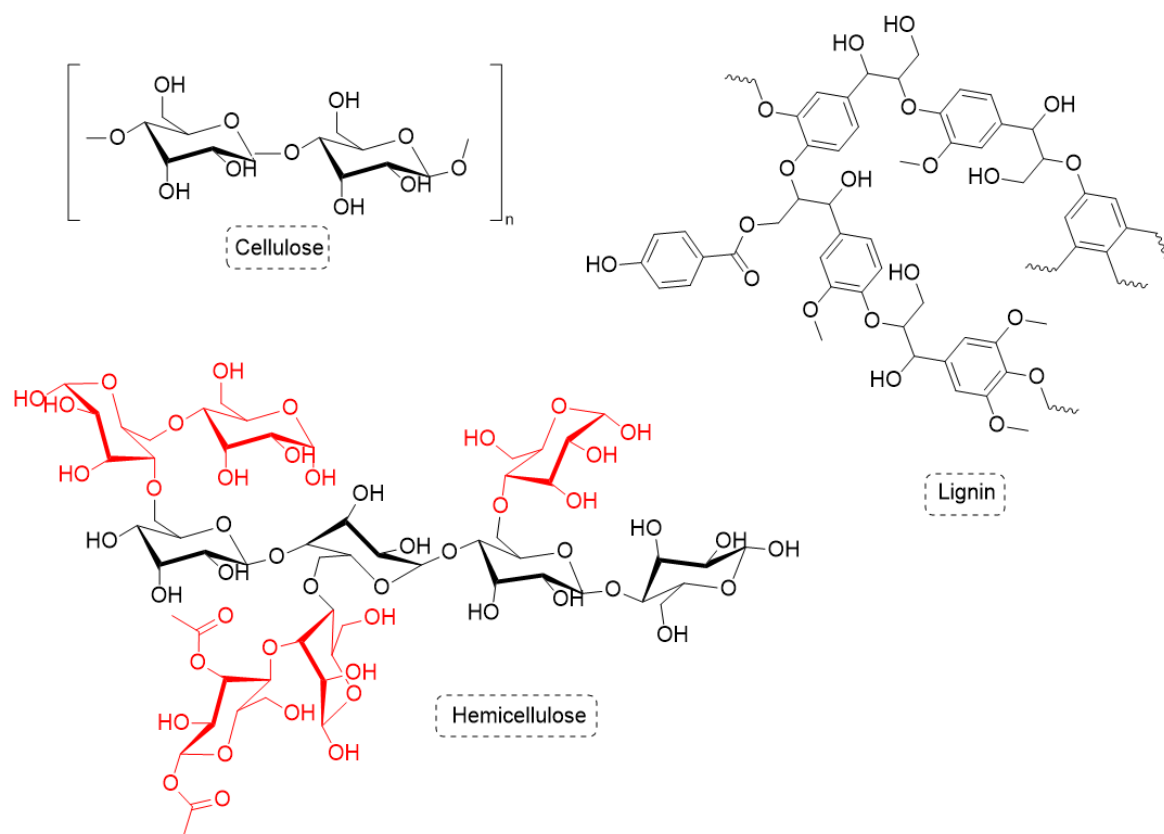

Figure 1. Three main biopolymers of woody biomass: cellulose, an example of hemicelluloses, and an example of lignin.

Torrefaction heats biomass between 200 °C and 350 °C, improving its energy potential and reducing greenhouse gases by 85% compared to coal [2,19,20]. Pyrolysis, above 350 °C, produces liquid and gas products through extensive degradation [13,14,21]. Catalysts like potassium (K), sodium (Na), and magnesium (Mg) enhance both processes [22,23]. Potassium carbonate, for example, reduces torrefaction time by 67%, increases heating value, and improves gas yields [24,25]. NaCl boosts pyrolysis yield and heating value [26], while $MgCl_2$ lowers pyrolysis temperature and increases yield in cabbage-based biochar [27]. MgO, however, shows low activity for sugar cane pyrolysis [28]. Additionally, the inert carrier gas in torrefaction-pyrolysis, such as CO_2 atmosphere, differs from N_2 due to CO_2's vibrational modes and electrophilic structure, allowing it to absorb more radiation and be more reactive [29]. This reactivity supports the Boudouard equilibrium, where solid carbon reacts with CO_2 to form CO above 700 °C. Studies have shown increased CO, H_2, and CH_4 production at these temperatures, influenced by heating rate [30–32]. Guizani et al. [33] found that adding 20–40% CO_2 to N_2 during pyrolysis of hardwood beech species increased mass loss by 10–13%, enhanced gas yields, and produced more carbon-rich char by altering hydrogen and oxygen interactions.

Limited studies have explored torrefaction-pyrolysis in pure CO_2, especially with woody biomass. Most research on catalysis in CO_2 has focused on expensive heavy metals (Pd, Pt, Ni), leaving earth metal catalysis in CO_2 of interest. To address the challenge, thus, this study aims to examine the effects of CO_2 on the torrefaction-pyrolysis of hard (Poplar) and soft (Fir) woods with different particle sizes (250 μm and 500 μm) and three catalysts (KCl, NaCl, $MgCl_2$) using various analytical methods. The novel approach combines torrefaction and pyrolysis in one protocol to provide a comprehensive understanding of how CO_2 influences both processes.

2. Materials and Methods

2.1. Materials

The wood samples were obtained from a local timber in the Grand Est area (France). The selected wood species for this study were Fir wood (*Abies pectinata*), and Poplar wood (*Populus nigra*) as they are all common

waste woods in the Vosges region in France. The woods were ground using a knife-mill SM100 (Retsch, Germany) equipped with trapezoidal meshes of 0.5 mm. The wood powder was sieved using meshes to obtain particle sizes of 250 μm and 500 μm. All wood samples were dried at 103 °C overnight prior to catalyst impregnation. Potassium chloride (KCl—99.5%) and sodium Chloride (NaCl—99.9%) were delivered by VWR. Meanwhile, crystalline anhydrous magnesium chloride ($MgCl_2$—99.0%) was obtained from Alfa Aesar.

2.2. Methods

2.2.1. Catalyst Impregnation

According to a procedure commonly adopted in the literature, earth metals were inserted into the biomass through chemical impregnation using KCl, NaCl, and $MgCl_2$ [34]. The catalytic impregnation solutions were prepared by dissolving KCl, $MgCl_2$, and NaCl with deionized water in three different concentrations 0.025 ± 0.005, 0.05 ± 0.004, and 0.1 M. Research has indicated that 0.025 M of catalyst could efficiently catalyze the transformation of furfurals produced from biomass into useful compounds such as cyclopentanone [35,36], 0.05 M improved accessibility to the acid site and mass diffusion [37], meanwhile, the concentration higher than 0.1 M might revealed negative consequences caused by char pore clogging [38]. Dry Fir and Poplar samples of 250 μm and 500 μm were impregnated with three types of catalyst. The samples were impregnated by mixing 3.0 g of oven-dried wood samples with 250 mL of salt solution. The mixture was stirred for 1 h at ambient conditions before undergoing vacuum filtration. Each sample was then placed in an oven at 103 °C until the weight was stable.

2.2.2. TGA Experiments

The behavior of impregnated and raw wood during torrefaction-pyrolysis was analyzed by thermogravimetric analysis using a simultaneous thermal analyzer (TGA/DSC-STA 449 F3 Jupiter, Netzsch, Selb, Germany) with a CO_2 flow of 50 mL/min. Oven-dried powder samples of approximately 10.0 mg were loaded in a ceramic crucible and heated from room temperature to 105 °C under a CO_2 atmosphere. That temperature was maintained for 10 min to remove residual moisture. Each sample was then heated to 350 °C at a heating rate of 20 °C·min^{-1}. The temperature was maintained at 350 °C for 30 min to observe torrefaction conditions. After that, the temperature was increased to 800 °C at a heating rate of 20 °C·min^{-1} and maintained at 800 °C for 30 min in a pyrolysis step. Finally, the atmosphere was switched to air, and the sample was kept at 800 °C for an additional 30 min for a complete combustion of all organic residue. The curve of solid weight percentage as a function of temperature was obtained (TG), and the derivative of the TG (DTG) as a function of time was considered. The TGA experiments were duplicated, and the average curves are presented herein. All the results of TGA experiments were controlled with the $\alpha \leq 0.1$ (maximum 10% error).

2.2.3. SEM and FTIR Tests

Each wood type was characterized by its fiber composition, surface morphology/topography, and chemical functional group by fiber analysis, SEM, and FTIR spectroscopy, respectively. Fiber analysis was used to determine the composition of hemicelluloses, cellulose, and lignin in lignocellulosic biomass materials [8,39]. A Whatman 41, circular, ashless filter paper with a 42.5 mm diameter was used. For SEM, approximately 2.0 mg of samples were placed on copper tape and mounted onto a JEOL Aluminum Specimen Mount (9.5 mm × 9.5 mm) from TED PELLA, INC. The mounted sample was coated in platinum using a Denton Vacuum Desk V Sputter and dried in a vacuum desiccator for 4 days before being imaged with a JEOL JSM-7600F Scanning Electron Microscope equipped with an Energy Dispersive X-ray (EDX) detector. EDX spectroscopy was used to determine the elemental composition of each sample. Furthermore, approximately 0.05 g of each sample was used for FTIR spectroscopy using a Thermo Scientific Nicolet iS10 FTIR spectrometer (Madison, WI, USA) equipped with an attenuated total reflectance (ATR) accessory. All spectra were normalized based on the H-C (sp^3) signal at ~2900 cm^{-1} in each spectrum. All the results of EDX experiments were controlled with the $\alpha \leq 0.1$ (maximum 10% error).

3. Results and Discussion

3.1. Characterization of Woody Sample

Fir (softwood) and Poplar (hardwood) are the two most common wood species in France's forests. In order to analyze the chemical composition within the raw sample of Fir and Poplar woods, some tests were performed, including fiber analysis and higher heating value (HHV) (Table 1). The Fir sample has a deep brownish color

compared to the Poplar sample, which shows more light brownish. The fiber analysis shows Fir contains cellulose at 45.24 wt.%, lignin at 32.33 wt.%, and hemicelluloses at 22.43 wt.%, meanwhile, Poplar contains cellulose at 63.93 wt.%, lignin at 23.89 wt.%, and hemicelluloses at 12.18 wt.%. Hardwood (Poplar) typically has a higher cellulose content compared to softwood (Fir). Cellulose is a polymer that works to increase the strength, hardness, and durability of wood [5,16]. This is why hardwoods are naturally more durable and stronger than softwoods. In terms of energy content, the calorific value test of HHV indicates that Fir has approximately 9.65% more energy (19.88 MJ/kg) than Poplar (18.13 MJ/kg).

Table 1. Wood characterization of Fir and Poplar.

Procedure [a]	Fir	Poplar
Sample image		
Fiber Analysis (wt.%)		
Cellulose	45.24	63.93
Hemicelluloses	22.43	12.18
Lignin	32.33	23.89
HHV (MJ/kg)	19.88	18.13

a: The experiment was performed duplicate with an error margin $\alpha \leq 10\%$.

In order to provide an overview of catalytic species retained after impregnation, selected samples with the same particle size (500 µm) were analyzed by SEM and EDX, as shown in Figure 2. A consistent magnification of 400× was adopted for imaging. The most notable information gained from SEM and EDX data includes the verification that impregnation was successful, as seen by the relative concentrations of K, Mg, Na, and Cl atoms in each of the impregnated samples analyzed. It can also be noted that in the areas examined, impregnation appears uniform based on the elemental mappings obtained. It is worth mentioning that the concentration of Cl retention in Poplar after impregnation with 0.1 M KCl is approximately twice as high as that of Fir impregnated with 0.05 M KCl, Poplar impregnated with 0.05 M NaCl, Poplar impregnated with 0.05 M MgCl$_2$, and approximately three times higher than raw Poplar. This indicates that the retention of Cl atoms from KCl and NaCl is directly dependent on the concentration of the impregnation solution, regardless of the wood. It is somewhat surprising that MgCl$_2$ didn't result in more retention of Cl atoms, as expected from its original composition.

It is important to highlight the significantly high concentration of K and Cl in raw Poplar and the complete absence of Mg and Na (Table 2). In fact, the lower K concentration in Poplar impregnated with 0.05 M NaCl and 0.05 M MgCl$_2$ with respect to the raw wood (Table 2) suggests that most of the Potassium naturally present in the wood leaches out during the impregnation process. The same effect is not observed with Cl.

FTIR was used to analyze samples before and after impregnation to determine if the impregnation process and the subsequent drying of impregnated samples at 103 °C for an extended time affected the composition of the woody biomass before torrefaction-pyrolysis. In Table 2, the ratios of C-O-C signals (~1100 cm^{-1}), pertaining to glycosidic bonds from cellulose and hemicelluloses, and OH signals (~3500 cm^{-1}) present in impregnated samples can be seen. It can be noted that while the changes in Poplar-impregnated samples are negligible, Fir seems more susceptible to the effect of drying in the presence of impregnated atoms. Indeed, there is a slight decrease in C-O-C relative to OH for all Fir-impregnated samples in comparison to the raw wood. It is possible that during drying, the extended exposure of the sample to an elevated temperature (103 °C) triggered the cleavage of some glycosidic bonds in the most thermally susceptible components, such as hemicelluloses.

The C-O-C bond vibration is only present in glycosidic bonds, which is the fundamental connection between sugar units to form polysaccharides, such as cellulose and hemicelluloses [40]. When a relative decrease in that signal is detected, it implies the rupture of the C-O-C connection. The decrease in C-O-C in Fir is largest in the presence of K (Table 2). The higher susceptibility of Fir to cleavage of glycosidic bonds can be correlated to its hemicellulose content. Fir has almost twice as many hemicelluloses (22.43 wt.%) as Poplar (12.18 wt.%), therefore, they are less thermally stable and more sensitive to the extended drying imposed after impregnation. The considerable difference in hemicellulose content can also be seen by the initial (C-O-C):(OH) ratios of Fir and Poplar (Table 2).
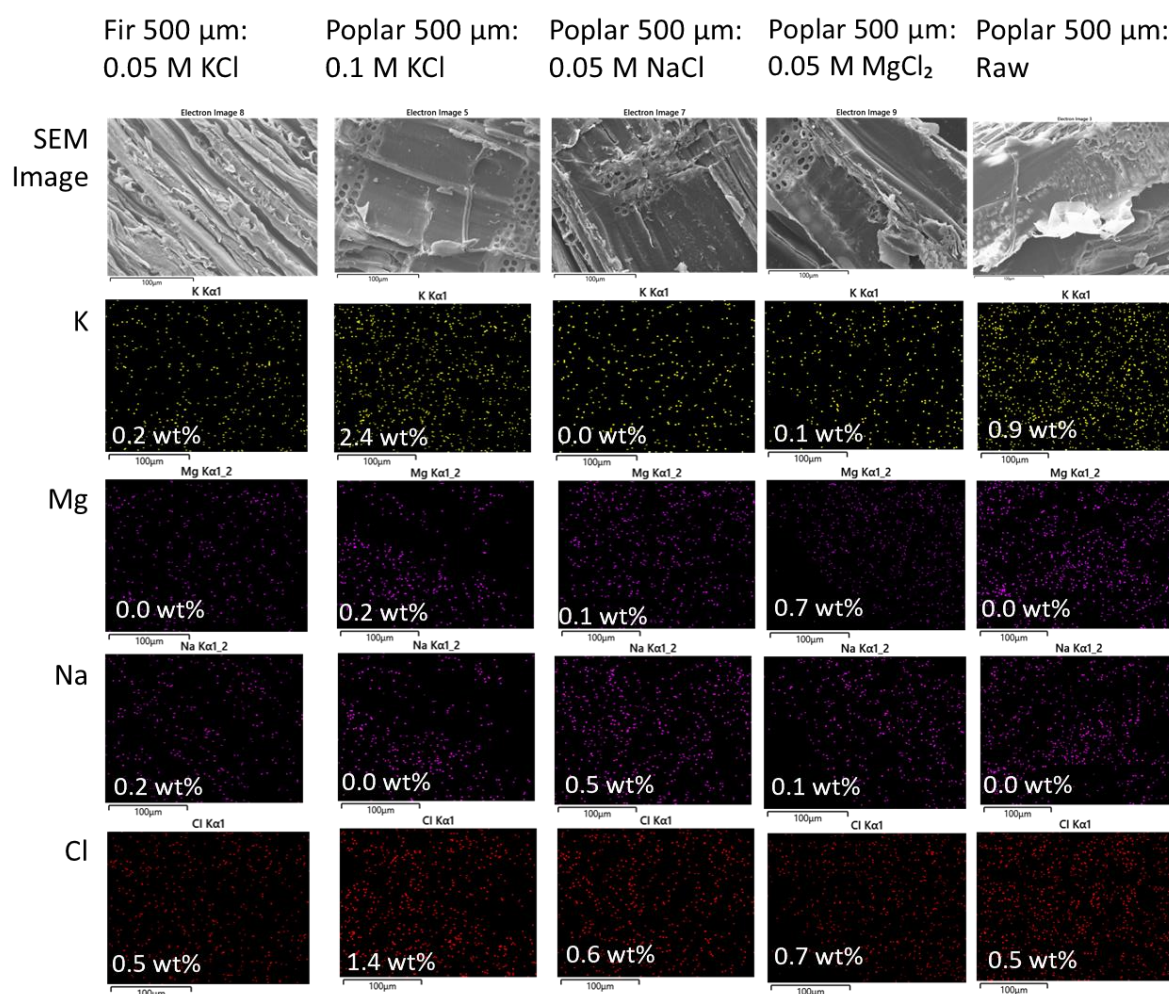
Figure 2. SEM and EDX results of selected samples.

Table 2. FTIR peak area results of Poplar and Fir impregnated samples.

Biomass	Normalized O-H Peak Area (a.u.)	Normalized C-O-C Peak Area (a.u.)	(C-O-C):(O-H) Peak Area Ratio
Fir (0.05 M)			
Fir Raw	7.54	16.92	2.24
Fir NaCl	9.78	20.17	2.06
Fir KCl	10.58	19.24	1.82
Fir MgCl$_2$	10.16	19.66	1.94
Poplar (0.05 M)			
Popar Raw	7.14	13.05	1.83
Poplar NaCl	8.63	15.16	1.76
Poplar KCl	10.08	19.65	1.95
Poplar MgCl$_2$	9.84	16.98	1.73

3.2. Thermogravimetric Analysis

TGA and DTG of Poplar and Fir raw samples were performed for two particle sizes (250 µm and 500 µm) in a CO_2 atmosphere. The results are presented in Figure 3. The thermodegradation of wood samples can be divided into two steps: torrefaction and pyrolysis. Torrefaction results in partial degradation of the wood polymers from 105 °C to 350 °C. Pyrolysis results in the extensive degradation of carbon-carbon bonds at temperatures between 350 °C and 800 °C.
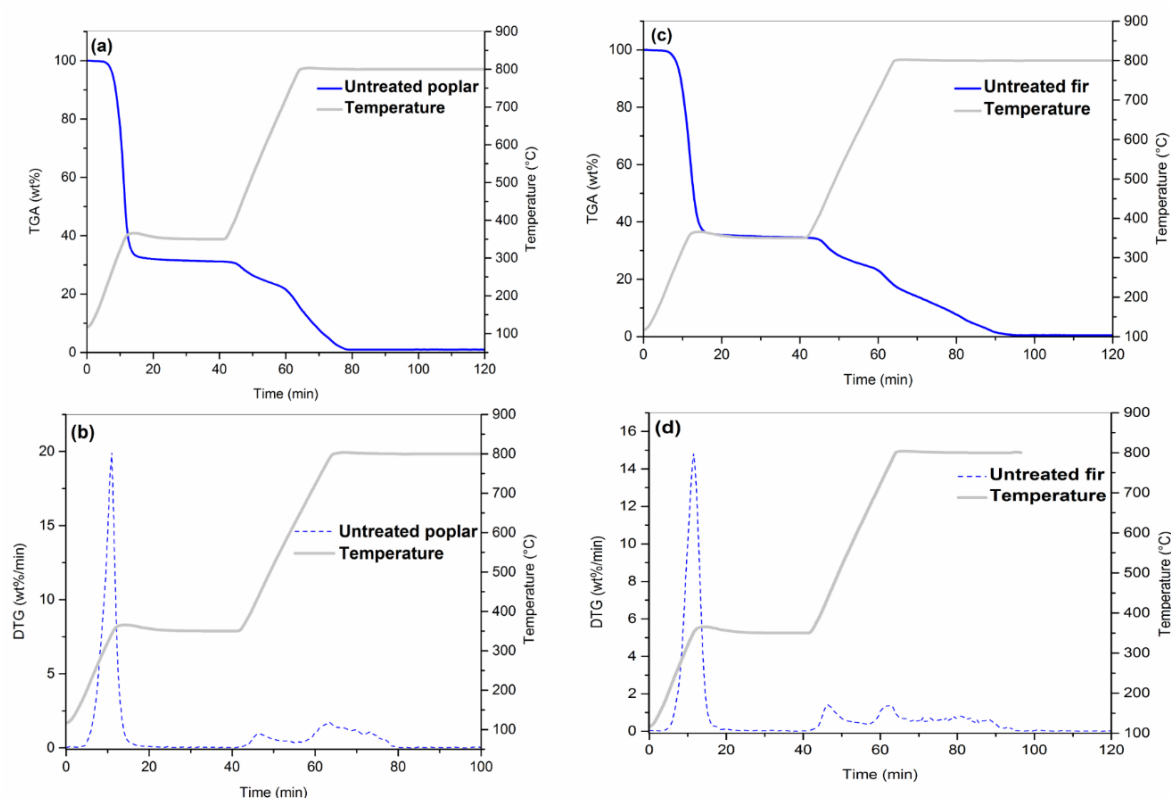
Figure 3. Raw sample of TGA (**a**) DTG, (**b**) curves of Poplar and TGA, (**c**) DTG, (**d**) curves of Fir.

One of the most notable results obtained from the raw data includes the similarity of the curves for different wood types, regardless of their classification as hard or soft woods. The most noticeable difference between the wood samples is the longer pyrolysis degradation for the Fir samples. In a CO_2 atmosphere, the torrefaction curve of these biomasses (105–350 °C, Figure 3) looks similar to those reported in the literature in an N_2 atmosphere [24,39]. This similarity agrees with what has been found during the torrefaction of other biomasses in a CO_2 atmosphere. In fact, it has been reported that CO_2 plays little role in physical properties during the torrefaction step [30,41]. However, during pyrolysis, the degradation of the remaining materials begins at approximately 450 °C, as expected, and continues until near completion at approximately 750 °C, unlike results reported under a nitrogen (N_2) atmosphere.

This continuing degradation can be attributed to the theoretical Boudouard equilibrium, which states that gaseous carbon dioxide (CO_2) will react with solid carbon to form carbon monoxide at temperatures greater than 700 °C, as seen in Equation (1) [42,43].

$$C(s) + CO_2(g) \leftrightarrows 2CO(g) \tag{1}$$

Multiple studies have explored the feasibility of the Boudouard reaction and have concluded that heating rate and biomass source influence the temperature that marks the onset of the Boudouard equilibrium [44,45]. Cho et al. exposed spent coffee grounds to both nitrogen and carbon dioxide atmospheres with a heating rate of 10 °C/min from ambient temperature to 900 °C [31,46]. The study determined that the TGA curves between the two gases were similar until around 350 °C and that under carbon dioxide, the Boudouard equilibrium shifted right at approximately 850 °C, causing total degradation and a higher concentration of carbon monoxide gas produced under these conditions. Kim et al. observed oak tree sugars in both nitrogen and carbon dioxide atmospheres from ambient temperature to 900 °C with a heating rate of 35 °C/min [32]. The study found that mass decay from the Boudouard reaction begins at a temperature greater than 720 °C and reaches a maximum at 830 °C.

The aforementioned phenomena allowed all those studies to conclude that the Boudouard reaction has very slow reaction kinetics. Similar conclusions were reached by Cho et al. [31,46], who compared TGA curves of red seaweed in both nitrogen and carbon dioxide atmospheres. The study found heating rate to be a contributing factor in the onset of the Boudouard reaction with the right being favored at approximately 850 °C using a heating rate of 100 °C/min while a heating rate of 5 °C/min allowed for the onset to begin at 740 °C with complete degradation to carbon monoxide taking a total of 16 min, therefore validating the Boudouard reaction to have very slow reaction kinetics. These studies confirm the feasibility of the Boudouard equilibrium to favor carbon monoxide formation

at approximately 750 °C and complete degradation in approximately 16 min after reaching 800 °C, as seen in the current study (Figure 3).

Compared to large-scale industrial processes, the environmental impact of experimental CO_2 utilization is probably going to be minimal. Even so, it's crucial to think about the possible effects and take precautions against them. The environmental impact of utilizing CO_2 for testing can be lessened, for instance, by using smaller volumes of CO_2, making sure that it is properly contained and disposed of, and using renewable energy for any related activities. Several concepts related to carbon capture, use, and storage (CCUS) have been put forth in earlier studies on the management of CO_2. The plan is to use pyrolyzed biochar to capture CO_2 directly from the air [47], use the catalytic chemical looping reaction to reduce industrial CO_2 emissions [48], and even use the CO_2 for the CO_2-expanded fluid extraction method in microalgae oil [49].

3.3. Catalytic Activity

From the three possible alkali earth metal and alkali metal catalysts, the presence of potassium had the greatest literature precedent in woody biomass torrefaction-pyrolysis. No known studies have explored how KCl affects the torrefaction-pyrolysis of woody biomass in a complete carbon dioxide atmosphere. Figure 4 shows the TGA/DTG curves of Poplar and Fir of different particle sizes impregnated with 0.05 M of KCl. It can be seen that the TGA degradation profile of these wood types is very similar, regardless of the particle size. There are three main degradation peaks on the DTG. There is a maximum of only 3% difference in weight loss between samples impregnated with KCl and raw wood. The presence of KCl causes less mass loss during torrefaction and more rapid degradation during pyrolysis for Poplar. During torrefaction, the weight loss of the sample impregnated with KCl was approximately 63.10% vs. 68.13% for the raw sample. The predicted error of the instrument is approximately 3%, therefore, the observed difference was deemed negligible. Upon increasing the concentration of KCl by two-fold to 0.1 M, the TGA and DTG curves (Figure 5) reveal a decrease of nearly 6.5% in mass loss during torrefaction with respect to the raw sample. This indicates that the presence of potassium in woody biomass causes a decrease in weight loss during torrefaction and an increase in the rate of degradation during pyrolysis.

In Figure 6, TGA and DTG curves of Poplar impregnated with different concentrations of NaCl are overlayed with the raw wood sample. The sample impregnated with 0.054 M of NaCl showed almost the same mass loss (69.47 wt.%) as the control (68.13 wt.%). When the concentration used was increased to 0.1 M, no difference was observed between the impregnated sample and the raw wood. In conclusion, NaCl did not have an observable impact on the thermal degradation of the woody biomass. Using the same procedures as the impregnations of NaCl and KCl, Poplar samples with a particle size of 500 μm were impregnated with a 0.054 M solution of $MgCl_2$. The DTG and TGA curves of these samples are presented in Figure 7. There was a very distinct difference between the raw wood and samples impregnated with $MgCl_2$ during both torrefaction and pyrolysis. Foremost, the presence of $MgCl_2$ increases weight loss during torrefaction by nearly 4.5%, from 68.13 wt.% for the raw wood to 72.60 wt.% for the impregnated sample. During pyrolysis, the initial degradation is similar between the raw wood and the impregnated sample. This degradation is presumed to be associated with the remaining crystalline cellulose regions in the biomass material. It is interesting to note that the complete degradation attributed to the Boudouard equilibrium is not present for samples impregnated with $MgCl_2$. Instead, the impregnated sample only attains complete degradation during combustion, as expected under a nitrogen atmosphere. The test was repeated with samples impregnated with 0.025 M and 0.012 M of $MgCl_2$, resulting in identical curves to those of the sample impregnated with 0.054 M of $MgCl_2$. This indicates that there is a saturation point for the effect of $MgCl_2$ in woody biomass. In order to determine the saturation point, Poplar samples were impregnated with 0.006 M and 0.003 M solutions. The sample impregnated with 0.003 M of $MgCl_2$ displays slightly more degradation before combustion. These concentrations were repeated with Fir with similar results in further discussion.

The lack of the Boudouard reaction for samples impregnated with $MgCl_2$ has not been extensively reported in the literature but was also observed by Aho et al. in the gasification of acid-washed pine doped with magnesium, potassium, and sodium [50]. The gasification was performed at 805 °C in an atmosphere containing 50% of N_2 and 50% of CO_2, in a TGA, with a heating rate of 50 °C/min. The rate of gasification of magnesium-doped samples lasted nearly five times longer than the rate of control, resulting in the need for further studies. However, some factors that could be contributing to the inhibition of the Boudouard equilibrium in the presence of $MgCl_2$ are the slow reaction kinetics of the Boudouard equilibrium in combination with the faster reaction kinetics of the magnesium ion in the presence of carbon dioxide in the redox reaction shown in Equation (2).

$$2Mg^{2+} + CO_2 \rightarrow 2MgO + C \tag{2}$$
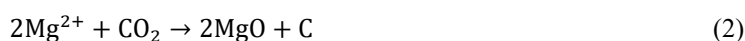
This reaction is very thermodynamically favorable and commonly reported in the literature, as magnesium is an element capable of oxidation in the presence of CO_2. Frost et al. determined that the combustion of magnesium

in the air would begin to form magnesium oxide at 500 °C, and the reaction rate would increase at 560 °C. Under carbon dioxide, however, the enthalpy of the reaction is −810.1 kJ [51]. Barabulica et al. reported the reaction of magnesium in various mixtures of nitrogen and carbon dioxide and determined that no reaction occurred in atmospheres containing less than 10% carbon dioxide. As the carbon dioxide concentration increased, the reaction rate increased [52]. However, this is not the only reaction possible for an explanation of this phenomenon. While it is likely to be occurring, the low concentration of magnesium present in the sample should not be enough to outcompete all signs of the Boudouard reaction, and therefore, it is thought that the (2+) charge of the magnesium could play a role in this effect. Moreover, magnesium's affinity to bind to oxygen could cause the formation of a more oxygen rich material at the end of torrefaction, leaving less carbon to react in the Boudouard reaction and delay its occurrence to a time and temperature outside of the range of this study. In order to confirm any of these hypotheses, future studies need to be conducted to analyze the composition of materials after torrefaction using FTIR and py-GCMS during gasification.

The main novelty of the work presented herein lies in the lack of the Boudouard reaction for samples impregnated with $MgCl_2$. The evidence in the experiments performed points to an inhibition of the Boudouard reaction in the presence of Mg^{2+}, which was not observed with any of the other salts investigated. As discussed earlier, this finding is in line with reports on the inhibition of the Boudouard reaction during the gasification of pine in the presence of magnesium [50]. It has also been shown that the presence of Mg^{2+} during the pyrolysis of sawdust favored crosslinking and repolymerization reactions of pyrolysis intermediates, resulting in an increased biochar yield and the formation of the stable metal oxide MgO [53]. One possible mechanistic explanation for these observations is that the crosslinking, condensation, and repolymerization reactions catalyzed by magnesium happen at a faster rate than the Boudouard reaction, offsetting its effect and resulting, globally, in a higher rate of biochar/solid carbon formation than the rate of solid carbon conversion to CO through the Boudoard reaction.
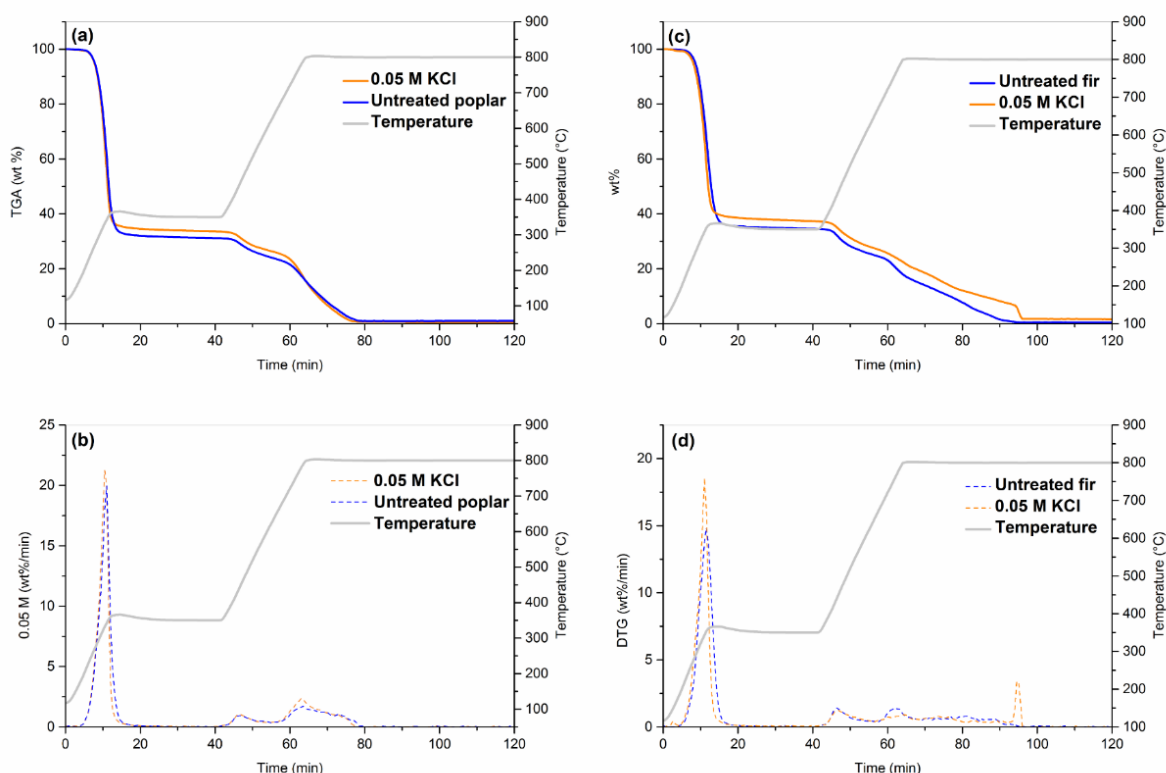

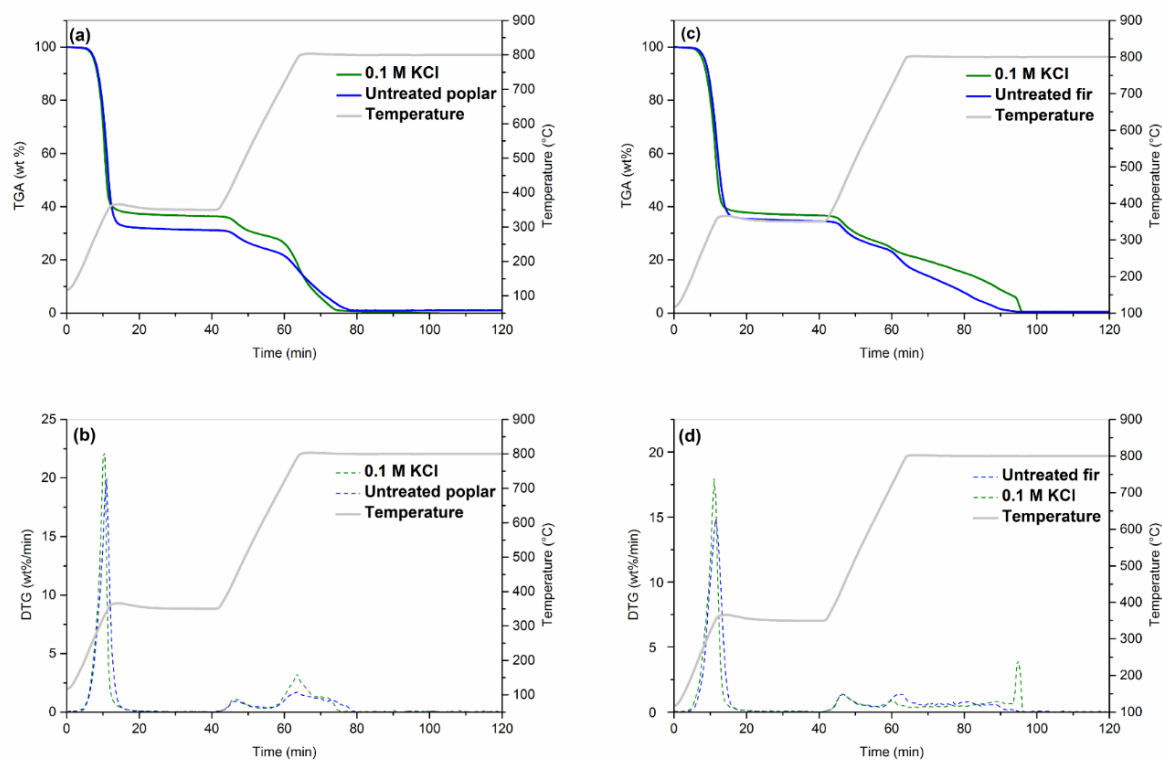**Figure 4.** KCl 0.05 M impregnated of TGA (**a**) DTG, (**b**) curves of Poplar and TGA, (**c**) DTG, (**d**) curves of Fir.

Figure 5. KCl 0.1 M impregnated of TGA (**a**) DTG, (**b**) curves of Poplar and TGA, (**c**) DTG, (**d**) curves of Fir.
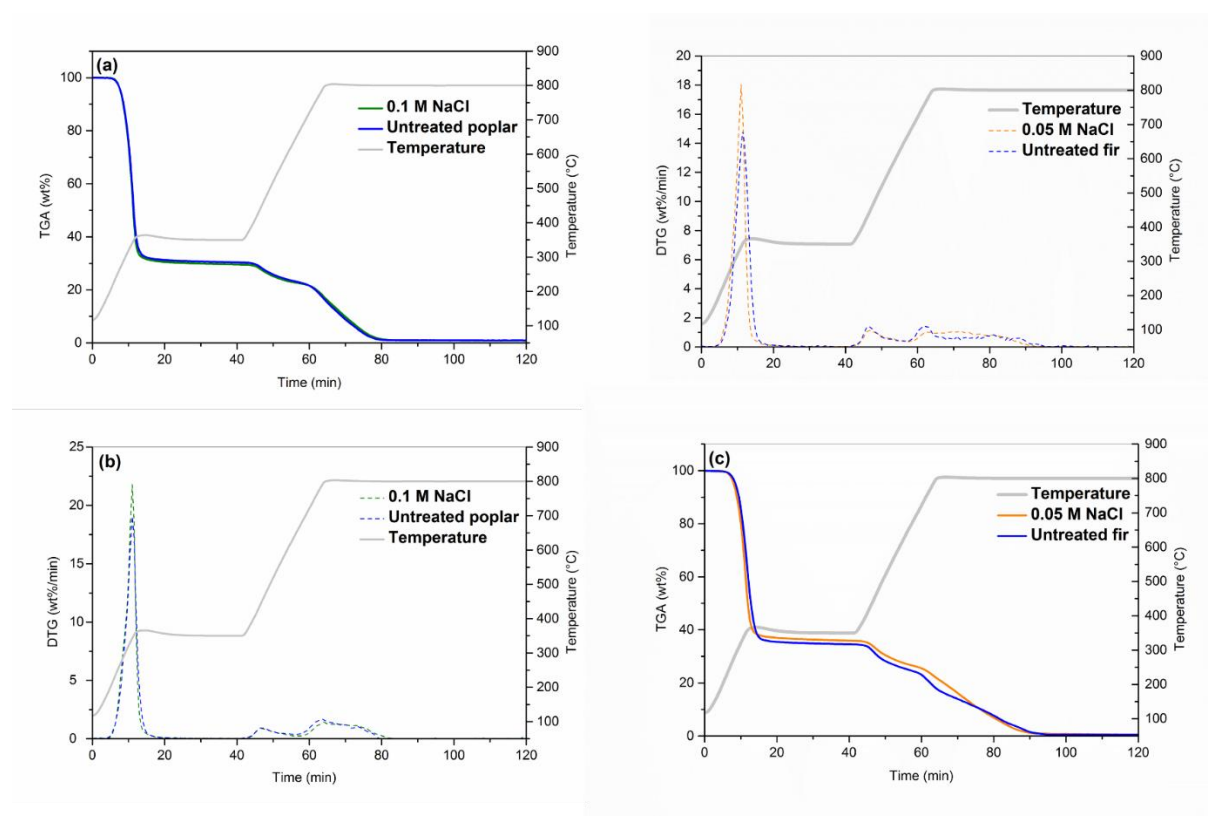

Figure 6. NaCl 0.1 M impregnated of TGA (**a**) DTG, (**b**) curves of Poplar and NaCl 0.05 M impregnated of TGA, (**c**) DTG, (**d**) curves of Fir.
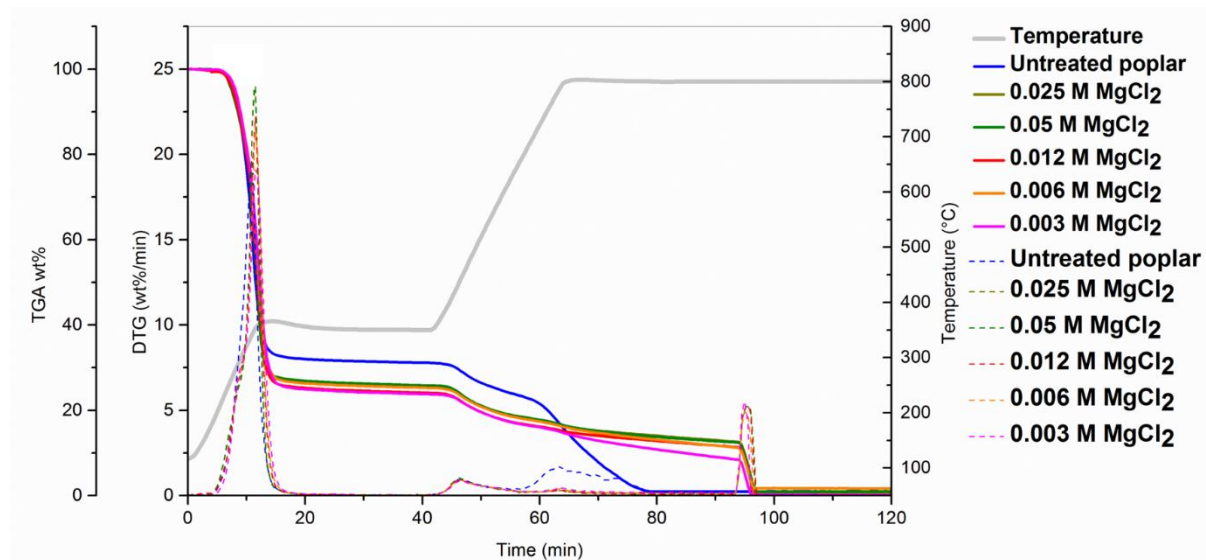
Figure 7. TGA and DTG curves of Poplar impregnated with different concentrations of MgCl₂.

3.4. Interaction Effect

The interaction effect from the catalysts can be defined as either synergistic or antagonistic. Synergistic effects are defined as a greater and/or faster degradation of the material treated with external material, in this study, such as the catalyst, than the untreated sample (raw) in a certain range, while, antagonistic effects are defined as less and/or slower degradation of the material treated with the catalyst than that of the untreated sample [54,55]. If degradation is the same for both treated and untreated samples, it can be said that there is no interaction effect between the catalyst and the sample [54]. Aniza et al. [54] analyzed the interaction effect of three extracted components from microalgae (lipid, protein, and carbohydrate) during thermochemical conversion using TGA. According to the study, the synergistic impact happens when glucose signals as a dominant molecule in the carbohydrate model, accounting for roughly 50% of the total mass loss. These findings motivate the current study's use of catalyst impregnation to examine the interaction effect within woody biomass. Figure 8A shows the TGA and DTG curves of Poplar at a particle size of 500 μm after impregnation with different concentrations of KCl. It can be noted that the curve for the sample impregnated with 0.1 M KCl is the most different from the control, with the curve for the sample impregnated with 0.025M KCl being the most similar.

To determine how impregnation with 0.1 M KCl affects both torrefaction and pyrolysis separately, the graph can be analyzed in two parts, with enlarged graphs of torrefaction (Figure 8B) and pyrolysis (Figure 8C). In Figure 8B, the DTG curve for the sample impregnated with 0.1 M of KCl is shifted left of the control, with a sharper peak. This shift indicates degradation is happening more rapidly and at a lower temperature, leading to the conclusion that KCl has a synergistic catalytic effect on Poplar for samples impregnated with 0.1 M and 0.05 M of KCl. The effect increases with increasing concentrations of KCl. It can be noted, however, that there appears to be less mass loss in samples containing KCl than in the control during torrefaction. This was similarly reported by a multitude of sources in both complete nitrogen and oxidative atmospheres and confirms that the impregnation of potassium contributes to weakening linkages and hydrogen bonding between cellulose and hemicellulose components [22,24]. In a purely speculative way, it can be proposed that the chemical pathway for K^+ to disrupt hydrogen bonds in cellulose and hemicelluloses occurs by replacing H^+, therefore opening the microfibril structure and making it more susceptible to thermal degradation.

The pyrolysis step can be observed in Figure 8C, where KCl appears to have a synergistic effect on the degradation of Poplar at approximately 800 °C. While this temperature is attributed to gasification in a carbon dioxide atmosphere, the implications of potassium at this temperature in lignocellulosic biomass are not commonly reported. However, Menendez et al. observed the microwave-assisted pyrolysis of coffee hulls with carbon dioxide and determined that potassium-rich samples catalyze self-gasification reactions like the Boudouard equilibrium [56]. It could be hypothesized that the degradation of potassium-rich samples during torrefaction leads to a more carbon-rich char participating in Boudouard gasification a enhancing the rate of degradation.
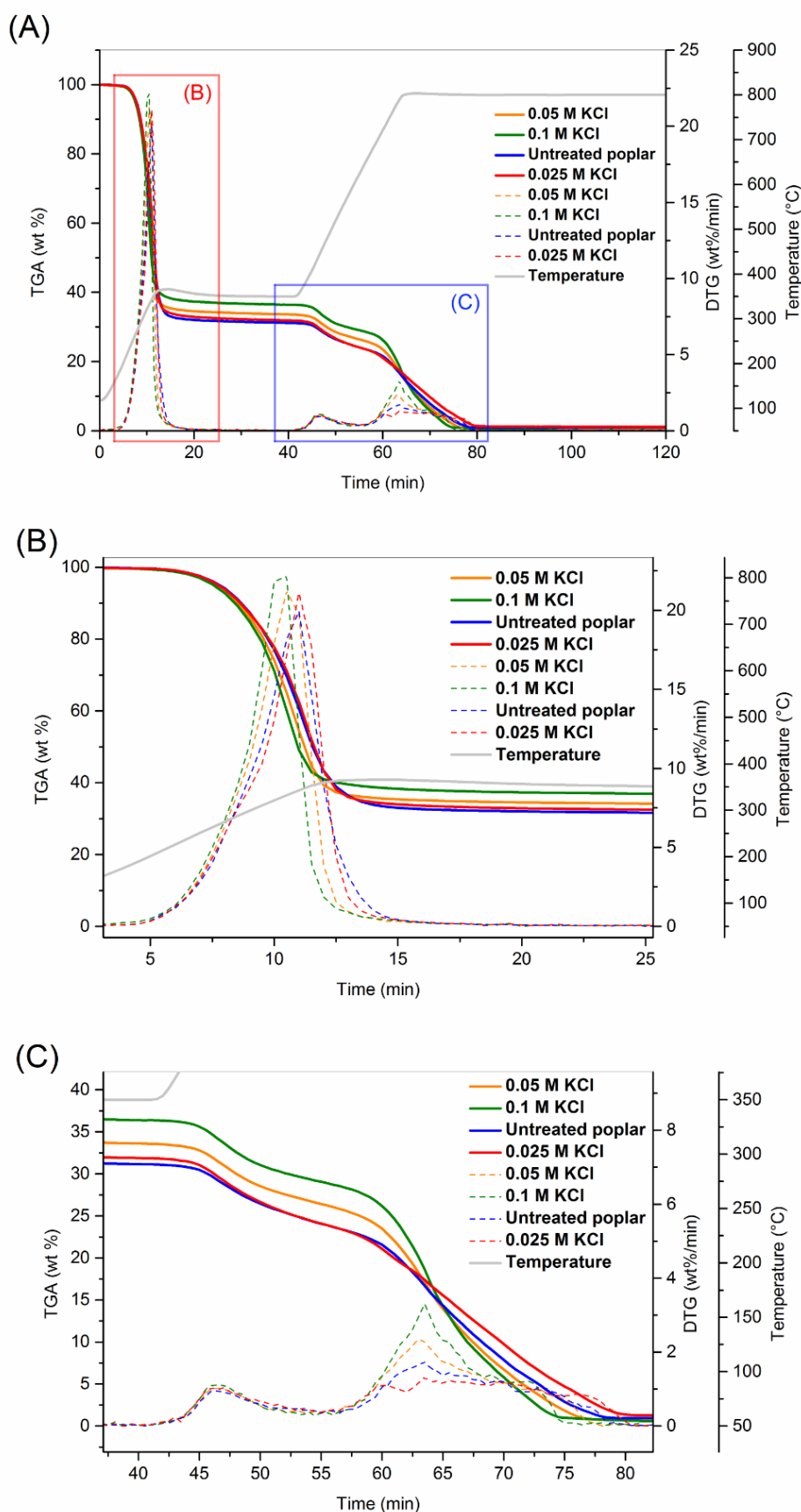
Figure 8. (**A**) TGA and DTG curves of Poplar impregnated with 0.1 M, 0.05 M, and 0.025 M solutions of KCl, (**B**) Enlarged section (torrefaction) Poplar, and (**C**) Enlarged section (pyrolysis) Poplar.

These results can be contrasted with Figure 9A, which shows the TGA and DTG curves of Fir samples impregnated with KCl at different concentrations. While Figure 9B shows a clear synergistic effect during

torrefaction similar to the one observed with Poplar, in Figure 9A, an antagonistic effect can be seen during the pyrolysis (~800 °C) of Fir samples impregnated with KCl. This indicates a fundamental difference between Fir and Poplar. Dupont et al. studied the gasification kinetics of different hard and soft woods. It was found that higher concentrations of silica had an inhibitory effect on gasification reactions despite the catalytic presence of potassium because of the formation of potassium silicates. The concentration of inorganic salts in both Poplar and generalized "soft woods" were measured and it was found that soft woods have approximately 3619 mg Si/kg of dry biomass while Poplar has 763 mg Si/kg of dry biomass (nearly a 5-fold difference in silica content) [57]. It could be hypothesized that the silica content in Fir could have an inhibitory effect on the gasification reactions during pyrolysis.
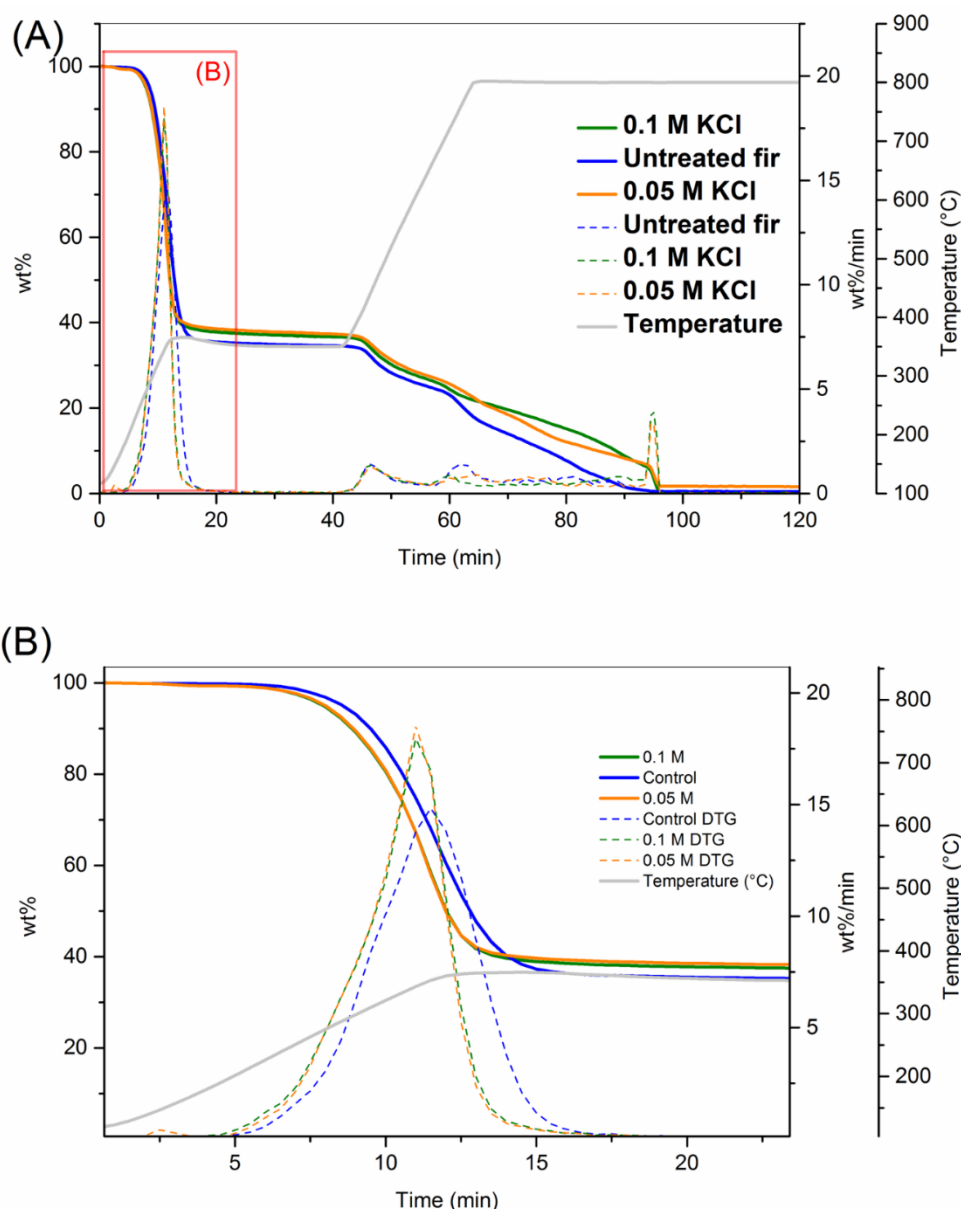
Figure 9. (**A**) TGA and DTG curves of Fir impregnated with 0.1 M, 0.05 M of KCl, and (**B**) Enlarged section (torrefaction) Fir.

In Figure 10A, the torrefaction-pyrolysis curve of NaCl impregnated Poplar samples is shown. It was stated that the difference in results is negligible, indicating that NaCl does not have strong effects on the torrefaction-pyrolysis of Poplar in a carbon dioxide environment. When looking at only the torrefaction curve of NaCl impregnated samples vs the control in Figure 10B, it can be seen that there are very slight synergistic effects in the DTG curve but that these are negligible. The same can be noticed in the Figure 10C with the pyrolysis of these samples—there is a slight synergistic effect around 800 °C, but by a negligible amount. The TGA-DTG curve of NaCl impregnated Fir samples can be seen in Figure 11A. In Figure 11B, the torrefaction step presents a slight

synergistic effect, while there is a slight antagonistic effect from the NaCl during the Pyrolysis step in Figure 11A. This indicates the effects of NaCl in the pyrolysis of impregnated Fir to be the opposite of impregnated Poplar, although both are so slight that they are negligible.
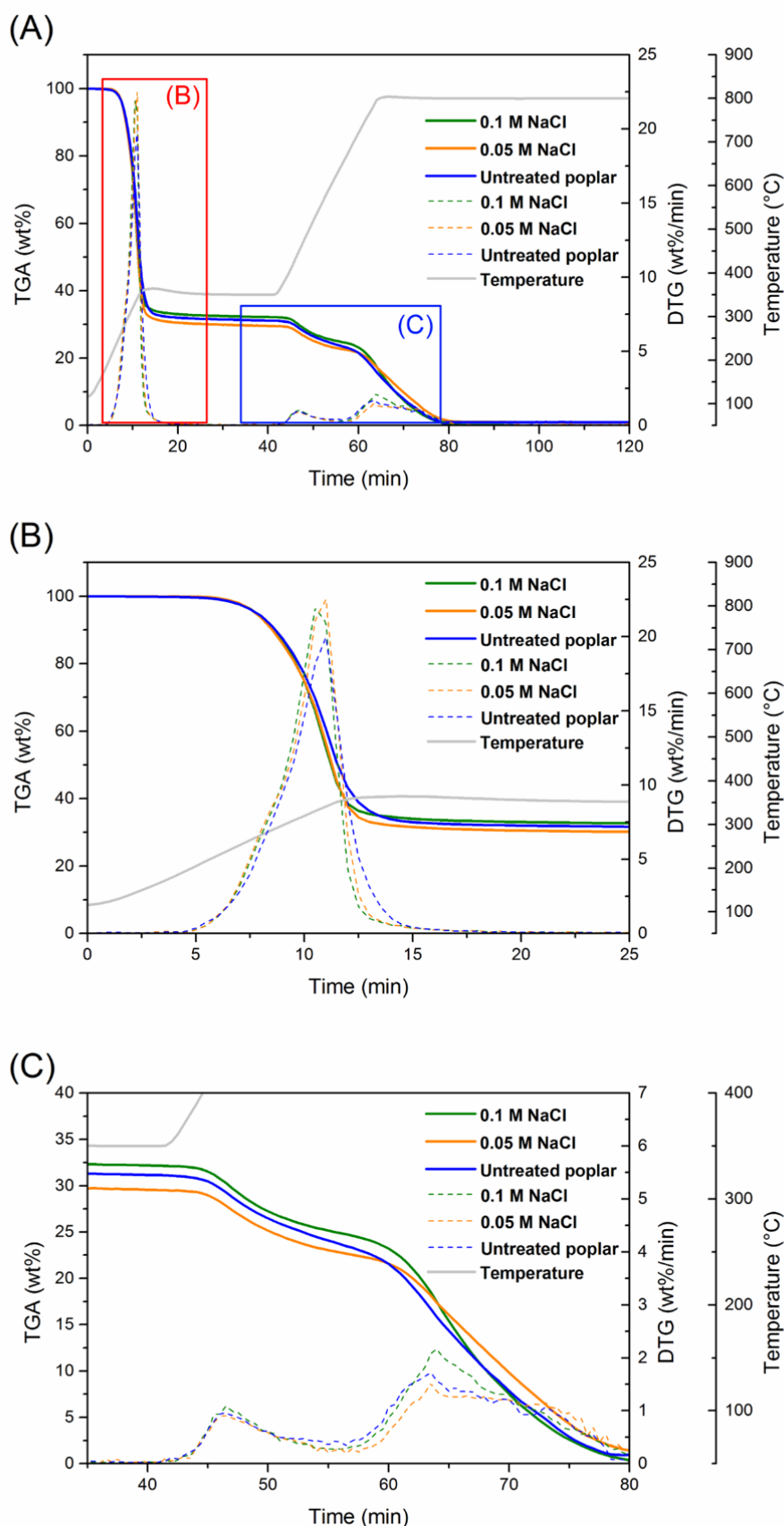

Figure 10. (**A**) Torrefaction-Pyrolysis TGA and DTG curves of Poplar impregnated NaCl with 0.1 M and 0.05 M, (**B**) Enlarged section (torrefaction) Poplar, and (**C**) Enlarged section (pyrolysis) Poplar.
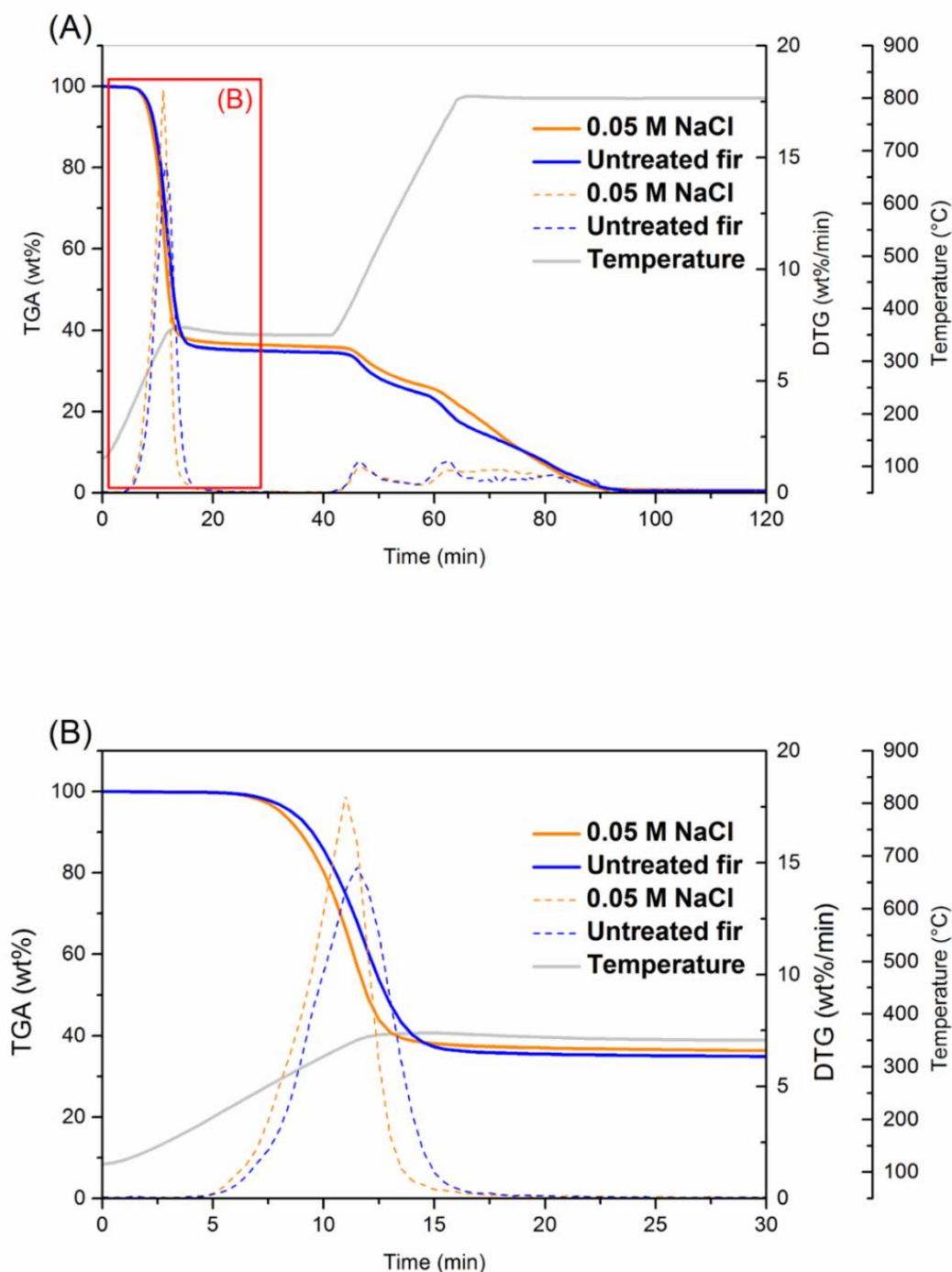
Figure 11. (**A**) Torrefaction-pyrolysis curve of Fir treated with NaCl and (**B**) Torrefaction curve of Fir treated with NaCl.

Figure 12 shows the torrefaction curve of $MgCl_2$-impregnated Poplar samples as an expanded graph of the entire torrefaction-pyrolysis seen in Figure 7. While $MgCl_2$ increases weight loss during the torrefaction step, there is a slight antagonistic effect of $MgCl_2$ on the rate of torrefaction see in Figure 12 with the DTG curve of the impregnated samples showing a cellulose peak shift right (indicating higher temperatures for degradation) and the appearance of a hemicellulose shoulder in the impregnated samples that is not shown in the impregnated samples. This indicates that $MgCl_2$ affects the degradation of hemicelluloses—similar to those results by Kawamoto et al. [58]. These results can be contrasted with those with Fir in Figure 13. Figure 13A shows the entirety of the $MgCl_2$-impregnated Fir torrefaction-pyrolysis graph which appears similar to that of $MgCl_2$-impregnated Poplar. However, in Figure 13B, the enlarged torrefaction TGA and DTG curves show $MgCl_2$ to have a synergistic effect with the lack of a hemicellulose shoulder.
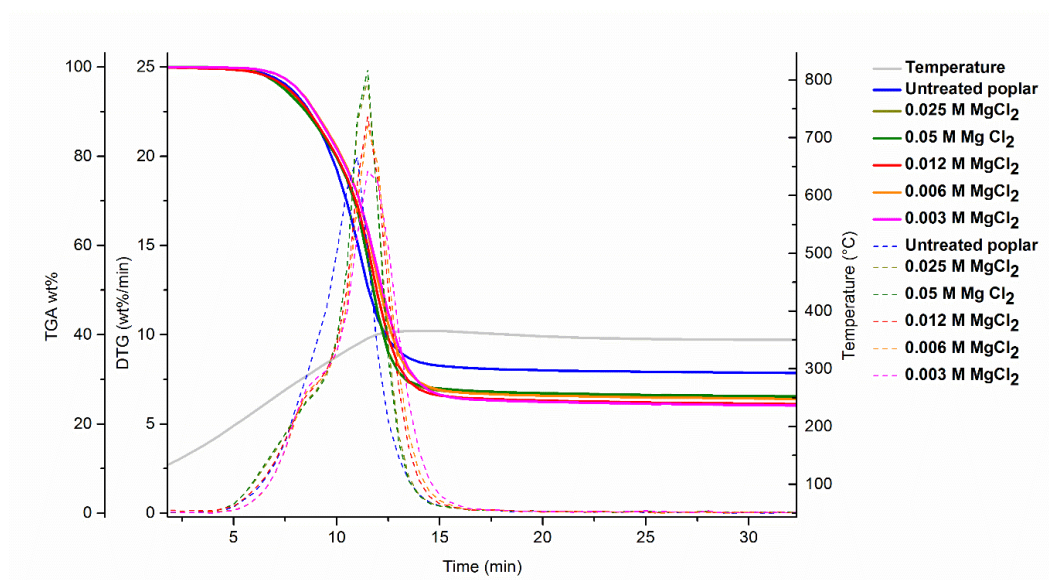
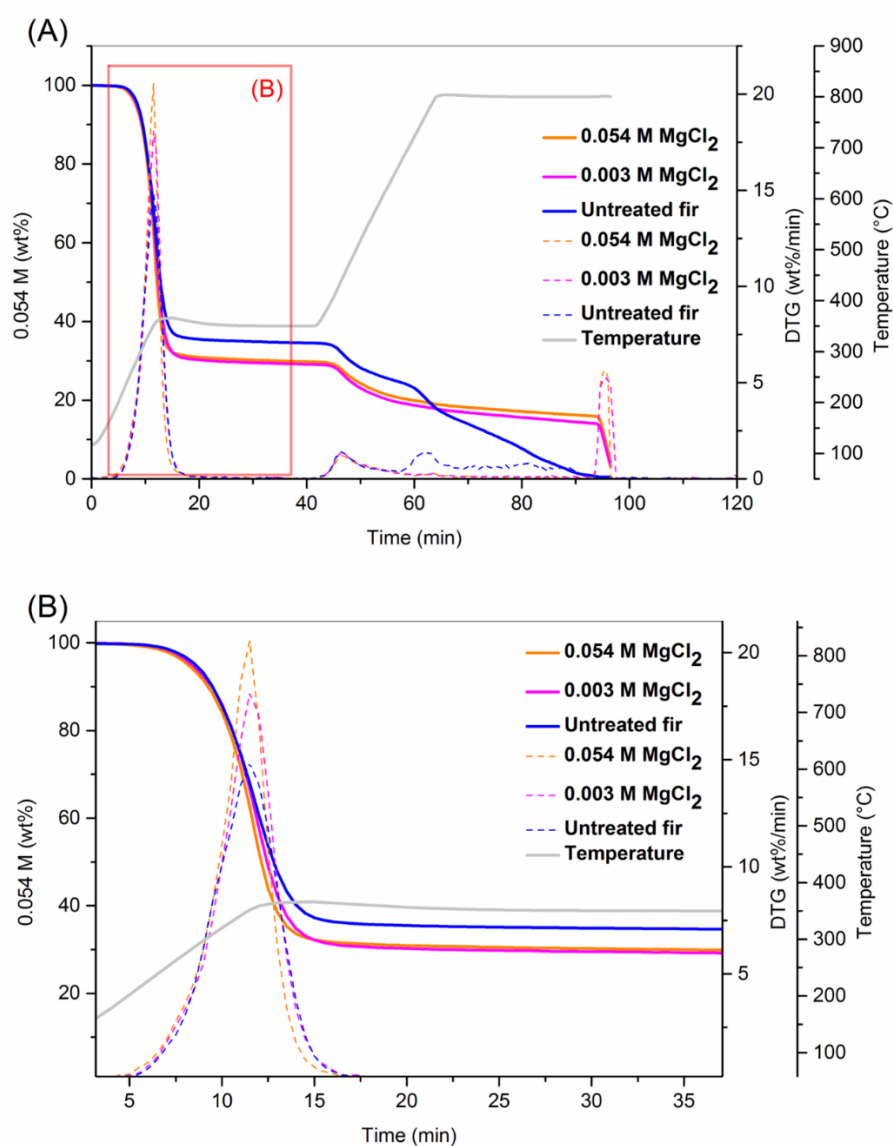**Figure 12.** Torrefaction curve of Poplar treated with MgCl₂ solutions.

Figure 13. (**A**) TGA-DTG curves of torrefaction-pyrolysis of Fir treated with MgCl₂ and (**B**) TGA DTG curves of torrefaction of Fir treated with MgCl₂.

A comparison of all catalytic impregnations of Poplar wood can be found in Figure 14. During torrrefaction, a synergistic effect is observed from impregnation with KCl with an antagonistic effect from impregnation with MgCl$_2$—where the hemicellulose shoulder is much more prominent than in the control sample seen in Figure 15A. This appearance of a broad shoulder could indicate the prolonged degradation of hemicellulose with a delayed degradation of cellulose when magnesium is present. During the pyrolysis segment, all impregnations displayed similar degradation rates as the control, but gasification was accelerated when exposed to KCl and inhibited when exposed to MgCl$_2$ as seen in Figure 15B. Catalytic activity when impregnated in Fir was drastically different from that of Poplar as seen in Figure 16. During the torrefaction step shown in Figure 17A, KCl has a greater synergistic effect than MgCl$_2$—while MgCl$_2$ results in greater mass loss. During the pyrolysis step in Figure 17B, the rate of degradation is similar for all samples. Upon gasification, MgCl$_2$ samples show an absence of gasification, while KCl shows an antagonistic effect in comparison to NaCl and the raw samples.

In terms of ionic reaction, when comparing the effects of KCl, NaCl, and MgCl$_2$ during the torrefaction of wood, the different behavior observed can be attributed primarily to the cations K$^+$, Cl$^+$, and Mg^{2+} since the anion Cl$^-$ is the same in all cases. For the Boudouard reaction inhibition, as discussed previously, it is believed that the charge (+2) of magnesium is critical in catalyzing condensation, crosslinking, and repolymerization reactions. Likewise, K$^+$ is believed to disrupt H-bonding while Na$^+$ doesn't have that effect, which could be related to specific cation properties such as radius. In order to fully elucidate these factors, a comprehensive screening of a series of compounds would be necessary.
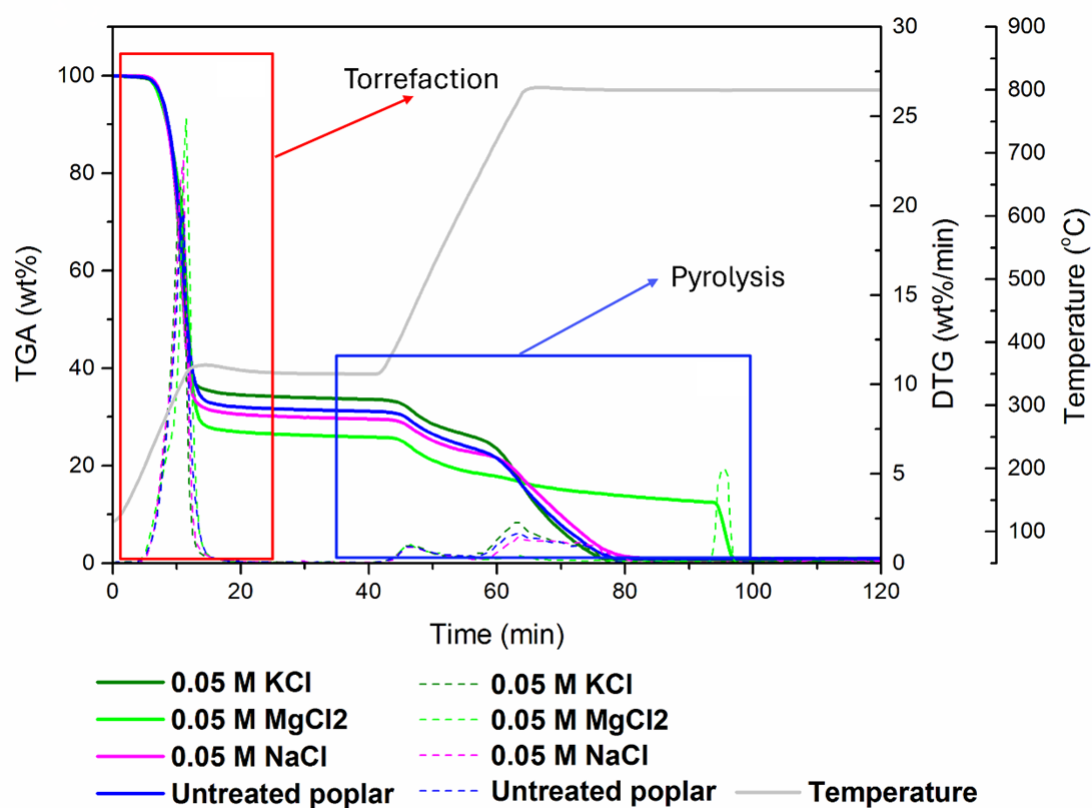

Figure 14. Torrefaction-pyrolysis TGA and DTG curves of Poplar treated with MgCl$_2$, NaCl, KCl.
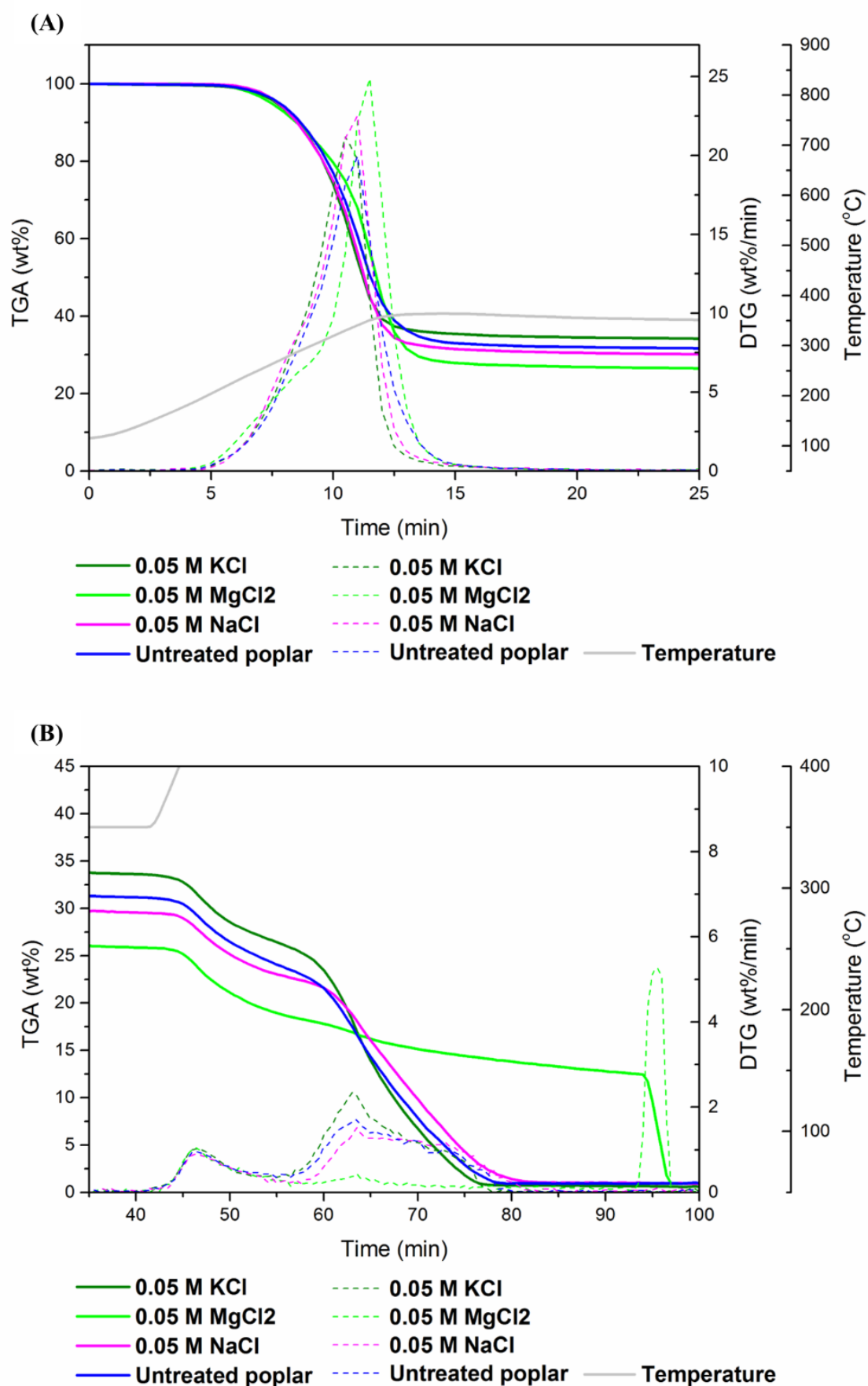
Figure 15. (**A**) TGA-DTG torrefaction curve of Poplar treated with $MgCl_2$, NaCl, KCl and (**B**) TGA-DTG pyrolysis curve of Poplar treated with $MgCl_2$, NaCl, KCl.
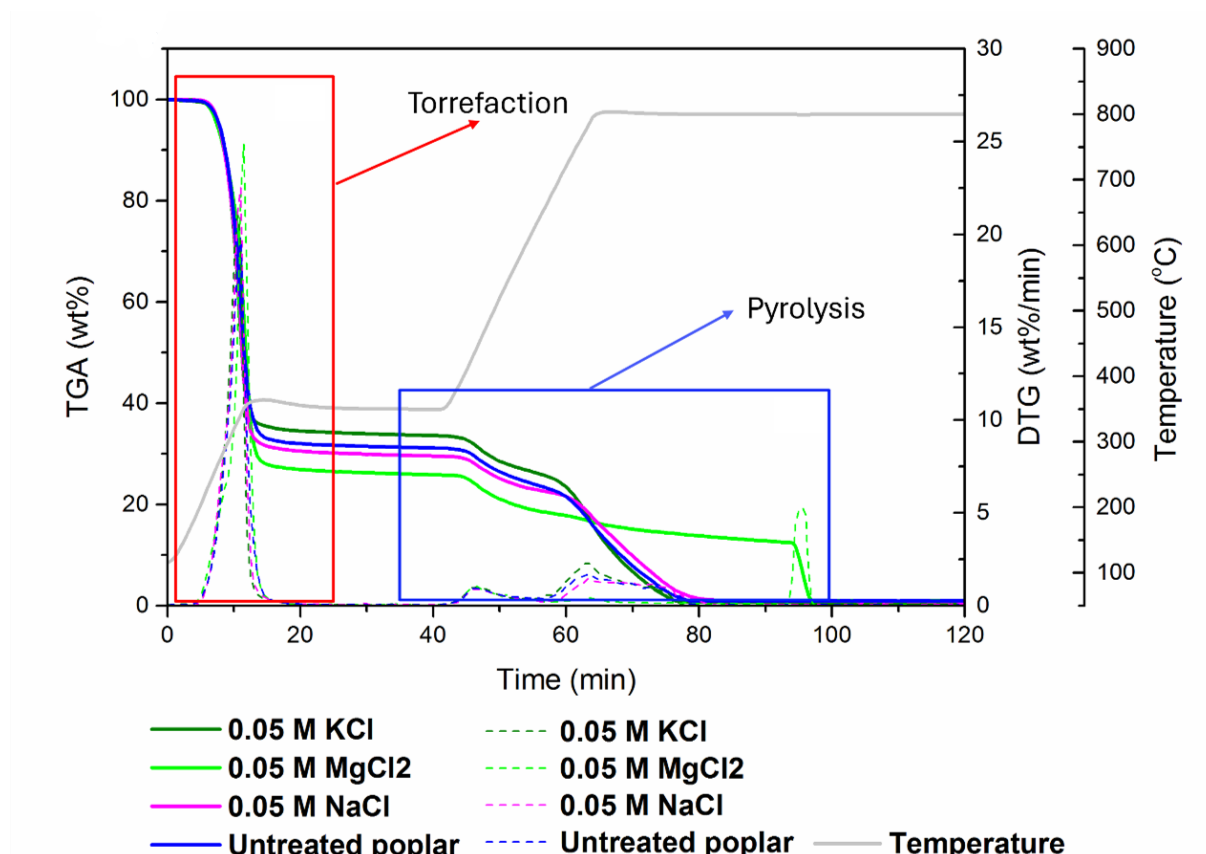
Figure 16. Torrefaction-pyrolysis TGA and DTG curves of Fir treated with $MgCl_2$, NaCl, KCl.
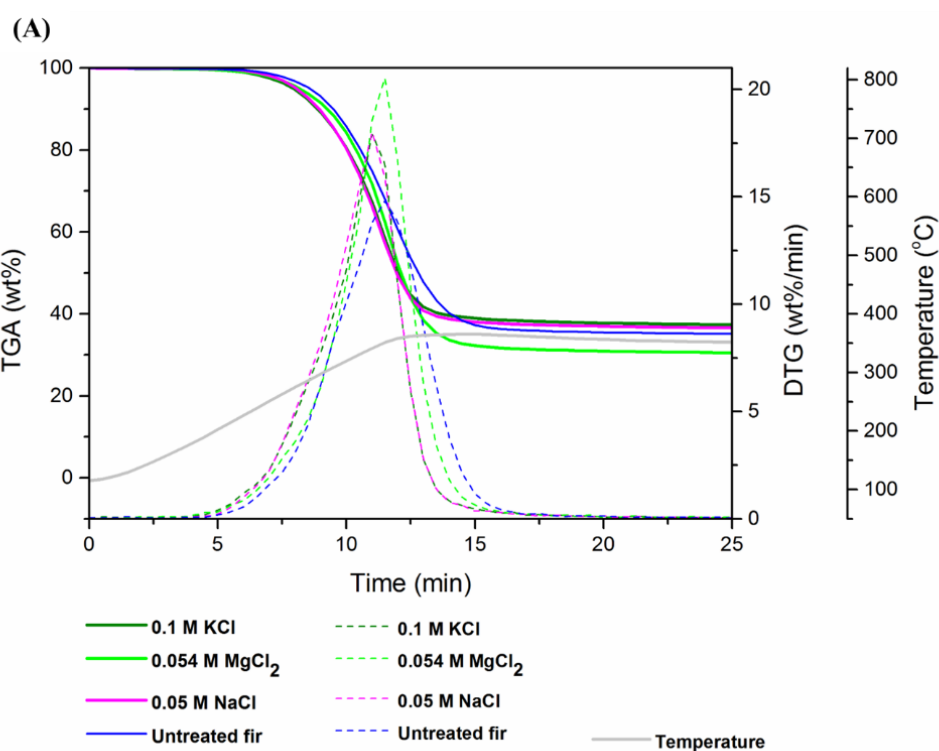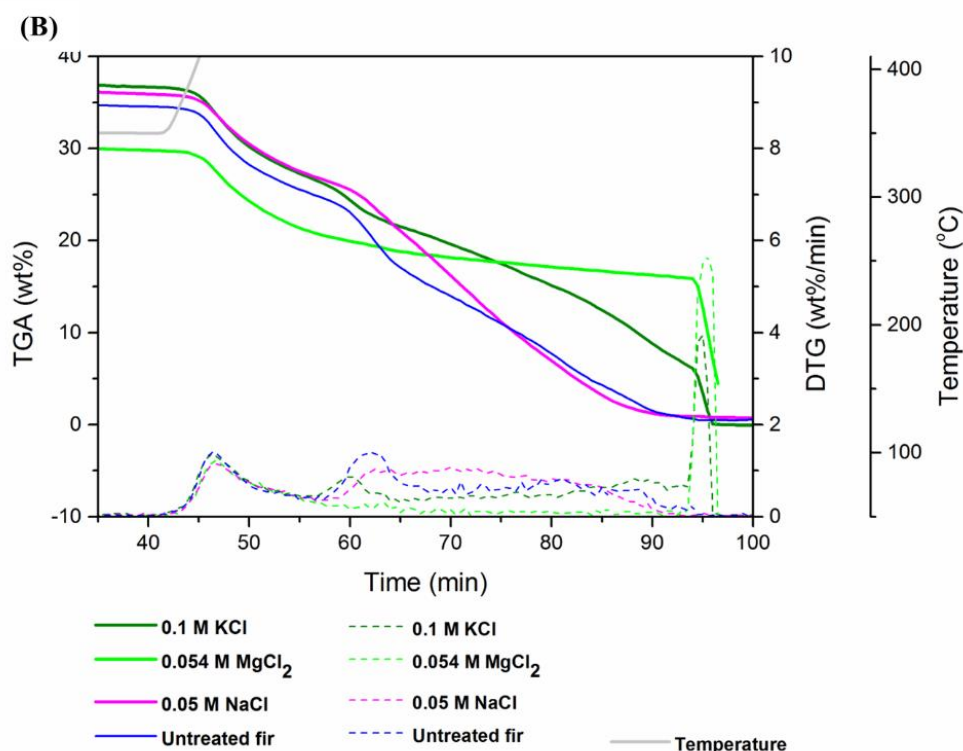

Figure 17. *Cont.*

Figure 17. (**A**) TGA-DTG torrefaction curve of Fir treated with $MgCl_2$, NaCl, KCl and (**B**) TGA-DTG pyrolysis curve of Fir treated with $MgCl_2$, NaCl, KCl.

4. Conclusions

Poplar and Fir wood species have different chemical compositions, which cause a difference in catalytic efficiency when exposed to different alkali and alkaline earth metals—namely, K, Na, and Mg. Both Poplar and Fir species show self-gasification in a carbon dioxide environment at temperatures greater than 700 °C. When employing catalytic thermal conversion to produce biofuel, the aK-catalyst outperforms the other catalyst materials (K, Na, and Mg) in a CO_2 atmosphere. When the K-catalyst is impregnated in Fir, the C-O-C compound decreases. This is in line with the fact that Fir's hemicellulose content (22.43 wt.%) is double that of Poplar (12.18 wt.%), which results in a less thermally stable molecule. This suggests that K may be able to have less interaction with CO_2 and better thermal resistance. K-impregnated Poplar samples showed faster self-gasification, possibly indicating a more carbon-rich state of biochar after torrefaction. Na-impregnated Poplar and Fir samples exhibited no self-gasification at magnesium loadings as little as 0.003 M impregnations. An explanation for this is currently unclear, and the observation is limited. The Boudouard equilibrium was detected in the thermal conversion at 780 °C. Furthermore, during torrefaction and pyrolysis, the synergistic impact is more noticeable when the K-catalyst is employed than when Na and Mg are used. This suggests that the K-catalyst's performance in this study is thermally stable. Further studies are suggested to be conducted at higher concentrations and using py-GCMS for an understanding of the underlying mechanisms in CO_2.

Author Contributions: E.W.S. experimental investigation, writing—original draft preparation; R.A. conceptualization, methodology, writing—original draft preparation; A.P. conceptualization, supervision, validation; R.L.Q. conceptualization, supervision, writing—reviewing; B.C. experimental; M.P., supervision, validation; W.-H.C. supervision, validation. All authors have read and agreed to the published version of the manuscript.

Institutional Review Board Statement: Not applicable.

Informed Consent Statement: Not applicable.

Data Availability Statement: Not applicable.

Conflicts of Interest: The authors declare no conflict of interest.

References

1. Nullis, C. WMO Greenhouse Gas Bulletin. More Bad News for the Planet: Greenhouse Gas Levels Hit New Highs. Switzerland: World Meteorological Organization 2022. Available online: https://wmo.int/news/media-centre/more-bad-news-planet-greenhouse-gas-levels-hit-new-highs (accessed on 30 April 2025).

2. Aniza, R.; Chen, W.-H.; Pétrissans, A.; et al. A review of biowaste remediation and valorization for environmental sustainability: Artificial intelligence approach. *Environ. Pollut.* **2023**, *324*, 121363. https://doi.org/10.1016/j.envpol.2023.121363.

3. Vuppaladadiyam, A.K.; Vuppaladadiyam, S.S.V.; Sahoo, A.; et al. Bio-oil and biochar from the pyrolytic conversion of biomass: A current and future perspective on the trade-off between economic, environmental, and technical indicators. *Sci. Total Environ.* **2023**, *857*, 159155. https://doi.org/10.1016/j.scitotenv.2022.159155.

4. Congyu, Z.; Jin, F.; Yong, Z.; et al. Life Cycle Assessment of Microalgal Carbon Fixation and Torrefaction for Carbon Neutralization: A State-of-the-Art Review. *Green Energy Fuel Res.* **2024**, *1*, 23–38. https://doi.org/10.53941/gefr.2024.100004.

5. Tubbesing, C.L.; Lara, J.D.; Battles, J.J.; et al. Characterization of the woody biomass feedstock potential resulting from California's drought. *Sci. Rep.* **2020**, *10*, 1096. https://doi.org/10.1038/s41598-020-57904-z.

6. Lin, S.L.; Aniza, R.; Lee, Y.Y.; et al. Reduction of traditional pollutants and polychlorinated dibenzo-p-dioxins and dibenzofurans emitted from a diesel engine generator equipped with a catalytic ceramic fiber filter system. *Clean Technol. Environ. Policy* **2018**, *20*, 1297–1309. https://doi.org/10.1007/s10098-018-1559-6.

7. Lee, Y.Y.; Lin, S.L.; Aniza, R.; et al. Reduction of atmospheric PM2.5 level by restricting the idling operation of buses in a busy station. *Aerosol Air Qual. Res.* **2017**, *17*, 2424–2437. https://doi.org/10.4209/aaqr.2017.09.0301.

8. Aniza, R.; Chen, W.-H.; Herrera, C.J.A.; et al. Bioenergy and bioexergy analyses with artificial intelligence application on combustion of recycled hardwood and softwood wastes. *Renew. Energy* **2024**, *237*, 121885. https://doi.org/10.1016/j.renene.2024.121885.

9. Pétrissans, A.; Lin, Y.-Y.; Nguyen, T.N.; et al. Influence of the heating rate on the thermodegradation during the mild pyrolysis of the wood. *Wood Mater. Sci. Eng.* **2023**, *18*, 412–421. https://doi.org/10.1080/17480272.2022.2039289.

10. Aniza, R.; Petrissans, A.; Petrissans, M. Multifunctional Nanotechnology Application for Wood Properties Enhancement: Adhesive and Coating. In *Nanomaterials Additives in Bioadhesives for Wood Composites*; Antov, P., Lubis, M.A.R., Lee, S.H., Taghiyari, H.R., Eds.; Springer Nature: Singapore, 2025; pp. 135–149.

11. Aniza, R.; Petrissans, A.; Petrissans, M. Life-Cycle Assessment of Nanoparticle in Wood Adhesive and Coating: The State-of-The Art. In *Nanomaterials Additives in Bioadhesives for Wood Composites*; Antov, P., Lubis, M.A.R., Lee, S.H., Taghiyari, H.R., Eds.; Springer Nature: Singapore, 2025; pp. 231–248.

12. Andrade Breves, R.; Ajiola, D.; de Vasconcelos Vieira Lopes, R.; et al. Bio-Based Polyurethane Composites from Macauba Kernel Oil: Part 1, Matrix Synthesis from Glycerol-Based Polyol. *J. Compos. Sci.* **2024**, *8*, 363.

13. Aniza, R.; Chen, W.-H.; Kwon, E.E.; et al. Lignocellulosic biofuel properties and reactivity analyzed by thermogravimetric analysis (TGA) toward zero carbon scheme: A critical review. *Energy Convers. Manag. X* **2024**, *22*, 100538. https://doi.org/10.1016/j.ecmx.2024.100538.

14. Chen, W.-H.; Escalante, J.; Xuan, L.L.; et al. Catalytic co-gasification optimization of biomass and polyethylene wastes in oxygen-rich environments. *Fuel* **2025**, *381*, 133214. https://doi.org/10.1016/j.fuel.2024.133214.

15. McKendry, P. Energy production from biomass (part 1): Overview of biomass. *Bioresour. Technol.* **2002**, *83*, 37–46. https://doi.org/10.1016/S0960-8524(01)00118-3.

16. Chen, W.-H.; Lin, B.-J.; Lin, Y.-Y.; et al. Progress in biomass torrefaction: Principles, applications and challenges. *Prog. Energy Combust. Sci.* **2021**, *82*, 100887. https://doi.org/10.1016/j.pecs.2020.100887.

17. Acharya, B.; Dutta, A.; Minaret, J. Review on comparative study of dry and wet torrefaction. *Sustain. Energy Technol. Assess.* **2015**, *12*, 26–37. https://doi.org/10.1016/j.seta.2015.08.003.

18. Wang, L.; Riva, L.; Skreiberg, Ø.; et al. Effect of Torrefaction on Properties of Pellets Produced from Woody Biomass. *Energy Fuels* **2020**, *34*, 15343–15354. https://doi.org/10.1021/acs.energyfuels.0c02671.

19. Cahyanti, M.N.; Doddapaneni, T.R.K.C.; Kikas, T. Biomass torrefaction: An overview on process parameters, economic and environmental aspects and recent advancements. *Bioresour. Technol.* **2020**, *301*, 122737. https://doi.org/10.1016/j.biortech.2020.122737.

20. Amit Kumar, S. Solar Thermal Technologies for Biofuel Production: Recent Advances and Future Prospectus. *Green Energy Fuel Res.* **2025**, *2*, 13–25. https://doi.org/10.53941/gefr.2025.100002

21. Chen, W.-H. Progress in Green Energy and Fuel for Sustainability. *Green Energy Fuel Res.* **2024**, *1*, 13–22. https://doi.org/10.53941/gefr.2024.100003.

22. Richa, L.; Colin, B.; Pétrissans, A.; et al. Potassium carbonate impregnation and torrefaction of wood block for thermal properties improvement: Prediction of torrefaction performance using artificial neural network. *Appl. Energy* **2023**, *351*, 121894. https://doi.org/10.1016/j.apenergy.2023.121894.

23. Nishimura, M.; Iwasaki, S.; Horio, M. The role of potassium carbonate on cellulose pyrolysis. *J. Taiwan Inst. Chem. Eng.* **2009**, *40*, 630–637.

24. Richa, L.; Colin, B.; Pétrissans, A.; et al. Catalytic and char-promoting effects of potassium on lignocellulosic biomass torrefaction and pyrolysis. *Environ. Technol. Innov.* **2023**, *31*, 103193. https://doi.org/10.1016/j.eti.2023.103193.

25. Guo, F.; Liu, Y.; Wang, Y.; et al. Pyrolysis kinetics and behavior of potassium-impregnated pine wood in TGA and a fixed-bed reactor. *Energy Convers. Manag.* **2016**, *130*, 184–191. https://doi.org/10.1016/j.enconman.2016.10.055.

26. Zhao, N.; Li, B.-X. The effect of sodium chloride on the pyrolysis of rice husk. *Appl. Energy* **2016**, *178*, 346–352. https://doi.org/10.1016/j.apenergy.2016.06.082.

27. Zhu, C.; Huang, K.; Xue, M.; et al. Effect of $MgCl_2$ Loading on the Yield and Performance of Cabbage-Based Biochar. *Bioengineering* **2023**, *10*, 836. https://doi.org/10.3390/bioengineering10070836.

28. Pradana, Y.S.; Daniyanto; Hartono, M.; Prasakti, L.; et al. Effect of calcium and magnesium catalyst on pyrolysis kinetic of Indonesian sugarcane bagasse for biofuel production. *Energy Procedia* **2019**, *158*, 431–439. https://doi.org/10.1016/j.egypro.2019.01.128.

29. Müller, T.E.; Leitner, W. CO_2 Chemistry. *Beilstein J. Org. Chem.* **2015**, *11*, 675–677. https://doi.org/10.3762/bjoc.11.76.

30. Nyakuma, B.B.; Wong, S.L.; Faizal, H.M.; et al. Carbon dioxide torrefaction of oil palm empty fruit bunches pellets: Characterisation and optimisation by response surface methodology. *Biomass Convers. Biorefinery* **2022**, *12*, 5881–5900. https://doi.org/10.1007/s13399-020-01071-8.

31. Cho, D.-W.; Cho, S.-H.; Song, H.; et al. Carbon dioxide assisted sustainability enhancement of pyrolysis of waste biomass: A case study with spent coffee ground. *Bioresour. Technol.* **2015**, *189*, 1–6. https://doi.org/10.1016/j.biortech.2015.04.002

32. Kim, J.; Lee, J.; Kim, K.-H.; et al. Pyrolysis of wastes generated through saccharification of oak tree by using CO2 as reaction medium. *Appl. Therm. Eng.* **2017**, *110*, 335–345. https://doi.org/10.1016/j.applthermaleng.2016.08.200.

33. Guizani, C.; Escudero Sanz, F.J.; Salvador, S. Effects of CO_2 on biomass fast pyrolysis: Reaction rate, gas yields and char reactive properties. *Fuel* **2014**, *116*, 310–320. https://doi.org/10.1016/j.fuel.2013.07.101.

34. Chen, D.; Chen, F.; Cen, K.; et al. Upgrading rice husk via oxidative torrefaction: Characterization of solid, liquid, gaseous products and a comparison with non-oxidative torrefaction. *Fuel* **2020**, *275*, 117936. https://doi.org/10.1016/j.fuel.2020.117936.

35. Dutta, S.; Bhat, N.S. Catalytic Transformation of Biomass-Derived Furfurals to Cyclopentanones and Their Derivatives: A Review. *ACS Omega* **2021**, *6*, 35145–35172. https://doi.org/10.1021/acsomega.1c05861.

36. Jung, D.; Duman, G.; Zimmermann, M.; et al. Hydrothermal carbonization of fructose—Effect of salts and reactor stirring on the growth and formation of carbon spheres. *Biomass Convers. Biorefinery* **2023**, *13*, 6281–6297. https://doi.org/10.1007/s13399-021-01782-6.

37. Niu, Q.; Du, X.; Li, K.; et al. Role of catalyst porosity and acidity in nitrogen transformation during catalytic fast pyrolysis of microalgae: Study on extracted protein and model amino acids. *Energy Convers. Manag.* **2024**, *322*, 119210. https://doi.org/10.1016/j.enconman.2024.119210.

38. Nsibi, C.; Pozzobon, V.; Escudero-Sanz, J.; et al. Catalytic Effects of Potassium Concentration on Steam Gasification of Biofuels Blended from Olive Mill Solid Wastes and Pine Sawdust for a Sustainable Energy of Syngas. *Sustainability* **2024**, *16*, 9040.

39. Chen, W.-H.; Aniza, R. Specific chemical bioexergy and microwave-assisted torrefaction optimization via statistical and artificial intelligence approaches. *Fuel* **2023**, *333*, 126524. https://doi.org/10.1016/j.fuel.2022.126524.

40. Md Salim, R.; Asik, J.; Sarjadi, M.S. Chemical functional groups of extractives, cellulose and lignin extracted from native Leucaena leucocephala bark. *Wood Sci. Technol.* **2021**, *55*, 295–313. https://doi.org/10.1007/s00226-020-01258-2.

41. Liu, Y.; Rokni, E.; Yang, R.; et al. Torrefaction of corn straw in oxygen and carbon dioxide containing gases: Mass/energy yields and evolution of gaseous species. *Fuel* **2021**, *285*, 119044. https://doi.org/10.1016/j.fuel.2020.119044.

42. Shahbeik, H.; Kazemi Shariat Panahi, H.; Dehhaghi, M.; et al. Biomass to biofuels using hydrothermal liquefaction: A comprehensive review. *Renew. Sustain. Energy Rev.* **2024**, *189*, 113976. https://doi.org/10.1016/j.rser.2023.113976.

43. Basu, P. Chapter 7—Gasification Theory. In *Biomass Gasification, Pyrolysis and Torrefaction*, 3rd ed.; Basu, P., Ed.; Academic Press: Cambridge, MA, USA, 2018; pp. 211–262.

44. Eseltine, D.; Thanapal, S.S.; Annamalai, K.; et al. Torrefaction of woody biomass (Juniper and Mesquite) using inert and non-inert gases. *Fuel* **2013**, *113*, 379–388

45. Uemura, Y.; Saadon, S.; Osman, N.; et al. Torrefaction of oil palm kernel shell in the presence of oxygen and carbon dioxide. *Fuel* **2015**, *144*, 171–179. https://doi.org/10.1016/j.fuel.2014.12.050.

46. Cho, D.-W.; Lee, J.; Yoon, K.; et al. Pyrolysis of FeCl3-pretreated spent coffee grounds using CO_2 as a reaction medium. *Energy Convers. Manag.* **2016**, *127*, 437–442. https://doi.org/10.1016/j.enconman.2016.09.036.

47. Quan, C.; Zhou, Y.; Gao, N.; et al. Direct CO_2 capture from air using char from pyrolysis of digestate solid. *Biomass Bioenergy* **2023**, *175*, 106891. https://doi.org/10.1016/j.biombioe.2023.106891.

48. Sun, Y.; Dong, B.; Wang, L.; et al. Technology selection for capturing CO_2 from wood pyrolysis. *Energy Convers. Manag.* **2022**, *266*, 115835. https://doi.org/10.1016/j.enconman.2022.115835.

49. Wang, T.; Hsu, C.-L.; Huang, C.-H.; et al. Environmental impact of CO_2-expanded fluid extraction technique in microalgae oil acquisition. *J. Clean. Prod.* **2016**, *137*, 813–820. https://doi.org/10.1016/j.jclepro.2016.07.179.

50. Aho, A.; DeMartini, N.; Pranovich, A.; et al. Pyrolysis of pine and gasification of pine chars—Influence of organically bound metals. *Bioresour. Technol.* **2013**, *128*, 22–29. https://doi.org/10.1016/j.biortech.2012.10.093.

51. Frost, D.L.; Goroshin, S.; Levine, J.; et al. Critical Conditions for Ignition of Aluminum Particles in Cylindrical Explosive Charges. *AIP Conf. Proc.* **2006**, *845*, 972–975. https://doi.org/10.1063/1.2263484.

52. Barabulica, I.; Secula, M.S.; Asoltanei, A.M.; et al. Experimental Study on the Reaction of Magnesium in Carbon Dioxide and Nitrogen Atmosphere. *ChemEngineering* **2024**, *8*, 41.

53. Zhang, S.; Wang, J.; Zhu, S.; et al. Effects of $MgCl_2$ and $Mg(NO_3)_2$ loading on catalytic pyrolysis of sawdust for bio-oil and MgO-impregnated biochar production. *J. Anal. Appl. Pyrolysis* **2020**, *152*, 104962. https://doi.org/10.1016/j.jaap.2020.104962.

54. Aniza, R.; Chen, W.-H.; Lin, Y.-Y.; et al. Independent parallel pyrolysis kinetics of extracted proteins and lipids as well as model carbohydrates in microalgae. *Appl. Energy* **2021**, *300*, 117372. https://doi.org/10.1016/j.apenergy.2021.117372.

55. Chen, R.; Zhang, S.; Cong, K.; et al. Insight into synergistic effects of biomass-polypropylene co-pyrolysis using representative biomass constituents. *Bioresour. Technol.* **2020**, *307*, 123243. https://doi.org/10.1016/j.biortech.2020.123243.

56. Menéndez, J.A.; Arenillas, A.; Fidalgo, B.; et al. Microwave heating processes involving carbon materials. *Fuel Process. Technol.* **2010**, *91*, 1–8. https://doi.org/10.1016/j.fuproc.2009.08.021.

57. Dupont, C.; Boissonnet, G.; Seiler, J.-M.; et al. Study about the kinetic processes of biomass steam gasification. *Fuel* **2007**, *86*, 32–40. https://doi.org/10.1016/j.fuel.2006.06.011.

58. Kawamoto, H. Review of reactions and molecular mechanisms in cellulose pyrolysis. *Curr. Org. Chem.* **2016**, *20*, 2444–2457.